

University of Warwick institutional repository: <http://go.warwick.ac.uk/wrap>

A Thesis Submitted for the Degree of PhD at the University of Warwick

<http://go.warwick.ac.uk/wrap/36213>

This thesis is made available online and is protected by original copyright.

Please scroll down to view the document itself.

Please refer to the repository record for this item for information to help you to cite it. Our policy information is available from the repository home page.

THE DESIGN OF SWITCHED RELUCTANCE MOTORS FOR EFFICIENT ENERGY CONVERSION

Alexandros M. Michaelides

Thesis submitted for the examination of degree of Doctor of Philosophy

Department of Engineering
University of Warwick
Coventry, CV4 7AL

September 1994

This copy of the thesis has been supplied on condition that anyone who consults it is understood to recognize that the copyright rests with its author and that no quotation from the thesis and no information derived from it may be published without the prior written consent of the author or the University (as may be appropriate).

To my family,

Michael, Androulla

and

Vangelis.

TABLE OF CONTENTS

Acknowledgements	xi
List of figures and tables	xii
List of symbols	xxiii
Abstract	xxviii
Preface	xxix
Chapter 1 The switched reluctance drive: an overview	1
1.1 Historical background to the reluctance motor.	1
1.2 A present day switched reluctance drive.	3
1.3 The switched reluctance motor.	5
1.4 Existing power converter circuits for the switched reluctance drive.	9
1.4.1 Power converter with bifilar motor windings.	9
1.4.2 Power converter with split dc supply.	11
1.4.3 Capacitor dump power converter.	11
1.4.4 Power converter with the asymmetric half-bridge.	13
1.4.5 Shared switch, asymmetric half-bridge power converter.	14
1.5 Rotor position measurement techniques.	16
1.5.1 Slotted disk arrangements.	16
1.5.2 Optical shaft encoders.	17
1.5.3 Brushless resolvers.	18
1.5.4 Sensorless position detection.	18

1.6 Phase current measurement and control.	18
1.7 Market applications of the switched reluctance drive.	20

Chapter 2 The switched reluctance drive: aspects of design, construction and testing 22

2.1 Switched reluctance motor design.	22
2.1.1 Low phase numbers.	23
2.1.2 Higher phase numbers - a new motor design.	27
2.2 Introduction to electromagnetic finite element analysis.	28
2.2.1 The need for finite element modelling.	28
2.2.2 Electromagnetic field equations.	29
2.2.3 Finite element model creation.	30
2.2.4 Field values computed using the finite element analysis package.	32
I. Flux linkage computation.	32
II. Energy considerations.	35
III. Instantaneous static torque: the Maxwell stress tensor.	36
2.3 Construction of power converter circuits.	37
2.3.1 Overview of semiconductor devices for power converters.	37
I. The ideal switch.	37
II. The thyristor.	38
III. The bipolar transistor.	39
IV. The MOSFET.	39
V. The insulated gate bipolar transistor (IGBT).	40
2.3.2 Selection of type and rating of the semiconductor devices.	40
2.3.3 Gate drive circuits for power MOSFETs.	41

I. Selection of the gate drive isolating device.	41
II. Gate drive circuit design for a top switch.	42
III. Bottom switch gate drive circuit design.	44
2.3.4 Snubber circuits.	44
2.4 The control board.	46
2.4.1 Current sensing and control.	47
I. Hysteresis type current chopping regulator.	47
II. Fixed frequency pwm current regulator.	47
2.4.2 The implementation of logic functions - XILINX.	49
2.5 Experimental arrangements.	50
2.5.1 Description of the test rigs.	50
2.5.2 Flux linkage measurement.	51
I. Measurement of rising current.	51
II. Measurement of decaying current.	53
III. Biasing the electromagnetic field.	53
2.5.3 Measurement of static torque.	54
I. The dc generator test rig.	54
II. The eddy current test rig.	54
2.5.4 Measurement of dynamic torque.	54
I. The dc generator test rig.	54
II. The eddy current test rig.	55
2.6 Review of fundamental aspects of switched reluctance motor technology.	55

Chapter 3 Electromagnetic analysis of the switched reluctance motor.

3.1 Electromechanical energy conversion theory.	58
3.1.1 Singly excited systems.	58
3.1.2 Exciting two phases simultaneously - a new	

modelling procedure.	61
I. Flux patterns in the 4-phase motor.	61
II. Computation of coenergy in a doubly excited system.	61
3.2 The 150W 4-phase motor.	68
3.2.1 Single phase excitation.	68
3.2.2 Simultaneous excitation of two phase windings in the 4-phase machine - normal machine operation.	70
3.2.3 Bulk saturation effects.	72
3.3 Electromagnetic design of switched reluctance motors for low torque ripple - a new alternative.	77
3.4 The 4kW 7-phase switched reluctance motor.	80
3.4.1 Electromagnetic field considerations.	84
3.4.2 Instantaneous / average torque considerations.	87
3.5 Summary of fundamental modelling considerations.	89

Chapter 4 The effect of end-core flux on the performance of the switched reluctance motor

4.1 The need for three-dimensional modelling.	91
4.2 Three-dimensional effects in the switched reluctance machine.	93
4.3 Comparison between two-dimensional and three-dimensional finite element analysis results with experimental results.	95
4.3.1 Flux linkage.	95
4.3.2 Static torque.	99
4.4 Correction charts for two-dimensional finite element modelling.	101
4.4.1 Flux linkage.	101
4.4.2 Comparison with a 140mm stack 7-phase switched reluctance motor.	106
4.4.3 Static torque.	106

4.5 Discussion on other effects.	109
4.5.1 Anisotropy.	109
4.5.2 Conductor overhang / inside coil radius.	112
4.5.3 Sources of error.	113
4.6 Conclusions.	115

Chapter 5 The SRDESIGN package: Modelling and Simulation 116

5.1 Modelling magnetisation curves for singly excited systems.	118
5.1.1 'Extreme' (aligned and unaligned) rotor positions.	118
5.1.2 Intermediate rotor positions.	119
I. Low excitation.	119
II. High excitation.	120
5.2 Modelling magnetisation curves for switched reluctance motors with two phases simultaneously excited.	122
5.2.1 'Extreme' rotor positions.	122
5.2.2 Intermediate rotor positions.	123
5.3 Dynamic operation considerations.	125
5.3.1 Base speed estimation.	127
5.3.2 Commutation.	127
5.3.3 Maximum speed for a given current.	131
5.3.4 Variation of current with angle.	132
5.3.5 Time stepping algorithm for current prediction.	133
5.4 Computation of output power and losses.	135
5.4.1 Computation of the rms phase current I_{rms} .	135
5.4.2 Copper losses.	136
5.4.3 Iron losses.	138
5.4.4 Output power, input power and efficiency.	140
5.5 Structure of the SRDESIGN package.	141

5.5.1 Unit CONSTANT.	141
5.5.2 Unit CURRCALC.	142
5.5.3 Unit DRAW.	142
5.5.4 Unit GLOBALS.	143
5.5.5 Unit INPUTS.	143
5.5.6 Unit MENUS.	143
5.5.7 Unit RESULTS.	143
5.5.8 Main Program.	144
5.6 Summary.	144

Chapter 6 SRDESIGN verification: dynamic testing of switched reluctance motors 146

6.1 The use of λ / i diagrams in SRDESIGN.	146
6.2 Testing the 4-phase 150W motor.	148
6.2.1 Experimental arrangement.	148
6.2.2 Test presentation.	149
6.2.3 Sources of error.	158
6.3 Testing the 4kW 7-phase motor.	159
6.3.1 Experimental arrangement.	159
6.3.2 7-phase motor testing.	159
6.4 SRDESIGN practicality.	164

Chapter 7 The 5-phase switched reluctance drive: design, construction and performance 169

7.1 5-phase motor design.	169
7.1.1 Selection of stator pole arc and back-iron width.	169
7.1.2 Stator / rotor pole arcs.	174
7.1.3 Rotor slot depth.	179

7.1.4 Choice of steel grade.	180
7.2 5-phase motor construction.	180
7.2.1 Construction procedure.	180
7.2.2 Potential improvements of the constructed 5-phase motor.	185
7.3 Measurement of flux linkage and static torque.	186
7.4 Static performance comparison between the 5-phase prototype and the 4-phase Oulton motor.	188
7.5 Dynamic performance prediction.	190
7.6 Experimental arrangement.	196
7.7 Test presentation.	197
7.7.1 On-state angle analysis.	199
7.7.2 Maximum drive efficiency analysis.	202
7.7.3 Drive and motor efficiency considerations.	206
7.8 Comparison of experimental results with simulated data.	208
7.9 Market applications of the 5-phase switched reluctance drive.	211
Chapter 8 Conclusion	215
8.1 Main conclusions and author's contribution to knowledge.	215
8.2 Areas of further work.	217
References	219
Appendices	226
A. Electromagnetic equations governing the finite element analysis software.	226
A.1 The two-dimensional finite element code	

(OPERA-2D).	226
A.2 The three-dimensional algorithm (OPERA-3D / TOSCA).	227
B. Data sheets for power semiconductor devices used in this project.	229
C. Comparison on the basis of equal copper losses.	236
D. Loss data and BH curves for LOSIL 500-50.	238
E. Operating principles of stepping motors.	240
E.1 The variable reluctance stepping motor.	240
E.2 The permanent magnet (PM) stepping motor.	240
E.3 The hybrid stepping motor.	241
F. A brief description of the induction motor.	244

ACKNOWLEDGEMENTS

I would like to thank Dr. Charles Pollock for his supervision and support throughout the project. Thanks are also due to the technical staff at the University, (especially Andy Leeson, Stuart Edris and Colin Major) and at Vector Fields Ltd for help in times of need, and to Electrodrives Ltd for support during the motor assembly stage. I would also like to thank my colleagues Po Wa Lee, Kevin Richardson, Helen Pollock, Chi-Yao Wu, Mike Barnes and Cliff Joliffe for useful discussions, but most of all Antigoni for continuous help and encouragement.

LIST OF FIGURES AND TABLES

Chapter 1

- Fig. 1.1 Principle of Davidson's six-step reluctance motor.
- Fig. 1.2 Block diagram of a switched reluctance drive.
- Fig. 1.3 Plan of the laminations of a typical 4-phase motor.
- Fig. 1.4 a) Equivalent circuit of a switched reluctance motor phase winding.
b) Typical waveforms.
- Fig. 1.5 Power converter with bifilar motor windings.
- Fig. 1.6 Power converter with split dc power supply.
- Fig. 1.7 Capacitor dump power converter.
- Fig. 1.8 Power converter with asymmetric half-bridge.
- Fig. 1.9 Shared switch, asymmetric half-bridge converter.
- Table 1.1 Shared switch converter switching algorithm.

Chapter 2

- Fig. 2.1 A 2-phase 4/2 motor.
- Fig. 2.2 The 2-phase 4/2 motor with a stepped gap, showing self-starting

capability.

- Fig. 2.3 3-phase 12/10 motor with 2 teeth per stator pole.
- Fig. 2.4 3-phase 12/10 motor, with short flux paths.
- Fig. 2.5 The proposed machine configuration. A 5-phase 10/8 motor showing short flux-paths both producing positive torque. Phases 1 and 2 are simultaneously excited.
- Fig. 2.6 a) The two-dimensional finite element mesh for the 150W 4-phase motor.
b) The three-dimensional finite element mesh for the 150W 4-phase motor (air regions not shown for clarity).
- Fig. 2.7 a) The upper switch drive circuit.
b) The lower switch drive circuit.
- Fig. 2.8 A complete turn off-snubber circuit.
- Fig. 2.9 A hysteresis type current chopping regulator.
- Fig. 2.10 The constructed fixed frequency pwm current regulator.
- Fig. 2.11 The dc generator test bed.
- Fig. 2.12 Circuit arrangement for flux linkage measurement.
- Fig. 2.13 Flux linkage measurement in a biased field.

Chapter 3

Fig. 3.1 A 2-phase 4/2 motor, illustrating movement through a rotor step.

Fig. 3.2 λ / i diagram of an ideal excitation cycle.

Fig. 3.3

- a) Flux pattern in a singly excited 4-phase motor.
- b) Flux pattern in a doubly excited 4-phase motor.
- c) Resulting primary **B**-field in a doubly excited 4-phase motor.
- d) Geometrical considerations in a 4-phase motor.
- e) Excitation sequence in the 4-phase motor.

Fig. 3.4 Integration path in a doubly excited system.

Fig. 3.5 λ / i diagram (4-phase motor, 1 phase excited).

Fig. 3.6 λ / θ diagram (4-phase motor, 1 phase excited).

Fig. 3.7 T / θ diagram (4-phase motor, 1 phase excited).

Fig. 3.8 System λ / i diagram (4-phase motor, 2 phases excited).

Fig. 3.9 λ / θ diagram (4-phase motor, 2 phases excited).

Fig. 3.10 T / θ diagram (4-phase motor, 2 phases excited).

Table 3.1 Average torque figures for the 150W 4-phase motor.

Table 3.2 Dimensions of the 4-phase motor models.

Fig. 3.11 λ / θ diagram (4-phase motor, leading phase).

- Fig. 3.12 λ / i diagram (4-phase Mk II motor).
- Fig. 3.13 T / θ diagram (4-phase motor, 2 phases excited).
- Fig. 3.14 T / θ diagram (4-phase Mk II motor).
- Table 3.3 Average torque figures for the 4-phase motor models.
- Fig. 3.15 a) The 4kW 7-phase motor laminations.
b) Excitation patterns in the 7-phase motor.
c) Flux distribution in the 7-phase motor (long loops).
d) Flux distribution in the 7-phase motor (short loops).
- Fig. 3.16 Energy conversion loop for low speed cycle (7-phase, $i_{bias} = 10A$).
- Fig. 3.17 Energy conversion loop for high speed cycle (7-phase, $i_{bias} = 10A$).
- Fig. 3.18 λ / θ diagram in the leading phase (7-phase motor, $i = 10A$).
- Fig. 3.19 T / θ diagram (7-phase motor, $i = 5A$ and $10A$).
- Table 3.4 Average torque figures for the 7-phase motor.

Chapter 4

- Fig. 4.1 The computed and experimental λ / i diagram for an 8/6 4-phase motor.
- Fig. 4.2 a) Flux distribution in an excited stator pole with the rotor in the aligned position ($i = 3A$).
b) Flux distribution in an excited stator pole with the rotor in the

unaligned position ($i = 3A$).

c) Flux distribution in the 4-phase motor (aligned position).

Fig. 4.3 Computed and experimental static torque profile of the 4-phase 8/6 motor. ($i = 5A$ and $10A$).

Fig. 4.4 Variation of end-core flux with rotor position in the experimental motor.

Fig. 4.5 Chart showing the correction factor which needs to be applied to two-dimensional solutions to account for end-core flux (aligned position).

Fig. 4.6 Percentage increment in flux linkage due to end-core effects as a function of rotor position.

a) $i = 5A$

b) $i = 10A$

Fig. 4.7 a) λ / θ diagram for the 7-phase machine ($i = 10A$).
b) Flux linkage increment / rotor position diagram (7-phase motor, $i = 10A$).

Fig. 4.8 Percentage increment in static torque due to end-core effects as a function of rotor position.

a) $i = 5A$

b) $i = 10A$

Fig. 4.9 Illustration of the difference in two-dimensional modelling results using different scaling approaches to account for anisotropy.

Fig. 4.10 λ / i diagrams for the experimental motor model assigned different

packing factors.

- Fig. 4.11 Illustration of overhang and inside coil radius.
- Fig. 4.12 Variation of end-core flux with inside coil radius and overhang (aligned position).
- Fig. 4.13 **Corrected** λ / i diagram based on a two-dimensional model of the experimental machine.

Chapter 5

- Fig. 5.1 Structure of the SRDESIGN program.
- Fig. 5.2 Obtaining magnetisation (λ / i) curves for singly excited systems.
- Fig. 5.3 λ / θ variation in singly excited systems.
- Fig. 5.4 Obtaining system λ / i characteristics for switched reluctance motors with two phases simultaneously excited.
- Fig. 5.5 λ / θ curves for doubly excited switched reluctance motors.
- Fig. 5.6 Dynamic operation considerations.
- Fig. 5.7 Illustration of principal winding dimensions.
- Fig. 5.8 Slot filling in the switched reluctance motor.

Chapter 6

- Fig. 6.1 Flux linkage / current diagram (4-phase motor, 1 phase excited).
- Fig. 6.2 The experimental 4-phase drive.
- Table 6.1 Sample SRDESIGN printout for the 150W 4-phase motor.
- Fig. 6.3 Notation used throughout chapter 6.
- Fig. 6.4 Torque / speed curve (4-phase motor, fixed commutation angles).
- Fig. 6.5 Power loss in the 4-phase motor (fixed commutation angles).
- Fig. 6.6 Maximum torque / speed characteristic (4-phase motor, angular conduction period = 15°).
- Fig. 6.7 Maximum torque / speed characteristic (4-phase motor, angular conduction period = 20°).
- Fig. 6.8
- a) Experimental i / θ profile @ 450rpm.
 - b) Experimental i / θ profile @ 1500rpm.
 - c) SRDESIGN i / θ profile @ 450rpm.
 - d) SRDESIGN i / θ profile @ 1500rpm.
- Fig. 6.9
- a) SRDESIGN λ / θ diagram @ 450rpm.
 - b) SRDESIGN λ / i diagram @ 450rpm.
- Fig. 6.10 The experimental 7-phase drive.
- Fig. 6.11 Maximum torque / speed characteristic (7-phase motor, short loops).

- Fig. 6.12 Efficiency curve (7-phase motor, short loops).
- Fig. 6.13 Maximum torque / speed characteristic (7-phase motor, long loops).
- Fig. 6.14 Efficiency curve (7-phase motor, long loops).
- Fig. 6.15
- a) SRDESIGN i / θ profile @ 1000rpm (short loops).
 - b) SRDESIGN i / θ profile @ 1000rpm (long loops).
 - c) SRDESIGN λ / θ diagram @ 1000rpm (short loops).
 - d) SRDESIGN λ / θ diagram @ 1000rpm (long loops).
 - e) SRDESIGN λ / i diagram @ 1000rpm (short loops).
 - f) SRDESIGN λ / i diagram @ 1000rpm (long loops).

Chapter 7

- Fig. 7.1 Dimensions of a 10/8 5-phase motor.
- Fig. 7.2 Variation of stator bore with average torque (constant stator pole arc).
- Fig. 7.3 Variation of average torque with stator pole arc / pitch ratio.
- Fig. 7.4 Illustration of the 'zero torque period' concept.
- Fig. 7.5
- a) Excitation cycle in the 5-phase motor.
 - b) **B**-field distribution in the 5-phase motor (short flux loops, 6° rotor position).
 - c) **B**-field distribution in the 5-phase motor (long flux loops, 6° rotor position).
- Fig. 7.6 a) Illustration of fringing effects in the unaligned position.

b) Rotor slot depth considerations.

Fig. 7.7 Final drawing of the 5-phase motor laminations.

Table 7.1 Dimensions of the experimental 5-phase motor.

Fig. 7.8 The 5-phase construction process, through a set of photographs.

Fig. 7.9 Flux linkage / current diagram (5-phase motor, 1 phase excited).

Fig. 7.10 Static torque profile for the 5-phase motor ($i = 12.75\text{A}$).

Table 7.2 Static torque developed by the 4-phase Oulton and 5-phase prototype motors (equal copper loss).

Fig. 7.11 a) Torque / speed curve predicted by SRDESIGN (asymmetric half-bridge converter).
b) Efficiency / speed curve predicted by SRDESIGN (asymmetric half-bridge converter).

Table 7.3 SRDESIGN simulated data for the 5-phase short flux loop motor (asymmetric half-bridge converter).

Fig. 7.12 a) Torque / speed curve predicted by SRDESIGN (shared switch converter).
b) Efficiency / speed curve predicted by SRDESIGN (shared switch converter).

Table 7.4 SRDESIGN simulated data for the 5-phase short flux loop motor (shared switch converter).

- Fig. 7.13 a) Section from the experimental 5-phase drive.
b) Photograph of the 5-phase drive.
- Fig. 7.14 a) Efficiency contours at half load (long loops, conduction angle = 18°).
b) Efficiency contours at half load (short loops, conduction angle = 18°).
- Fig. 7.15 a) Efficiency contours at half load (long loops, conduction angle = 13.5°).
b) Efficiency contours at half load (short loops, conduction angle = 13.5°).
- Fig. 7.16 a) Variation of torque and efficiency with speed (300V, long loops).
b) Variation of torque and efficiency with speed (300V, short loops).
- Fig. 7.17 a) Experimental current profile at 900rpm, 25Nm (long loops).
b) Experimental current profile at 900rpm, 25Nm (short loops).
- Fig. 7.18 Torque / speed profile (firing angle = 0° , unaligned position).
- Fig. 7.19 Representation of the phase current pulse at $\omega = 1283\text{rpm}$, $T = 21.7\text{Nm}$.
- Fig. 7.20 Comparison of experimental results with SRDESIGN (firing angle = 1.5° , short loops, conduction angle = 13.5°).
- Fig. 7.21 a) Experimental current profile at 800rpm (short loops).
b) SRDESIGN simulated phase current profile at 800rpm (short loops).

- Fig. 7.22 a) SRDESIGN simulated λ / θ diagram at 800rpm (short loops).
 b) SRDESIGN simulated λ / i diagram at 800rpm (short loops).

Table 7.5 Comparison of the 5-phase drive efficiency with competing induction motors and switched reluctance drives (all constructed in D112 frames).

Appendix E

Fig. E.1 A 2-phase PM stepping motor.

Fig. E.2 A 4-phase hybrid stepper motor.

Fig. E.3 Hybrid stepper operating principles.

Appendix F

Fig. F.1 The 3-phase inverter-fed induction motor.

LIST OF SYMBOLS

A	Magnetic vector potential.
A	Cross-sectional area.
A_o	Area enclosed by the operating trajectory on the λ / i diagram.
A_r	Area on the λ / i diagram representing energy returned to the supply.
B	Flux density.
c	Commutation ratio.
C	Capacitance.
C_o	Zero crossing of a function.
d	Diameter.
D	Displacement current.
E	Electric field strength.
f	Frequency.
F	Force.
g	airgap length.
H	Magnetic field intensity.

i, I	Current.
J	Current density.
k_{he}	Back-emf constant at high excitation.
k_{le}	Back-emf constant at low excitation.
K_c	Coil fill factor.
K_e	Eddy current constant.
K_h	Hysteresis constant.
K_s	Slot fill factor.
l	Length.
L	Winding inductance.
M	Slope (gradient) of a function.
n	Efficiency.
N_{ph}	Number of turns per phase.
N_r	Number of rotor poles.
N_s	Number of stator poles.
P	Power.

P_{Cu}	Copper loss.
P_{fw}	Windage and friction loss.
P_{Fe}	Iron loss.
P1	Phase 1 of the switched reluctance motor.
pf	Packing factor.
q	Number of phases.
r	Rotor pole pitch.
R	Winding resistance per phase.
R	Radius.
$step$	Step angle.
s	Stator pole pitch.
S	Vector describing a surface.
Sa,b,c	Switching devices.
t	Time.
t_s	Stator pole width.
t_{si}	Sampling interval.

T	Torque.
v, V	Voltage.
V_b	Back-emf.
v_o	Volume.
W	Energy.
y	Stator back-iron (yoke) thickness.
α	Temperature coefficient of resistance.
β_s	Stator pole arc.
β_r	Rotor pole arc.
$\alpha_f, \beta_f, \gamma_f$	Coefficients of the sigmoidal function.
ϵ	Electric permittivity.
θ	Rotor (angular) position.
λ	Winding flux linkage.
μ	Permeability.
ρ	Resistivity.
σ	Conductivity.

τ	Maxwell stress tensor.
ϕ	Reduced scalar potential.
Φ	Magnetic flux.
Ψ	Total magnetic scalar potential.
ω	Rotational speed.
ω_b	Base speed.
Ω_j	A region in space containing current.

ABSTRACT

A new switched reluctance motor configuration is proposed, in which the windings are arranged to encourage short magnetic flux paths within the motor. Short flux path motor configurations have been modelled extensively using electromagnetic finite element analysis. It is demonstrated that short flux paths significantly reduce the MMF required to establish the **B**-field pattern in a motor; as a result copper losses are reduced. In addition, hysteresis and eddy current losses are decreased as the volume of iron in which iron losses are generated is reduced.

Short flux paths are formed when two adjacent phase windings, configured to give neighbouring stator teeth opposite magnetic polarity, are simultaneously excited. In order to accurately model short flux path machines, a thorough electromagnetic analysis of doubly excited systems is adopted. The proposed modelling theory forms the basis for design considerations that can optimise the performance of the 4-phase and 5-phase switched reluctance motors.

The electromagnetic theory of doubly excited systems is used in conjunction with a dynamic simulation program, written in Turbo Pascal, to design a 5-phase switched reluctance motor that exploits the advantages of short flux paths. Test results from the constructed prototype confirm that short flux paths significantly improve the efficiency of the switched reluctance motor. The 5-phase prototype achieves higher efficiency than all known prior art switched reluctance motors and industrial induction machines constructed in the same frame size. At the [1300rpm, 20Nm] operating point the efficiency of the 5-phase drive was measured to be 87%. The corresponding motor efficiency was in excess of 89.5%.

PREFACE

The switched reluctance motor (SRM) is an electric motor consisting of a salient pole stator with concentrated excitation windings and a salient pole rotor with no conductors or permanent magnets. Torque is produced by the tendency of the rotating member to move to the position which maximises the flux linking the excited stator phase. Rotation is maintained by switching on and off the current in the phase windings in synchronism with the position of the rotor. The direction of the torque does not depend on the sign of the flux and current, but only on the sign of the rate of change of reluctance with rotor position. This offers the advantage of simple, unipolar power converter circuits.

Switched reluctance motors of three and four phases have received considerable attention in recent years, as low cost robust variable speed drives. The 3-phase 6/4 (i.e. 6 poles on the stator and 4 poles on the rotor) motor ensures starting capability in either direction. However, the torque profile of this motor contains a significant amount of ripple. In contrast, the 4-phase 8/6 configuration can operate with two phases simultaneously excited which helps to minimise the problem with torque dips. The penalty incurred is that of increased iron loss, due to the higher fundamental switching frequency.

This thesis describes the design and development of a 5-phase 10/8 switched reluctance drive. The 5-phase motor exploits the advantages of a new winding configuration which encourages short flux paths within the motor. Short flux paths reduce the MMF required to establish the **B**-field pattern in the motor, leading to a significant reduction in copper losses. In addition, the volume of iron in which hysteresis and eddy current losses are generated is reduced considerably. The proposed 5-phase motor can operate with (at least) two phases excited at any time to produce smooth torque with high efficiency.

A thorough electromagnetic analysis of doubly excited systems, which relates to

switched reluctance motors operating with two phase windings conducting at any time, is proposed in this thesis. Mutual coupling and saturation effects are investigated. Accurate electromagnetic modelling forms the basis for design considerations that can optimise the performance of the 4-phase and 5-phase switched reluctance motors.

Electromagnetic finite element analysis (FEA) is used extensively to model the static performance of a number of different switched reluctance drives. The finite element analysis program is used not only as a motor design tool but also as a means of validating the electromagnetic theory of doubly excited switched reluctance motors. Switched reluctance motor structures are modelled using two and three-dimensional finite element analysis. The effect of end-core flux on the performance of the switched reluctance motor is investigated.

Finite element analysis is employed in the lamination design of the 5-phase prototype together with a sizing / dynamic simulation program, which is developed in Turbo Pascal. Test results from the constructed 5-phase motor confirm the significant benefits arising when the machine is configured for short flux paths.

The thesis has eight chapters, a list of references and six appendices. Chapter 1 gives a historical background to the reluctance motor before describing in more detail the components of the present day switched reluctance drive.

Chapter 2 describes the more usual switched reluctance motor designs and highlights their merits and shortcomings. The new motor design is subsequently described in which the windings are configured for short flux paths. The advantages of the proposed configuration over prior art motors are highlighted. In addition, the chapter introduces finite element analysis, the 'software tool' used for electromagnetic design of switched reluctance motors. The design and construction of 'hardware tools', such as drive circuits for power converters and controller components is also described. These were employed to test a number of different

switched reluctance motors throughout the project. The chapter concludes with an account of the experimental procedures which have been adopted.

Chapter 3 introduces an electromagnetic analysis of doubly excited systems which relates to switched reluctance motors operating with two phases excited at any time. The new modelling procedure includes the effects of mutual coupling and accounts for the increased flux density, present in some parts of the magnetic circuit when two phases are simultaneously excited. The chapter focuses on the implementation of the modelling theory on a 150W 4-phase and a 4kW 7-phase machine. The design of 4-phase switched reluctance drives for low torque ripple is proposed. Finite element analysis results from a 4kW 7-phase motor, configured for long and short flux paths, highlight the advantages offered by the latter configuration.

Chapter 4 describes the effect of end-core flux on the performance of the switched reluctance motor. The chapter begins with a description of three-dimensional effects in the switched reluctance motor. The superiority of three-dimensional modelling is asserted by comparing test results from the 150W 4-phase motor with two-dimensional and three-dimensional finite element modelling results. Correction charts are set up to account for end-core flux at a range of rotor positions and excitations, to alleviate the need for three-dimensional modelling of the switched reluctance motor. An extensive discussion into three-dimensional modelling of anisotropic material structures is also given. In addition, a useful description of the effect of end-core flux on instantaneous static torque production is presented.

The following chapter describes the work that was undertaken in this project to develop SRDESIGN; a program written in Turbo Pascal for dynamic simulation of switched reluctance drives. The principal mathematical formulations incorporated in the program are described.

The accuracy of the dynamic simulation program is verified in chapter 6, where

simulated data from the 150W 4-phase and 4kW 7-phase motors is compared with experimental results.

Chapter 7 describes the design, construction and testing of the 5-phase switched reluctance drive. Finite element analysis is used to compare the static performance of the 5-phase motor with that of a 4-phase machine (based on the Oulton motor). Test results from the 5-phase prototype are compared with simulated data obtained using SRDESIGN. The performance of the 5-phase motor is compared to that of a 'standard' and 'high efficiency' induction motor of the same frame size.

The main conclusions of the work are highlighted in chapter 8. The author's contribution to knowledge is described and areas of future work are proposed.

The list of references is followed by appendices containing mathematical derivations and power device data sheets. 'Members' of the stepping motor family are also reviewed and a brief description of operation of the induction motor is given.

Chapter 1

THE SWITCHED RELUCTANCE DRIVE: AN OVERVIEW

1.1 Historical background to the reluctance motor.

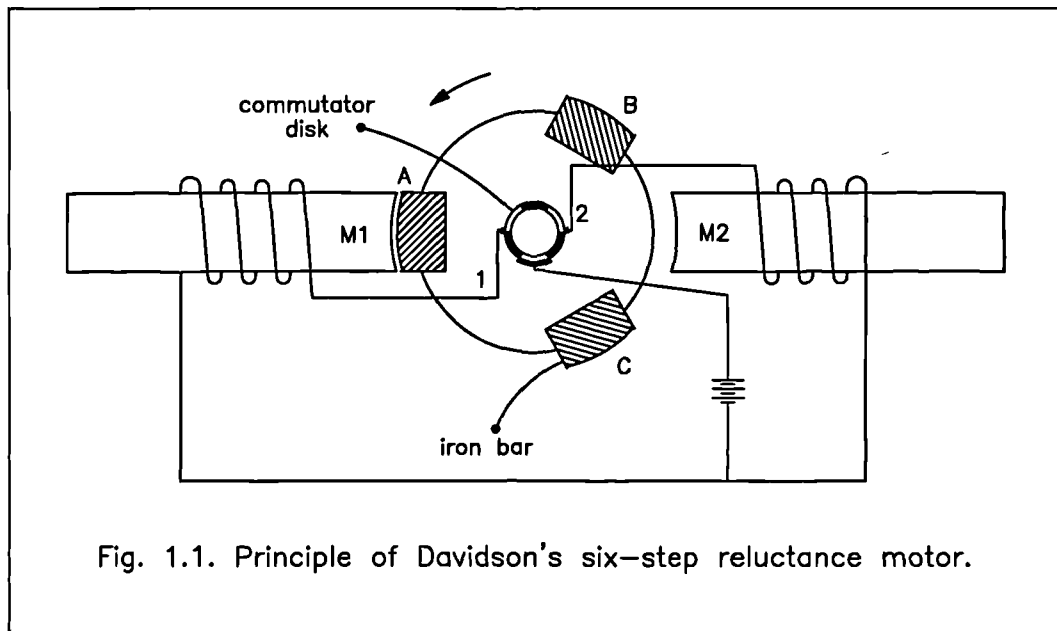
The operation of the switched reluctance motor relies on the 'alignment principle' which gives rise to reluctance torque. When a salient pole rotor is turned from the position of alignment with the excited phase of a salient pole stator, a torque tending to realign the members will be developed. The phenomenon has been known ever since the first experiments on electromagnetism. In the first half of the 19th century, scientists all over the world were experimenting with this effect in order to produce an electromechanical energy conversion device. Their early designs were named 'electromagnetic engines'. In a book [1] published in 1859, H. M. Noad describes much of this early development work. Some of the early designs which he describes show remarkable similarity to the switched reluctance motor of today.

In 1838, W. H. Taylor obtained a patent for his electromagnetic engine in the United States and subsequently, on the 2nd of May 1840, he was granted a patent [2] in England for the same engine. The structure was composed of a wooden wheel, on the surface of which were mounted seven pieces of soft iron, called armatures, equally spaced around the periphery. The wheel rotated within a suitable framework in which four electromagnets were mounted. The soft iron pieces could pass over each electromagnet in turn without touching it. In his description of the engine, Taylor said that "the magnets must also be so fixed in the framework that when the centre of one of them is opposite the centre of an armature, another magnet shall have one of its edges just opposite the edge of an armature, and the third its contrary edge opposite a contrary edge of another

armature and the fourth magnet directly in the centre between the two". This arrangement ensured that there was always at least one of the electromagnets capable of producing torque irrespective of the direction of rotation. It is for the same reason that today's reluctance motors have different numbers of rotor and stator poles. Taylor's wheel had a mechanical commutator which magnetised an electromagnet until a soft iron pole piece was brought into alignment and then demagnetised that electromagnet when its "attractive power" ceased to "operate with advantage". A lever arrangement on the commutator allowed the turn-on angle of the electromagnets to be altered so that the engine could be stopped and reversed. Taylor also pointed out that current needs only to flow through the electromagnet in one direction, making the connection to the power source a simpler task. A detailed account of this engine was given in the *Mechanics Magazine* [3] in 1840. This resulted in many other scientists describing similar work which they had completed.

One such person was Robert Davidson of Aberdeen who wrote to the editor of *Mechanics Magazine* [4] claiming priority over Taylor's invention, as he had built a very similar machine himself. Davidson pursued his ideas further and in September 1842 successfully powered an electric locomotive on the Edinburgh to Glasgow Railway [5,6], using a six-step reluctance motor. The motor comprised of two electromagnets, mounted 180 mechanical degrees apart in space, as shown in fig. 1.1. Between them was a wooden rotor on which three equally spaced rectangular bars of iron were fixed. Switching between the two electromagnets was being synchronised to appropriate rotor angles by a commutator. The commutator consisted of a disk, divided into twice as many parts as there were armatures, each part being alternately copper or some non-conducting material. The disk was mounted on the motor shaft and revolved at the rotor speed. One end of the winding on each 'stator pole' was connected to the negative battery terminal. The other "extremity" of each winding made contact with the rotating disk. The disk also made contact with a wire feeding into the positive battery terminal.

One problem faced by all the early inventors was the size of the batteries which were required to power their machines. Another major problem was likely to have been heating losses in the iron which was not laminated. In addition, the unbalanced nature of the magnetic forces required very rigid construction or very large air gaps in order to avoid contact between the stationary and moving parts.



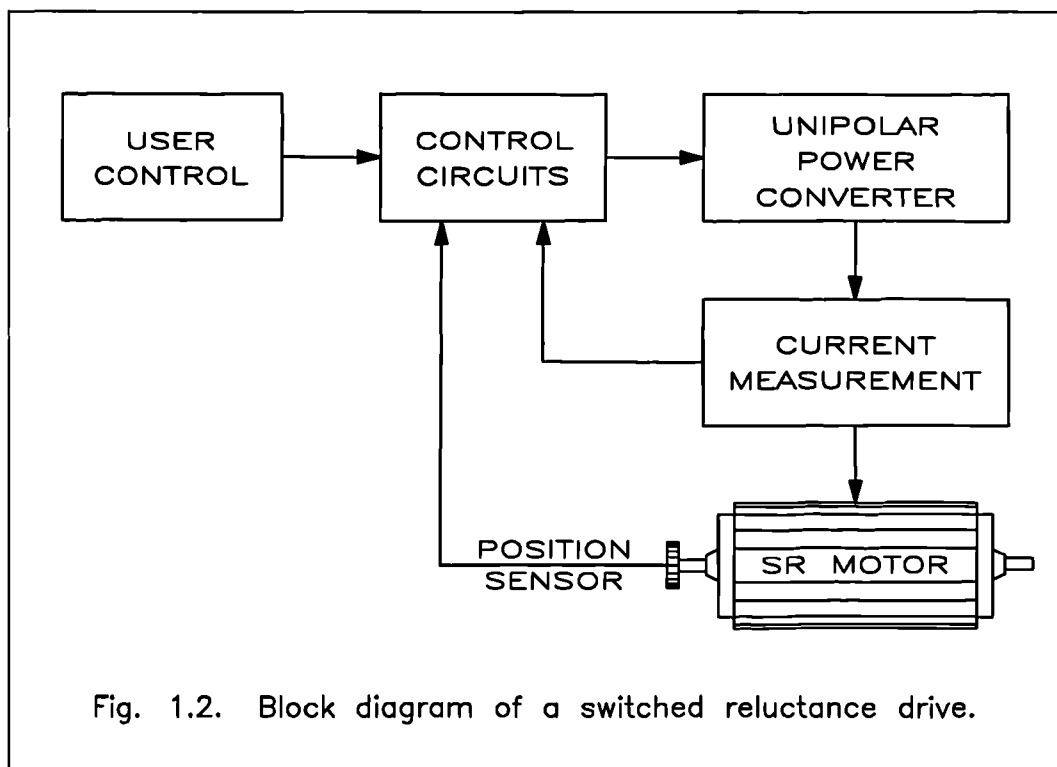
The latter solution led to unnecessarily high copper losses. Davidson's locomotive reached a disappointing 4 mph over a distance of 1.5 miles. Current in the motor windings fell off with time due to lack of proper cooling arrangements. Other electromagnetic engines with similarities to reluctance motors were constructed by Bain, Wheatstone and Henley [1]. However these motors all suffered from torque pulsations and were soon superseded by the invention of the dc machine.

1.2 A present day switched reluctance drive.

One hundred and twenty years after these early experiments, the switched reluctance motor began to realize its full potential. The modern era of power electronics and computer-aided design brought the switched reluctance motor into the variable speed drive market [7,8]. The simple brushless structure of the motor

makes it very reliable in operation and keeps construction costs at bay. High permeability-low loss materials and rigid construction, which allows a small air gap between the stationary and rotating members, have increased the motor efficiency. The unipolar power converter which has replaced the mechanical commutator is reliable and robust.

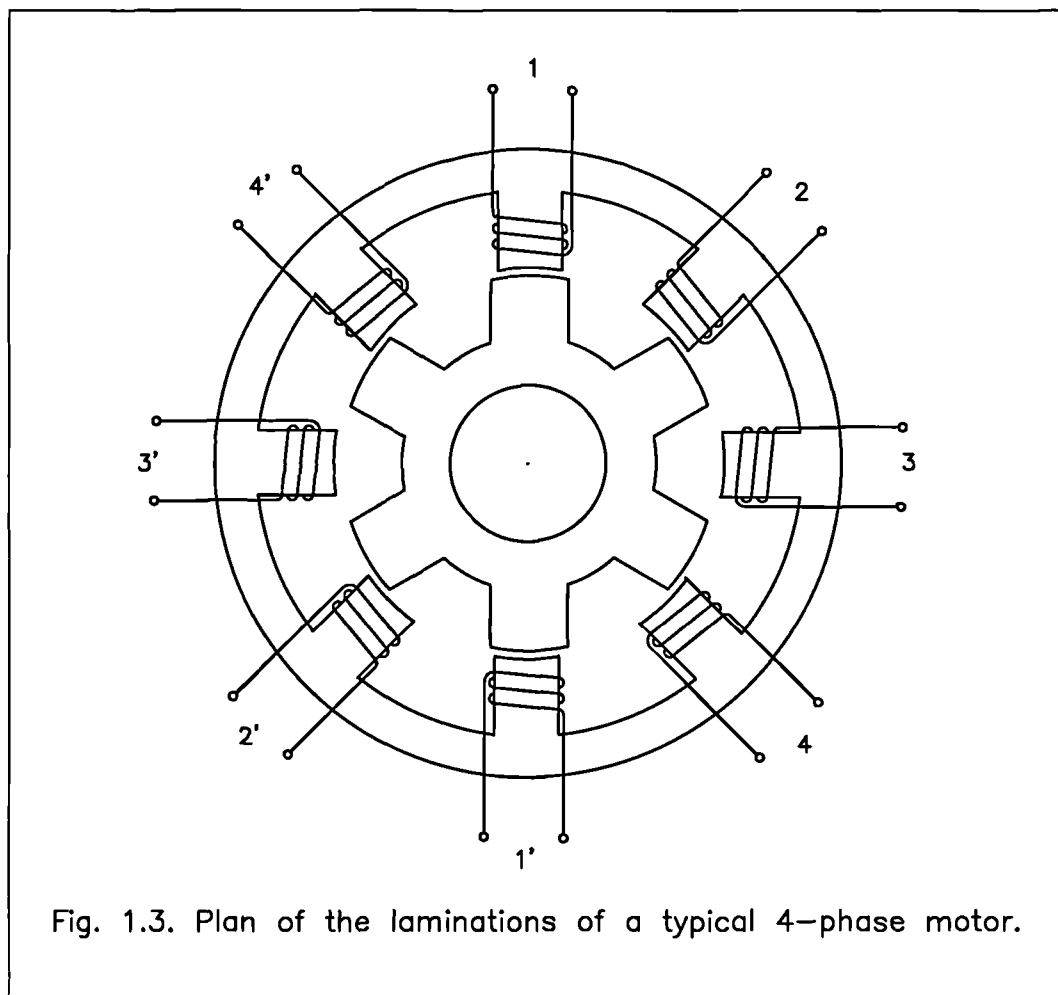
A block diagram of a typical switched reluctance drive is shown in fig. 1.2. Unlike induction motors or dc motors the switched reluctance motor cannot run directly from an ac or dc supply. The flux in the switched reluctance motor is not constant, but must be established from zero every working step. A power converter circuit must supply unipolar current pulses, timed accurately to coincide with the rising inductance period of each phase winding. It is therefore advantageous to feed rotor position information from a shaft mounted sensor back to the control board. The power converter must also regulate the magnitude of the current, to meet the (torque and speed) demand placed on the drive by the load. A phase current measuring device and current regulator should therefore be present.



The major parts of the switched reluctance drive shall be described in more detail in subsequent sections of this chapter.

1.3 The switched reluctance motor.

The switched reluctance motor has a salient pole stator with concentrated excitation windings and a salient pole rotor with no conductors or permanent magnets. A plan view of a typical 4-phase switched reluctance motor is shown in fig. 1.3. The 4-phase motor has eight stator poles and six rotor poles. A coil is wound around



each stator pole and is connected, usually in series, with the coil on the diametrically opposite stator pole to form a phase winding; e.g. coils 1 and 1' form phase P1. The reluctance of the flux path between the two diametrically opposite

stator poles varies as a pair of rotor poles rotates into and out of alignment. Since inductance is inversely proportional to reluctance, the inductance of a phase winding is a maximum when the rotor is in the aligned position, and a minimum when the rotor is in the unaligned position. In fig. 1.3 the position of the rotor is such that two rotor teeth are aligned with the stator teeth of phase P1. This is the position of minimum reluctance and hence maximum inductance. The stator teeth of phase P3 are shown to be facing the rotor interpolar air slots. This is the position of maximum reluctance (minimum inductance) in phase P3.

The equivalent circuit of a switched reluctance motor phase winding (neglecting mutual interaction with other phases) comprises the winding resistance, R , and the variable winding inductance, L , as shown in fig. 1.4a. The winding inductance, L , varies not only with rotor position, θ , but also with current, i . This is because the magnetic circuit becomes substantially saturated when the phase current, i , is high and there is significant overlap between the excited stator poles and the associated rotor pole pair. The equivalent circuit satisfies Faraday's voltage law,

$$v = iR + \frac{d\lambda}{dt} \quad (1.1)$$

where the flux linkage, λ , is given by

$$\lambda = L(\theta, i)i \quad (1.2)$$

Typical phase current and flux linkage waveforms are shown in fig. 1.4b. A pulse of positive torque is produced if current flows in a phase winding as the inductance of that phase winding is increasing. The 'lines of force' acting on the structure behave like stretched elastic bands and attempt to pull the members into alignment. In the aligned position the magnetic forces will tend to close the air gap by pulling opposite members together. The stator is, under such conditions, subjected to compressive forces while the rotor is under tension. A negative torque contribution is avoided if the current is reduced to zero before the inductance starts to decrease again. Rotation is maintained by switching on and off the current in the stator phase windings in synchronism with the rotor position. The rotor speed can be

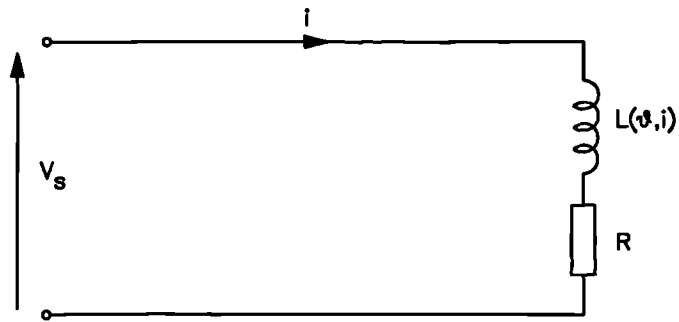


Fig. 1.4a. Equivalent circuit of a switched reluctance motor phase winding.

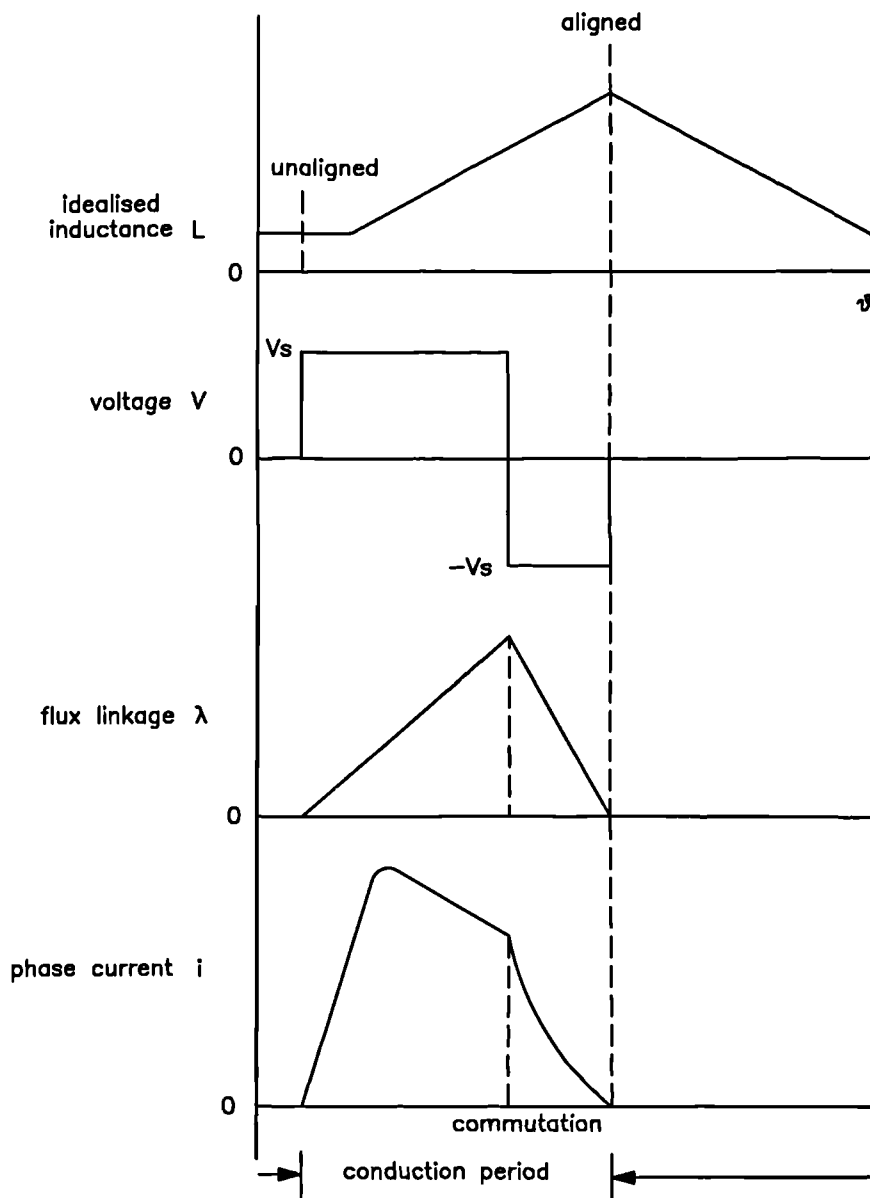


Fig. 1.4b. Typical waveforms.

varied by changing the frequency of the current pulses.

Switched reluctance motors can operate with any number of phase windings; however there are some guidelines governing the choice of stator and rotor pole numbers [7,8] and therefore phase windings. To ensure starting torque in either direction there should be at least three stator phases. Additionally there should be different numbers of stator and rotor pole pairs. Usually there is one more stator pole pair than rotor pole pairs, though many other combinations are possible. Both the stator and rotor should be made of laminated steel to reduce the iron losses in the motor. The number of stator and rotor poles has a significant influence on the performance of the switched reluctance motor, and a choice must be made with the particular application in perspective. Low torque ripple may be achieved by increasing the number of stator and rotor teeth. As a penalty, the higher switching frequencies 'fluxing' this structure would incur excessive eddy current losses at very high speeds. It is for this reason that low cost, single phase switched reluctance machines have been developed [9] and successfully operated at speeds up to 20,000rpm. In addition, configurations that encourage short flux paths within the switched reluctance motor have been reported [10], reducing losses overall while retaining low torque ripple capability.

The absence of permanent magnets or coils on the rotor means that there are no excitation¹ forces acting on the structure. Torque is produced purely due to the variation of reluctance in the magnetic flux path, introduced by the saliency of the rotor laminations. The direction of the reluctance torque is irrespective of the direction of the **B**-field through the rotor, and hence the direction of current in the stator phase windings is not important. The need for unipolar phase current in the switched reluctance motor results in simpler and more reliable power converter circuits.

¹ Excitation forces are induced when a permanent magnet or wound rotor is present in a stator reduced magnetic field.

1.4 Existing power converter circuits for the switched reluctance drive.

The purpose of the power converter circuit is to provide some means of increasing and decreasing the supply of current to the phase windings. Many different power converter circuits have been proposed for the switched reluctance motor. The circuits which have been proposed, tested and most widely used shall be described and the advantages and disadvantages of each highlighted.

1.4.1 Power converter with bifilar motor windings.

Much of the early research work on switched reluctance drives concentrated on the development of power converter circuits for motors with bifilar windings [11,12]. The single motor winding is replaced by two closely coupled bifilar windings. One of these windings is connected to a single switching device and the other to a freewheeling diode as shown in fig. 1.5. When the switching device is turned on, current builds up in the main winding. The voltage across the secondary winding reverse biases the diode. When the switch turns off, current flow transfers to the secondary winding. A potential difference dV above the applied voltage V_s is required to forward bias the diode and allow stored magnetic energy to flow back into the supply. Depending on the degree of coupling between the two windings and their turns ratio, the voltage across the main switching device may rise to over twice the supply voltage at the instant of turn-off. The switching device must be rated to withstand this.

Although this power converter utilises only one switch per phase, the voltage rating of that device must be at least twice the rating of the motor windings. A second disadvantage of this power converter lies in the inefficient use of the copper in the motor since only one of the bifilar windings in each pair can carry current at any time.

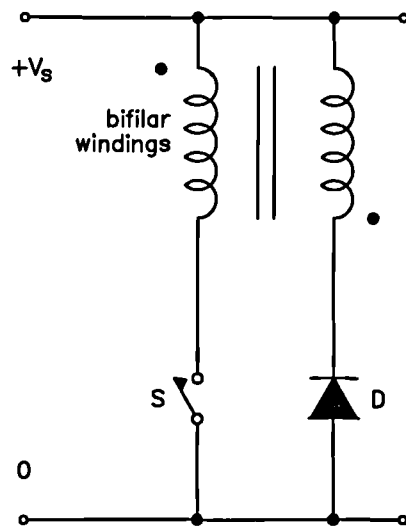


Fig. 1.5. Power converter with bifilar motor windings.

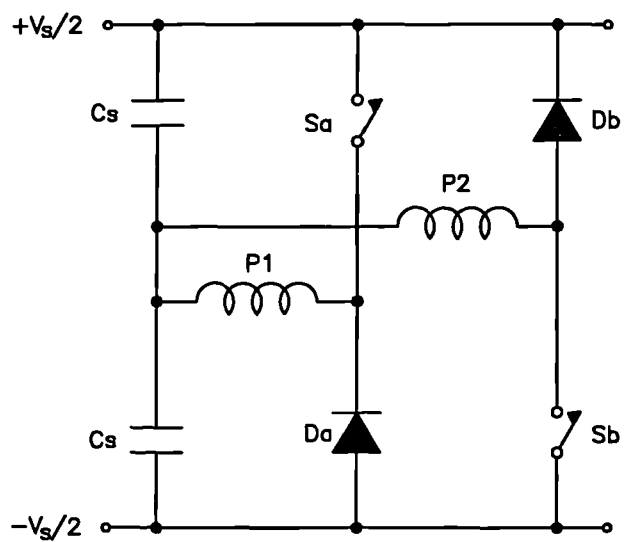


Fig. 1.6. Power converter with split dc power supply.

1.4.2 Power converter with split dc supply.

One of the simplest power converter circuits suitable for controlling the unipolar phase current in a switched reluctance motor uses a split dc supply [13,14]. Figure 1.6 shows the simplest form of this power converter. Two phase windings are connected to the central tap point of a bipolar dc supply. The other ends of the two phase windings are each connected to a switching device and associated freewheeling diode. The switching device and diode associated with each phase winding are connected in opposite positions to ensure that there is no power flow imbalance between the two supply capacitors. This arrangement means that this power converter circuit is only suitable for motors which have an even number of phases.

This power converter requires only one switching device and associated freewheeling diode per phase. Each switch and diode must be rated to withstand the complete supply voltage plus any transient voltages due to the switching. However only half this voltage can appear across the motor winding in the positive or negative direction. The available supply voltage is therefore under-utilised.

1.4.3 Capacitor dump power converter.

This power converter, shown in fig. 1.7, has been proposed [15] in an attempt to minimise the number of switching devices per phase, while ensuring that the switches do not have to be rated much in excess of the motor voltage rating. Each phase has a main switch (S_a , S_b and S_c) which can be turned on to increase the current in the respective phase winding. When the switch is turned off, the stored energy in the phase winding is transferred to the dump capacitor C . A buck chopper circuit is used to return energy from the dump capacitor to the supply. However the mean capacitor voltage must be maintained well above the supply rail in order to rapidly reduce the phase current to zero after commutation. The main switches and freewheeling diodes must therefore be rated in excess of the motor voltage. The low reverse voltage dV impressed across the phase winding upon

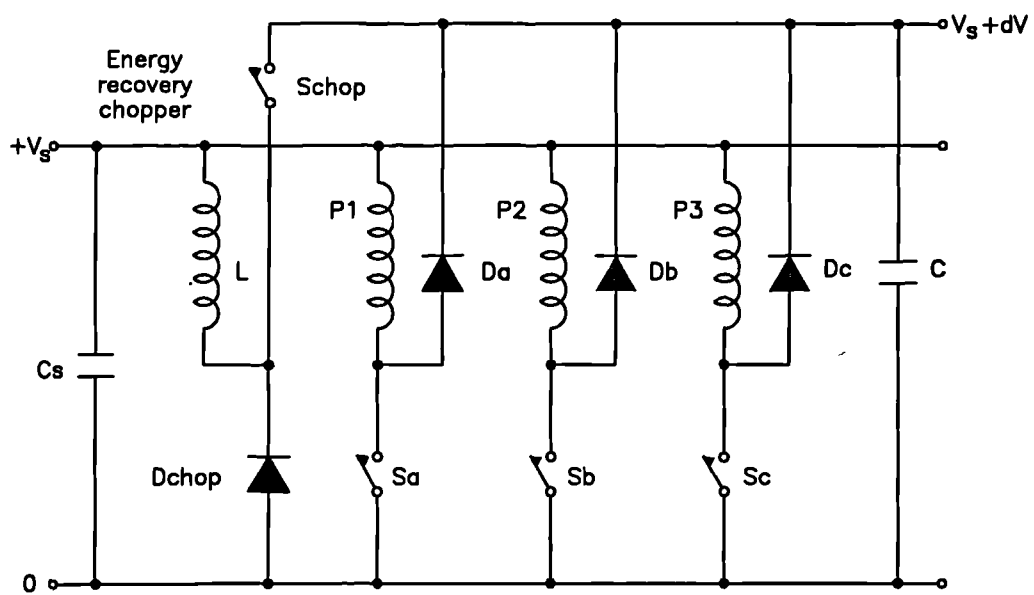


Fig. 1.7. Capacitor dump power converter.

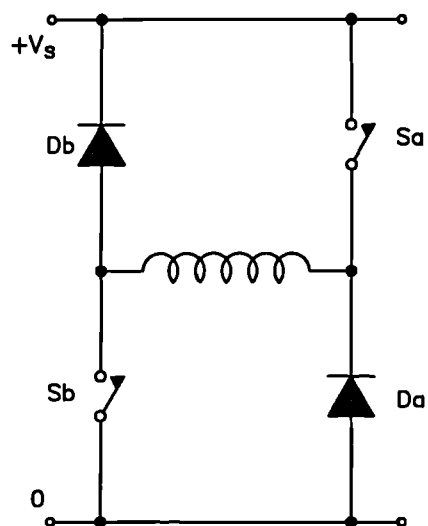


Fig. 1.8. Power converter with asymmetric half-bridge.

commutation may limit the drive performance, especially at high speeds. The chopper circuit adds to the *C*-dump converter component count; however this is not as high as the component count of the asymmetric half-bridge power converter which is described below.

1.4.4 Power converter with the asymmetric half-bridge.

Some papers [16,17] have proposed using the asymmetric half-bridge as the power converter for the switched reluctance drive. The asymmetric half-bridge is shown in fig. 1.8 connected to one phase winding of a switched reluctance motor. One switching device, *S_a*, connects the positive supply rail to one end of the phase winding. This switch is called the upper or floating switch since the drive circuit for such a switch must be isolated from the lower supply rail. The second switching device, *S_b*, connects the other end of the phase winding to the lower supply rail and is referred to as the lower switching device. The inductive nature of the motor phase windings means that the asymmetric half-bridge must also incorporate a freewheeling diode for each switching device. Each diode provides a path for freewheeling motor current when the associated switching device is turned off. The switches and diodes must be rated to withstand the supply voltage plus any switching transients. The motor windings are rated at the supply voltage. This circuit therefore allows the motor to be rated close to the maximum switch voltage. This is important where the dc supply voltage or the available switch voltage may be limited.

The asymmetric half-bridge has three main modes of operation. The first, a positive volt loop, occurs when both switching devices, *S_a* and *S_b*, are turned on. The supply voltage is connected across the phase winding and the current in the phase winding increases rapidly, supplying energy to the motor. The second mode of operation is a zero volt loop. This occurs if either of the two switching devices are turned off while current is flowing in the phase winding. In this case the current continues to flow through one switching device and one diode. Energy is neither taken from nor returned to the dc supply. The voltage across the phase

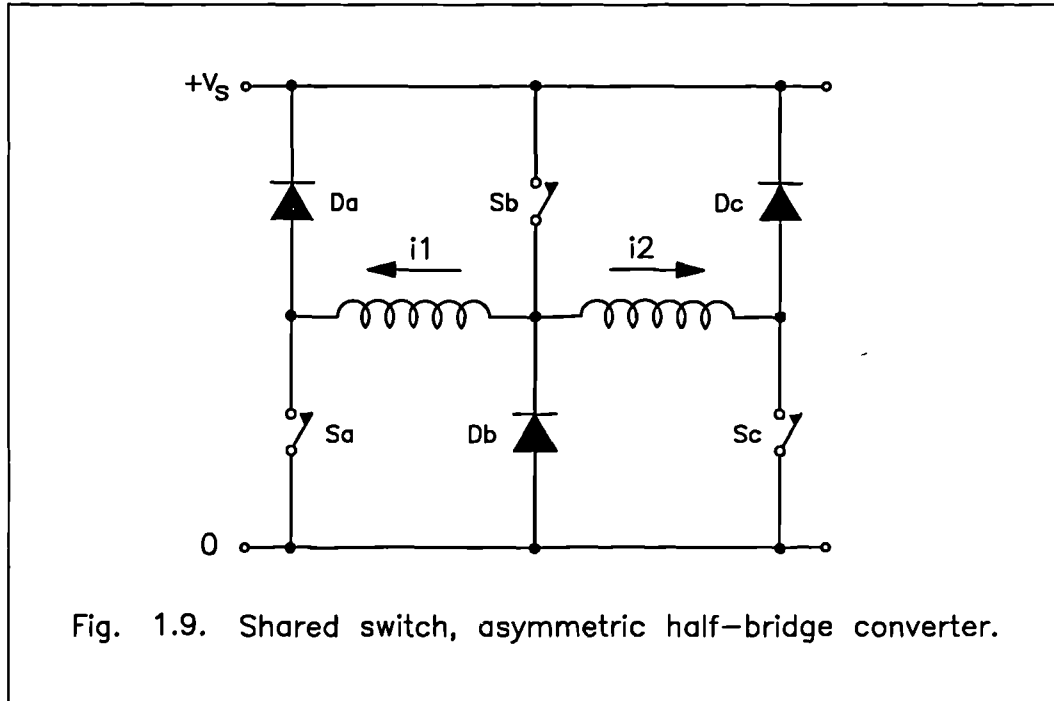
winding during this time is equal to the sum of the saturation voltages of the two semiconductor devices. This voltage is very small compared to the supply voltage and so the current in the phase winding decays very slowly. The final mode of operation is a negative volt loop. Both the switching devices are turned off. The current is forced to flow through both the freewheeling diodes. The current in the phase winding decreases rapidly as energy is returned from the motor to the supply. The asymmetric half-bridge thus offers three very flexible modes for current control. The zero volt loop is very important in minimising the current ripple at any given switching frequency. The zero volt loop also tends to reduce the power flow to and from the motor during chopping by providing a path for motor current to flow without either taking energy from or returning it to the supply capacitors.

The major advantage with this circuit is that all the available supply voltage can be used to control the current in the phase windings. As each phase winding is connected to its own asymmetric half-bridge there is no restriction on the number of phase windings. However as there are two switches per phase winding it is best suited to motors with few phase windings.

1.4.5 Shared switch, asymmetric half-bridge power converter.

A family of power converter circuits has been developed [18] which are based on the asymmetric half-bridge, but use less than two switches per phase. A section from the simplest form of the power converter circuit is shown in fig. 1.9. Two phase windings are connected to three switching devices. The central switch in the diagram, S_b , is connected to two phase windings and must therefore be rated to withstand at least twice the motor phase current. The operation of this switch affects the flow of current in either of the two phase windings to which it is connected. This imposes a restriction on the operation of the circuit as a positive volt loop in one phase cannot be accompanied by a negative volt loop in the adjoining phase. By carefully selecting the phase windings which are connected to the same switch it is possible to ensure that this restriction does not impose a

severe limitation on the operation of the drive.



The switching steps involved in the excitation of phase windings P1 and P2 are shown in Table 1.1. Current i_1 can be built up in a positive volt loop by simultaneously switching devices Sa and Sb on. When current i_1 reaches a predetermined level, I_m , it can be maintained constant by chopping switch Sb at high ($\sim 20\text{kHz}$) frequency. The duty cycle of the pwm voltage waveform is dependent on the magnitude of I_m . In order to subsequently increase the current i_2 in a positive volt loop, devices Sb and Sc must be switched on. Therefore the chopping operation of i_1 is transferred to Sa. Current i_2 can be maintained at a constant level I_m by chopping switch Sc. During this period the top switching device Sb is carrying the sum of the currents i_1 and i_2 , i.e. $2I_m$ and must be rated accordingly.

It is possible to subsequently decrease the current in P1 while maintaining the level of i_2 , by switching device Sa off and interchanging the functions of Sb and Sc. At this time, phase winding P1 is impressed with an average negative voltage, V_{neg} , where

$$V_{neg} = V_s - V_c \quad (1.3)$$

The term V_c denotes the average voltage that is impressed across phase winding P2 during chopping, and is dependent on the magnitude of i_2 and the back-emf seen by P2.

i_1	i_2	Sa	Sb	Sc
incr	zero	on	on	off
hold	zero	on	chop	off
hold	incr	chop	on	on
hold	hold	chop	on	chop
decr	hold	off	chop	on

Table 1.1 Shared switch converter switching algorithm.

1.5 Rotor position measurement techniques.

For motoring operation the phase current pulses must be carefully timed to coincide with the rising inductance period of each phase winding. This means that the controller requires information on the position of the rotor relative to the stator phases. Depending on the performance required and speed of operation various techniques may be suitable [19]. A selection of rotor position measurement techniques shall be presented in this section.

1.5.1 Slotted disk arrangements.

One of the most common techniques is to use a slotted disk, driven by the motor shaft, in conjunction with optoelectronic devices. The optoelectronic devices are fixed, with the optical transmitter on one side of the disk and the receiver on the

other side. As the disk rotates, a tooth or a slot is between the optotransmitter and the receiver arrangement, hence producing an on / off signal. The resolution of such a system is dependent on the number of optical devices used.

The optoelectronic devices may be replaced by RF transducers in dusty environments. As an aluminium tooth reaches an RF transducer, eddy currents are induced which alter the transducer coil inductance. The coil is fed with a high frequency ac waveform so as to amplify eddy current effects.

Alternatively, a permanent magnet rotating element may be employed which is attached to the shaft. The rotating magnetic field can then be sensed using search coils or Hall effect transducers. The Hall effect transducers must be used if information about the stationary position is required. This information is usually necessary for the switched reluctance drive to determine which phase to excite at start up. Slotted disk arrangements are cost effective and robust and need only be as complicated as the system demands.

1.5.2 Optical shaft encoders.

Optical shaft encoders may be purchased as a complete unit. Incremental encoders consist of a disk divided into (fine) alternate opaque and transparent sectors. The disk is mounted on the shaft and a single light source / detector arrangement is used as the sensing device. The disadvantage of this arrangement is that the angular information is stored in an external counter. If the information in the counter is lost, the angular position cannot be extracted. Furthermore, at start up the disk must be rotated through one revolution marker to determine the shaft angle. These problems are overcome by the use of absolute encoders. The absolute encoder disk is radially divided into N sectors, each sector also being divided up along its length into opaque and transparent sectors. This arrangement forms a digital word of maximum count 2^N representing rotor position. Encoders constitute a more expensive option than a few discrete optical devices but provide more accurate position information if it is required.

1.5.3 Brushless resolvers.

Very fine position information can be provided by the combination of a brushless resolver and resolver to digital converter [20]. The simplest form of resolver has a rotating member with a single phase winding and a stationary member with two windings at 90° to each other. The resolver and resolver to digital converter arrangement exploits the sinusoidal relationship between the shaft angle and output voltage to produce a (typically) 12 bit digital word representing the angular position. Such systems are costly and are therefore only suitable for very high performance drives.

1.5.4 Sensorless position detection.

It is possible to derive rotor position information from the phase windings of the motor. In one sensorless position detection method a 'mini' high frequency square wave voltage is applied to an unexcited phase [21-24]. The resulting current pulse magnitude increases as the phase inductance decreases to reach a minimum at the unaligned position. A threshold current level may be set which relates to a particular rotor position and upon detection a particular phase winding may be excited or commutated. Such readings may however be affected by mutual coupling effects between phase windings. Alternatively, it is possible to monitor the current in the (active) phase winding during chopping to determine the rotor position from the rate of change of current [21]. This however implies that the range for which position detection is possible is restricted to low speeds else the motor back-emf will affect accuracy. Sensorless position detection is an ongoing research area which exploits the recent advances in digital signal processing.

1.6 Phase current measurement and control.

Current pulses must be applied in a phase winding of the switched reluctance motor when a pair of rotor poles is approaching alignment. The timing, duration

and magnitude of the current pulses determine the torque output and machine efficiency. However, the nonlinear relationship between torque, current and rotor position presents complications in feedback control systems for the switched reluctance drive. Several control models have been proposed for the drive [25,26], though some simplification of the nonlinear characteristics is usually made.

Programmable gate arrays offer increased potential in this area, allowing a large amount of logic circuitry to be implemented in a single device. The flexibility of user programming reduces the risks involved in changing a circuit design. More complex control may be required for high-power switched reluctance drives, particularly where a wide speed range is required at constant power, and microprocessor controllers have been developed and used to this effect [27,28].

At low speeds, the back-emf is small and the current must be limited with the aid of either a 'hysteresis type' current chopping regulator or a fixed frequency pwm current regulator. A Hall effect current transducer can be used to measure the phase current in the switched reluctance motor. Hall effect transducers can be multiplexed between several phase windings. These transducers are relatively expensive and therefore not suitable for small, low cost drives. Recently, MOSFETs, called SENSEFETs, have become available, in which part of the silicon substrate is used to measure the current. These devices, successfully employed in switched reluctance drives [21], offer the possibility of switches modulating the current flowing through them.

The base speed, ω_b , is the highest speed at which maximum current can be supplied at rated voltage with fixed firing angles. If these angles are kept fixed beyond ω_b , the maximum torque at rated voltage decreases significantly. However, if the conduction angle is increased by advancing the turn-on angle, maximum current can still be forced in the motor windings. This sustains the torque level high enough to maintain a constant power characteristic over a considerable speed range.

1.7 Market applications of the switched reluctance drive.

The switched reluctance drive offers many advantages over competing drives. The structure of the motor is simple, robust and hence very reliable in operation. Manufacturing costs are also kept at bay. Starting torque can be very high and, under running conditions, the bulk of the losses occur on the stator where they can readily be dissipated. The motor is, in addition, very competitive on power / weight and power / cost ratios.

The requirement for unipolar phase current means that the SRM can employ simple power converter circuits. These power converters do not exhibit shoot-through problems and therefore prove more reliable and easier to protect. The need for some form of position feedback and current feedback increases circuit complexity and cost, but once added can offer useful control features such as optimisation of the developed torque at all operating speeds.

The major disadvantage of the switched reluctance motor is the inherent torque ripple that is produced by the stepping action of the motor. However, efforts have been made which illustrate the potential of the motor to produce low torque ripple. One technique requires the precise wave-shaping of phase current, which must be stored in electronic memory and subsequently forced in the phase winding [8]. It has been shown [29] that neural networks are capable of learning the current profiles required to minimise torque ripple. In a treatment of multi-tooth per pole structures Wallace and Taylor [30] demonstrated how maximum torque and minimum torque ripple can be achieved by the same motor design.

High levels of acoustic noise are also caused by the pulsed nature of torque production, though research at the University of Warwick [31] has shown that the problem can be reduced by 'clever switching'. The new active control technique employs two complimentary effects to minimise stator vibration. Firstly, the

magnitude of any step change in the voltage is minimised, particularly at turn-off. Secondly, at commutation, if the voltage across the phase winding is decreased in two successive steps, with the second occurring half a resonant cycle after the first, the resulting vibrations will be out of phase and therefore cancel.

Many applications for switched reluctance drives have been considered. These range from traction [32,33] and battery powered vehicles [34] to small drives for domestic appliances [17]. High performance drives have also been constructed for servo drive applications [35] and spindle drives [16]. These papers all show that switched reluctance drives are suitable for a range of applications providing the cost of the power converter and the control electronics can be kept to a minimum.

Chapter 2

THE SWITCHED RELUCTANCE DRIVE: ASPECTS OF DESIGN, CONSTRUCTION AND TESTING

Some switched reluctance motor design principles shall be described in section 2.1. Basic considerations aim at justifying the traditional design methodology. At the same time, shortcomings of existing designs are highlighted. A new switched reluctance motor design is then presented, which offers significant advantages over prior art motors.

Section 2.2 of this chapter aims at introducing finite element analysis, the software tool that was used in this project to model existing motor configurations and design the proposed switched reluctance motor. The hardware tools employed to test the constructed switched reluctance prototype and prior art motors are subsequently described. A detailed account of all experimental procedures is presented.

2.1 Switched reluctance motor design.

The relationship between the fundamental switching frequency and speed is derived from the fact that, if the poles are wound oppositely in pairs to form the phases, then each phase produces a pulse of torque on each passing rotor pole. The fundamental switching frequency in one phase is therefore

$$f = \eta N_r \quad (2.1)$$

where η is the rotational speed in rev/s. If there are q phases, the step angle is

$$step = \frac{2\pi}{qN_r} \quad (2.2)$$

The non-uniform nature of torque production leads to torque ripple and contributes to acoustic noise. The torque ripple can be reduced by increasing N_r , the number of rotor teeth. However, the resulting increase in the fundamental switching frequency will induce higher core losses.

It can be shown that peak static torque in multiphase stepping motors can be obtained when half the phases are simultaneously excited [36], i.e. in a machine with q phases the static torque is maximised if

$$\text{phases excited} = q/2 \text{ for } q \text{ even} \quad (2.3a)$$

$$\text{phases excited} = (q\pm 1)/2 \text{ for } q \text{ odd} \quad (2.3b)$$

The overlap between current pulses of adjacent phase windings leads to smoother torque production capability.

2.1.1 Low phase numbers.

The simplest switched reluctance motor and power converter is single phase. A 2/2 1-phase motor is practical only if the starting problem can be overcome. In 1-phase motors zero torque zones are inevitable and sufficient load inertia must exist to push the rotor through them. Single phase motors can, however, operate at extremely high speeds [9] before their performance is limited by excessive eddy current losses.

Zero torque zones can be minimised with a low cost, 2-phase 4/2 machine. A primitive form of the 2-phase motor is shown in fig. 2.1. The rotor is shown to reside in a zero torque position. In theory, an infinitesimal displacement of the rotor is needed to enter the rising inductance region of phase 1. In practice though, the torque output is small for several degrees on either side of this point.

Some form of starting assistance or parking mechanism should be present in the 4/2 2-phase motor. A stepped airgap structure [37], shown in fig. 2.2, has been

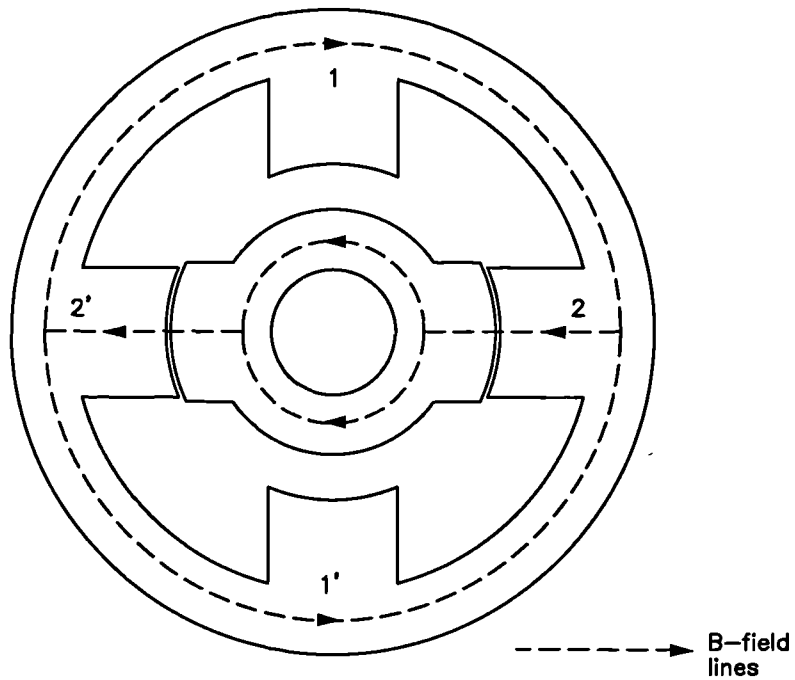


Fig. 2.1. A 2-phase 4/2 motor.

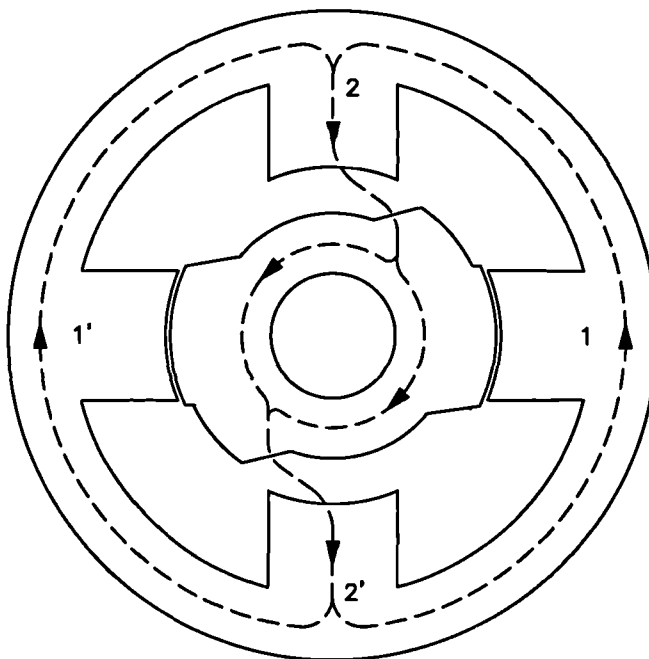


Fig. 2.2. The 2-phase 4/2 motor with a stepped gap [37], showing self-starting capability.

suggested for this purpose. The authors of reference [37] suggested that this structure extended the region of positive inductance variation, to provide positive $dL / d\theta$ for at least one of the phase windings at any rotor position.

The most commonly described forms of switched reluctance motor are those with stator / rotor pole numbers of 6/4 (3-phase) and 8/6 (4-phase). The 6/4 3-phase machine has starting torque capability in either forward or reverse direction. The 12/8 3-phase machine (a 6/4 'multiplied' by 2) offers the advantages of shorter end windings and shorter flux paths which lead to reduced copper and iron losses respectively.

A 12/10 3-phase structure shown in fig. 2.3, with two teeth per stator pole, was developed by Harris and Finch [38]. In comparison to the 6/4 3-phase motor, the authors reported a significant increase in torque per ampere. On the other hand, the increase in steps / rev resulted in higher core losses. In addition, the stator pole structure restricted the winding area available. Therefore, the benefits of this configuration were thought to be restricted to low speeds [39].

Hendershot [40] reported a similar 12/10 3-phase machine, in the form shown in fig. 2.4, in which the stator had unevenly spaced teeth. The stator teeth were energised as pairs of adjacent poles having opposite magnetic polarities so as to create a magnetic circuit between each pole pair. The induced short flux paths reduced the core losses in the machine. However, the unevenly spaced teeth on the stator resulted in restrictions in the winding area available. Therefore, the torque developed by this 3-phase 12/10 motor is expected to be reduced.

The 4-phase 8/6 switched reluctance motor ensures starting torque from any rotor position and, in addition, delivers smoother torque compared to its 3-phase counterpart (ref. eqn. 2.3).

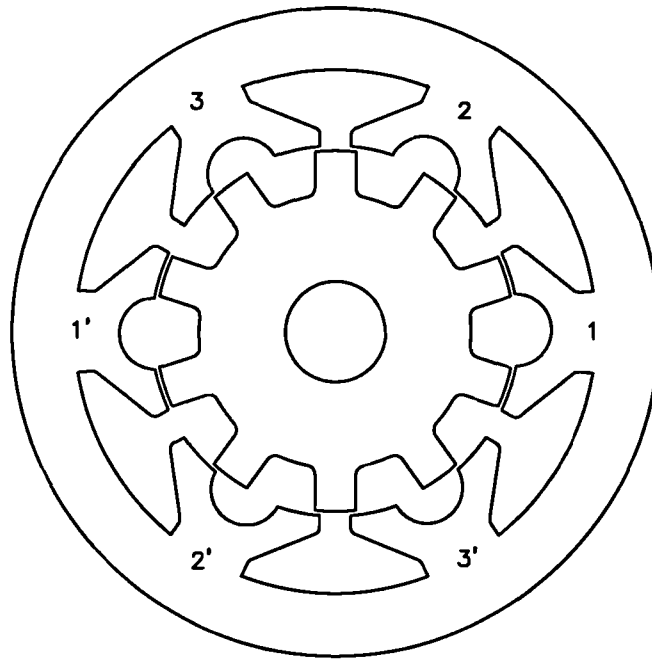


Fig. 2.3. 3-phase 12/10 motor with 2 teeth per stator pole [38].

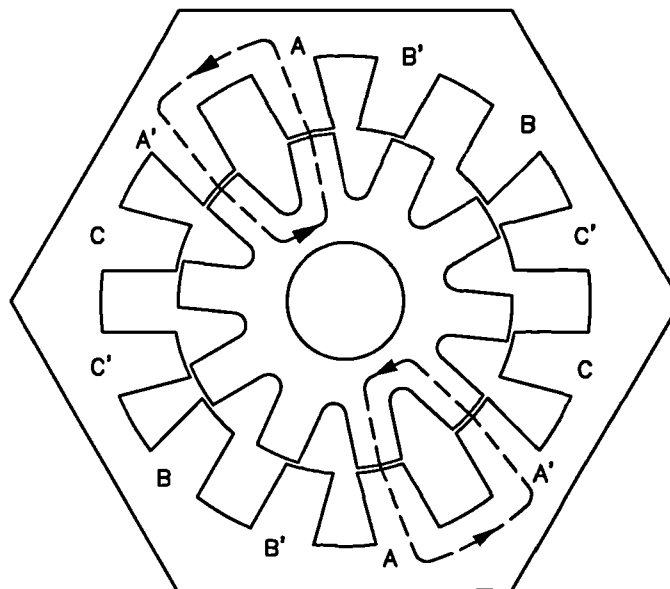
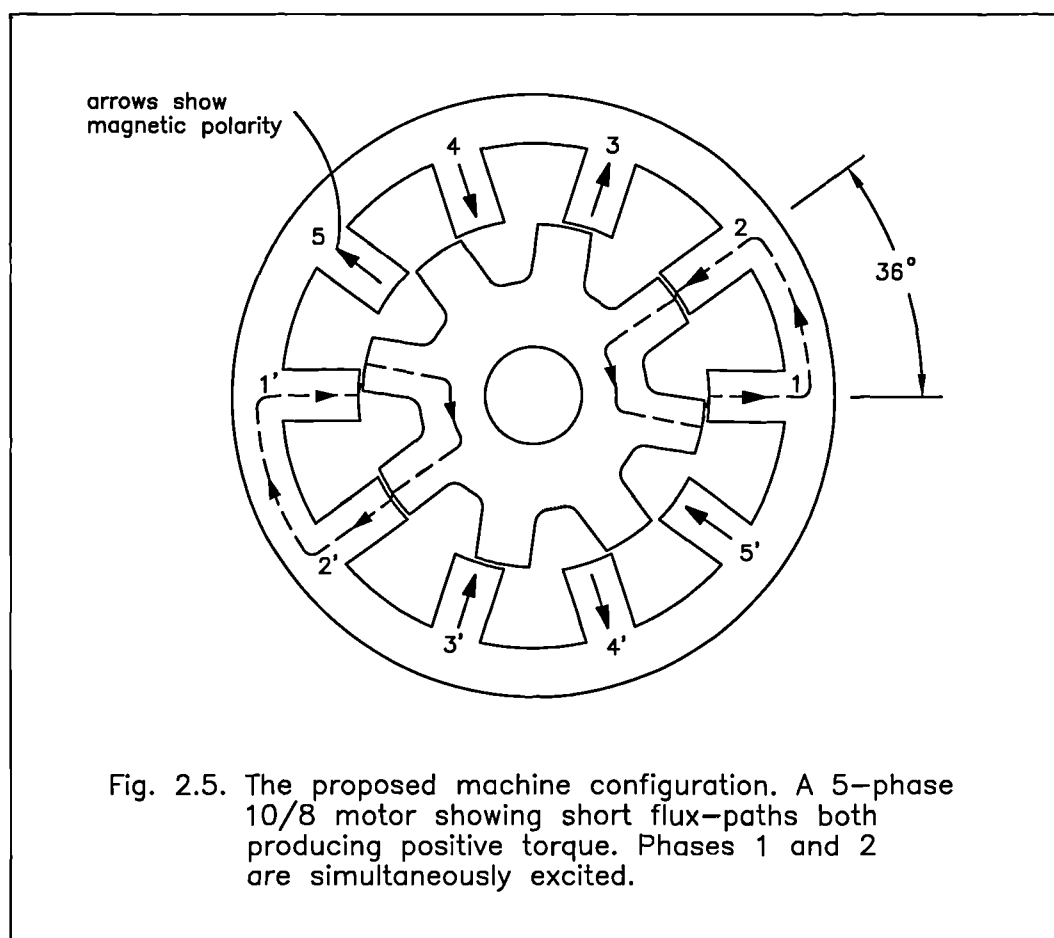


Fig. 2.4. 3-phase 12/10 motor, with short flux paths [40].

2.1.2 Higher phase numbers - a new motor design.

The use of the shared switch power converter was demonstrated in the control of a 7-phase switched reluctance motor [41]. It was shown that the efficiency of the motor was improved considerably by arranging the windings to encourage short flux paths. Michaelides and Pollock [10] described results of research into computer-aided modelling of short flux paths. It was demonstrated that the MMF required to produce the nominal flux linkage level in the excited stator poles was reduced significantly by configuring the motor for short flux paths.

Figure 2.5 illustrates the flux distribution in a section of a 5-phase switched reluctance motor. If the phase windings are arranged so that adjacent stator poles have opposite magnetic polarity, then the B -field associated with any two adjacent



phase windings forms a short magnetic circuit linking the excited stator poles via the rotor teeth. Short flux paths can only be realised in switched reluctance motors with an odd number of phases, if a discontinuity in the B -field distribution is to be avoided. Furthermore, to benefit fully from this technique, there should be considerable overlap between current pulses in adjacent phase windings. Sufficient overlap does not occur in the 3-phase motor. Five-phase and 7-phase motors are therefore thought to be suitable, cost effective configurations. Experimental results, taken from the 7-phase motor, demonstrated the superior performance offered by the short flux loop configuration. A 5-phase motor, that would exploit the advantages of short flux loops in a simpler 'package', is now proposed. The 10/8 structure can ensure improved torque production and lower torque ripple compared to its 4-phase 8/6 counterpart. Although the fundamental switching frequency is increased, lower iron losses can be expected from the 10/8 structure because the motor is excited with short loops.

The stator and rotor poles of the proposed 10/8 and 14/12 structures are symmetrical about their centre lines and equally spaced around the stator and rotor periphery. This poses no restriction to winding area or torque output. A detailed analysis of the 7-phase machine and the design and development of a 5-phase prototype will be described in subsequent chapters of this thesis.

2.2 Introduction to electromagnetic finite element analysis.

2.2.1 The need for finite element modelling.

Modern electrical machines must be designed to meet specified operating conditions that are set by the load demand, while maintaining optimum efficiency and reliability. In addition, the power / cost and torque / volume ratios must be maximised. In order to meet these requirements, reliable machine performance predictions at the design stage must be established. An accurate model of the

switched reluctance motor magnetic circuit cannot be constructed using simple analytical functions or equivalent circuit representations. This is due to the complexity introduced by the doubly salient structure and the highly nonlinear relationship between the stator phase current and flux. In recent years, numerical techniques have been developed that can overcome certain limitations of analytic methods such as their restriction to linear, steady state problems, and provide efficient solutions to a wide range of problems. For example, it has been possible for several years to compute the magnetic forces acting on the members of a switched reluctance motor, taking into account the three-dimensional geometry and saturation effects of the material, using the finite element method.

Finite element analysis is the most widely used numerical method for transient and steady state solutions to two and three-dimensional electromagnetic problems. The enormous capabilities of this technique are largely due to considerable advances in computers. This computer-based numerical technique for solving partial differential equations is implemented by representing the domain of the problem under consideration by a collection of finite elements. The nodes associated with each element are the points in space where the field values are calculated. Governing equations for each element are set up and subsequently combined in order to describe a global property (variable).

2.2.2 Electromagnetic field equations.

The governing laws of electromagnetism can be concisely expressed by Maxwell's equations [42]. In differential form, these are

$$\nabla \times \mathbf{E} = -\frac{\partial \mathbf{B}}{\partial t} \quad (2.4)$$

$$\nabla \times \mathbf{H} = \mathbf{J} + \frac{\partial \mathbf{D}}{\partial t} \quad (2.5)$$

and

$$\nabla \cdot \mathbf{D} = \rho \quad (2.6)$$

$$\nabla \cdot \mathbf{B} = 0 \quad (2.7)$$

Maxwell's equations form the basis of two and three-dimensional finite element programs. When the frequency is low, displacement currents can be neglected. Equation 2.5 is therefore reduced to

$$\nabla \times \mathbf{H} = \mathbf{J} \quad (2.8)$$

The magnetic flux density, \mathbf{B} , is related to magnetic field strength, \mathbf{H} , by

$$\mathbf{B} = \mu(\mathbf{H} - \mathbf{H}_c) \quad (2.9)$$

where μ denotes the material permeability. The magnetic field remanence, \mathbf{H}_c , relates only to permanent magnet materials and may therefore be omitted in the treatment of the switched reluctance motor model. The displacement current \mathbf{D} is related to electric field strength by

$$\mathbf{D} = \epsilon \mathbf{E} \quad (2.10)$$

and the current density, \mathbf{J} , is expressed as

$$\mathbf{J} = \sigma \mathbf{E} \quad (2.11)$$

Throughout this project, the software used for two and three-dimensional electromagnetic modelling of the switched reluctance machine was supplied by Vector Fields Ltd. The basic electromagnetic field theory on which the packages are based [43,44] follows from the laws of electromagnetism and may be found in Appendix A.

2.2.3. Finite element model creation.

In OPERA-3D the finite element model of a switched reluctance motor is created by describing the projection of the required three-dimensional geometry onto a two-dimensional XY plane cross section. The three-dimensional mesh is then

formed by extruding the section in the third dimension. The level of discretisation in the third dimension is dependent on the stack length of the individual model and the required accuracy.

Boundary conditions can provide a way of reducing the size of the finite element representation of symmetrical problems. Symmetry considerations reveal that the three-dimensional finite element model of a typical switched reluctance motor may be divided into four identical regions by means of two bisecting planes. The first plane bisects the model parallel to the XY plane, mid-way along the stack length of the machine. The second, a ZX plane divides the base plane into two semicircular regions. Only one of these four regions is therefore modelled. A pair of matching surfaces is identified, namely the ZX and Z(-X) surfaces, where the potential values have the reverse sign but equal magnitude. These surfaces are assigned a negative periodicity boundary condition. This implies that field values along the Z axis are assigned to zero.

During the early stages of the project only the 3D software was available. However, a two-dimensional model of the switched reluctance machine could be constructed in OPERA-3D / TOSCA. This consists of a single element slice through the machine. The conductors are defined as long parallel bars intersecting the mesh at right angles. The symmetry boundary condition is specified on the ZX and Z(-X) surfaces. The faces of the slice have the Neumann (default) boundary condition imposed on them i.e.

$$\frac{\partial \phi}{\partial n} = 0 \quad (2.12)$$

This is a weak boundary condition setting the direction of the flux to be tangential at these boundaries. With the tangential flux direction imposed, these boundaries can be considered as reflection boundaries, with a mirror image of the solution on either side of the boundary. Hence the slice appears to be one (in the middle) of a stack of similar slices. This produces the effect of an infinite model in the axial direction. The setup of a typical two-dimensional and three-dimensional model of

a 4-phase switched reluctance motor is illustrated in fig. 2.6a,b respectively.

Two independent finite element meshes are created and subsequently ‘stitched’, namely the stator and rotor meshes. The conductors do not form a part of the finite element mesh. The air regions, in which the conductors resided, are assigned the reduced scalar potential formulation whereas magnetic volumes are assigned the total scalar potential formulation. The finite element mesh may be created such that solutions to the problem at different rotor positions can be obtained by allowing the rotor to rotate, in steps of one degree, with respect to a fixed stator position. The appropriate symmetry boundary conditions are then imposed and the model submitted for analysis. The analysis is completed using the TOSCA computer algorithm, which is briefly described in Appendix A.

2.2.4 Field values computed using the finite element analysis package.

I. Flux linkage computation.

The flux of \mathbf{B} over a surface element dS regarded as a vector, is given by the product of the component of \mathbf{B} normal to the surface, and the area of dS . Hence, the magnetic flux, Φ , over a finite stator pole area, S_p , is

$$\Phi = \int_s \mathbf{B} \cdot d\mathbf{S}_p \quad (2.13)$$

This integral can be readily obtained in OPERA by the use of a POLAR or CARTesian patch that computes field values over a predetermined surface (capital letters in the text represent the command that must be typed in). The flux linkage, λ , associated with a phase winding of N turns is defined as

$$\lambda = N\Phi \quad (2.14)$$

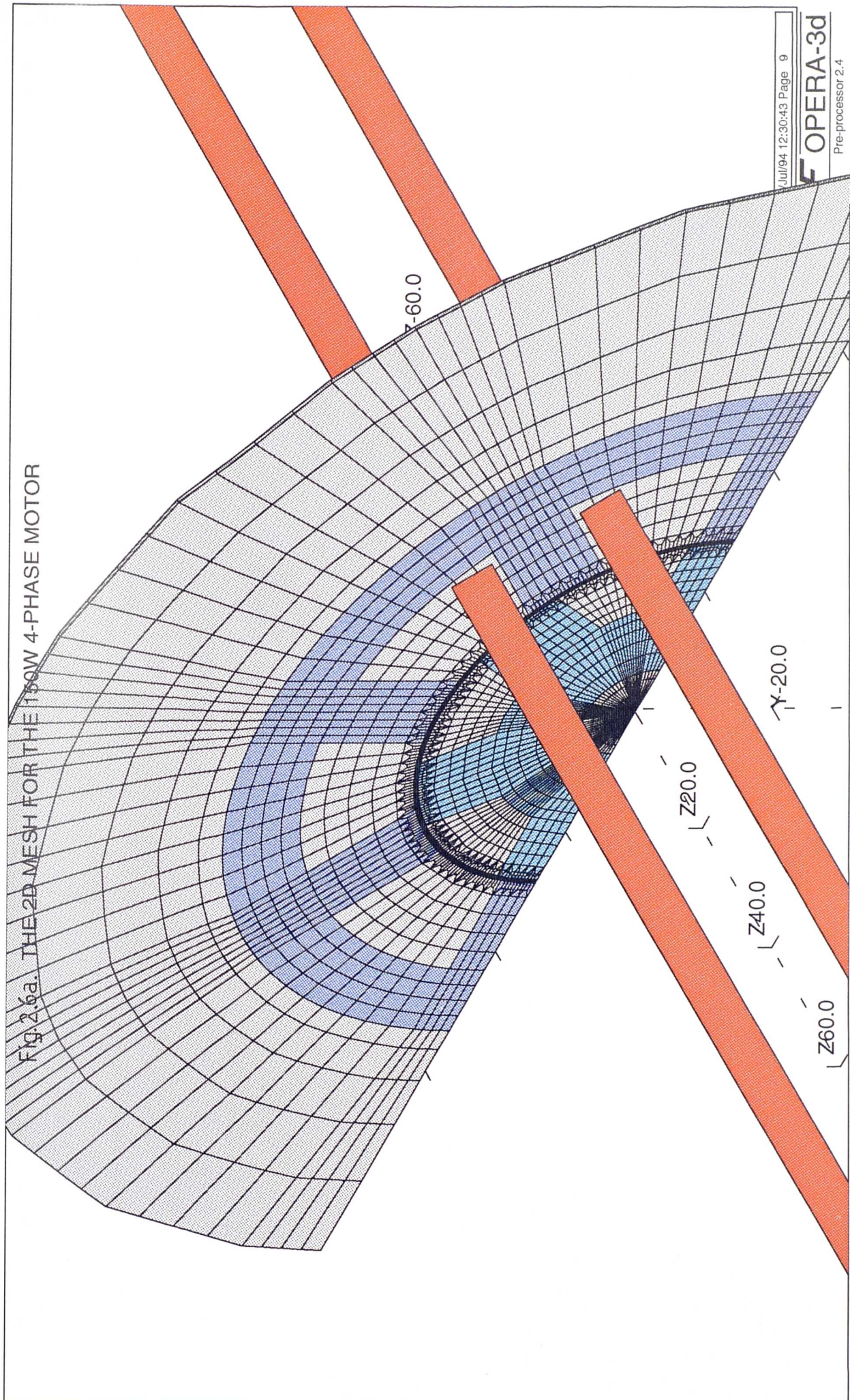
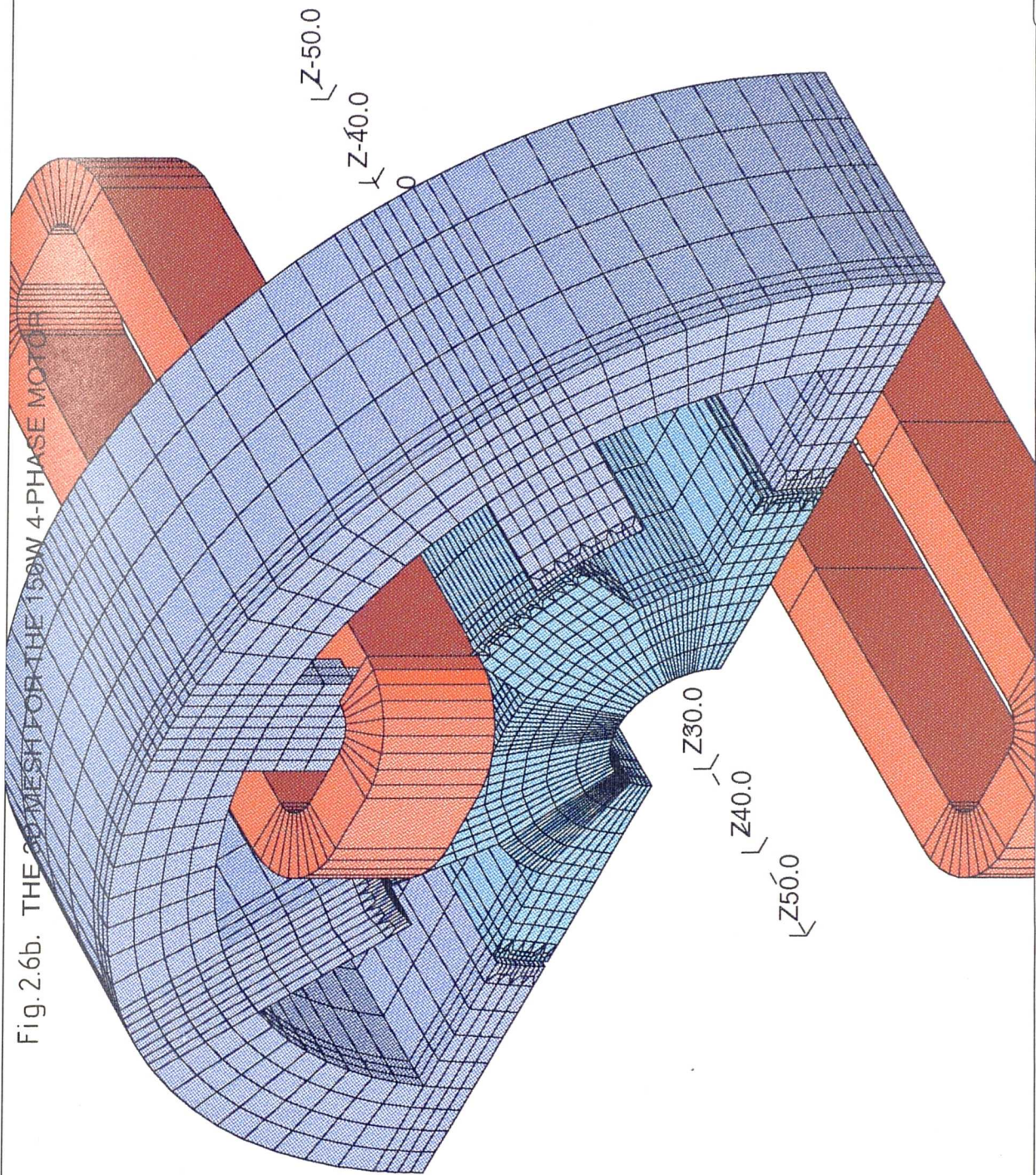


Fig. 2.6b. THE 3D MESH FOR THE 150W 4-PHASE MOTOR



II. Energy considerations.

Poynting's theorem [45] finds its source from the vector identity

$$\nabla \cdot (\mathbf{E} \times \mathbf{H}) = \mathbf{H} \cdot (\nabla \times \mathbf{E}) - \mathbf{E} \cdot (\nabla \times \mathbf{H}) \quad (2.15)$$

Substitution of Maxwell's equations yields

$$\nabla \cdot (\mathbf{E} \times \mathbf{H}) = \mathbf{H} \cdot \frac{\partial \mathbf{B}}{\partial t} - \mathbf{E} \cdot \mathbf{J} - \mathbf{E} \cdot \frac{\partial \mathbf{D}}{\partial t} \quad (2.16)$$

Integrating over a volume, v_o , and applying the divergence theorem on the term on the left hand side of the equation gives

$$-\oint_s (\mathbf{E} \times \mathbf{H}) \cdot d\mathbf{S} = \int_{v_o} (\mathbf{E} \cdot \mathbf{J} + \mathbf{H} \cdot \frac{\partial \mathbf{B}}{\partial t} + \mathbf{E} \cdot \frac{\partial \mathbf{D}}{\partial t}) dv_o \quad (2.17)$$

If there were no power sources within the volume considered, then the first integral on the right of eqn. 2.17 would represent the total Ohmic power dissipated within the volume. If sources are present within the system, then the result of integrating over the volume of the source represents the input power into the system. The second and third terms on the right represent the total power stored in the magnetic and electric fields. The sum of the terms on the right equals the total power radiated out of the volume. In the treatment of the magnetostatic switched reluctance motor model using the finite element analysis package, an ideal 'no loss' system is considered. The radiation power is therefore assumed to be zero. The displacement current term is only significant at high frequencies and is therefore ignored.

The electrical energy, W_E , input to the switched reluctance motor system is equal to the stored magnetic energy, W_M , that is

$$\int_{v_o} \mathbf{J} \cdot d\mathbf{A} dv_o = \int_{v_o} \mathbf{H} \cdot d\mathbf{B} dv_o \quad (2.18)$$

The system coenergy, W_C , is defined as

$$W_c = \int_{v_o} \mathbf{B} \cdot d\mathbf{H} dv_o \quad (2.19)$$

In linear systems, the stored magnetic energy and coenergy terms are equal, i.e.

$$\int_{v_o} \mathbf{H} \cdot d\mathbf{B} dv_o = \int_{v_o} \mathbf{B} \cdot d\mathbf{H} dv_o = \frac{1}{2} \int_{v_o} \mathbf{B} \cdot \mathbf{H} dv_o \quad (2.20)$$

In nonlinear systems, such as the switched reluctance machine,

$$\int_{v_o} \mathbf{B} \cdot \mathbf{H} dv_o = \int_{v_o} \mathbf{H} \cdot d\mathbf{B} dv_o + \int_{v_o} \mathbf{B} \cdot d\mathbf{H} dv_o \quad (2.21)$$

The energy terms can be readily obtained in OPERA by typing ENERgy. Electromechanical energy conversion principles may be applied in order to extract information on the torque production of the machine. It is also useful to note that, in singly excited systems, the flux linking the stator pole phase winding can be computed using energy considerations.

III. Instantaneous static torque: the Maxwell stress tensor.

The Maxwell stress tensor is defined as

$$\tau = \frac{1}{\mu_0} \begin{bmatrix} \frac{1}{2}(B_x^2 - B_y^2 - B_z^2) & B_x B_y & B_x B_z \\ B_x B_y & \frac{1}{2}(B_y^2 - B_x^2 - B_z^2) & B_y B_z \\ B_x B_z & B_y B_z & \frac{1}{2}(B_z^2 - B_x^2 - B_y^2) \end{bmatrix} \quad (2.22)$$

The diagonal terms in the matrix are equivalent to tensions whilst off diagonal terms represent shear stresses. The forces acting on the rotor of a switched reluctance machine, at a particular rotor position and excitation, may be found by SELEcting the rotor surface and computing the INTEgral of the Maxwell stress tensor over the selected surface. The resultant torque about a specified pivot point (centre of shaft) is also computed.

Inaccuracies in the calculation of forces using Maxwell stresses occur when the selected surface is an interface between air and a magnetic body. This is because finite element analysis results give a poor approximation to reality at a corner of the body. In order to accurately compute the forces acting on the rotor, it is advisable to mesh the airgap of a switched reluctance motor with four layers of eight-node brick elements. The iron structure (rotor) is selected, and subsequently enclosed by two layers of air elements. This gives the best possible chance of the integration of forces over the selected surface being accurate [44].

2.3 Construction of power converter circuits.

This section describes the construction of the power converter circuits which were used for dynamic testing of switched reluctance motors. The power converter components, i.e. the power switches, power diodes, drive circuits and snubbers, were selected / constructed in the early part of the project. The same components were employed in the dynamic testing of different switched reluctance machines, rated from 150W to over 4kW. Different power converter configurations could be realised by making the appropriate connections to the power switches and diodes.

2.3.1 Overview of semiconductor devices for power converters.

I. The ideal switch.

Several types of semiconductor power devices, including BJTs, MOSFETs, GTOs and IGBTs, can be turned on and off by control signals applied to the control terminal of the device. These devices are known as controllable switches. No current flows when the switch is off, and when it is on, current can only flow in one direction.

The ideal controllable switch has the ability to block arbitrarily large forward and reverse voltages with zero current flow when off. Furthermore, it can conduct

arbitrarily large current with zero voltage drop when on. An ideal device switches from on to off or vice-versa instantaneously when triggered and requires negligible power from the control source in order to be triggered [46].

Semiconductor switches are not ideal, but have certain operational characteristics. There is a maximum rated voltage which can be applied across their terminals in the off-state before the devices breakdown. They do not offer zero impedance in the on-state and hence there is usually a maximum forward current rating to avoid damage to the semiconductor. Semiconductor switches also have a finite transition time between states so there are power losses in the device during this time. This imposes a limit on the operating frequency of the switch.

II. The thyristor.

The thyristor is a semiconductor device which comprises four semiconductor layers, and operates as a switch having two stable states, on and off. There are many variants in the thyristor family, two in particular being the most common, the silicon controlled rectifier (SCR) and the gate turn-off thyristor (GTO). The thyristor is triggered into the on-state by a short duration gate current pulse, provided that the device is in its forward blocking state. Once the device begins to conduct, it is latched on and the gate pulse can be removed. The major difference between the SCR and the GTO is in their turn-off mechanism. The SCR can only be turned off by reducing the main current through the device below a holding current level to allow forward blocking to take place. This commutation requires additional components to divert the principal current. The GTO however has a simpler turn-off process which can be initiated by a negative gate current pulse, reducing the amount of extra circuitry required.

Both these devices are capable of supporting large voltages and carrying large currents. They are generally the most cost efficient way of switching very large powers. However they have low switching speeds which limits their operating frequency to below 5kHz. When used for motor control applications, this low

switching frequency may produce unacceptable audible harmonics in the motor windings. The SCR was used in some of the early power converter designs [11], but the complicated commutation circuitry meant that it was superseded by designs using the GTO [13,14].

III. The bipolar transistor.

The bipolar transistor is the most widely available power semiconductor device and is therefore quite competitively priced. It is available in both npn and pnp types, thus offering flexible circuit design choices. A sufficiently large base current, dependent on the collector current, results in the device being fully on. The BJT is a current controlled device, and base current must be continuously supplied to keep it in the on-state. This requirement, however, adds to the cost of the base drive circuitry. There is a wide range of device ratings available although, in the higher power range, better silicon utilisation is offered by the thyristor. Below 10kW bipolar transistors can offer higher switching frequencies than thyristors, though not quite high enough to put the switching noise into the ultrasonic range. The on-state voltage of the power transistor is usually in the 1-2V range and hence conduction power loss is small.

IV. The MOSFET.

The name MOSFET stands for a Metal Oxide Semiconductor Field Effect Transistor. A power MOSFET has a vertically oriented, four layer structure of alternating p-type and n-type doping. This switching device requires continuous application of a gate-to-source voltage, of magnitude higher than the threshold voltage V_{th} , in order to be in the on-state. No gate current flows except during the transitions from on to off or vice-versa, when the gate capacitance is being charged or discharged. Upon application of a gate-to-source voltage of appropriate magnitude, a load current conduction channel is initiated from drain to source.

The MOSFET exhibits very fast switching speeds and can be operated at ultrasonic

switching frequencies. However, at higher voltages ($>250\text{V}$) the on-state losses of this switch exceed those of the BJT. The MOSFET offers poor utilisation of the silicon area compared to the bipolar transistor and can therefore be more expensive if the manufacturing volume is low. This can be offset by snubberless operation and as a result the MOSFET has been used in low power switched reluctance drives [17].

V. The insulated gate bipolar transistor (IGBT).

This is a relatively new device which combines the low current, gate voltage control requirement of the MOSFET with the high off-state and low on-state voltage characteristics of the bipolar transistor. The switching times of this device are better than those of the bipolar transistor, in particular the turn-on time. IGBTs have not yet reached their full potential but are a very suitable device for all switched reluctance drives. Voltage ratings up to 2000V and current ratings of several hundred amperes are projected. At present, pre-packaged IGBT modules, in which several devices are connected in parallel to increase the total current-carrying capability, are manufactured.

2.3.2 Selection of type and rating of the semiconductor devices.

Power MOSFETs were selected to construct the power converter circuit. MOSFETs simplify the drive circuitry considerably because they are voltage controlled devices, and offer high switching speeds. They have great ruggedness due to the absence of the second breakdown mechanism present in bipolar transistors.

The rating of the power switches was chosen with the feasible power converter configurations in mind. Two configurations were considered, namely the asymmetric half-bridge and the shared switch converter [18]. The former configuration was employed in the proposed 5-phase drive, as it provided maximum control flexibility (see chapter 1) and could therefore be used to optimise the performance of the 5-phase motor. The latter configuration reduced the number

of switches required to operate the drive, posed no compromise to the winding area and could power a motor of any phase number. It was therefore used to control the current in the circuits of the 7-phase motor. However, the top switches of the shared switch converter would have to be rated at approximately twice the motor current. The largest motor that required testing was in excess of 4kW, designed to operate at 600V and carry a maximum phase current of 15A. All switches ought to be able to withstand the supply voltage plus any switching transients. The top switching devices of a shared switch converter ought to carry current in excess of 30A. SEMIKRON SKM 181F power MOSFETs were therefore selected for the construction of the power converter circuits. BYT 261 fast recovery power diodes were also employed in the power converter circuits. The data sheets for these semiconductor devices may be found in Appendix B.

2.3.3 Gate drive circuits for power MOSFETs.

I. Selection of the gate drive isolating device.

The top switching devices of any power converter configuration must have their gate drive circuit referenced to the source rather than to the ground. The drive circuit may be 'floated' with respect to ground by means of a pulse transformer, an optocoupler or an optical fibre.

When pulse transformers are employed, the control signal may be modulated by a high frequency (1MHz) oscillator output before being applied to the primary terminals of a compact HF transformer. The secondary terminals can then be connected to a full wave rectifier and filter capacitor arrangement. The output signal is commonly applied to a totem pole amplification stage.

The optocoupler is a semiconductor device consisting of a light emitting diode, an output transistor and often a built-in schmitt trigger circuit. The capacitance between the LED and the base of the receiving transistor within the optocoupler must be as small as possible. This is to avoid re-triggering of the power MOSFET, at both turn-on and turn-off, due to the jump in potential between the floating

source terminal and the ground of the control board. Electrical shields are frequently used to reduce this problem. As an alternative fibre-optic cables can be used, where the LED is kept on the control board and the fibre-optic cable transmits the signal to the receiving transistor which is placed on the drive circuit board.

Optocouplers are low cost, compact units which reduce the gate drive component count and were hence chosen to isolate the MOSFET gate drive. As a precautionary measure, opto-isolators were employed on both top and bottom switch drive circuits. The optocouplers that were to be incorporated in the power MOSFET drive circuits ought to have the following characteristics:

a) High common mode transient immunity (CMR figure). Typically, the MOSFET is capable of switching 600V within 0.1 μ s though additional protection devices, such as snubbers, limit the dv / dt rate. The requirement for high CMR was posed only on the top switch drive.

b) High speed; typically, a propagation delay time of 500ns is tolerated.

Very few optocouplers featured high common mode transient immunity at a high test voltage. Testing of devices also revealed that the guaranteed CMR figure drops dramatically when the optocoupler is subjected to a voltage higher than the test voltage.

II. Gate drive circuit design for a top switch.

The top switch gate drive circuit, shown in fig. 2.7a, was powered from a +15V - 5V supply. The -5V rail was incorporated to speed up the gate discharge path at turn-off. The input on / off signal was isolated from the main control board by the high speed, TTL compatible HCPL2611 optocoupler. The on / off 5V control signal on the optocoupler output was fed to a voltage translation stage. A Baker's clamp [47] circuit diverted excess current from the base of the BC109 transistor into the collector, to ensure that the device was not driven hard into saturation. The Baker's clamp increased the speed of the circuit considerably. A totem pole amplification stage followed the voltage translation stage. A gate resistor value of

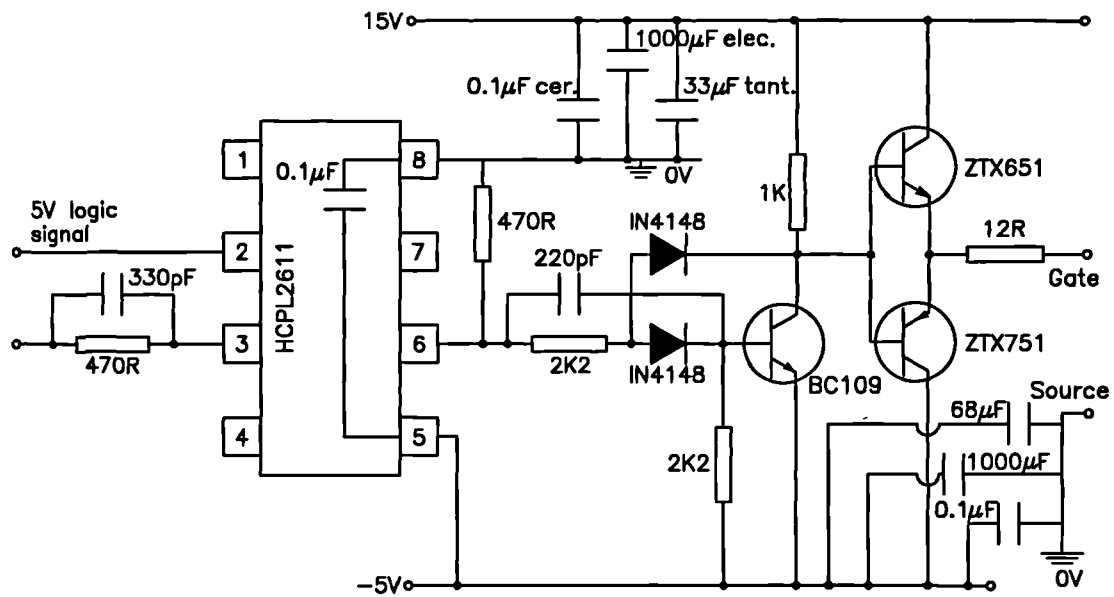


Fig. 2.7a. The upper switch drive circuit.

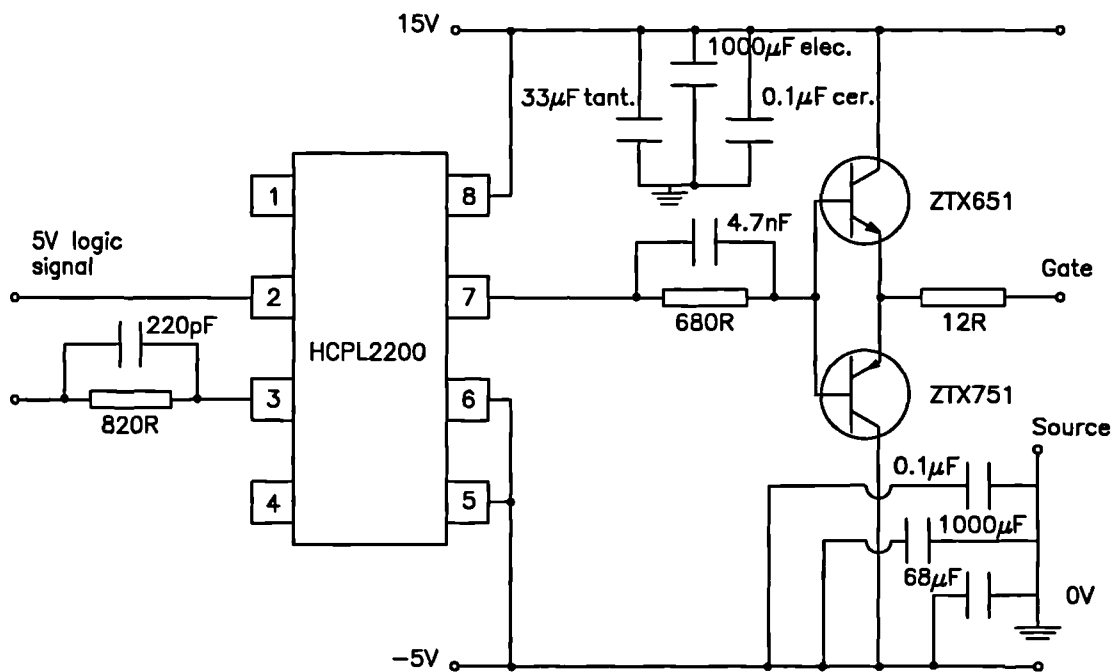


Fig. 2.7b. The lower switch drive circuit.

12 Ω was chosen, to damp out oscillations in the circuit while maintaining an acceptable switching speed.

The modes of operation of the circuit are given below:

a)"On-state": The optocoupler output is low and the BC109 transistor is switched off. The ZTX651 npn transistor is switched on, base current being provided through the totem pole 1k Ω base resistor. Taking into account the voltage drop across the 12 Ω gate resistor and the collector-emitter junction of the ZTX651, the gate is charged to approximately 14V.

b)"Off-state": The optocoupler output is high and the BC109 transistor is switched on. The collector-emitter junction of the BC109 may be regarded to be shorted, i.e. the transistor acts as a closed switch. The ZTX751 pnp transistor is switched on, discharging the gate capacitance.

III. Bottom switch gate drive circuit design.

The bottom switch gate drive circuit, shown in fig. 2.7b, was powered from a +15V -5V supply. The input on / off signal was isolated from the main control board by the high speed, CMOS compatible HCPL2200 optocoupler. CMOS compatibility removes the need for a voltage translation stage. The optocoupler output was fed to a totem pole amplification stage. The signal was then applied between the gate and source terminals of the MOSFET.

2.3.4 Snubber circuits.

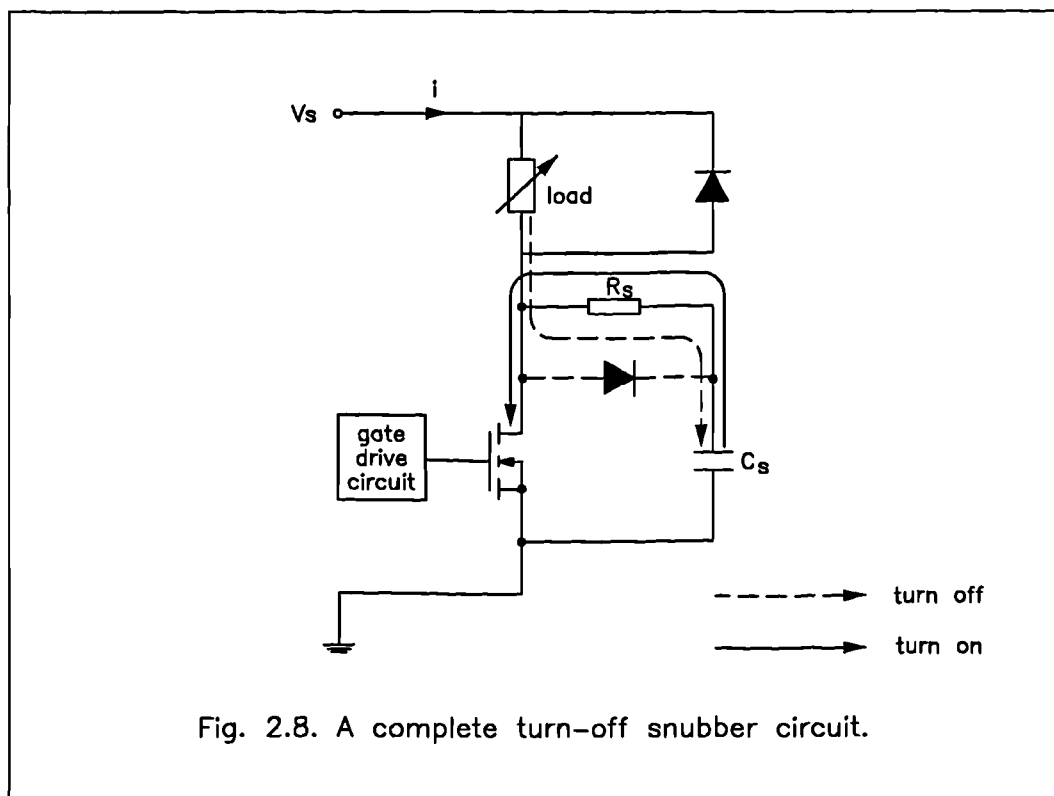
Snubber circuits are employed in order to reduce transistor switching stresses and losses by improving their switching trajectories. There are three basic types of snubbers:

- a) Turn-off snubbers
- b) Overvoltage snubbers
- c) Turn-on snubbers

The goal of a turn-off snubber is to provide a zero voltage across the transistor

while the current in the device reduces to zero. Overvoltage snubbers are employed to minimise overvoltages at turn-off caused by stray inductances in the circuit. Turn-on snubbers are used to reduce turn-on losses at high switching frequencies.

Compact R_s - C_s snubber units were employed to reduce the turn-off switching losses and protect the power MOSFET from excessive dv/dt rates and overvoltages. A complete turn-off snubber circuit is shown in fig. 2.8. As the switch opens, current



is diverted into the initially uncharged snubber capacitor which limits the value as well as the rate of rise of the switch voltage. This allows the drain current to reduce significantly, before the voltage across the device rises to an appreciable level. Switching losses are therefore reduced. At turn-on, the snubber capacitor discharges through a closed switch. The discharge current is limited by the snubber resistor, connected in series with the snubber capacitor. The energy stored in the snubber capacitor is dissipated as heat in the snubber resistor. Therefore, no additional energy dissipation due to the snubber occurs in the transistor.

The presence of the snubber resistor is detrimental at turn-off; unnecessary heating losses are incurred though the resistor provides good damping. The energy associated with stray inductances in the circuit is absorbed in the R_s - C_s network, thereby containing the voltage overshoot to a safe level and guarding against excessive dv / dt rates. If desired, the snubber resistor may be shunted by a diode.

Snubber circuits reduce power losses in the switching device. However, snubber losses are incurred at turn-on as the capacitor stored energy is dissipated as heat through the snubber resistor. It is therefore important to select appropriate values for the snubber resistor and capacitor so that the snubber reduces switching losses and stresses considerably but does not cause excessive heating losses. A simple mathematical model was developed and incorporated into a Turbo PASCAL program to simulate the response of the system at turn-off. Theoretical predictions were supported by laboratory work. At turn-off, it was found that the drain voltage rise time is very much dependent on the capacitance of C_s . For a given load and current the larger the snubber capacitor, the slower the drain voltage rises. Large valued resistors provide good damping in the system though the smaller the snubber resistor, the slower the drain voltage rises. Experimental work also suggested that the transistor current fall time at turn-off, and the drain voltage fall time at turn-on are dictated primarily by the characteristics of the switching device.

The values of the capacitance and resistance of the turn-off snubber that was selected are given below:

$C_s = 0.0047\mu f$ polypropylene. Polypropylene capacitors can withstand high voltage, fast rise time pulses and have an excellent high frequency performance. $R_s = 13.6\Omega$. Five 2W carbon film resistors were connected in parallel to provide a power dissipation capability of 10W.

The fast recovery power diodes were also 'snubbed' for protection.

2.4 The control board.

The information extracted from the rotor position sensor and the current measuring

devices is fed back to the drive controller. The controller must then produce the correct switching signals for the power converter to supply timely, magnitude regulated current pulses to the motor phase windings. The design of a 'clever' controller can maximise the performance of the drive.

2.4.1 Current sensing and control.

I. Hysteresis type current chopping regulator.

In its basic form, the circuit consists of two amplifier comparator circuits and an SR bistable, as shown in fig. 2.9. A small percentage perturbation about the required phase current level is chosen, and the appropriate current limit signals (i_{min} and i_{max}) are set. Level i_{min} is fed into the inverting input of comparator I, while level i_{max} forms the input to the non-inverting terminal of comparator II. The measured current level forms the input to the second terminal of each comparator. The output signals from the comparators are fed into the SR bistable. The SR bistable truth table, given in fig. 2.9, reveals how the current is contained within the prescribed levels.

This circuit is simple and robust. However, having set limits i_{min} and i_{max} , the circuit has no control over the chopping frequency. The power switch may therefore be subjected to excessive switching stresses. For this reason, a fixed frequency pwm current regulator was preferred. This circuit will now be described in more detail.

II. Fixed frequency pwm current regulator.

An inverting amplifier and potentiometer arrangement was used to set the required phase winding current, as shown in fig. 2.10. The device was calibrated so that

if $v_{cd} = 0V$ then $i_{req} = 0A$
 $v_{cd} = -12V$ then $i_{req} = 20A$

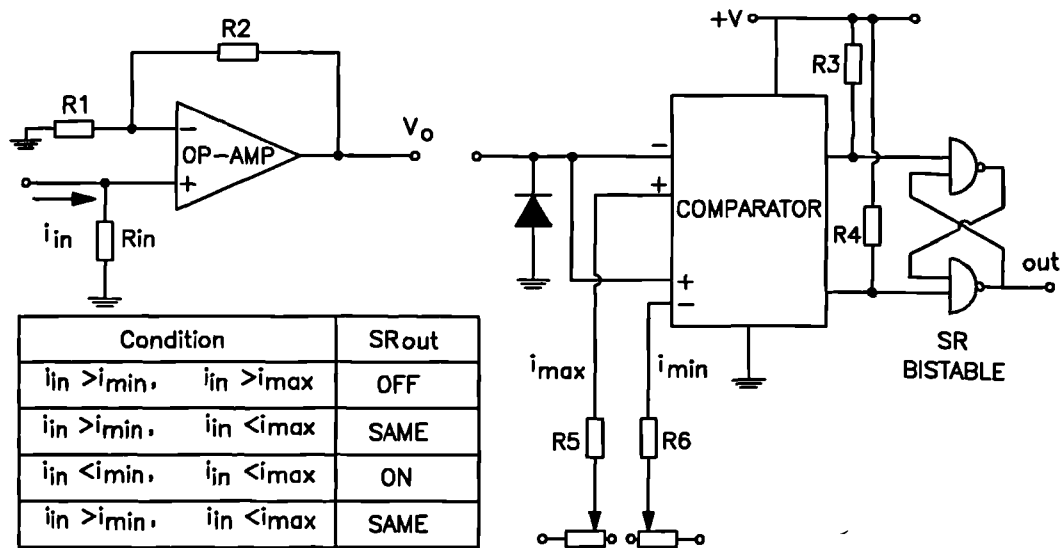


Fig. 2.9. A hysteresis type current chopping regulator.

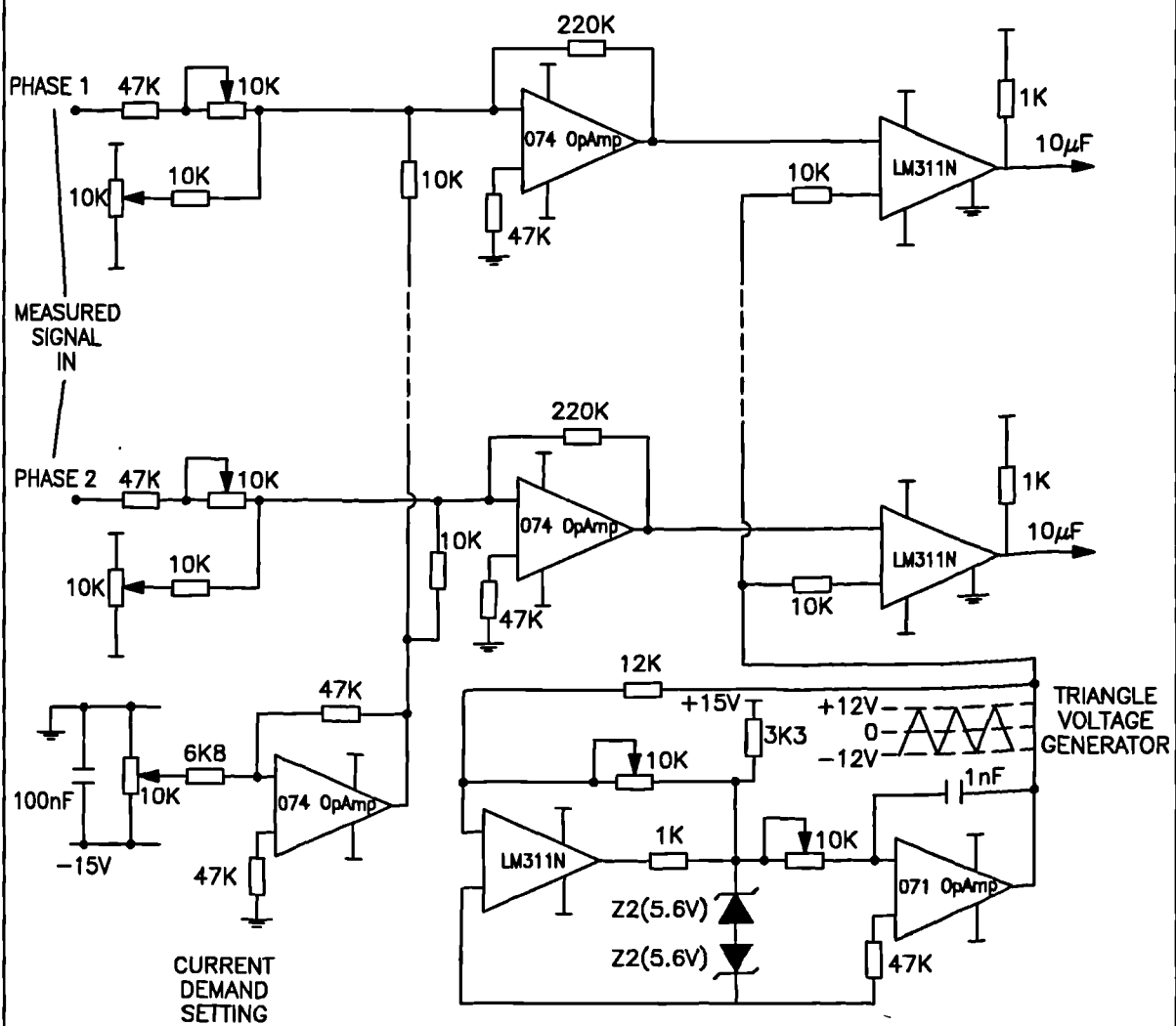


Fig. 2.10. The constructed fixed frequency pwm current regulator.

where v_{cd} denotes the current demand signal and i_{req} the interpreted phase current requirement. The current demand signal was fed into the inverting input of an adder (inverting summing amplifier). Current flowing in the motor phase windings was sensed by LEM Hall effect transducers. The measured phase current signal from the LEM module board was also fed to the inverting input of the adder. The resulting error signal was equal to the difference between the current demand and the actual current measurement. This was compared to the instantaneous amplitude of a triangle wave. An operational amplifier comparator, together with an integrator was used to generate the triangle waveform, shown in fig. 2.10. The frequency of the triangle wave set the chopping frequency of the power switch, and could be altered by trimming a variable resistor pot. A TTL on / off signal was transmitted from the current feedback board to the digital control board. As an example, if the error signal was 0V ($i_{ph} = i_{req}$) a square wave of 50% pulse width would be transmitted. This would indicate that the chopping power switch ought to be on half the time in order to maintain the present current level.

2.4.2 The implementation of logic functions - XILINX.

Recent breakthroughs in logic architectures have resulted in Application Specific Integrated Circuits (ASICs) which can be configured by the user [48]. These user programmable gate arrays offer the logic integration benefits of custom VLSI. The flexibility of user programming allows easy design changes.

The XILINX development system consists of three stages namely the design entry, design implementation and design verification. The design entry software consists of libraries and netlist interfaces for standard CAE software (e.g. FutureNet). The programmable gate array libraries allow design entry with standard TTL gates and Boolean equations. The design implementation software converts schematic netlists and Boolean equations into efficient designs for programmable gate arrays. The software includes sub-programs to perform gate minimisation, placement and routing, and interactive circuit editing. The design verification stage may be performed using simulation software (SILOS) or testing on XILINX demonstration boards. The XILINX development system was used to implement the control logic

in the 5-phase and 7-phase drives.

2.5 Experimental arrangements.

This section describes the experimental arrangement that was employed for static and dynamic tests on the switched reluctance motors.

2.5.1 Description of the test rigs.

A 'dc generator test rig', shown in fig. 2.11, was designed to carry out extensive testing on integral kW switched reluctance machines. The prime mover was mounted on the test bed and coupled via a VibroMeter torque transducer to the

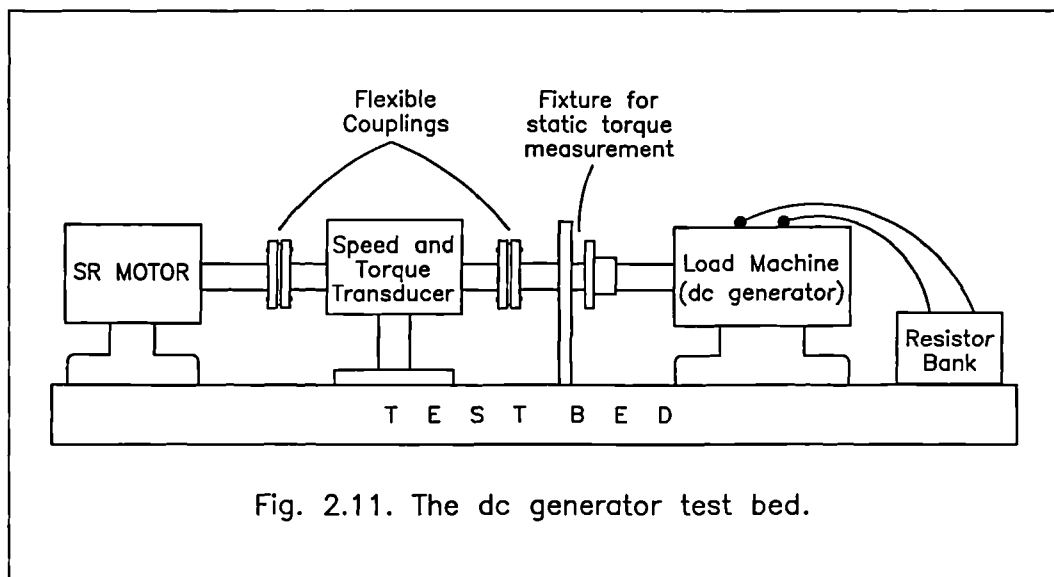


Fig. 2.11. The dc generator test bed.

load machine. The torque transducer measuring shaft was supported by the transducer housing which was bolted directly to the test bed. Double element flexible couplings were used to connect the measuring shaft to the test and load machines. The torque transducer was used in conjunction with the ISC 228 signal conditioner to measure the rotational speed and average torque produced by the test machine. The load machine was a separately excited dc generator. A small resistance-high power load was connected across the terminals of the dc generator

armature. As an accessory, a mechanical fixture could be mounted to lock the rotor of the prime mover. This was useful for static torque and phase winding flux linkage measurements.

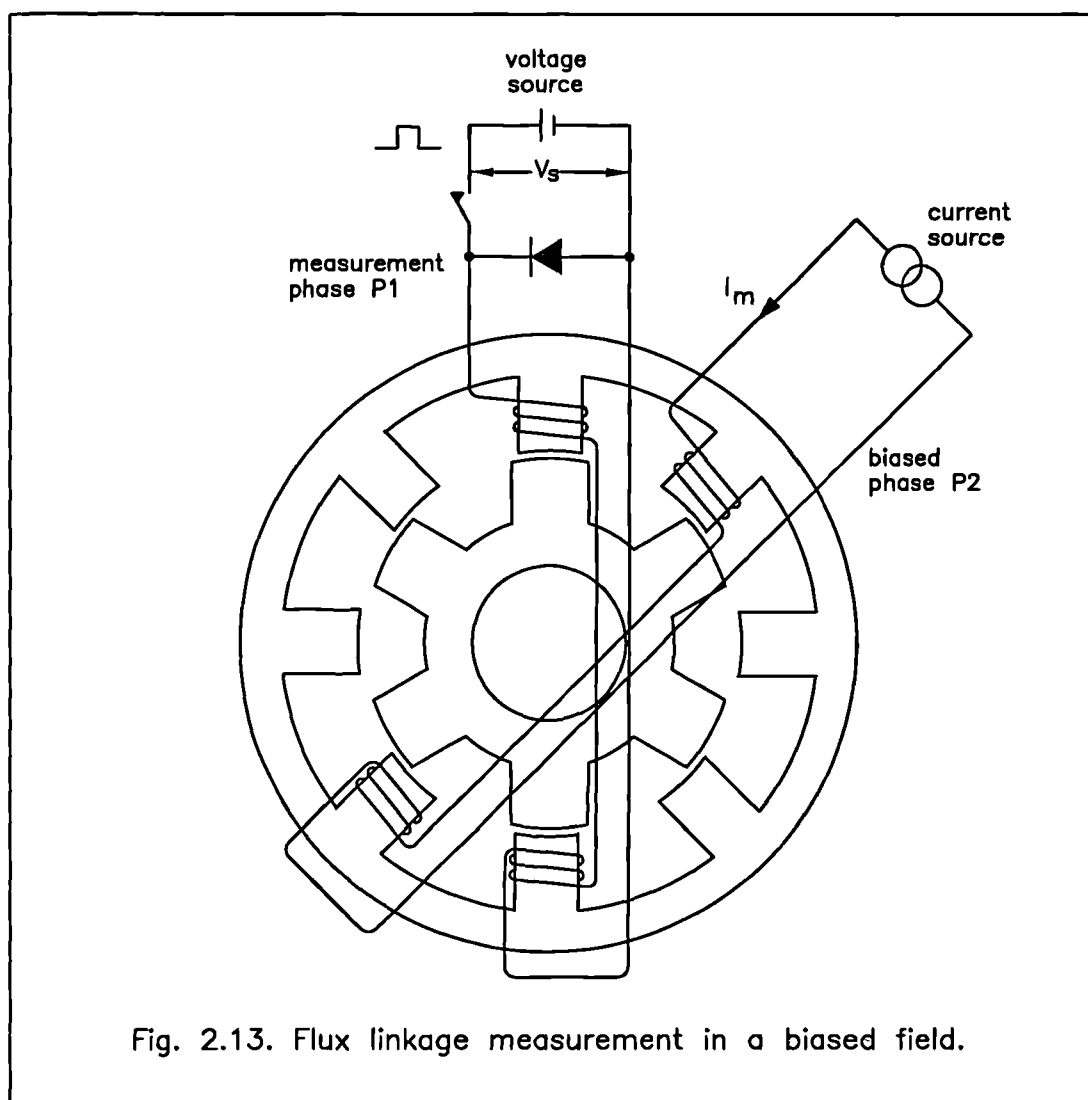
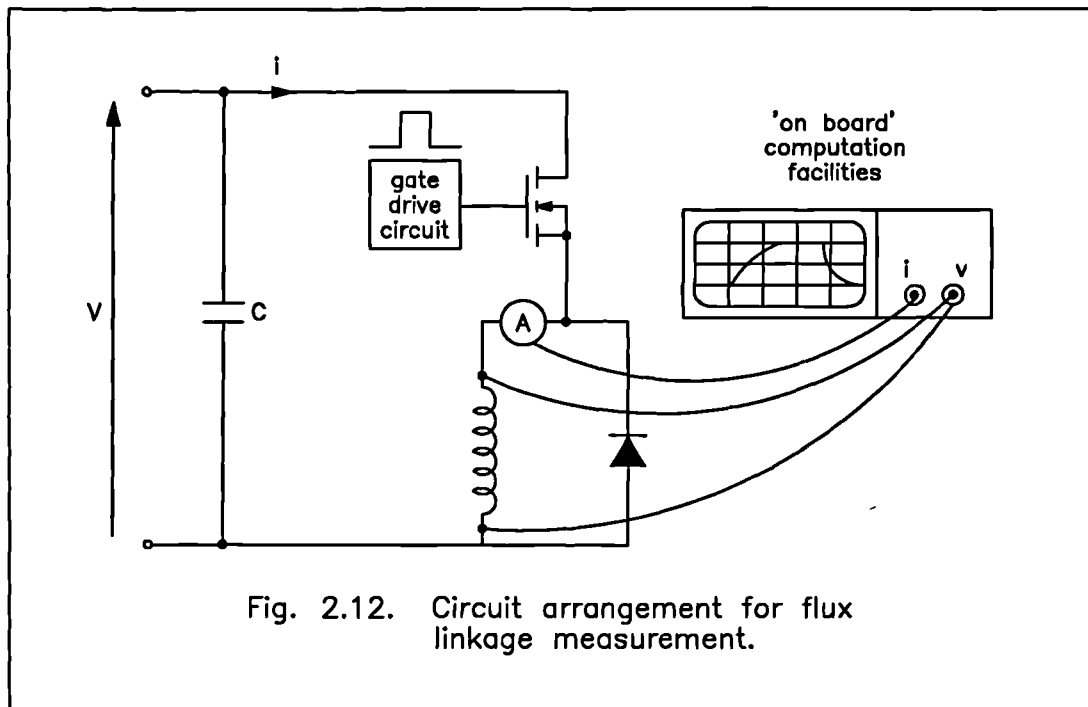
Sub-kW switched reluctance machines were mounted on an 'eddy current test bed'. The shaft of the test machine was connected to the shaft of the eddy current brake via a flexible coupling arrangement.

2.5.2 Flux linkage measurement.

This section describes the experimental procedure that was adopted in order to measure the flux linking a phase winding of the switched reluctance machine. The required rotor position was selected with the aid of a position sensor and / or an LCR meter, and the rotor was clamped using the mechanical fixture arrangement. The electric circuit arrangement, shown in fig. 2.12, consisted of a power MOSFET, the source terminal of which was connected to one terminal of the phase winding undergoing measurement. The other end of the phase winding was connected to the negative terminal of a dc power supply and decoupling capacitor arrangement. A freewheeling diode, connected across the motor winding, provided a path for the current once the main switching device was turned off. The other phase windings of the switched reluctance motor were left open-circuit.

I. Measurement of rising current.

The switching device was turned on and measurement commenced. A step increase in voltage across the circuit terminals caused an (approximately) exponential rise in the phase current waveform, the profile of which was dictated by the instantaneous value of the time constant R / L_{inst} . The measurement was terminated once the phase current waveform attained the value experienced by the motor at full load, I_m . The phase winding voltage and phase current waveforms were recorded. Faraday's voltage equation, in integral form, was applied in order to compute the winding flux linkage i.e.



$$\int_0^{\Lambda} d\lambda = \int_0^{V_m} v dt - R \int_0^{I_m} i dt \quad (2.23)$$

where Λ denotes the flux linking the phase winding when $i(t)$ reaches I_m . The initial flux linkage value $\lambda(0) = 0$, as both $v(t)$ and $i(t)$ were zero at $t = 0$. The two integrals on the right hand side of eqn. 2.23 were computed using measurement facilities on-board a Gould digital oscilloscope. An accurate reading of the circuit resistance, R , was taken using a 4-terminal ohmmeter. Although the circuit resistance varied with temperature, the effect was minimised by conducting the experiment on a ‘single shot’ basis.

II. Measurement of decaying current.

A step voltage was applied to the test winding and, once the phase current attained a steady-state value, the switching device was turned off. The winding was disconnected from the voltage source and the profile of the decaying current was recorded. The measurement was terminated when the phase current was reduced to zero. Faraday’s equation was used to compute the winding flux linkage. At $t = 0$, the boundary conditions were specified as $v(0) = V$, $i(0) = I_m$ and $\lambda(0) = \Lambda$.

III. Biasing the electromagnetic field.

Switched reluctance motors of 4 and 5 phases operate with two phase windings simultaneously excited. In order to measure the flux linking phase winding P1, while the neighbouring phase P2 is carrying rated current I_m , the following procedure was adopted: it was necessary to connect phase P2 across the terminals of a constant current source and not a voltage source, as shown in fig. 2.13. The current source ensured that level I_m was maintained in phase P2, irrespective of step changes in the voltage across phase P1. Therefore P2 was connected across an asymmetric half-bridge arrangement. A separate high-voltage power supply powered the bridge and a pwm current regulator, operating at 20kHz, maintained

a constant current chopping level of I_m . Subsequently the flux linkage in phase P1 was measured as described in section I.

2.5.3 Measurement of static torque.

I. The dc generator test rig.

The required rotor position was selected with the aid of a position sensor, and the rotor was locked mechanically. The appropriate phase winding(s) was (were) excited with dc current, and the static torque was obtained from the torque transducer / signal conditioner arrangement.

II. The eddy current test rig.

No suitable mechanical fixture was provided to lock the rotor of the test machine. The eddy current brake was decoupled from the prime mover and a pulley-and-weights arrangement was mounted on the shaft of the test machine. The appropriate phase winding(s) was (were) energised and the necessary force was applied on the pulley in order to keep the rotor in position. The rotor position was subsequently recorded using a position sensor.

2.5.4 Measurement of dynamic torque.

I. The dc generator test rig.

The level of torque presented to the prime mover was varied by varying either the field current, i.e. the strength of the magnetic field on the stator of the separately excited dc generator, or the armature resistance. The power developed was dissipated, in the form of heat, in a load resistor connected across the armature of the dc machine.

II. The eddy current test rig.

The eddy current brake develops load torque by the interaction of a dc magnetic field, produced by stator winding excitation, and induced eddy currents in a solid rotor [49]. The power developed is dissipated in the form of heat. The level of torque presented to the prime mover by the brake was varied by varying the strength of the magnetic field on the stator. The torque developed in the machine was transmitted to the stator, which was free to rotate over a limited arc. The degree of rotation of the stator frame was recorded on a spring balance. Torque could therefore be directly measured on a scale. Torque indicating scales could be changed so as to alter the range of the instrument.

A digital tacho was used to record rotational speed, ω . The shaft power output was obtained by computing the product of T_{ave} ω . The electrical input power was measured with a Voltech power analyzer connected across the dc link capacitor.

2.6 Review of fundamental aspects of switched reluctance motor technology.

This chapter has reviewed the fundamental motor design methodology of previous researchers. The ‘traditional’ phase numbers and pole combinations i.e. 3-phase 6/4 or 12/8 and 4-phase 8/6 structures have been described. A new design of switched reluctance motor has been proposed, in which the windings are arranged to encourage short magnetic flux paths. It was demonstrated that switched reluctance motors of five and seven phases can be configured for short flux paths. This is achieved by arranging the phase windings such that each stator pole has opposite magnetic polarity to its neighbouring poles, and simultaneously exciting two adjacent phase windings.

Furthermore, this chapter has illustrated the use of the finite element method, in the prediction of phase winding flux linkage and static torque in the switched

reluctance motor.

The construction of the power converter and control electronics, that were common to all the drives tested, has been described. Power MOSFET switching devices were chosen to provide high switching speeds and simplify gate drive electronics. Simple R_f - C_f snubbers were connected across the MOSFETs to decrease switching losses and stresses. The design of the opto-isolated gate drivers for the upper and lower switching devices has been presented.

The control board featured LEM Hall effect current measuring devices. A fixed frequency pwm current regulator was constructed to provide current magnitude regulation. Implementation of logic equations was performed in logic cell arrays.

The experimental procedures for static and dynamic testing of switched reluctance machines has been described. All experimental results that will be presented in subsequent chapters have been obtained by adopting the procedures described.

Chapter 3

ELECTROMAGNETIC ANALYSIS OF THE SWITCHED RELUCTANCE MOTOR

This chapter focuses on electromechanical energy conversion theory and its application to the switched reluctance motor. The virtual work principle, as applied to singly excited electromagnetic systems, is described. The virtual work principle is frequently used by designers to compute the average torque produced in a switched reluctance motor. The established modelling procedure works well for 1, 2 and 3-phase switched reluctance motors (referred to in the thesis as singly excited motors) where there is no (or little) overlap between phase current pulses.

The chapter introduces a thorough electromagnetic analysis of doubly excited systems which relates to switched reluctance motors operating with two phases simultaneously excited [50]. These include the 4-phase 8/6 and 5-phase 10/8 switched reluctance motors. The new modelling procedure that is proposed includes the effects of mutual coupling and increased flux density present in some parts of the steel when two phases are excited at any time. The variation of winding flux linkage with phase current and rotor position is described for such motors. The accurate electromagnetic modelling proposed forms the basis for design considerations that can optimise the performance of switched reluctance motors. The design of 4-phase motors for low torque ripple is described. Finite element analysis results from a 4kW 7-phase motor configured for long and short flux paths are also presented. It is shown that short flux loops significantly improve the torque production capability of the 7-phase machine.

3.1 Electromechanical energy conversion theory.

3.1.1 Singly excited systems.

In a lossless electromechanical energy conversion device operating as a motor, an incremental change in the electrical energy input, dW_e , will cause one component of energy, dW_f , to be stored in the field and another component, dW_{mech} , to be made available to the load. The energy balance equation is

$$dW_e = dW_f + dW_{mech} \quad (3.1)$$

Introducing Faraday's law, dW_f may be expressed as

$$dW_f = i d\lambda - T d\theta \quad (3.2)$$

where i denotes the current in a particular phase winding and λ its associated flux linkage; the term T represents (average) torque while $d\theta$ denotes angular displacement. By application of the chain rule the increment in field energy, dW_f , can also be expressed in terms of the flux linkage, λ , and rotor position, θ , as

$$dW_f = \left. \frac{\partial W_f}{\partial \lambda} \right|_{\theta=const} d\lambda + \left. \frac{\partial W_f}{\partial \theta} \right|_{\lambda=const} d\theta \quad (3.3)$$

Comparison of eqn. 3.2 with eqn. 3.3 reveals that

$$T = - \frac{\partial W_f(\lambda, \theta)}{\partial \theta} \quad (3.4)$$

The system coenergy, W_c , can be defined as

$$W_c = \int_0^I \lambda(i, \theta) di \quad (3.5)$$

The coenergy may be expressed in terms of the stored energy by

$$W_c = i\lambda - W_f \quad (3.6)$$

Torque, T , is also given by the rate of change of coenergy with respect to the rotor

angle, at constant excitation i.e.

$$T = \frac{\partial W_c(i, \theta)}{\partial \theta} \quad (3.7)$$

In order to estimate the average torque produced in the switched reluctance motor, it is essential to know how the phase winding flux linkage, λ , varies with phase current, i , and rotor position, θ . The change in coenergy, ΔW_c , during one repetitive excitation cycle of duration $\Delta\theta$, is equivalent to the area enclosed by the operating trajectory described on the λ / i diagram. The average torque is given by

$$T_{ave} = \Delta W_c \frac{N_s N_r}{2\pi (N_s - N_r)} \quad (3.8)$$

Figure 3.1 illustrates the laminations of a typical 2-phase switched reluctance motor with four teeth on the stator and two teeth on the rotor. This machine is operated by ensuring that one stator phase winding is conducting at any time. Referring to fig. 3.1 (consider solid lines), the stator teeth of phase P1 face the interpolar airgap depth. This is known as the ‘unaligned’ rotor position which marks the beginning of the excitation cycle. The stator teeth of P2 are aligned with the rotor teeth. This is known as the ‘aligned’ rotor position which, in the 2-phase motor, marks the end of the (repeatable) excitation cycle.

The ideal excitation cycle can be described with the aid of a λ / i diagram, shown in fig. 3.2. The start of the excitation cycle is marked upon application of full positive volts across the terminals of phase P1. In the ideal case the current rises to its maximum value I_m instantaneously. This current level is maintained throughout the duration of the excitation cycle by means of a current chopping regulator. The rotor poles rotate to take up a position of minimum reluctance, that is, to align with the magnetised stator teeth (ref. dashed lines in fig. 3.1). During this time the phase winding flux linkage rises from λ_{un} to λ_{al} . At alignment, after the rotor has moved by 90° , full negative volts are impressed on the terminals of phase P1 to instantaneously reduce the current to zero. At the same time, full positive volts are impressed on the terminals of P2 to move the rotor 90° further.

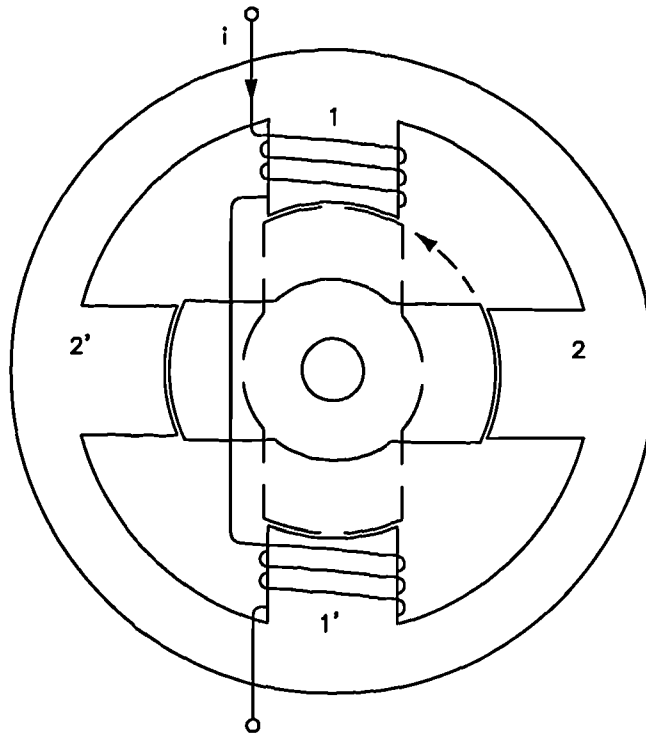


Fig. 3.1 A 2-phase 4/2 motor, illustrating movement through a rotor step.

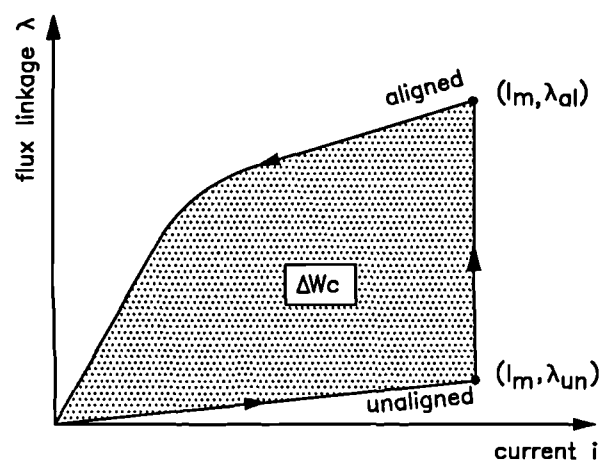


Fig. 3.2. λ/i diagram of an ideal excitation cycle.

3.1.2 Exciting two phases simultaneously - a new modelling procedure.

I. Flux patterns in the 4-phase motor.

The 4-phase 8/6 switched reluctance motor is fundamentally a doubly excited system, as two phase windings are carrying current at any time to produce continuous torque. Fig. 3.3a illustrates the flux pattern arising in the motor if phase winding P1 is excited. The **B**-field links the excited stator poles via the rotor body and stator yoke. The stator yoke carries half the flux linking the excited stator poles. However, at this rotor position phase P2 is also in the torque producing region, as shown in fig. 3.3b. The **B**-fields produced by the two excited phases cause most parts of the magnetic circuit to be driven at higher flux densities. In the stator yoke the **B**-fields oppose each other only in the sections that lie between adjacent excited poles. In these sections a balancing flux exists, complementing the resulting **B**-field flux pattern as shown in fig. 3.3c.

The effective torque zone for each phase of the 4-phase 8/6 motor is 30°, as illustrated in fig. 3.3d. However, the stepping action which results in the **B**-field pattern described in fig. 3.3c is repeated every 15°. This is confirmed by the plot of the ideal phase current pulses in the four phases, shown in fig. 3.3e. The stepping action will be referred to as the excitation cycle.

II. Computation of coenergy in a doubly excited system.

The energy balance equation that was introduced in section 3.1.1 can be re-written for a system with two excitation sources as

$$dW_f = i_1 d\lambda_1 + i_2 d\lambda_2 - T d\theta \quad (3.9)$$

The increment in field energy, dW_f , can also be expressed in terms of $d\lambda_1$, $d\lambda_2$ and $d\theta$ as

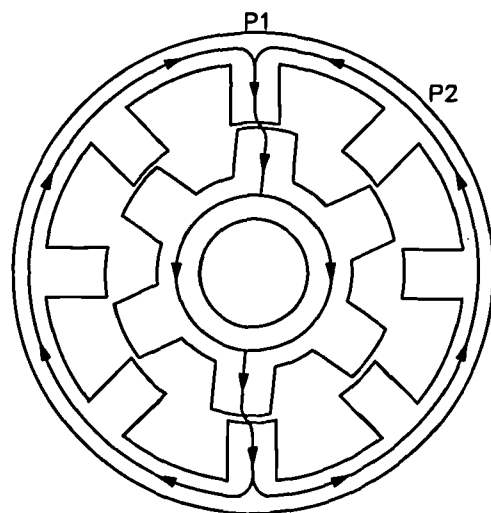


Fig. 3.3a. Flux pattern in a singly excited 4-phase motor.

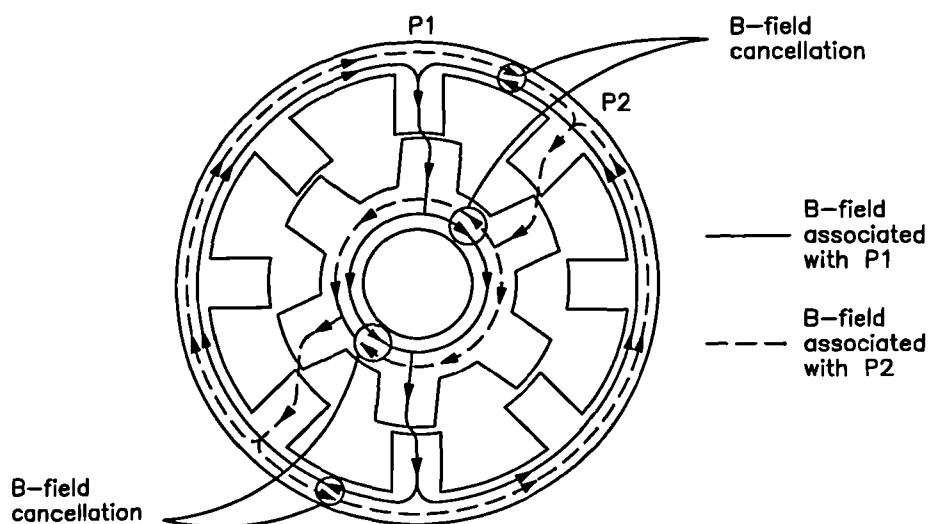


Fig. 3.3b. Flux pattern in a doubly excited 4-phase motor.

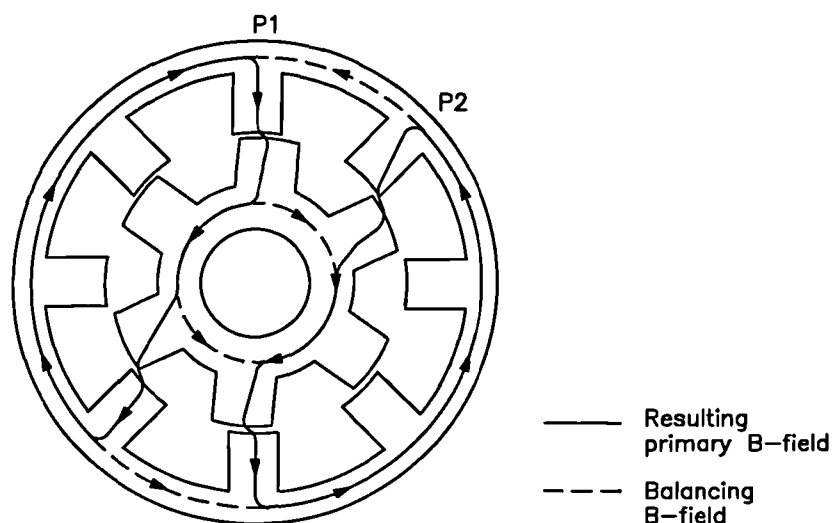
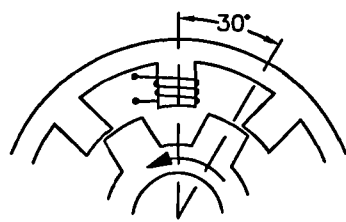
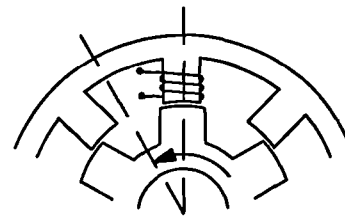


Fig. 3.3c. Resulting primary B-field in a doubly excited 4-phase motor.



turn-on (0°) position



turn-off (30°) position

Phase current conduction period
(Effective torque zone) $= 30^\circ$

Fig. 3.3d. Geometrical considerations in a 4-phase motor.

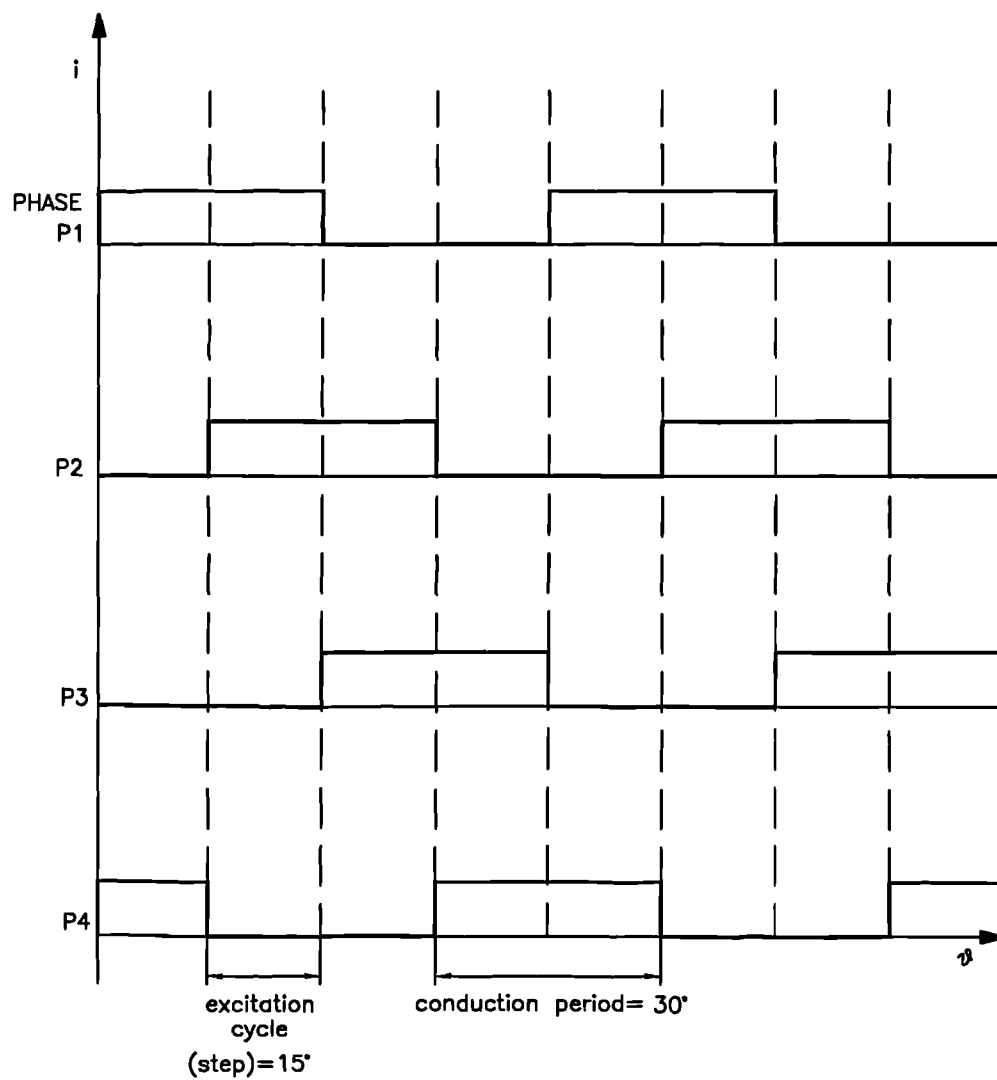


Fig. 3.3e. Excitation sequence in the 4-phase motor.

$$dW_f = \frac{\partial W_f}{\partial \lambda_1} \Big|_{\lambda_2, \theta = \text{con}} d\lambda_1 + \frac{\partial W_f}{\partial \lambda_2} \Big|_{\lambda_1, \theta = \text{con}} d\lambda_2 + \frac{\partial W_f}{\partial \theta} \Big|_{\lambda_1, \lambda_2 = \text{con}} d\theta \quad (3.10)$$

As a result

$$T = \frac{-\partial W_f(\lambda_1, \lambda_2, \theta)}{\partial \theta} \quad (3.11)$$

Similar expressions may be derived using the coenergy W_c , where

$$W_c = \lambda_1 i_1 + \lambda_2 i_2 - W_f \quad (3.12)$$

The torque, T , is given by the rate of change of coenergy with respect to the rotor angle, θ ,

$$T = \frac{\partial W_c(i_1, i_2, \theta)}{\partial \theta} \quad (3.13)$$

In order to obtain the coenergy W_c of a doubly excited system, such as a switched reluctance motor with two phases simultaneously excited, at a particular rotor position and winding excitation, the integral $\int dW_c$ must be evaluated in steps, as illustrated in fig. 3.4. It is assumed that the rotor is turning in an anticlockwise direction; rotor position P marks the beginning of the conduction cycle in the 4-phase machine. At this position phase P2 has been conducting maximum current i_{2p} for 15° of rotor rotation and the current in phase P1 now increases from 0 to i_{1p} . It is therefore necessary to first compute the coenergy associated with the excitation of the leading phase P2, before attempting to calculate the coenergy associated with the excitation of P1 in the presence of i_{2p} :

1. Step OA; $i_1 = i_2 = 0$ and θ varies from zero to θ_p :

Now $di_1 = di_2 = 0$ and $T = 0$, therefore

$$\int_0^A dW_c = \int_0^A (\lambda_1 di_1 + \lambda_2 di_2 + T d\theta) = 0 \quad (3.14)$$

2. Step AB; $i_1 = 0$, $\theta = \theta_p$ and i_2 varies from zero to i_{2p} :

$$\int_A^B dW_c = \int_0^{i_{2p}} \lambda_{2AB} di_2 \quad (3.15)$$

3. Step BP; $i_2 = i_{2p}$, $\theta = \theta_p$ and i_1 varies from 0 to i_{1p} :

$$\int_B^P dW_c = \int_0^{i_{1p}} \lambda_{1BP} di_1 \quad (3.16)$$

Hence

$$W_c(i_{1p}, i_{2p}, \theta_p) = \int_0^{i_{2p}} \lambda_{2AB} di_2 + \int_0^{i_{1p}} \lambda_{1BP} di_1 \quad (3.17)$$

where

$$\lambda_{2AB} = \lambda_2(i_1=0, i_2, \theta_p) \quad (3.18)$$

$$\lambda_{1BP} = \lambda_1(i_2=i_{2p}, i_1, \theta_p) \quad (3.19)$$

Equation 3.17 dictates that two separate integrals i.e. $\int \lambda_2 di_2$ and $\int \lambda_1 di_1$ must be computed in order to estimate the coenergy at the start of the excitation cycle. First, the integral of flux linkage in the leading phase (λ_2) wrt to current i_2 is calculated, assuming that the trailing phase is carrying no current ($i_1 = 0$). Subsequently the integral of flux linkage in the trailing phase (λ_1) is computed wrt i_1 , assuming that the leading phase is conducting full current ($i_2 = i_{2p}$). These are then added together to give the total coenergy associated with the two excited phases.

The average torque output of the 4-phase machine can be determined by evaluating the change in the coenergy of the system from position P at the start of the conduction cycle, to position P' at the end of the cycle, as shown in fig. 3.4. At position P', the integral $\int dW_c$ may be evaluated in steps following any suitable integration path to obtain

$$W_c(i_{1p'}, i_{2p'}, \theta_{p'}) = \int_0^{i_{1p'}} \lambda_{1A'B'} di_1 + \int_0^{i_{2p'}} \lambda_{2B'P'} di_2 \quad (3.20)$$

where

$$\lambda_{1A'B'} = \lambda_1(i_2=0, i_1, \theta_{p'}) \quad (3.21)$$

$$\lambda_{2B'P'} = \lambda_2(i_1=i_{1p'}, i_2, \theta_{p'}) \quad (3.22)$$

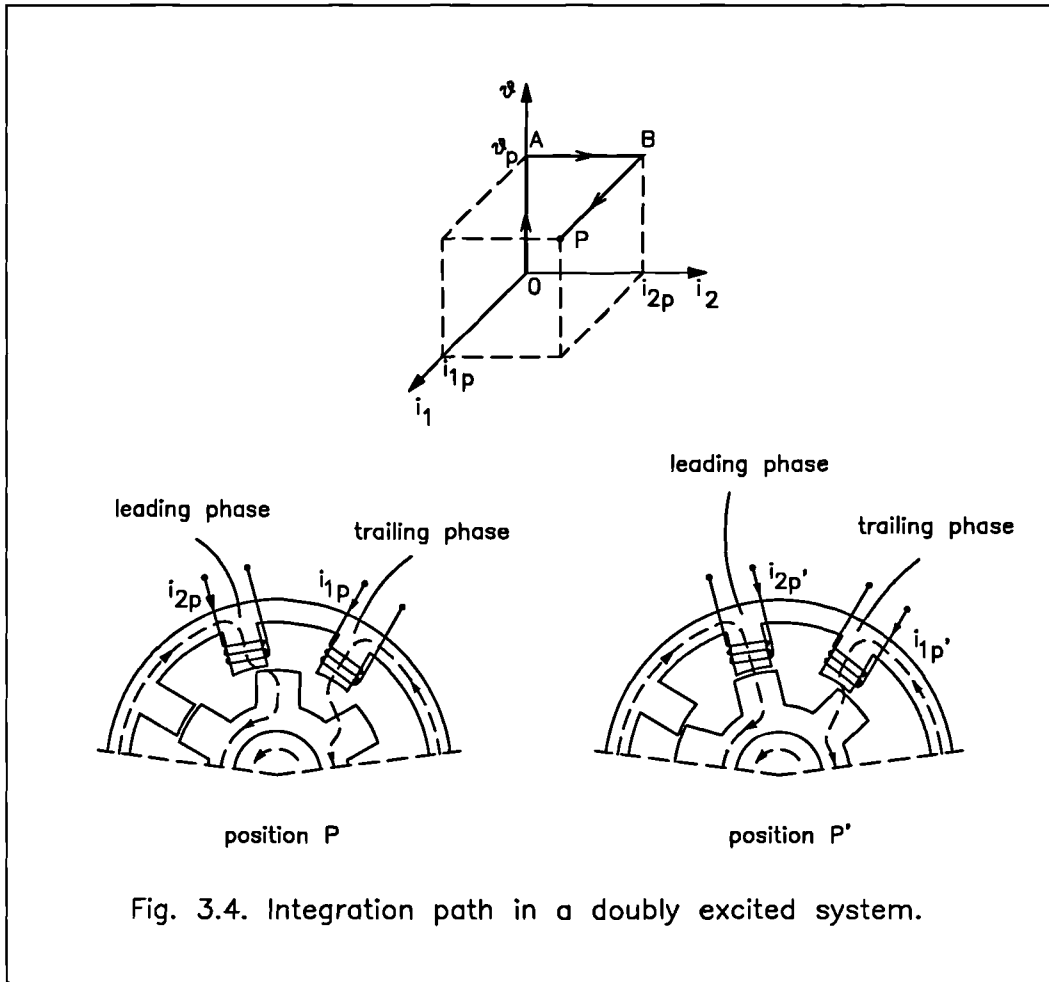


Fig. 3.4. Integration path in a doubly excited system.

The rotor has moved one complete step between positions P and P' and is now in the same position relative to phase P1, as it was to phase P2 at position P. Examination of equations 3.17 - 3.22 reveals that

$$\int_0^{i_{2p}} \lambda_{2AB} di_2 = \int_0^{i_{1p'}} \lambda_{1A'B'} di_1 \quad (3.23)$$

assuming $i_{2p} = i_{1p'}$. Therefore, the change in coenergy over the conduction cycle is given by

$$W_{c_{p'}} - W_{c_p} = \int_0^{i_{2p'}} \lambda_{2B'P'} di_2 - \int_0^{i_{1p}} \lambda_{1BP} di_1 \quad (3.24)$$

where

$$\lambda_{2B'P'} = \lambda_2(i_1 = i_{1p'}, i_2, \theta_{p'}) \quad (3.25)$$

$$\lambda_{1BP} = \lambda_1(i_2 = i_{2p}, i_1, \theta_p) \quad (3.26)$$

Computation of the first integral in eqn. 3.24 yields the λ / i curve at the end of the excitation cycle ('aligned' characteristic). In order to obtain this integral the rotor is positioned at P', a bias current $i_{1p'}$ is applied to phase P1 and the flux linkage of phase winding P2 is integrated for different excitations up to $i_2 = i_{2p} = i_{2p'}$. The second integral in eqn. 3.24, which represents the λ / i characteristic at the start of the cycle, can be obtained in a similar fashion as dictated by eqn. 3.26. In this doubly excited system the area enclosed by the **system** λ / i characteristic that is defined by these curves is equal to the electrical energy per step that is converted to mechanical work.

Results obtained from two-dimensional electromagnetic finite element modelling shall be presented in subsequent sections of this chapter. Two switched reluctance motors were extensively modelled; a 150W 4-phase machine and a 4kW 7-phase motor. These motors were available for testing and their dimensions could readily be obtained. The switched reluctance motor models were created and analysed using OPERA / TOSCA, as described in chapter 2. The performance of these motors was characterised by implementation of the electromechanical energy conversion theory presented in this section.

3.2 The 150W 4-phase motor.

The 4-phase switched reluctance motor that was modelled, was constructed as part of earlier development work in the laboratory. The analysis that follows includes flux linkage and static torque computations on the 4-phase motor, for a range of rotor positions and current levels. For comparison purposes the analysis includes results into modelling of the 4-phase motor with one and two phases excited at the same time. Magnetic interaction effects between simultaneously excited phase windings are investigated.

Magnetic interaction effects include mutual coupling between adjacent phase windings and saturation. Mutual coupling arises when flux generated from current flowing in one phase winding is linked by an adjacent phase winding. Saturation must be taken into account since some parts of the magnetic circuit will carry increased flux when two phases are excited. Magnetic saturation degrades the performance of the switched reluctance motor. In a saturated 4-phase structure operating with two phases simultaneously excited, the flux linking a phase winding at a specified rotor position and excitation would increase if the second phase was switched off. This is because the stator and rotor yokes would operate at a lower flux density.

3.2.1 Single phase excitation.

The λ / i characteristic for one phase of this machine at the aligned and unaligned positions is shown in fig. 3.5. In comparison to measurement, two-dimensional model solutions consistently underestimate the flux linkage value. The effect is particularly noticeable at positions where the excited stator poles face the interpolar airgap depth. This error can be attributed to end-core flux, which is not accounted for in two-dimensional modelling. A full analysis of three-dimensional effects in the switched reluctance motor will be presented in chapter 4.

FIG. 3.5 FLUX LINKAGE / CURRENT DIAGRAM (4-PH MOTOR, 1 PH EXCITED)

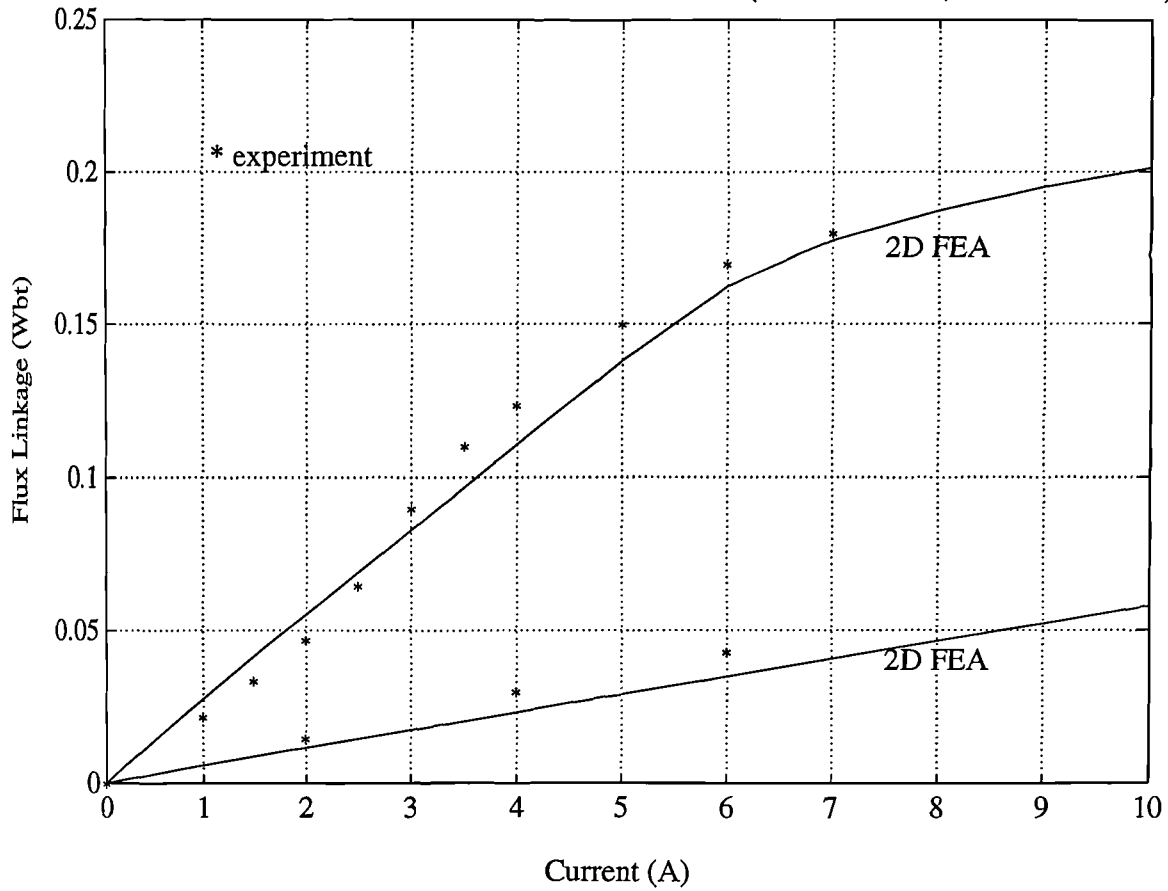
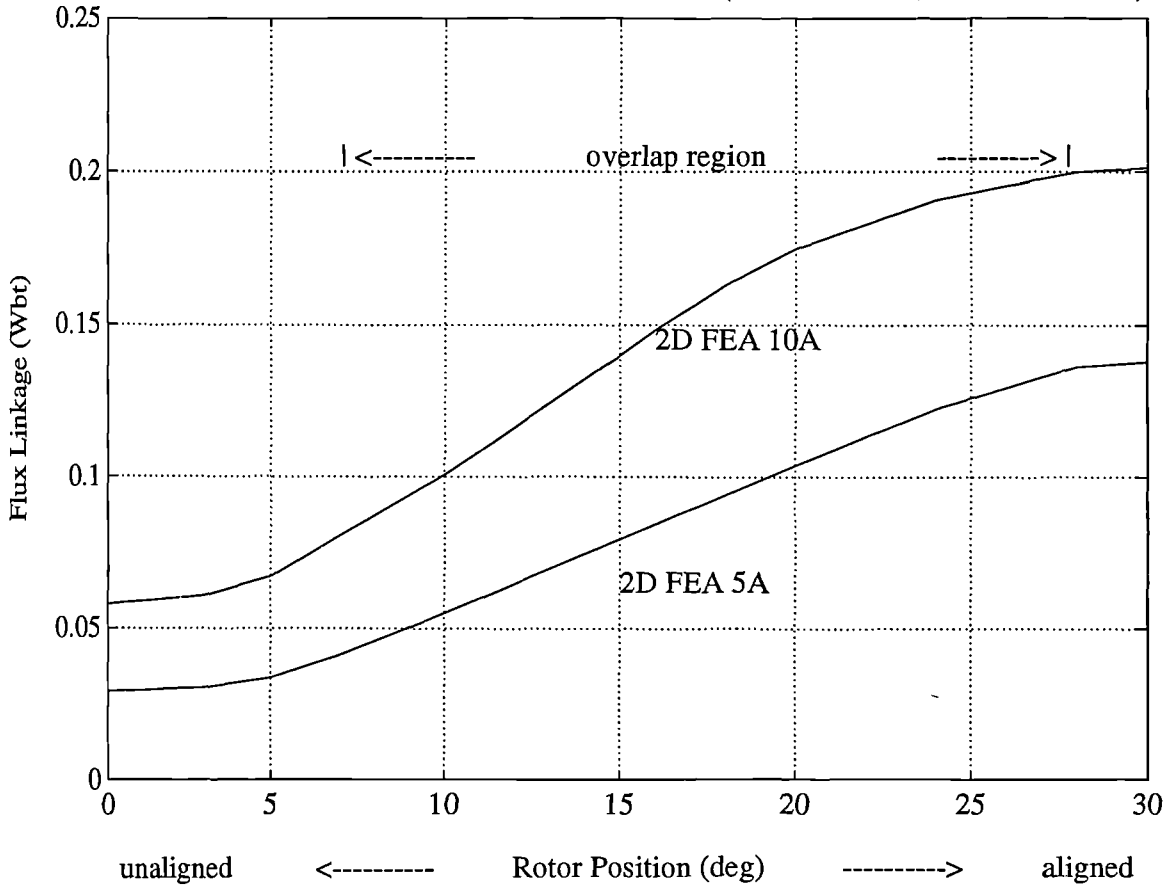


FIG. 3.6 FLUX LINKAGE / ROTOR POSITION (4-PH MOTOR, 1 PH EXCITED)



The λ / θ characteristic for one phase of the 150W, 4-phase motor is illustrated in fig. 3.6. When the excitation is low, the relationship between flux linkage and rotor position in the region where the excited stator poles and associated rotor poles overlap (henceforth referred to as the overlap region) is linear. This is because, although the reluctance of the magnetic circuit decreases as the rotor poles reach alignment, the excitation is not high enough to saturate the iron. At high excitations, the relationship between flux linkage and angular position in the overlap region may be characterised by a linear followed by a sigmoidal function. The degree of saturation depends on path reluctance and excitation.

The measured static torque produced by the experimental 4-phase machine, as a function of rotor position, is illustrated in fig. 3.7. Also shown is the static torque profile of the machine, predicted by the two-dimensional finite element model. At a particular rotor position and excitation, static torque was computed by evaluating the Maxwell stress integral over the rotor surface. Finite element analysis predictions show good agreement with experiment, though there is a tendency to underestimate the measured static torque value at early rotor positions ($\theta = 0^\circ$ - 15°). This may again be attributed to three-dimensional effects which shall be investigated in chapter 4.

3.2.2 Simultaneous excitation of two phase windings in the 4-phase machine - normal machine operation.

The system λ / i characteristic, drawn by adopting the new field computation procedure for motors with two phases simultaneously excited, is shown in fig. 3.8. In order to obtain the characteristic that marks the end of the excitation cycle, the rotor was positioned such that a pair of rotor poles was aligned with phase P2 (see position P' in fig. 3.4). The selected bias current was then applied to phase P1 and the flux linking P2 was measured for different excitations up to 10A. The (unaligned) characteristic that marks the beginning of the excitation cycle was obtained by applying similar considerations to phases P1 and P2 at rotor position P. A system λ / i diagram was also constructed for a 5A phase current bias.

FIG. 3.7 STATIC TORQUE / ROTOR POSITION (4-PH MOTOR, 1 PH EXCITED)

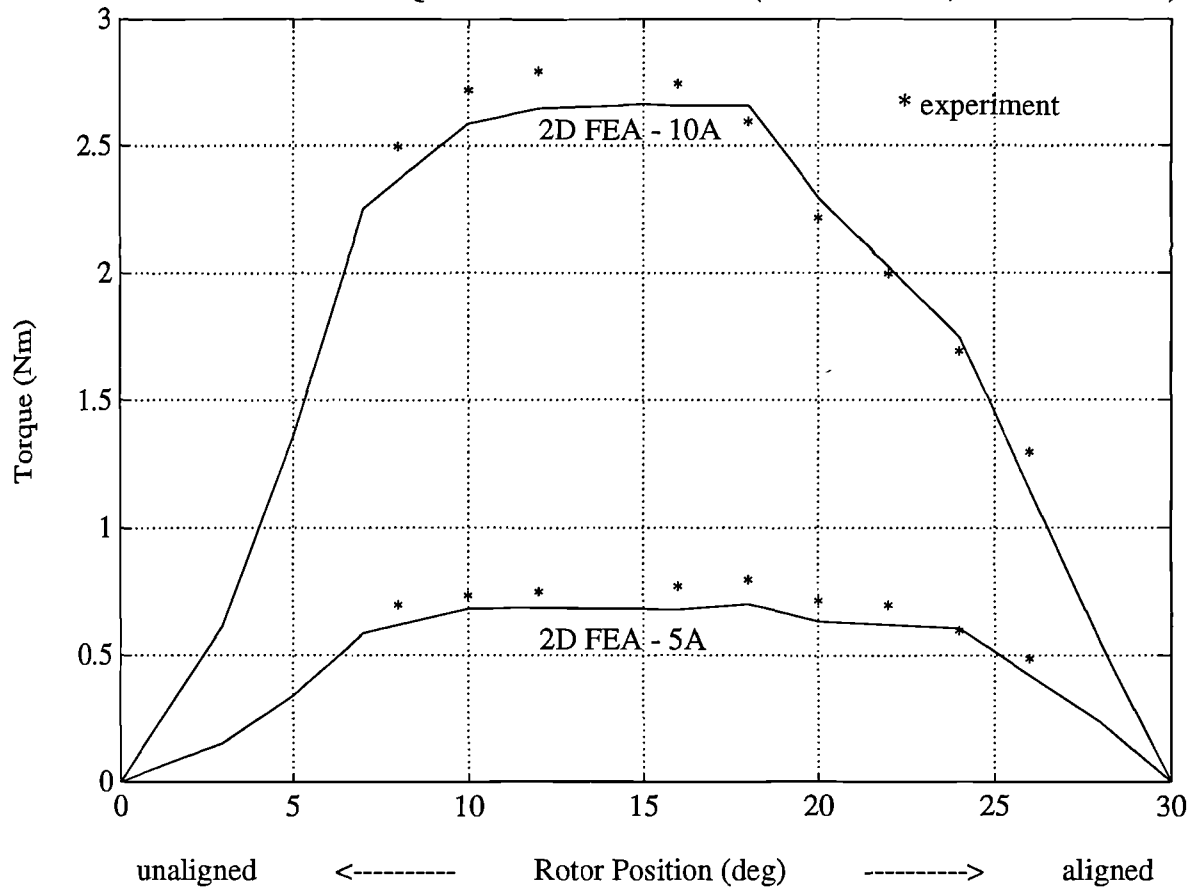
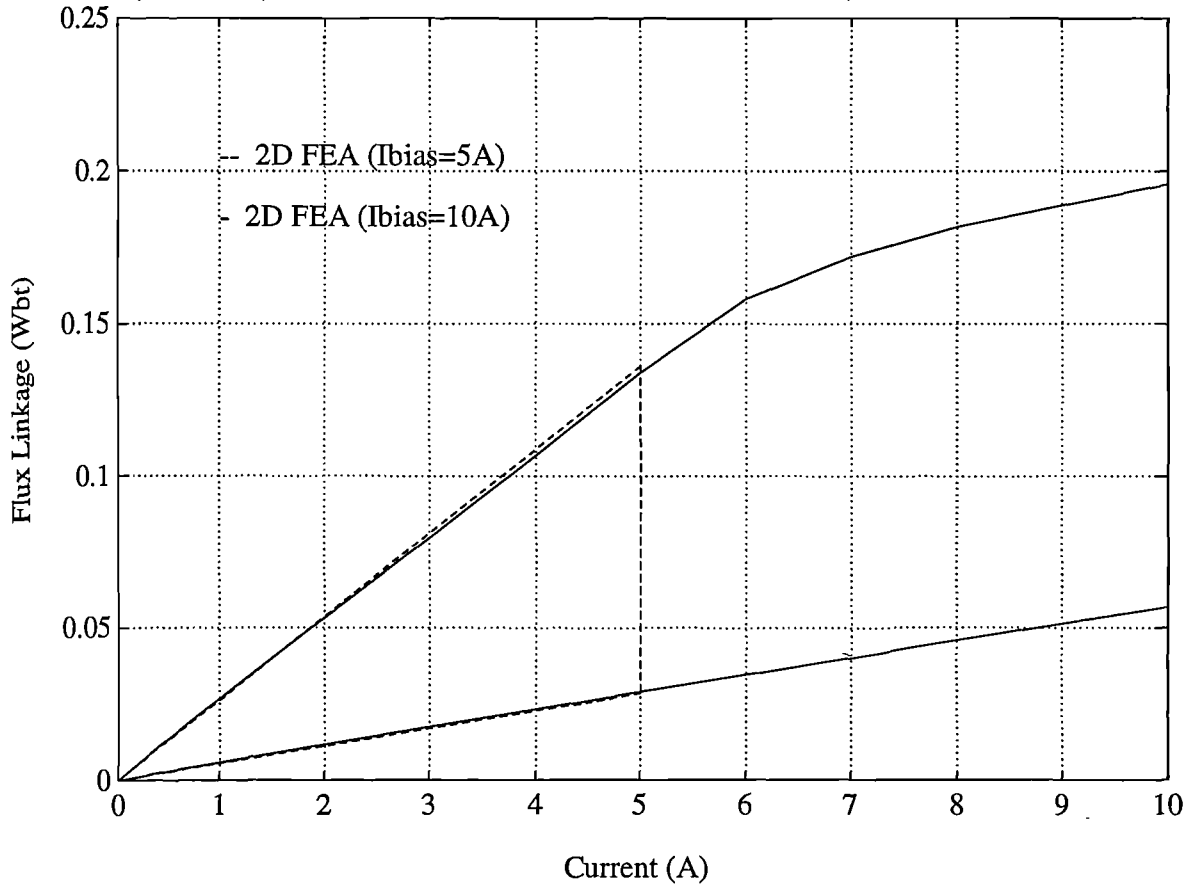


FIG. 3.8 (SYSTEM) FLUX LINKAGE / CURRENT DIAGRAM (4-PH MOTOR, 2 PH EXCITED)



The variation of flux linkage with rotor position in the doubly excited 4-phase motor is shown in fig. 3.9. The excitation cycle of a 4-phase switched reluctance motor spans 15° . In one cycle the rotor poles associated with the leading phase move from the 15° rotor position to the 30° (aligned) position. In the same cycle, the rotor poles associated with the trailing phase are displaced from the 0° (unaligned) position to the 15° rotor position, as shown in fig. 3.3d,e. The λ / θ profile of both the trailing (0° - 15°) and leading (15° - 30°) phases is depicted. The characteristic is similar to that of a typical, singly excited switched reluctance motor. In the overlap region, from $\theta = \theta_{bo}$ to $\theta = \theta_{bo} + \beta_s / 2$ (where θ_{bo} denotes the beginning of the overlap), the λ / θ characteristic follows a linear relationship. From $\theta = \theta_{bo} + \beta_s / 2$ to $\theta = \theta_{bo} + \beta_s$ the profile follows a sigmoidal relationship.

The static torque profile of the 4-phase motor, with two phases conducting simultaneously, is illustrated in fig. 3.10. The T / θ profile is drawn with respect to the absolute rotor position, i.e. the unaligned rotor position of the trailing phase. The characteristic, obtained by evaluating the Maxwell stress integral at discrete positions, spans one rotor step angle. Average torque can be computed by averaging the instantaneous static torque values over the step angle.

$$T_{ave} = \frac{1}{step} \int_0^{step} T(\theta) d\theta \quad (3.27)$$

This is in close agreement with the value obtained by the use of the coenergy principle as applied to doubly excited systems. A comparison between the different methods of computing average torque in the 4-phase motor (coenergy-singly excited, coenergy-doubly excited and Maxwell stress) is given in Table 3.1. Table 3.1 suggests that if mutual coupling and saturation effects are neglected, average torque values calculated by the coenergy method are overestimated.

3.2.3 Bulk saturation effects.

Extensive finite element analysis of doubly excited switched reluctance motors has revealed a departure from the customary λ / θ characteristic when the stator and

FIG. 3.9 FLUX LINKAGE / ROTOR POSITION (4-PH MOTOR, 2 PH EXCITED)

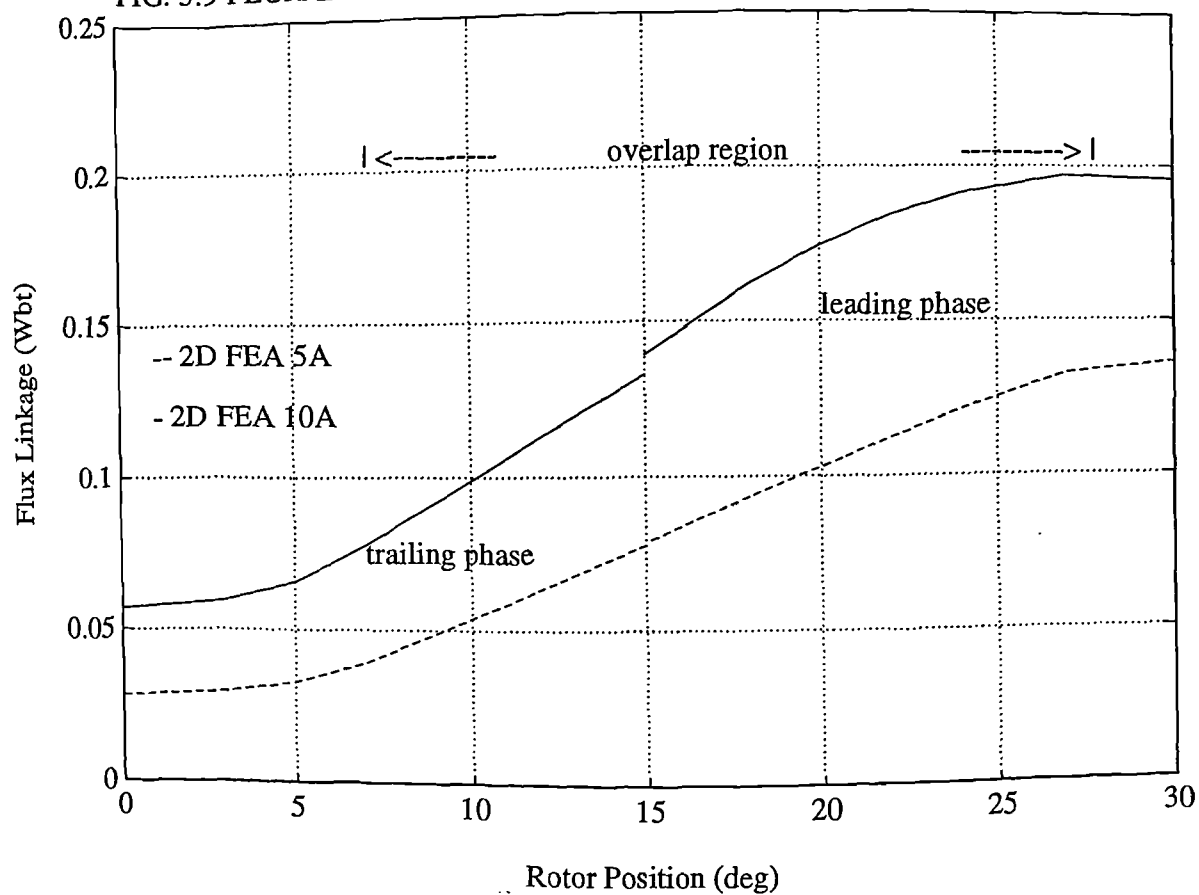
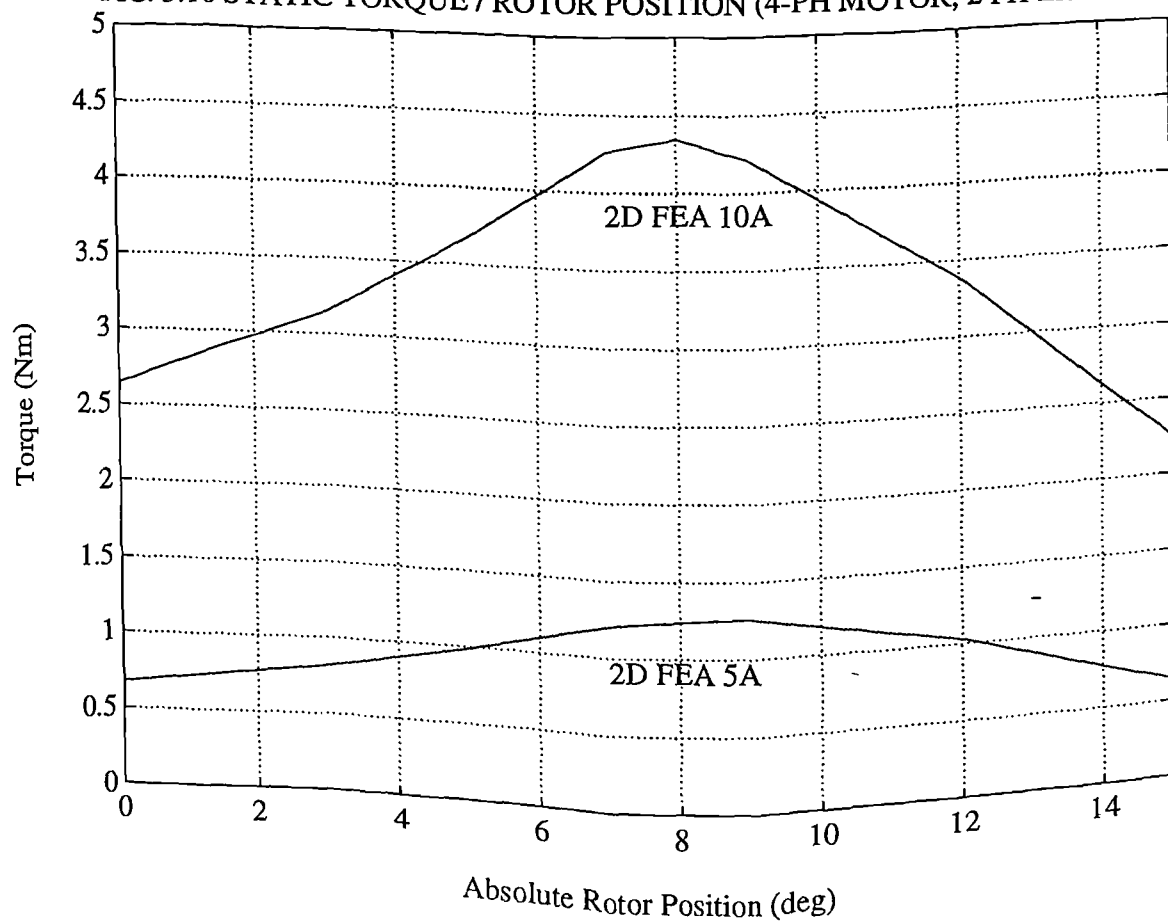


FIG. 3.10 STATIC TORQUE / ROTOR POSITION (4-PH MOTOR, 2 PH EXCITED)



/ or rotor yoke sections are heavily saturated. In order to investigate the effects of stator yoke saturation, the back-iron width of the 4-phase finite element model was varied by changing the stator slot depth. The stator bore and pole arc were held constant. The geometry of the 4-phase finite element models, referred to as Mk I, II and III, may be found in Table 3.2.

Current	Torque (coenergy singly excited)	Torque (coenergy doubly excited)	Torque (Maxwell stress)	Overestimation by singly excited theory
5A	1.05Nm	1.00Nm	0.99Nm	6.4%
10A	3.65Nm	3.52Nm	3.5Nm	4.0%

Table 3.1. Average torque figures for the 150W 4-phase motor.

	Mk I	Mk II	Mk III
stator diameter (mm)	106.5	106.5	106.5
stator back-iron width (mm)	10.0	7.00	5.00
stator pole arc (rad)	0.365	0.365	0.365
stator pole height (mm)	14.775	17.775	19.775
airgap length (mm)	0.6	0.6	0.6
rotor diameter (mm)	55.75	55.75	55.75
rotor pole arc (rad)	0.436	0.436	0.436
stack length (mm)	50.0	50.0	50.0
packing factor	0.92	0.92	0.92
turns per phase	220	220	220

Table 3.2. Dimensions of the 4-phase motor models.

The customary λ / θ relationship can be ‘distorted’ in cases where the magnetic circuit is heavily saturated. Consider the λ / θ characteristic of the 4-phase Mk I, II and III motors, shown in fig. 3.11. The diagram only shows the flux linkage in the leading phase, as this is the one most affected by saturation. In the Mk I motor the flux linkage reaches a peak at the aligned position. In the Mk II and III motors, the flux linkage value reaches a maximum before the approaching rotor poles reach alignment. The peak flux value occurs earlier as the back-iron width is reduced. Beyond this peak, and while the overlap angle increases, the flux linking the leading stator phase P1 decreases. In contrast, it can be shown that the flux linkage of the trailing stator phase P2 continues to rapidly increase so that the energy balance equation

$$W_c + W_f = i_1 \lambda_1 + i_2 \lambda_2 \quad (3.28)$$

is adhered to.

Long flux loop motor configurations are more susceptible to saturation effects because the stator yoke constitutes a significant part of the overall magnetic flux path length. Magnetic interaction between adjacent phases becomes more pronounced as the back-iron width is reduced, largely due to saturation. Figure 3.12 shows the **system** λ / i characteristic of the 4-phase Mk II motor; also demonstrated is the significant error that arises if the effects of mutual coupling and saturation, brought about by exciting the second phase, are ignored.

These and subsequent comparisons between the 4-phase Mk I, II and III assumed equal copper loss. This was found to be most appropriate because a comparison based on equal MMF (excitation) would not take into account the increased copper area which becomes available as the yoke thickness is decreased. The mathematical analysis that describes the setup of finite element models for equal copper loss can be found in Appendix C.

FIG. 3.11 FLUX LINKAGE / ROTOR POSITION DIAGRAM (4-PH MOTOR, LEADING PHASE)

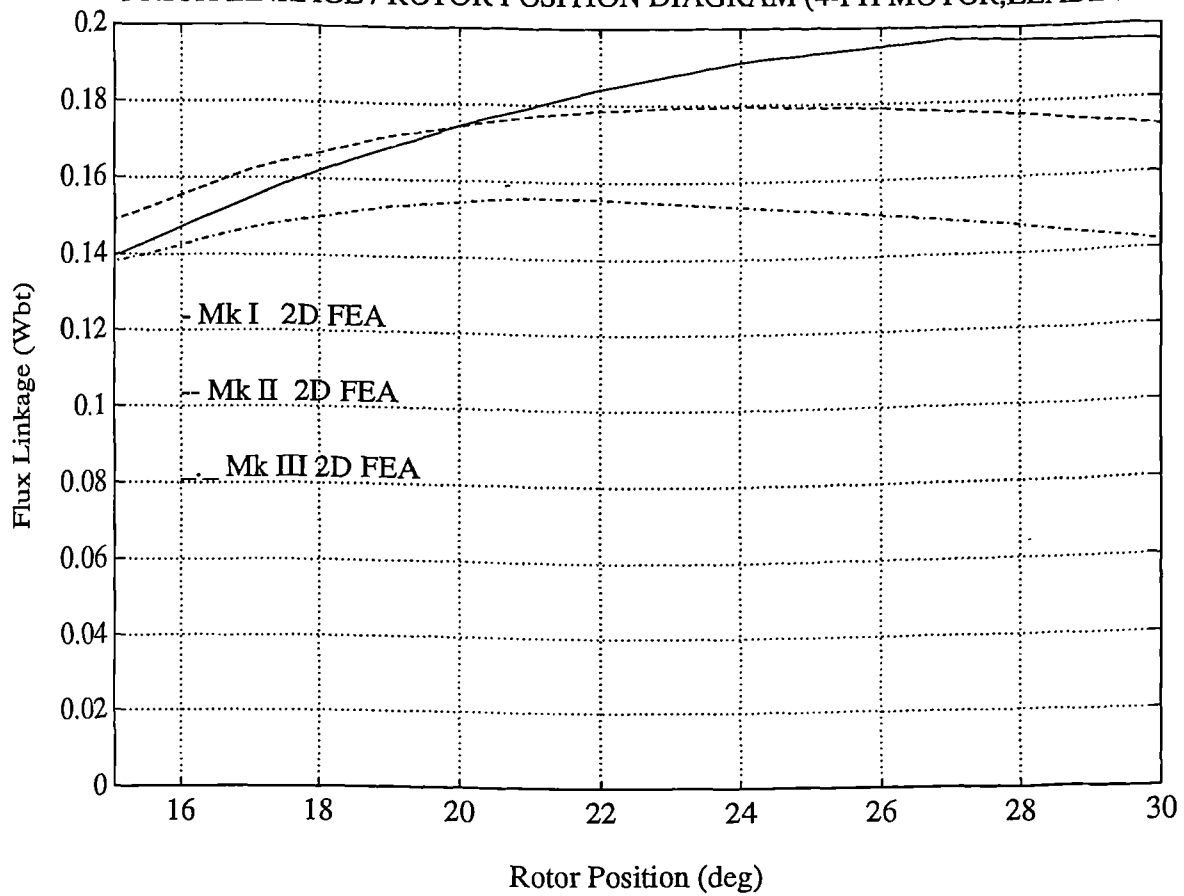
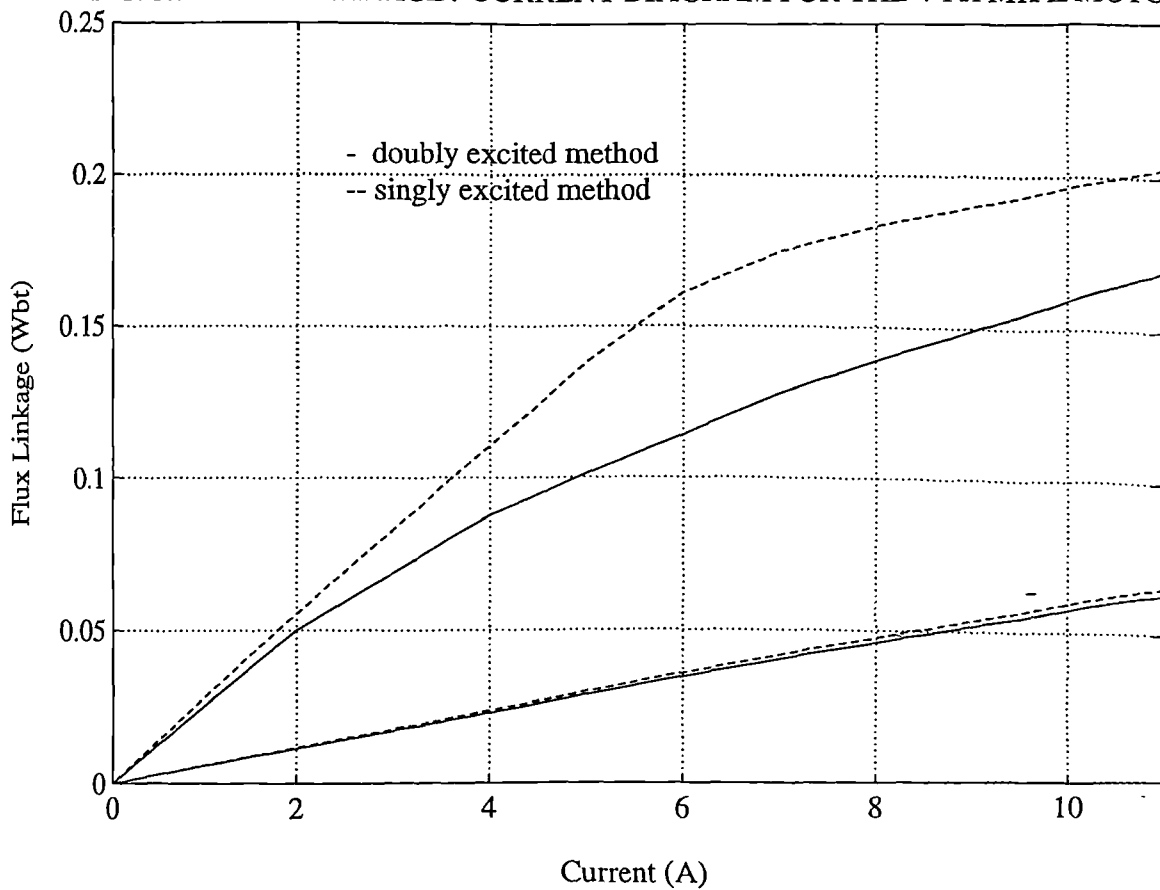


FIG. 3.12 FLUX LINKAGE / CURRENT DIAGRAM FOR THE 4-PH MK II MOTOR



3.3 Electromagnetic design of switched reluctance motors for low torque ripple - a new alternative.

Figure 3.13 shows the variation of static torque with rotor position for the three different 4-phase motors. Instantaneous static torque was computed by integrating the Maxwell stress tensor over the rotor surface. Figure 3.13 illustrates that the back-iron width not only affects the average torque for a given copper loss but also controls the shape of the static torque profile. In this case a flatter torque / angle characteristic may be achieved by compromising the yoke thickness.

The choice of the appropriate yoke thickness coupled with ‘clever’ switching can extend the flat torque period. This observation is particularly useful in applications where low torque ripple is a principal requirement. The variation of static torque with rotor position in the 4-phase Mk II motor is illustrated in fig. 3.14. When the rotor pole associated with the trailing phase is at the 9° position, the leading phase is commutated. The conduction period of each phase is therefore 24° ($15^\circ + 9^\circ$) rather than the usual 30° . In fig. 3.14 it can be seen that while the rotor turns from 9° to 15° (relative to the trailing phase) the torque output of the motor is increased by switching off the excitation of the leading phase and reducing the motor to a singly excited system. While the static torque increases in doing so, the copper losses decrease! By commutating the current before alignment, the deeply saturated stator yoke is ‘relieved’ magnetically. A lower reluctance path is set up for the overlapping (trailing) phase which, for the same MMF, now produces significantly higher torque. The magnetic flux path, set up when the leading phase is energised during the $24^\circ - 30^\circ$ period, could be thought of ‘absorbing’ MMF. Furthermore, at rotor positions near alignment, the B -field produced by the leading phase causes predominantly tensile rather than shear forces to act on the rotor. As a result P1 does not contribute significantly to torque production.

The commutation of the leading phase before alignment also results in substantially reduced torque ripple. The Mk II 4-phase motor design for low torque ripple does

FIG. 3.13 STATIC TORQUE / ROTOR POSITION (4-PH MOTOR, 2 PH EXCITED)

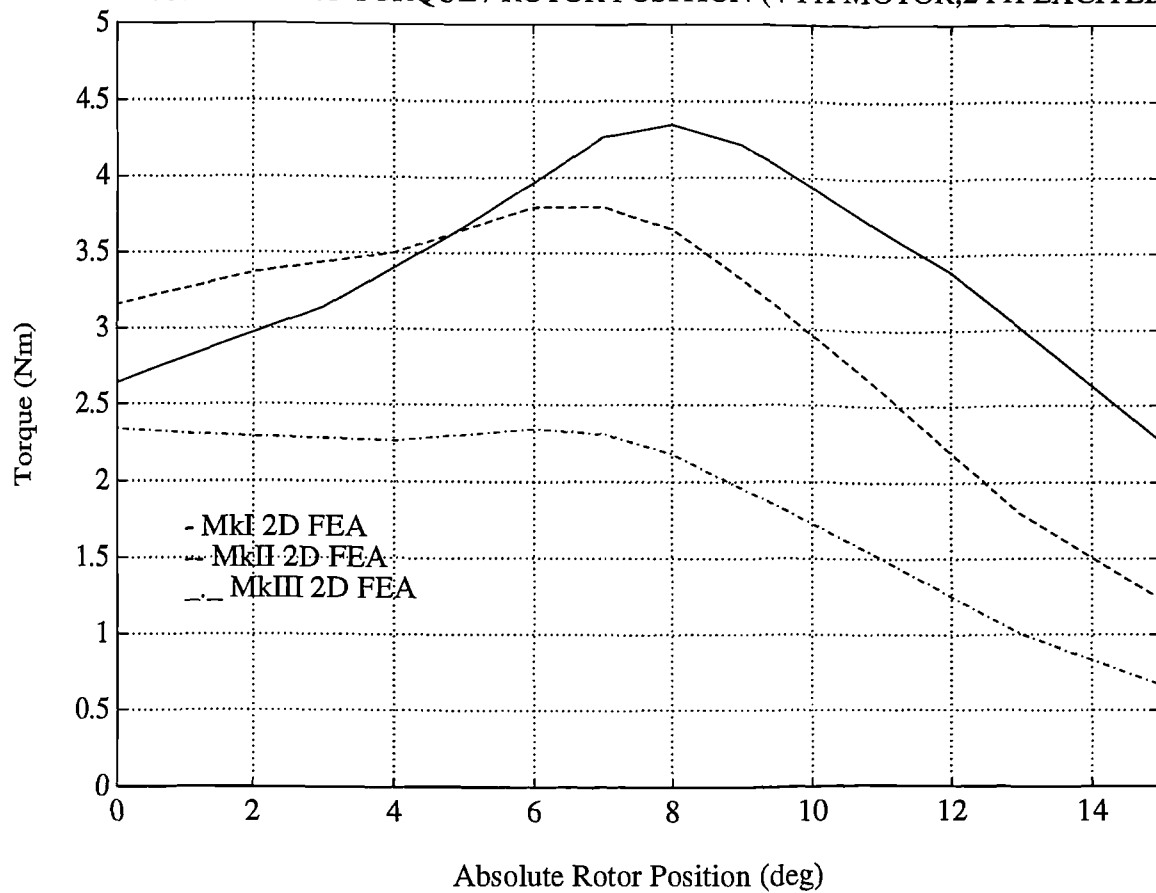
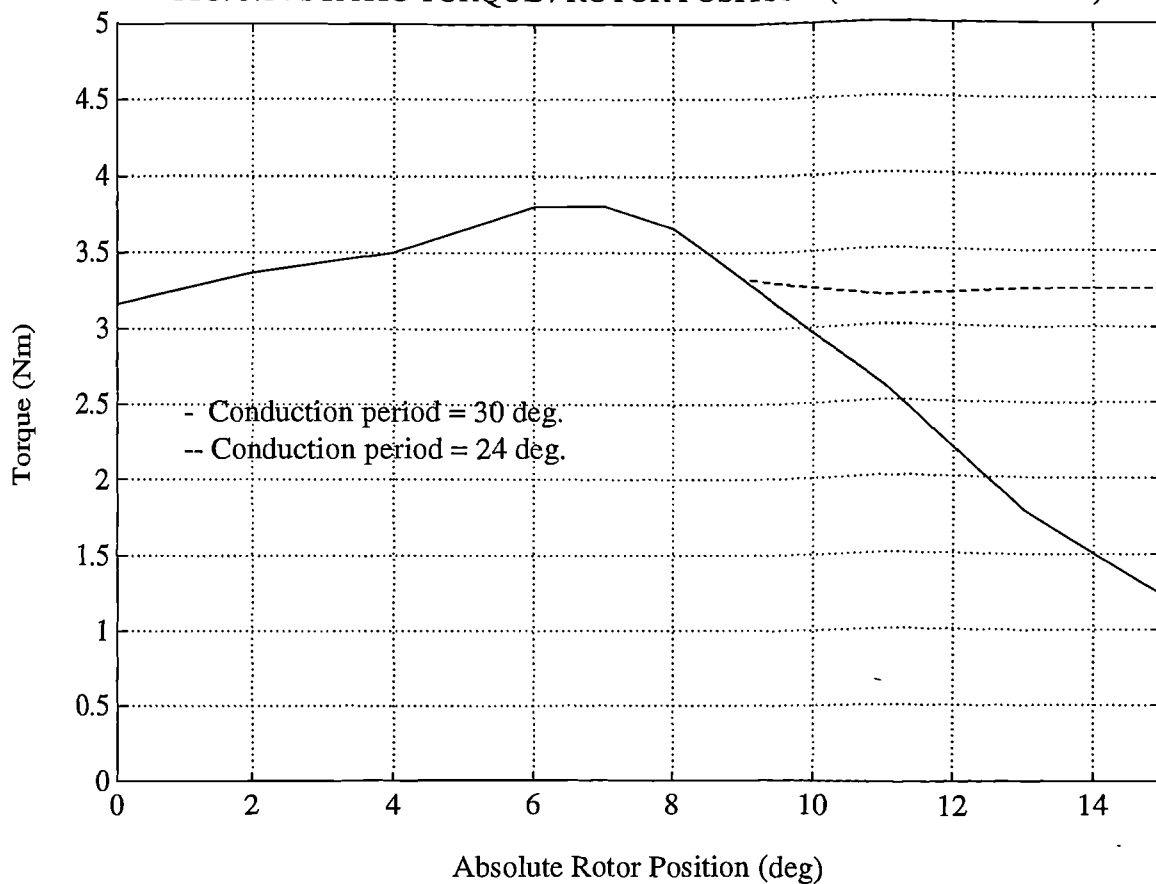


FIG. 3.14 STATIC TORQUE / ROTOR POSITION (4-PH MkII MOTOR)



not compromise the average torque output as Table 3.3 suggests. For a 24° phase current conduction period the 4-phase Mk II model achieves comparable torque to Mk I for equal copper loss and lower operating current density.

	Torque (Maxwell stress) $\theta_c=30^\circ$	Torque (Maxwell stress) $\theta_c=26^\circ$	Torque (coenergy doubly excited) $\theta_c=30^\circ$	Torque (coenergy singly excited) $\theta_c=30^\circ$
Mk I	3.51Nm	3.46Nm	3.52Nm	3.64Nm
Mk II	3.06Nm	3.44Nm	3.04Nm	4.35Nm
Mk III	1.90Nm	-	1.85Nm	4.30Nm

Table 3.3. Average torque figures for the 4-phase motor models.

A smooth torque characteristic can be achieved by careful selection of critical motor dimensions i.e. the stator yoke and rotor pole arc. Dynamic operation parameters such as the rated speed and resulting commutation angles must also be considered. Phase current profiling has been suggested as a means of achieving smooth torque (ref. discussion in [8]), though the electromagnetic design of a 4-phase motor for low torque ripple proposed in this thesis should simplify phase current control.

Table 3.3 lists average torque values for the three 4-phase finite element models, computed for equal copper loss. It is demonstrated that the virtual work principle applied to doubly excited systems yields average torque values which compare favourably with torque computed from Maxwell stress (ref. $\theta_c=30^\circ$ columns). Significant errors can arise using traditional coenergy methods in which magnetic interaction effects are neglected.

3.4 The 4kW 7-phase switched reluctance motor.

In chapter 2, it was shown that motors with an odd number of phase windings can be configured to encourage short magnetic flux patterns. It was asserted that this configuration would decrease the MMF required to establish the flux in the airgap while also decreasing the iron losses in the machine. A 4kW 7-phase 14/12 prototype machine was constructed in order to investigate the performance of small step-angle structures and evaluate the effectiveness of the shared switch, asymmetric half-bridge converter [41]. It was therefore suitable to model this machine in finite element analysis, in order to examine the advantages offered by short flux loops and be able to validate FEA predictions with experimental results.

The design of the 7-phase machine, illustrated in fig. 3.15, was not optimised. This is because the stator and rotor laminations were stamped out of existing induction motor laminations. This led to a significant compromise in the stator yoke width and pole depth. Results will be presented from two-dimensional modelling of the machine, configured for short and long flux loops.

Short flux loops can be established by simultaneously exciting at least two phase windings. Equation 2.3 dictates that in order to obtain peak static torque from the 7-phase machine, three phase windings need to carry current at the same time. However, the switching algorithm that was developed for the shared switch converter allows the current in only two phase windings to be simultaneously controlled [18]. The current in the third phase winding would have to be partially dependent on the voltage across one of the other two. This would be an undesirable feature and therefore modelling of the 7-phase machine was confined to simultaneous excitation of two phases.

In the analysis, two excitation cycles as described below shall be considered. In the 7-phase machine the beginning of the repeatable excitation cycle is defined as the point in space where a particular phase winding P1 is energised, while a second phase winding P2 has been conducting for one rotor step. The end of the cycle is

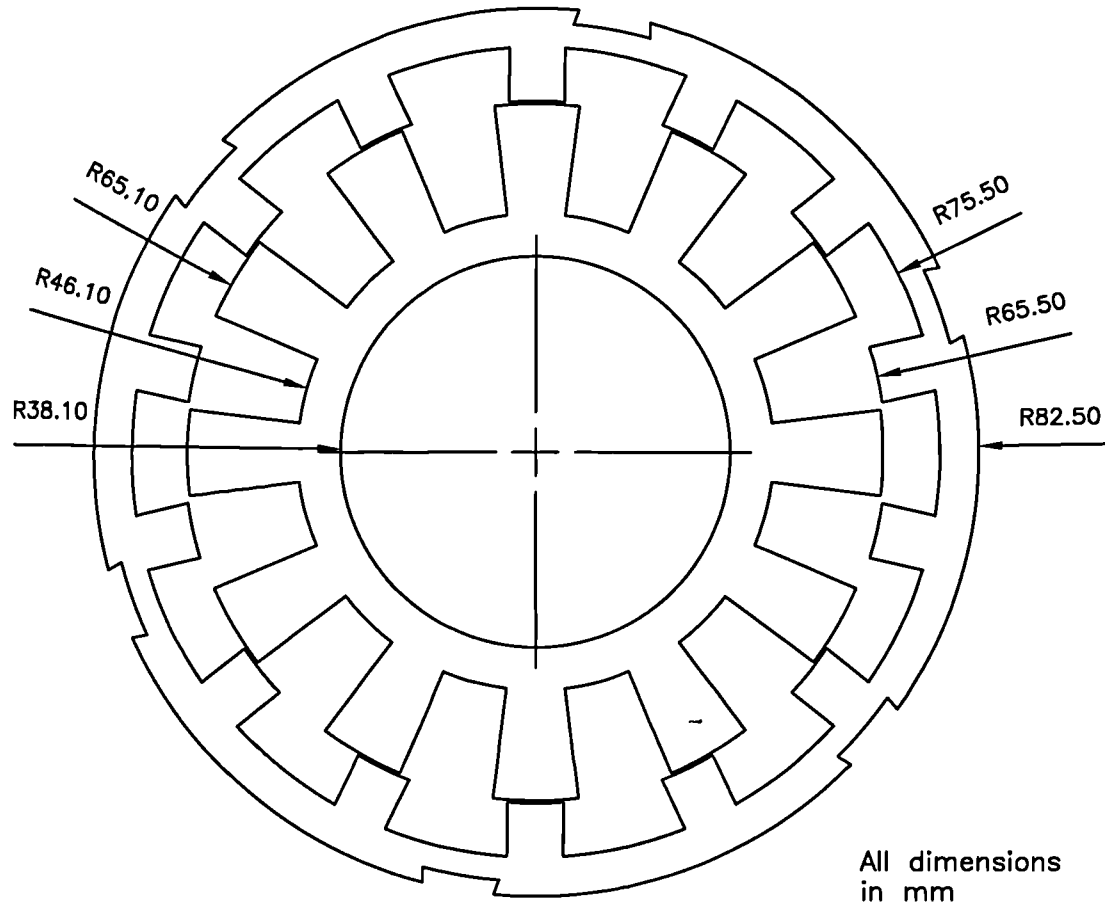


Fig. 3.15a. The 4kW 7-phase motor laminations.

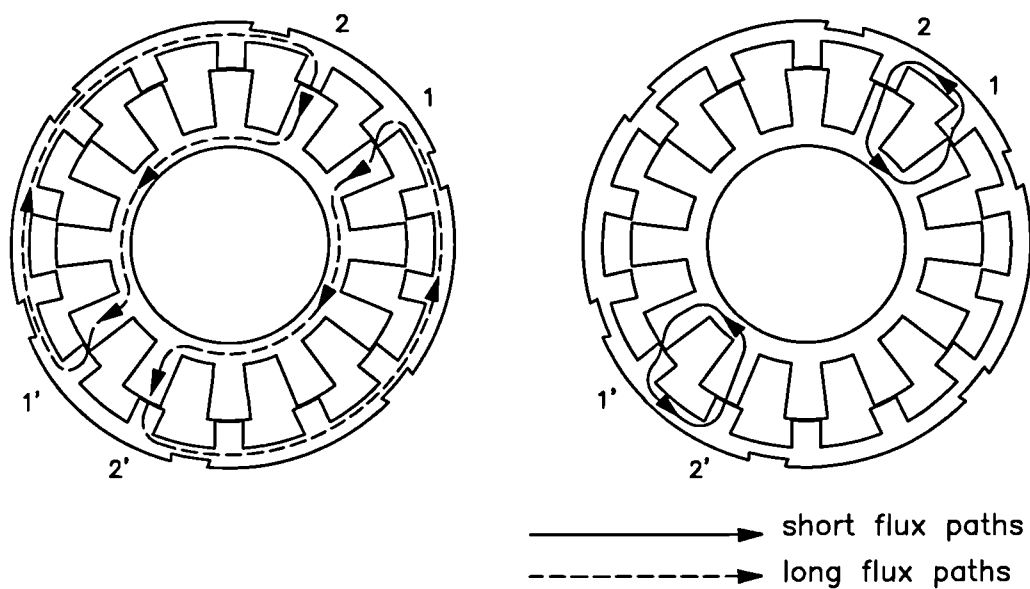


Fig. 3.15b. Excitation patterns in the 7-phase motor.

Fig.315c. FLUX DISTRIBUTION IN THE 7-PH MOTOR (LONG LOOPS)

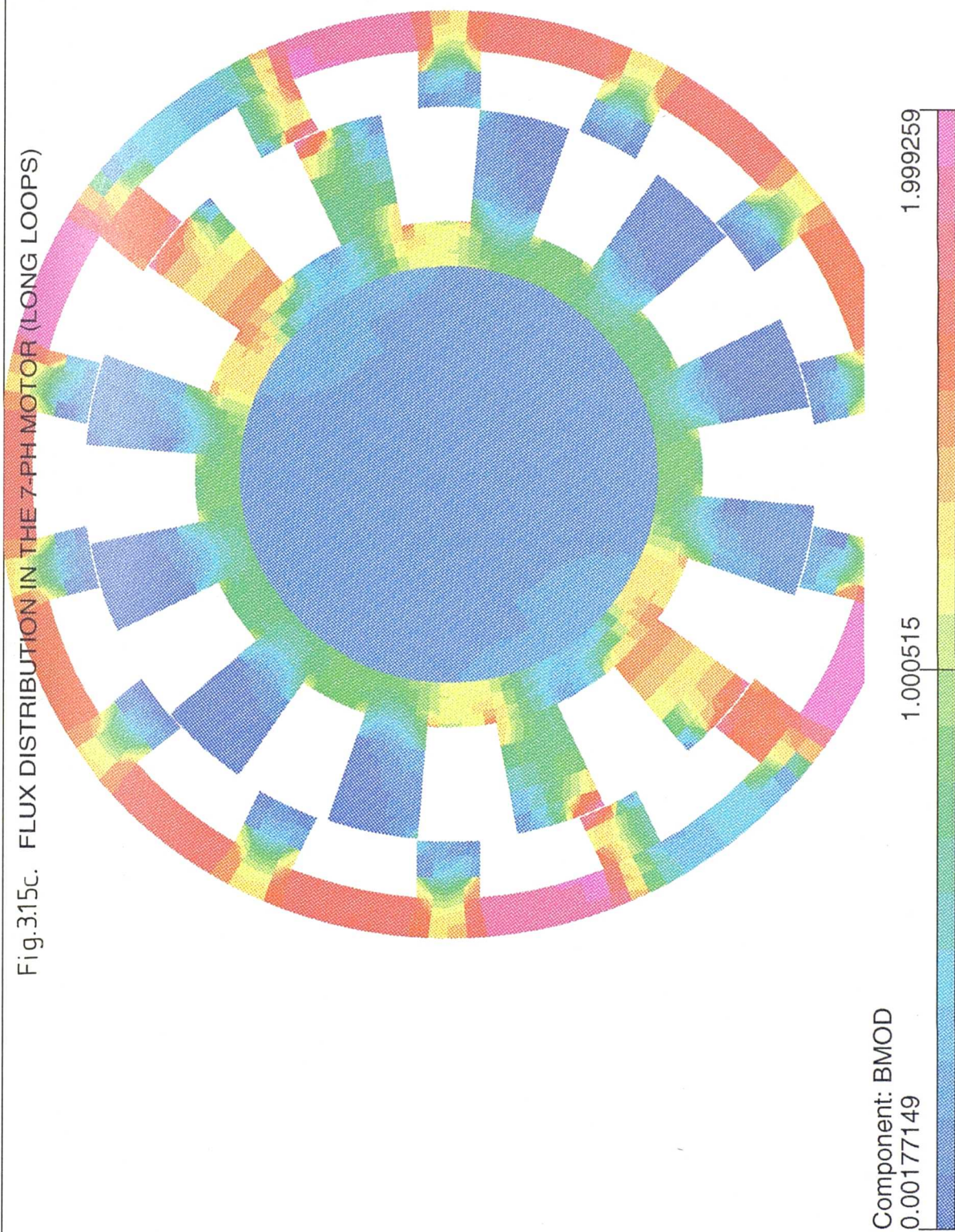
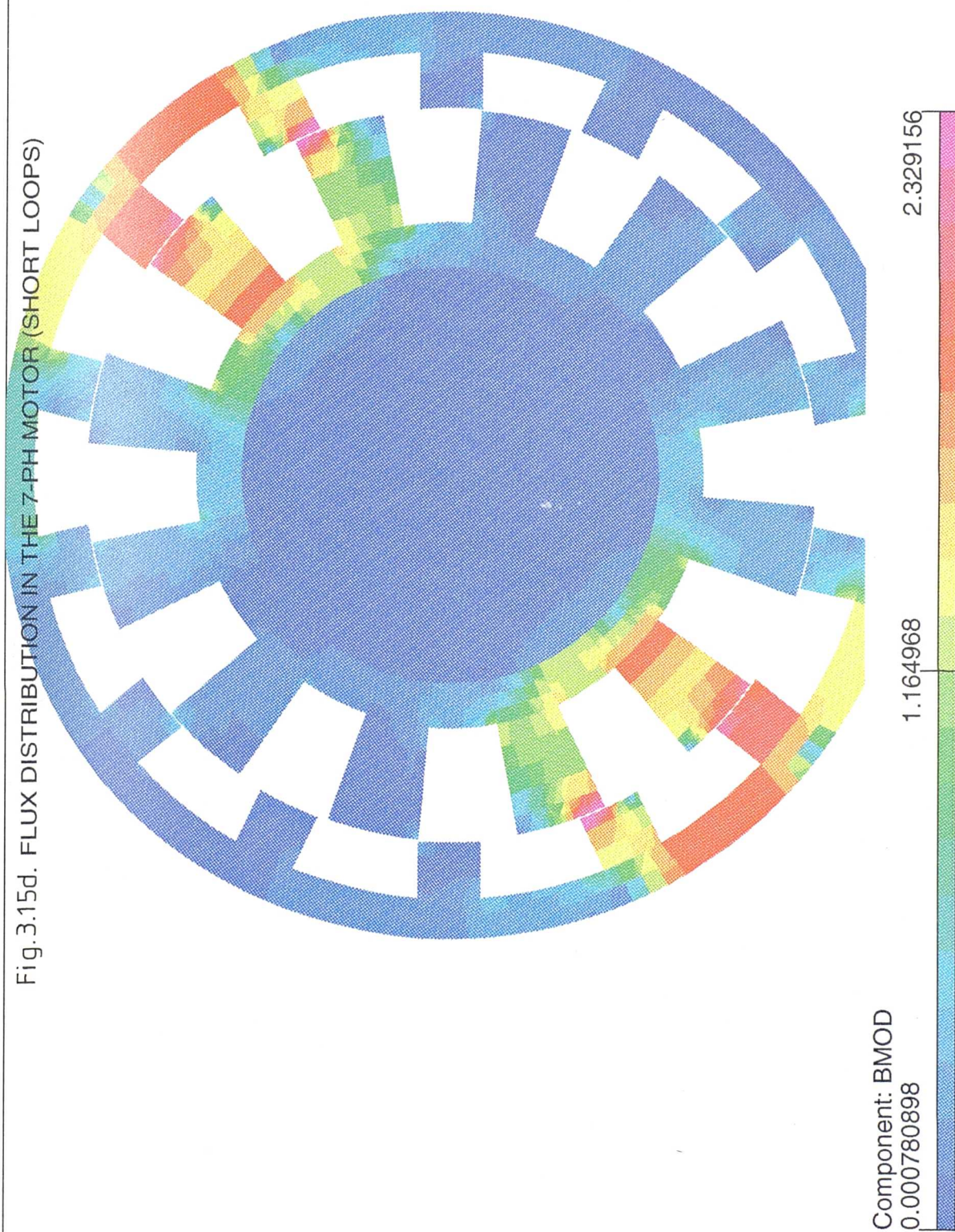


Fig. 3.15d. FLUX DISTRIBUTION IN THE 7-PH MOTOR (SHORT LOOPS)



marked by the de-energisation of P2, one step angle later, while a third phase winding is being energised. At high speeds a phase winding must be excited at the unaligned position so as to provide sufficient time for the current to build up in the phase winding. The excitation cycle in which a phase is fired at the unaligned position and conducts for two rotor steps will be referred to as the high speed cycle. At lower speeds firing may be delayed until just prior to the overlap period between the excited stator and associated rotor poles, such that the conduction period lies entirely within the pole overlap period. A low speed cycle will be examined in which firing is delayed by 3° .

3.4.1 Electromagnetic field considerations.

The ideal λ / i trajectory assumes square current pulses and spans an angle equal to two rotor steps. It can be constructed by the use of magnetic circuit considerations developed for motors operating with two phases conducting at any time. Figure 3.16 shows a plot of the **system** λ / i diagram for the 7-phase machine, configured for long and short flux loops and operating in the low speed excitation cycle. A phase current bias of 10A is assumed. A similar plot describing the high speed excitation cycle is shown in fig. 3.17. The area enclosed by the λ / i trajectory is a measure of the average torque developed in the switched reluctance motor (see eqn. 3.8). It is therefore evident that short flux loop excitation results in higher torque output. It is also noted that the benefit is greater where the reluctance of the iron constitutes a substantial part of the total magnetic circuit reluctance.

The λ / θ characteristic of the leading phase of the 7-phase machine, configured for long and short flux loops, and excited with 10A is shown in fig. 3.18. In comparison with the 4-phase (Mk I) motor, the magnetic interaction between the excited phase windings in the 7-phase machine is more acute. This is due to the close proximity of one stator pole winding to another which implies a higher level of mutual coupling between adjacent phases. In addition, the simultaneous excitation of two phase windings rapidly saturates the stator yoke (the thickness of

FIG. 3.16 ENERGY CONVERSION LOOP FOR LOW SPEED CYCLE (7-PH, $I_{bias}=10A$)

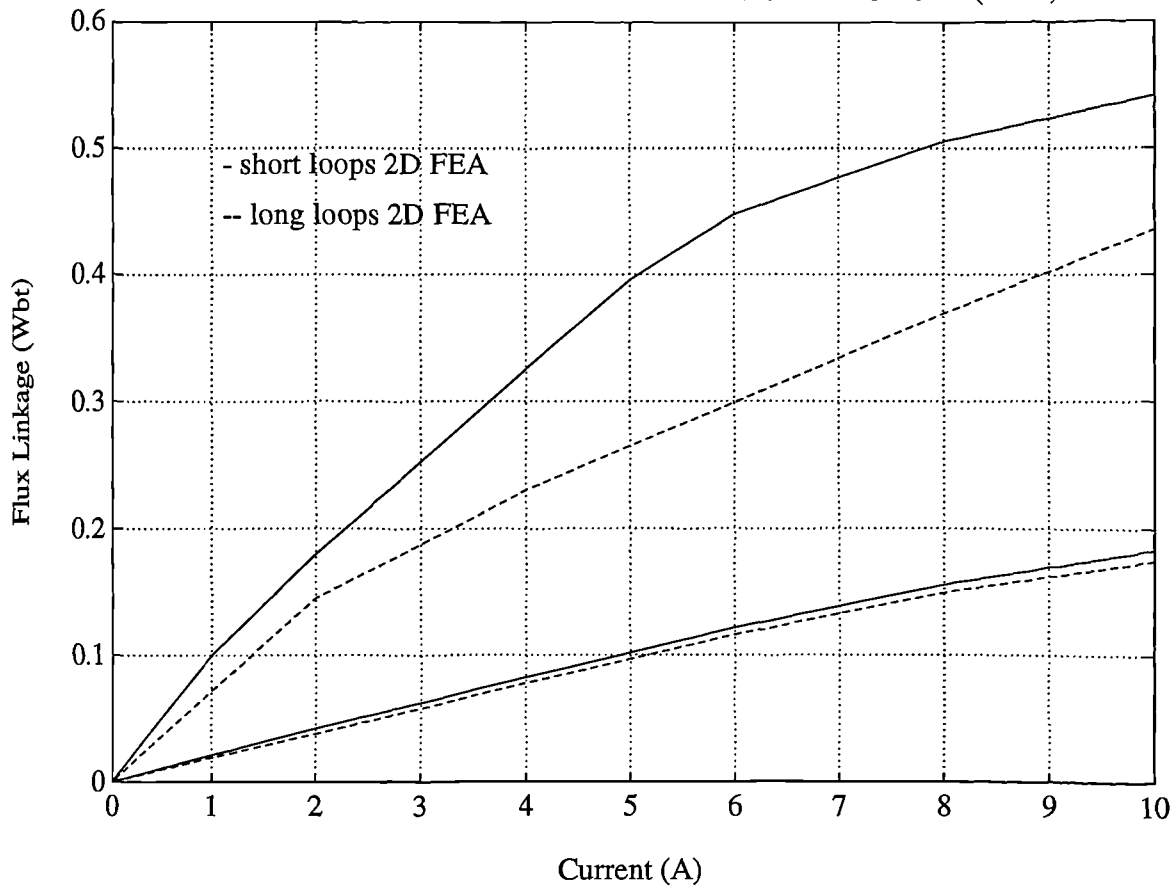


FIG. 3.17 ENERGY CONVERSION LOOP FOR HIGH SPEED CYCLE (7-PH, $I_{bias}=10A$)

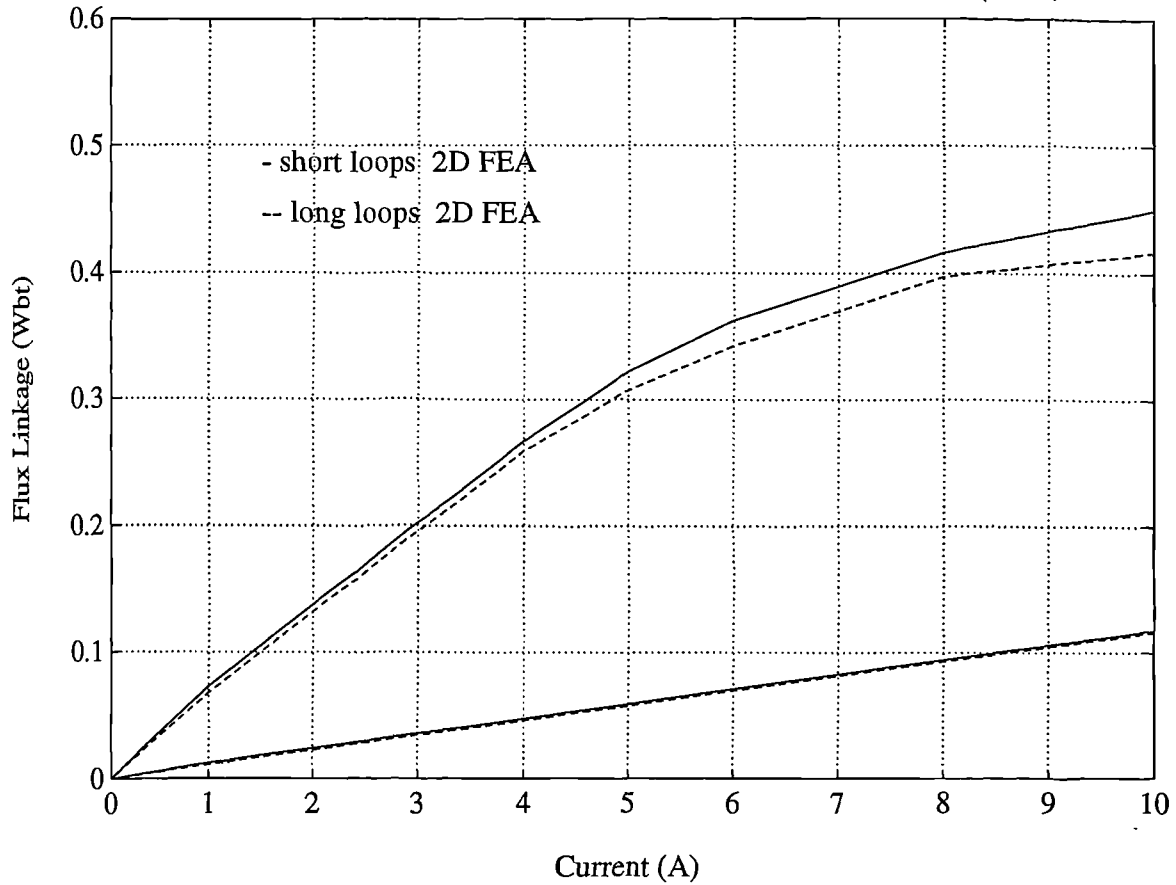


FIG. 3.18 FLUX LINKAGE / ROTOR POSITION IN THE LEADING PHASE (7-PH, I=10A)

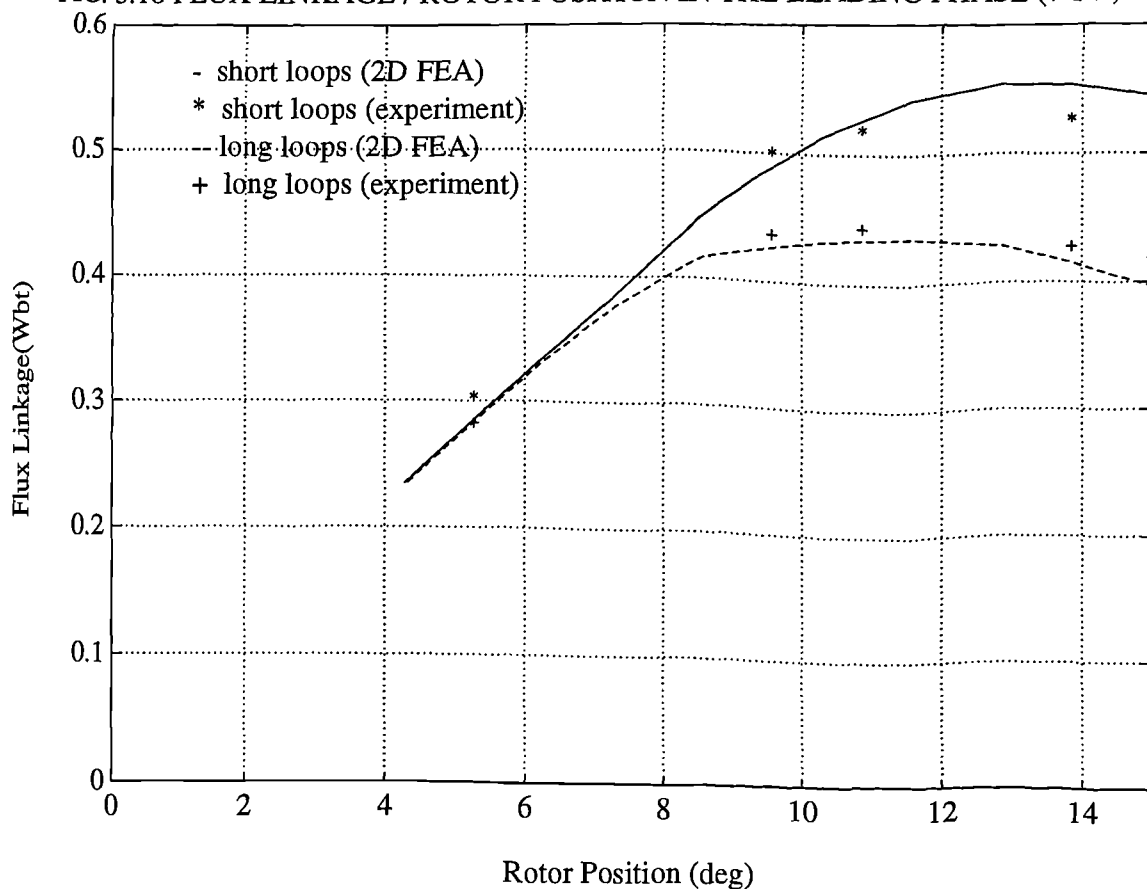
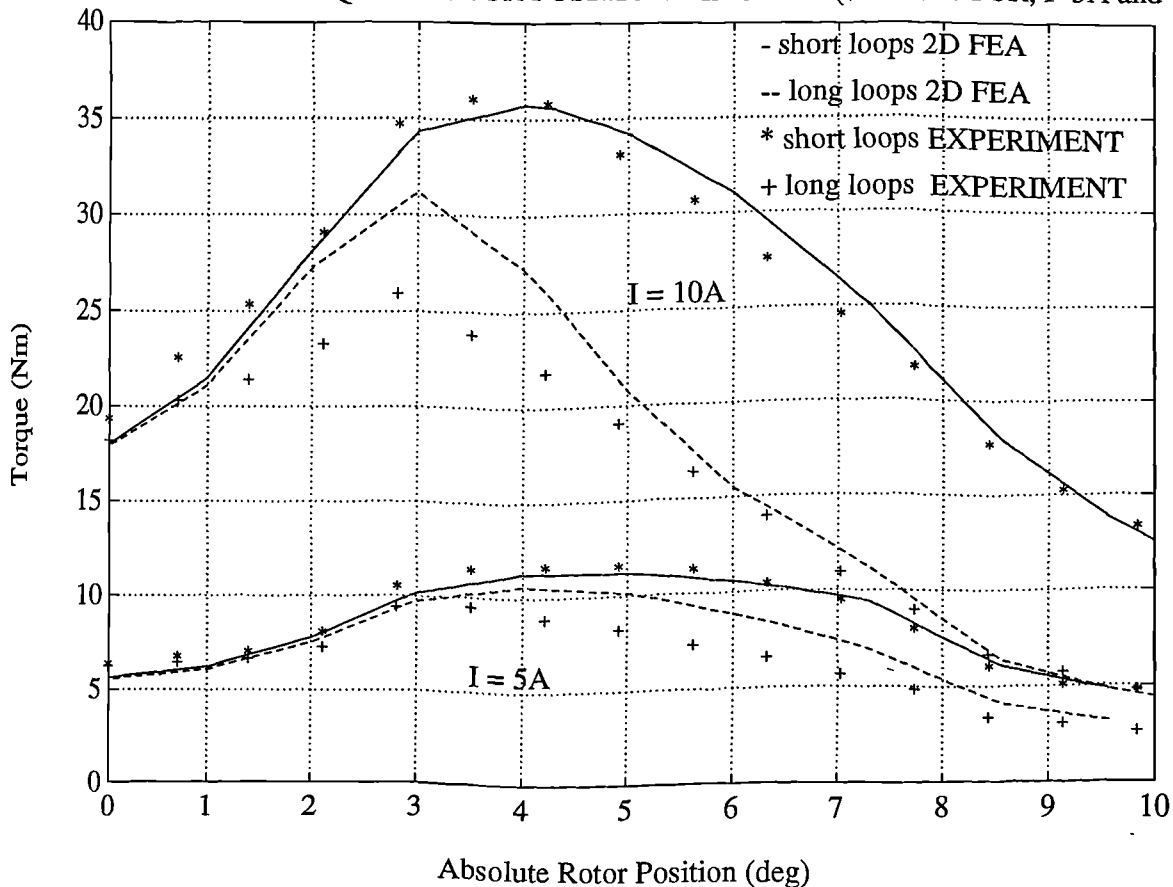


FIG. 3.19 STATIC TORQUE / ROTOR POSITION DIAGRAM (7-PH MOTOR, I=5A and 10A)



which is insufficient) hence degrading performance.

For the same current level, a significant increase in phase winding flux linkage resulted by configuring the motor for short flux loops. The flux linking the excited stator poles of the long flux loop machine was limited by bulk saturation of the stator yoke sections. The phase winding flux linkage reached a maximum of 0.44Wbt, 5° before alignment; beyond this point it began to decrease though the overlap between the stator and rotor poles increased. The lower reluctance path set up in the short flux loop machine allowed the phase winding flux linkage to rise to 0.55Wbt; no significant decrease in λ was noted toward alignment. The static torque production of the long flux loop configuration was therefore severely compromised due to saturation effects, in sharp contrast to the short flux loop configuration.

Referring to the long flux loop configuration (see fig. 3.15), the **B**-field is essentially encouraged to separate in two long loops that link stator coils 1-2' and 1'-2. Both long and short flux loop configurations attempt to maximise the mutual **B**-field linking the excited stator coils. However, the latter configuration encourages the **B**-field to follow a short path to link coils 1-2 and 1'-2'. In a sense, this is the natural **B**-field path of minimum reluctance. The short flux loop configuration is significantly less sensitive to back-iron thickness because only a small arc of the stator periphery forms part of the magnetic pattern. This feature offers an additional design advantage since, for a specified rotor diameter, the back-iron width of the machine can be reduced to offer larger copper area.

3.4.2 Instantaneous / average torque considerations.

The measured static torque produced by the 7-phase machine, as a function of rotor position, is illustrated in fig. 3.19. Measurements were taken for phase currents of 5A and 10A in two adjacent phase windings. Also shown is the static torque profile of the machine, predicted by the use of the two-dimensional finite element analysis model. The long and short flux loop characteristics considered are similar

at rotor positions early in the excitation cycle. In this region the reluctance of the magnetic circuit is dominated by the interpolar airgap depth facing one of the excited stator phases. As the associated rotor poles move into alignment with the excited stator poles, the reluctance of the iron becomes more significant, and substantially higher torque is produced by the short flux loop motor configuration.

Good agreement between the instantaneous static torque predicted by the two-dimensional model and measurement, was obtained for the short flux loop configuration. End-core effects in the 7-phase machine are minor because the stack length is large. However, in the long flux loop configuration, finite element results consistently overestimated measured values. The dimensions of the machine, including the sensitive airgap length, were accurately entered during the model creation stage. In any case, errors in geometry would affect both long and short loop configurations. Referring to fig. 3.15, the grooves in the back iron of the machine were not included in the finite element model. This is an 'innocent' omission which is frequently made. However, in this particular machine, the back-iron thickness is small and the grooves randomly positioned with respect to the poles. This was a design restriction, set by the use of existing induction motor laminations. The grooves may have therefore increased the magnetic path reluctance enough to cause a noticeable error in the results. This would only be visible in the long flux loop configuration, where the back-iron periphery constitutes a significant part of the path reluctance.

The average static torque may be evaluated by averaging the instantaneous static torque values over the angle that the excitation cycle spans. The results of this study are summarised in Table 3.4. Also tabulated is the average torque, computed using the coenergy principle as applied to doubly excited systems. Long and short flux loop configurations were considered. Good agreement is noted between results obtained by the two methods.

	Low Speed Cycle		High Speed Cycle	
	Torque (Maxwell stress)	Torque (coenergy doubly excited)	Torque (Maxwell stress)	Torque (coenergy doubly excited)
Long	20.77Nm	20.85Nm	25.73Nm	28.53Nm
Short	32.48Nm	33.69Nm	28.73Nm	30.30Nm

Table 3.4. Average torque figures for the 7-phase motor.

3.5 Summary of fundamental modelling considerations.

A new procedure of applying the virtual work principle to switched reluctance motors which operate with two phases conducting at any time has been described. The electromagnetic theory of doubly excited systems does not neglect magnetic interaction effects between simultaneously excited phases, hence leading to more accurate modelling of the switched reluctance motor. The procedure which has been described shall facilitate the modelling of short flux loop machines, but can also be applied to the 'traditional' 4-phase 8/6 structure. The method proposed allows much of the existing dynamic modelling theory to be adopted providing the correct λ / i characteristics are computed.

It has been shown that in 4-phase switched reluctance motors the stator yoke thickness must be carefully chosen to allow for the overlap of phase current pulses. If the chosen yoke thickness is small, bulk saturation effects will severely limit torque production. This phenomenon, however, will not 'show up' in the modelling if the virtual work principle as applied to singly excited systems is adopted.

It has also been illustrated that careful selection of the yoke thickness, coupled with matching commutation angles, can optimise the performance of the 4-phase drive. Although the 4-phase switched reluctance motor is doubly excited (the effective torque zone is equal to twice the step angle) the back-iron width need not be equal to the stator pole width. The yoke thickness can be reduced to allow for more copper area, and the commutation angles appropriately adjusted to give optimum, low ripple torque production.

Modelling of the 7-phase motor with the windings configured for long and short flux paths, has demonstrated the benefits of the latter configuration. The torque developed by the switched reluctance machine was computed by the methods of virtual work or Maxwell stress. Good agreement was obtained between the two methods when applied to the 4-phase and 7-phase motors, providing the new modelling theory for doubly excited motors was adopted.

Chapter 4

THE EFFECT OF END-CORE FLUX ON THE PERFORMANCE OF THE SWITCHED RELUCTANCE MOTOR²

4.1 The need for three-dimensional modelling.

Finite element analysis is considered to be highly suited to handle the modelling complexities introduced by the deeply saturated, doubly salient iron structure of the switched reluctance motor. Having decided to use commercially available finite element analysis software, the question posed by researchers is whether the switched reluctance machine can be modelled, with sufficient accuracy, using a two-dimensional code. A useful, early discussion on inductance estimation and three-dimensional effects in switched reluctance motors may be found in [51]. Simkin and Trowbridge [52] reported that inductance calculations on a stepping motor using a two-dimensional computer program had shown good agreement with measurement when the rotor teeth were aligned with the excited stator teeth. However in the 'unaligned' position, that is, the position at which the rotor slots are aligned with the excited stator teeth, values for computed and measured inductances disagreed. In the latter position the airgap facing the excited stator poles is large causing strong axial components of field to arise. These were not modelled by the two-dimensional program and the errors were thought to be caused by this.

Williamson and Shaikh [53] demonstrated the superiority of three-dimensional models for calculating λ / i diagrams for the switched reluctance motor and

²This chapter is based on a paper, written by A. Michaelides and C. Pollock, which has been accepted for publication in *IEE Proc. B*.

concluded that the difference between the results obtained using two-dimensional and three-dimensional models cannot be accounted for by assuming a single-valued end winding inductance. However, the authors of the paper did not explicitly suggest a suitable procedure for estimating the end winding flux at any rotor position or excitation.

Despite these observations, finite element analysis packages that employ two-dimensional formulations are established as the primary tool in switched reluctance motor design. Users of finite element analysis packages have found that two-dimensional models require far less cpu time to solve and occupy little disk space in contrast to three-dimensional models. Typically a two-dimensional nonlinear problem (one particular excitation level and rotor position), processed on a Sun Sparcstation10, requires twenty minutes of cpu time to solve and occupies 2Mb of disk space. Its three-dimensional counterpart would require six times the cpu time and occupy up to ten times the disk space. In addition, most two-dimensional formulations are today available in PC form, which makes them more attractive. It is widely accepted that the two-dimensional formulation for electromagnetic finite element analysis is easier to implement and expand. Recently C. Biddlecombe [54] and D. Roger [55] have reported advances in the two-dimensional code to include heat and bending calculations. Implementation of these advances in three dimensions is a few years away, mainly due to the complexity of the three-dimensional algorithm. The description of basic equations on which two and three-dimensional algorithms are based (see Appendix A) illustrates this: in two dimensions, a simple equation relating A_z to the applied J_z is solved for the magnetic field.

The purpose of this chapter is to illustrate the effect of end-core flux on the λ / i / θ diagram and on the predicted values of static torque in the switched reluctance motor. The phase winding flux linkage and static torque of a 4-phase 8/6 switched reluctance motor are determined as a function of phase current and rotor position using a two-dimensional finite element model. The base plane lamination is extruded to different stack lengths to form three-dimensional finite element models.

The flux linkage and static torque characteristics of each model are determined and compared with results obtained from the two-dimensional model. An experimental motor of stack length exactly equal to one of the models is used to verify computed results. Correction charts are set up providing appropriate coefficients, to allow users of two-dimensional software to account for three-dimensional effects, at a range of excitations and rotor positions. The sensitivity of the end-core flux value to magnetic circuit parameters such as applied MMF, conductor overhang and magnetic saturation is also examined. An application to an alternative 7-phase 4kW switched reluctance motor is presented. OPERA -3D / TOSCA was used throughout this work [44].

4.2 Three-dimensional effects in the switched reluctance machine.

There are three different three-dimensional effects that must be carefully considered in order to correctly compute phase winding flux linkage and static torque:

- a) anisotropy of the laminations,
- b) end winding flux and
- c) axial fringing.

Like most electrical machines, the switched reluctance motor is laminated in order to minimise eddy current losses. Finite element modelling of the individual laminations and the interlamination insulation would require a mesh of unrealistic element number. In the three-dimensional finite element code, laminated structures can be solved by specifying the packing factor, pf , and the direction normal to the laminations. These parameters enable the program to calculate the effect of the laminations using anisotropic material properties, i.e. by assigning a high permeability in the direction parallel to the laminations and a considerably lower permeability in the direction perpendicular to them. In directions parallel to the laminations, the program uses

$$\mu = pf \mu_{iron} + (1 - pf)\mu_0 \quad (4.1)$$

and normal to the laminations

$$\mu = \frac{\mu_0 \mu_{iron}}{pf \mu_0 + (1 - pf)\mu_{iron}} \quad (4.2)$$

where μ_{iron} is the relative permeability of iron obtained from the **BH** curve data. The value of the relative permeability is dependent on the magnetic field intensity at any point in space. The symbol μ_0 denotes the absolute permeability.

In a two-dimensional finite element model, the effect that the laminated structure of the machine has on stator flux linkage and static torque production may be accounted for in one of two different approaches:

Method A: The original **BH** curve data may be used and the field values per unit length, obtained from finite element model solutions, multiplied by the stack length times the packing factor.

Method B: The **BH** curve data can be manually scaled by multiplying the value of the flux density, at all MMFs, by the packing factor. This approach closely approximates the method employed in the three-dimensional code (ref. eqn. 4.2). Once two-dimensional model solutions have been correctly scaled to account for anisotropy, the remaining discrepancy between corrected two-dimensional solutions and measurement must be due to end-core flux.

End-core flux can be accounted for by considering three-dimensional effects that arise at the ends of the machine stack. The dominant effect is end winding flux i.e. the **B**-field lines generated from current flowing in the conductor region which extends beyond the lamination stack, and link the phase winding via the main magnetic circuit. One other end-core effect is axial fringing, or bulging of flux in the axial direction. The **B**-field lines, fringing axially from the ends of the stator pole stack into the rotor pole ends, can be lines generated from both J_z and J_{xyz} (end winding) current. The phenomenon is minimal in the unaligned position, and occurs as a pair of rotor teeth align with the excited stator teeth. The effect that

this magnetic flux path has on the phase winding flux linkage, is accounted for only in three-dimensional modelling.

In order to accurately determine end-core effects, three-dimensional model solutions were compared with corresponding solutions from a two-dimensional model that was prepared using **BH** curve data scaled by the packing factor (method B). This scaling method was solely used for comparison purposes. A second two-dimensional model was prepared using the original **BH** curve data; scaling method A was imposed on solutions of this model. It is the intention of the author to provide information on the difference between two-dimensional model solutions obtained by the use of these two scaling approaches.

4.3 Comparison between two-dimensional and three-dimensional finite element analysis results with experimental results.

The base plane used for the two and three-dimensional finite element models corresponds to the lamination of the experimental 150W 4-phase 8/6 switched reluctance motor. Comparisons will now be presented between two-dimensional model solutions, solutions from a three-dimensional model of stack length equal to that of the experimental machine, and measurement. Scaling method A was employed for two-dimensional model solutions.

4.3.1. Flux linkage.

The λ / i characteristic for one phase of this machine at the aligned and unaligned positions is shown in fig. 4.1. Two and three-dimensional finite element model predictions are shown alongside experimental results. A significant error in computing λ , using two and three-dimensional finite element code, was noted at very low currents. This was thought to be caused by the ‘reverse curvature’

relationship that magnetic materials exhibit at very low values of H . This was not included in the definition of the BH curve, in order to assist convergence in nonlinear problems (it is advisable that μ decreases monotonically with H). At higher current levels, flux linkage calculations using two-dimensional and three-dimensional modelling show good agreement with experimental results when the rotor pole is aligned with the excited stator pole (high flux linkage position). However, in the unaligned position results from two-dimensional modelling of the machine are in error while calculations using a three-dimensional model maintain good agreement with measurement. Two-dimensional model solutions consistently underestimate the flux linkage value, the effect being particularly noticeable at positions where the excited stator pole faces the interpolar airgap depth. These findings are in agreement with observations made by previous authors [52,53].

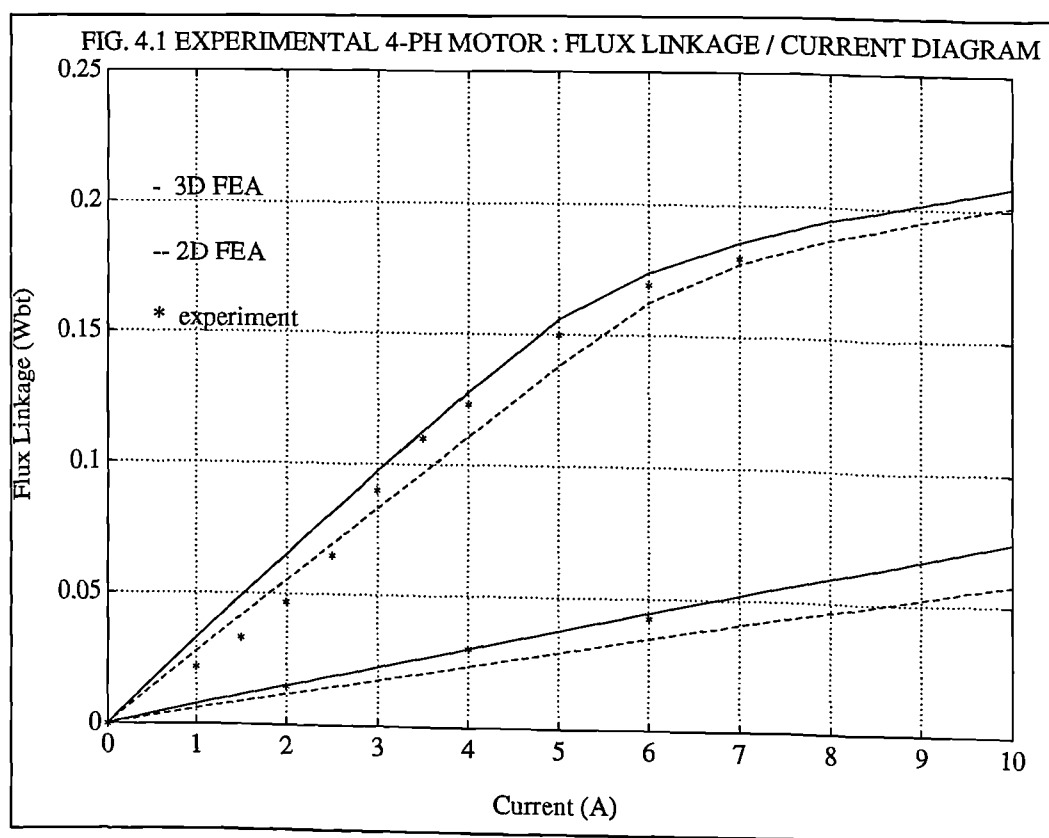
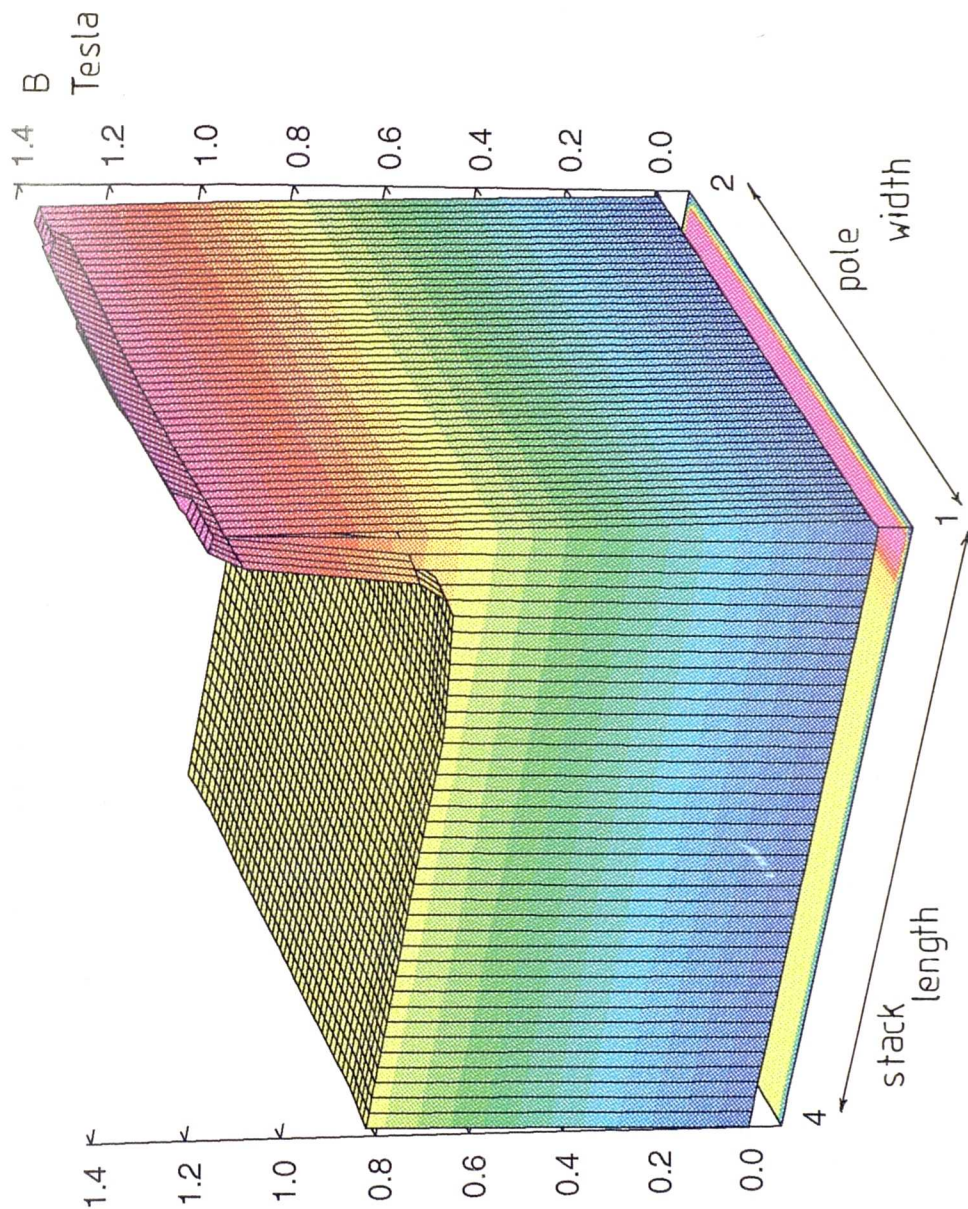


Figure 4.2a illustrates the flux linking the excited stator pole when this is aligned with a rotor pole while fig. 4.2b shows the flux linking the same pole, for the same excitation, in the unaligned position. Strong axial fields arise due to end windings,

Fig. 4.2a. FLUX DISTRIBUTION IN STATOR POLE (ALIGNED POSN)



Component: -NX*BX-NY*BY
 Maximum = 1.410363, Minimum = -0.00420393
 Integral = 218.755

1=34.4528
 5.179748
 25.5

2=34.4528
 -5.179748
 25.5

3=34.4528
 -5.179748
 0.0

4=34.4528
 5.179748
 0.0
 Cartesian

1=34.84
 8.549999
 25.5

2=34.84
 -8.55
 25.5

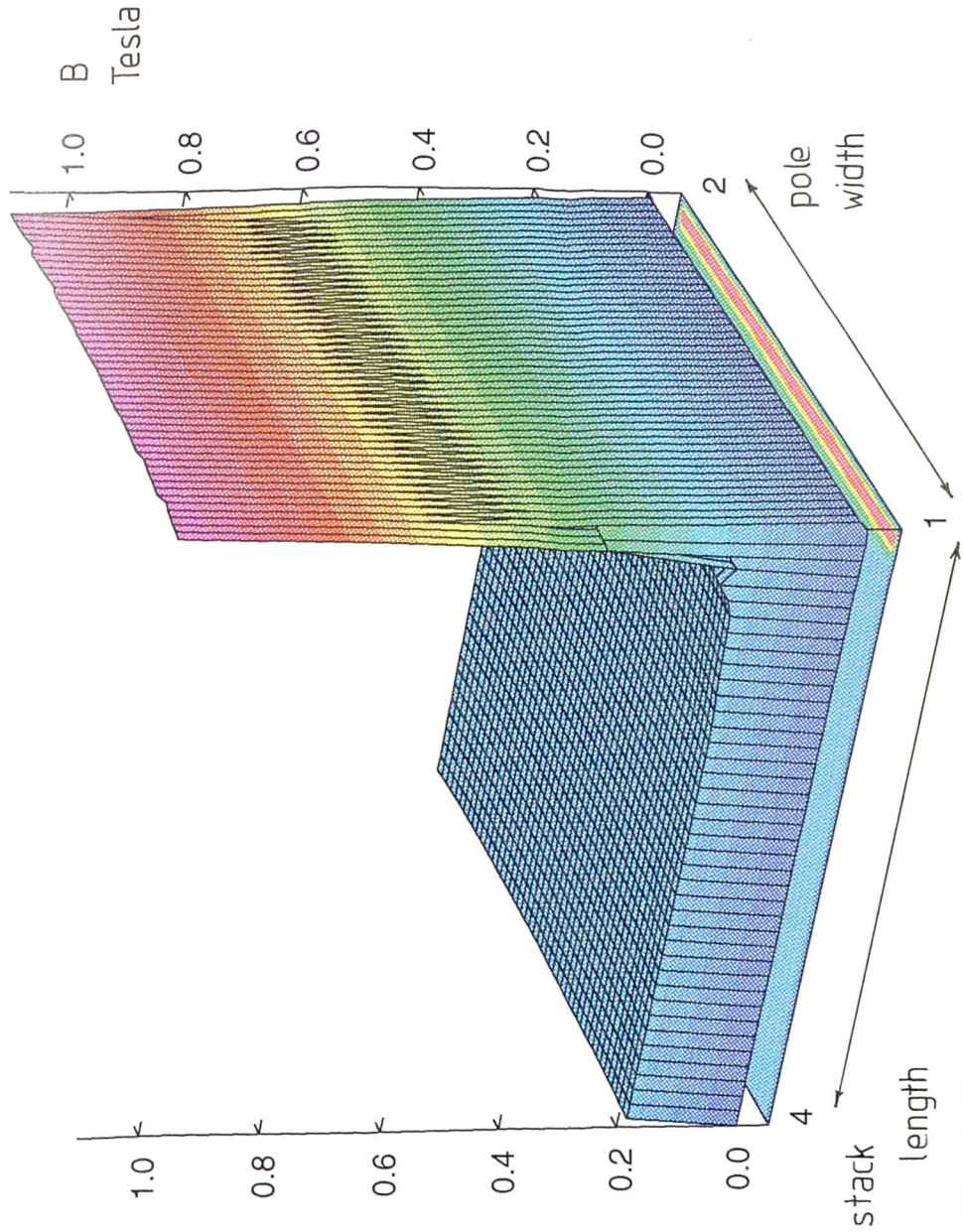
3=34.84
 -8.55
 0.0

4=34.84
 8.549999
 0.0
 Polar

VF OPERA-3d

Post-processor 2.4

Fig. 4.2b. FLUX DISTRIBUTION IN STATOR POLE (UNALIGNED POSN)



Component: -NX*BX-NY*BY
 Maximum = 1.103628, Minimum = -0.00464177
 Integral = 51.8202

1=-5.179749
 34.4528
 25.5

2=5.179749
 34.4528
 25.5

3=-5.179749
 34.4528
 0.0

4=-5.179749
 34.4528
 0.0
 Cartesian

1=34.84
 98.55
 25.5

2=34.84
 81.45
 25.5

3=34.84
 81.45
 0.0

4=34.84
 98.55
 0.0

Polar

VF OPERA-3d

Post-processor 2.4

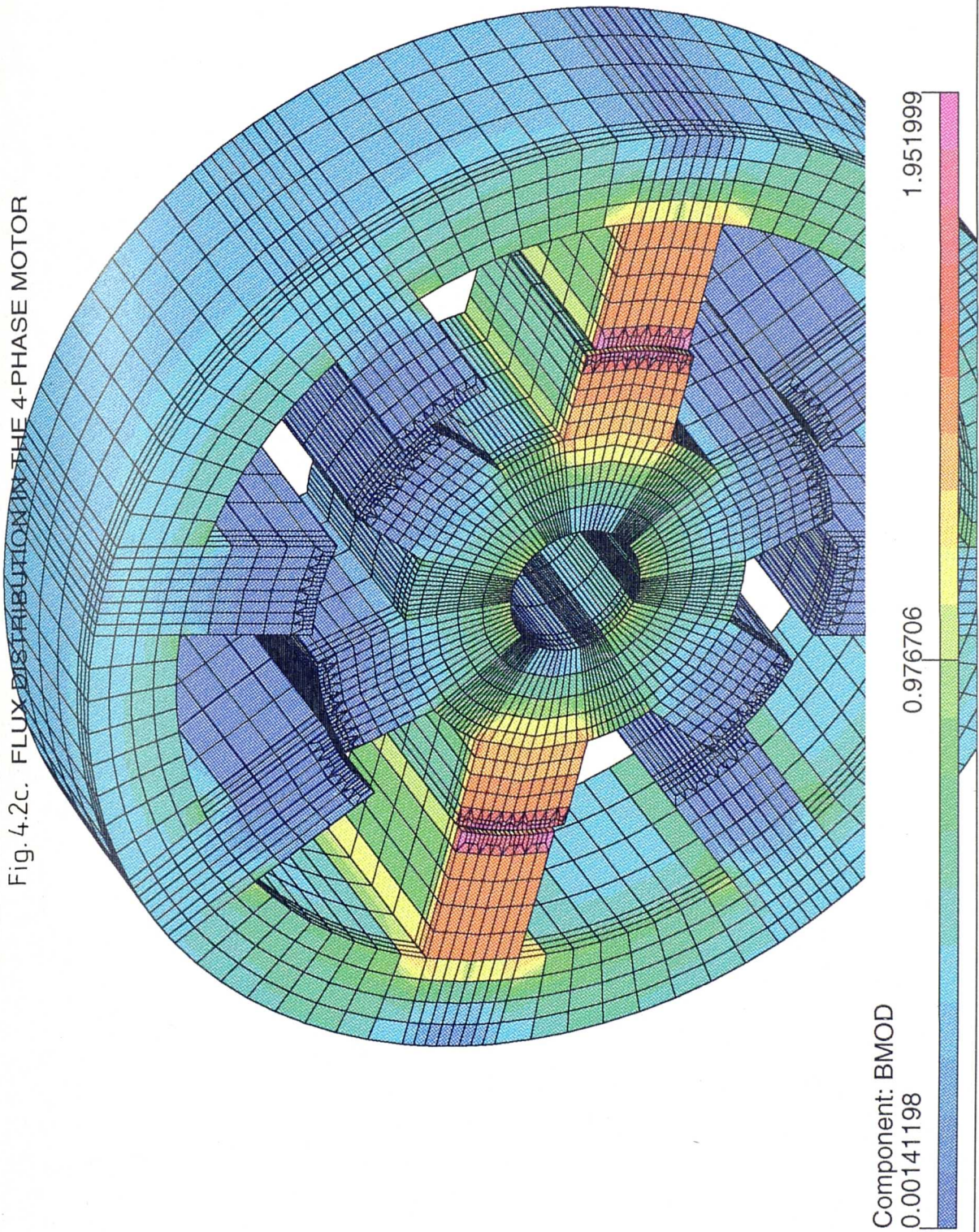
especially in the latter case. However, as the motor structure is laminated and the permeability in the (Z) direction normal to the laminations is low, \mathbf{B} -field lines find it difficult to penetrate the magnetic material axially. High flux densities therefore appear at the ends of the structure, where flux is encouraged to follow a path parallel to the laminations. These effects are not accounted for in two-dimensional modelling. A view of the \mathbf{B} -field distribution in the 4-phase motor is shown in fig. 4.2c; the rotor is in the aligned position, where axial fringing effects are pronounced. This is confirmed by the increased flux density appearing at the stator and rotor pole tips.

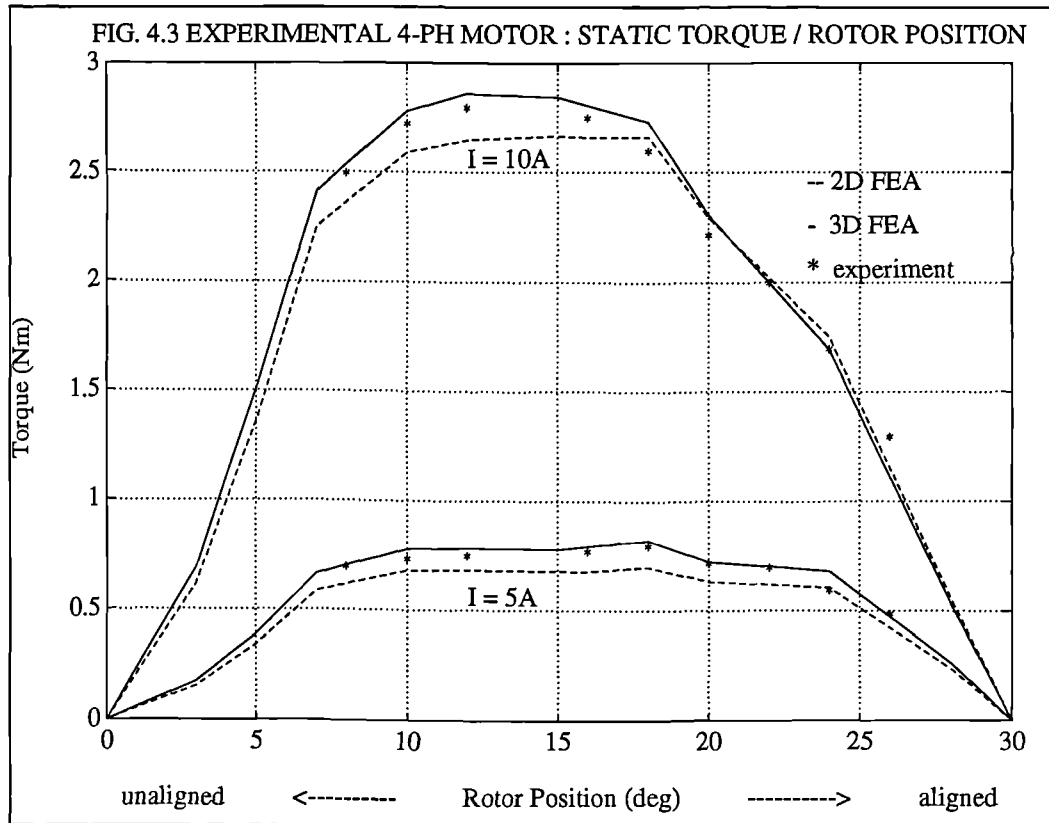
4.3.2. Static torque.

The static torque produced by the switched reluctance motor at a particular rotor angle and excitation can be obtained by computing the integral of the Maxwell stress tensor τ over the appropriate surface. In order to accurately compute the forces acting on the rotor, the airgap of the machine was meshed with four layers of eight-node brick elements. The iron structure (rotor) was selected, and enclosed by two layers of air elements before computing the integral of the Maxwell stress tensor. This gave the best possible chance of the integration of forces over the selected surface being accurate.

The measured static torque produced by the experimental 4-phase machine, as a function of rotor position, is illustrated in fig. 4.3. Also shown is the static torque profile of the machine, predicted by the use of two-dimensional and three-dimensional finite element models. Figure 4.3 is drawn for phase currents of 5A and 10A. Superior agreement with experimental results was obtained from three-dimensional model solutions.

Fig. 4.2c. FLUX DISTRIBUTION IN THE 4-PHASE MOTOR





4.4 Correction charts for two-dimensional finite element modelling.

The base plane lamination of the 4-phase 8/6 machine was extruded to create two further three-dimensional models, 100mm and 150mm in stack length. The λ / i / θ characteristic and static torque profile of the machines modelled was determined and compared with the characteristic that was obtained using two-dimensional modelling. For comparison purposes, scaling approach B was imposed on two-dimensional model solutions, as described in section 4.2.

4.4.1 Flux linkage.

The end-core flux, ϕ_e , was obtained by subtracting the value of flux linking the excited stator poles computed on a two-dimensional model, from the

corresponding value computed using a three-dimensional model. The value of end-core flux is not constant over the excitation range. In the linear region of operation, ϕ_e increases in proportion to excitation. The end-core flux reaches a peak value when the excited stator poles are operated at the 'knee' point of the **BH** curve (measurements taken at the centre of the core). Beyond this point ϕ_e begins to decrease due to the marked decrease in the permeability of iron.

The variation of end-core flux with rotor position in the experimental 4-phase motor is illustrated in fig. 4.4. It is seen to be heavily dependent on the excitation. At high excitations ($i = 10\text{A}$), ϕ_e decreases monotonically as a rotor pole moves into alignment with the excited stator pole. This is due to the fact that the machine is driven harder into saturation as the overlap of the poles increases and the end windings 'see' a low permeability, high reluctance path resulting in less end-core flux. In contrast, at lower excitations ($i = 5\text{A}$) the relative permeability is constant (at most rotor positions) and the reluctance of the magnetic circuit decreases as the overlap of the poles increases. The end-core flux is therefore found to increase as the rotor poles move into alignment with the excited stator poles, only decreasing slightly due to saturation near alignment.

Figure 4.5 indicates the correction factor which needs to be applied to a two-dimensional solution to account for end-core flux. The chart shows the percentage increment in flux linkage due to end-core effects, as a function of current, when a rotor pole is aligned with the excited stator pole. Depending on the airgap length and structure of a machine, the MMF required to establish the necessary flux linkage value (or flux density over the appropriate magnetised pole surface) varies. It must therefore be emphasised that the correction diagram should be used as a function of flux density in the stator pole, and not as a function of current. It is for this reason that the nominal value of flux density in the excited stator pole is also depicted on the diagram. The flux density values were extracted from two-dimensional model solutions and were equal to those of three-dimensional model solutions taken midway along the stack.

FIG. 4.4 EXPERIMENTAL 4-PH MOTOR : END CORE FLUX / ROTOR POSITION

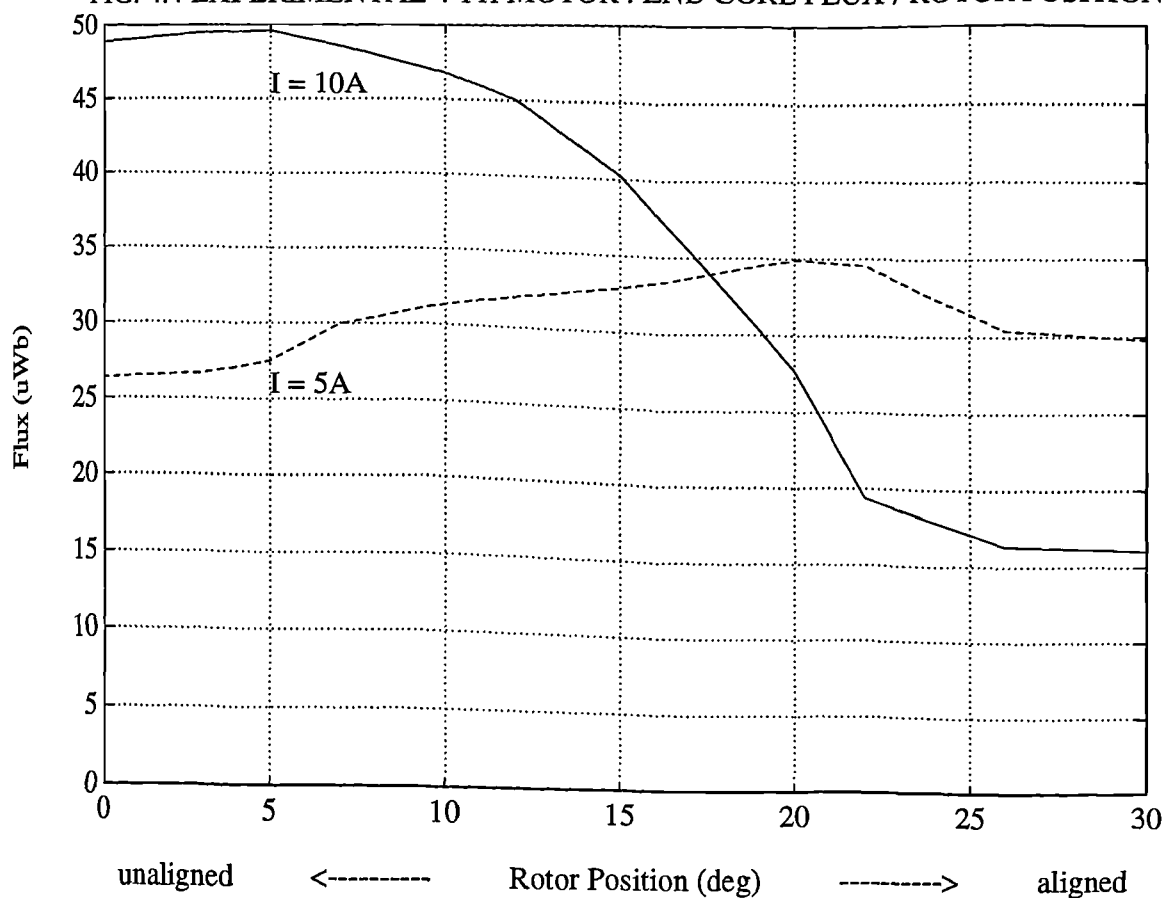
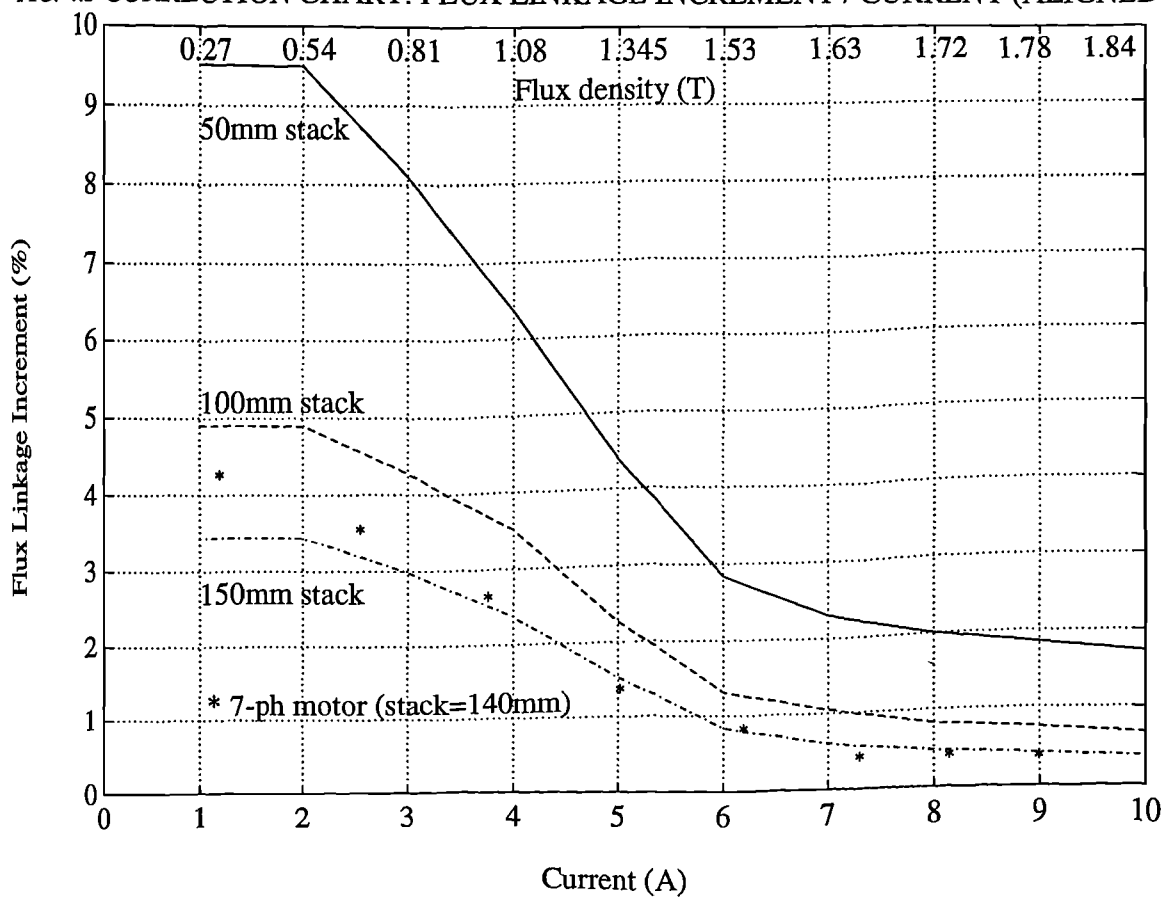


FIG. 4.5 CORRECTION CHART: FLUX LINKAGE INCREMENT / CURRENT (ALIGNED POSN)



The reluctance of the path which the end winding B -field must follow can be separated into two parts. Firstly, there is the air region which B -field lines must penetrate to reach the stator teeth. The reluctance of this path is essentially constant. Secondly, there is the main (iron) magnetic circuit linking the magnetised stator poles via the rotor body and back iron. The reluctance of this path increases with excitation. Hence, at low excitations the current flowing in the end windings has a more significant impact on the value of the phase winding flux linkage because the permeability of the magnetic material is high. In the saturation region the permeability of iron approaches unity and the end winding effects are small. The error in two-dimensional finite element model solutions is greater when a machine of short stack length is modelled due to the fact that the end winding constitutes a significant part of the conductor.

Figures 4.6a and 4.6b illustrate the percentage increment in flux linkage due to end-core effects, as a function of rotor position, for an excitation level of 5A and 10A respectively. Two-dimensional modelling incurs significant errors at rotor positions where the excited stator pole faces the interpolar airgap depth (0° being the unaligned position), though maintaining good accuracy at positions where there is complete overlap between the magnetised stator pole and a rotor pole (30° being the aligned position). In the unaligned position, the error incurred in two-dimensional model solutions is very much constant over the excitation range as the interpolar airgap depth dominates the magnetic circuit reluctance. In the overlap region the error decreases as the rotor poles move into alignment.

In order to predict the percentage increase in flux linkage due to three-dimensional effects at any rotor position, the end-core flux at the unaligned and aligned rotor positions must be known; an appropriate function must then be fitted to approximate the profiles of fig. 4.6. It can be observed that, at high excitations, straight line approximations can be adopted. At the unaligned and aligned rotor positions, the appropriate correction factors at any excitation level can be readily obtained from fig. 4.5 - 4.6. The correct value of average torque can then be computed from the amended λ / i diagram upon application of the coenergy

FIG. 4.6a CORRECTION CHART: FLUX LINKAGE INCREMENT / ROTOR POSITION ($I=5A$)

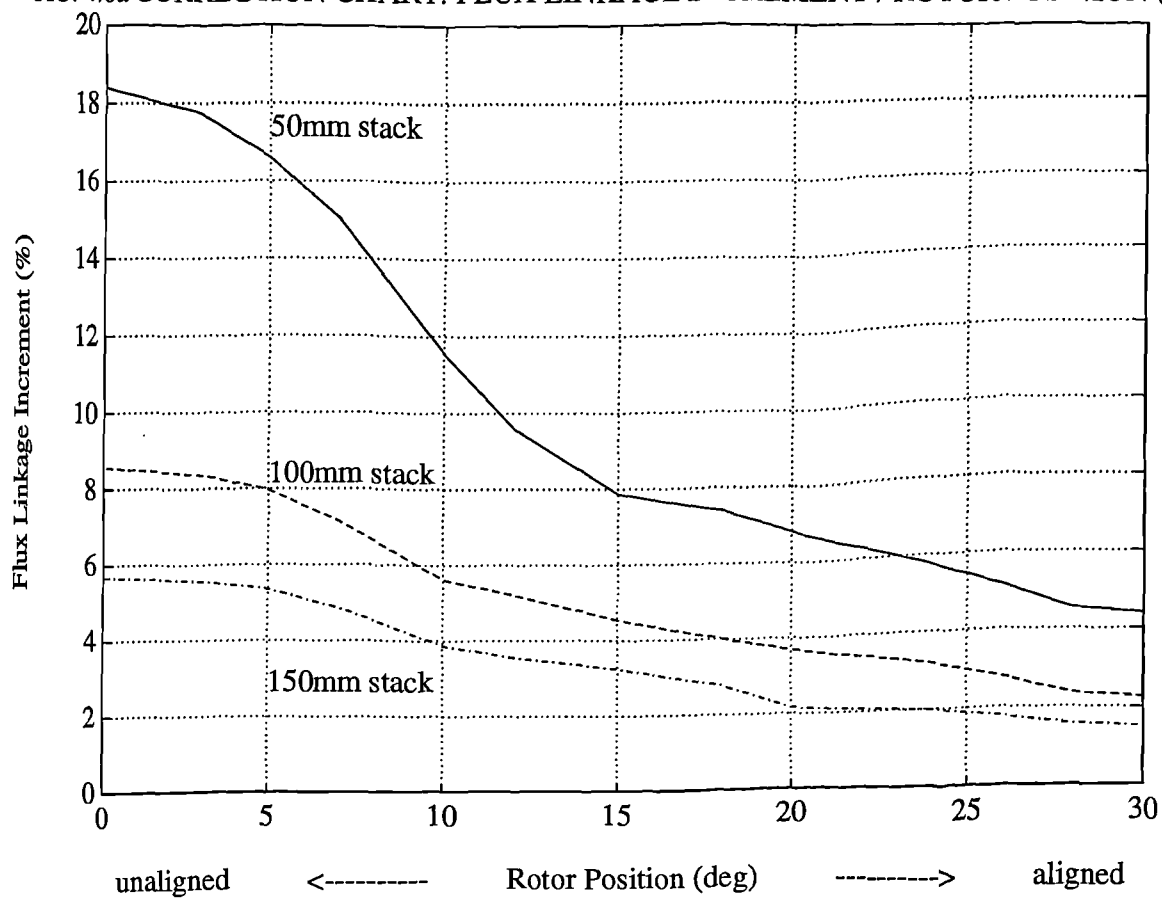
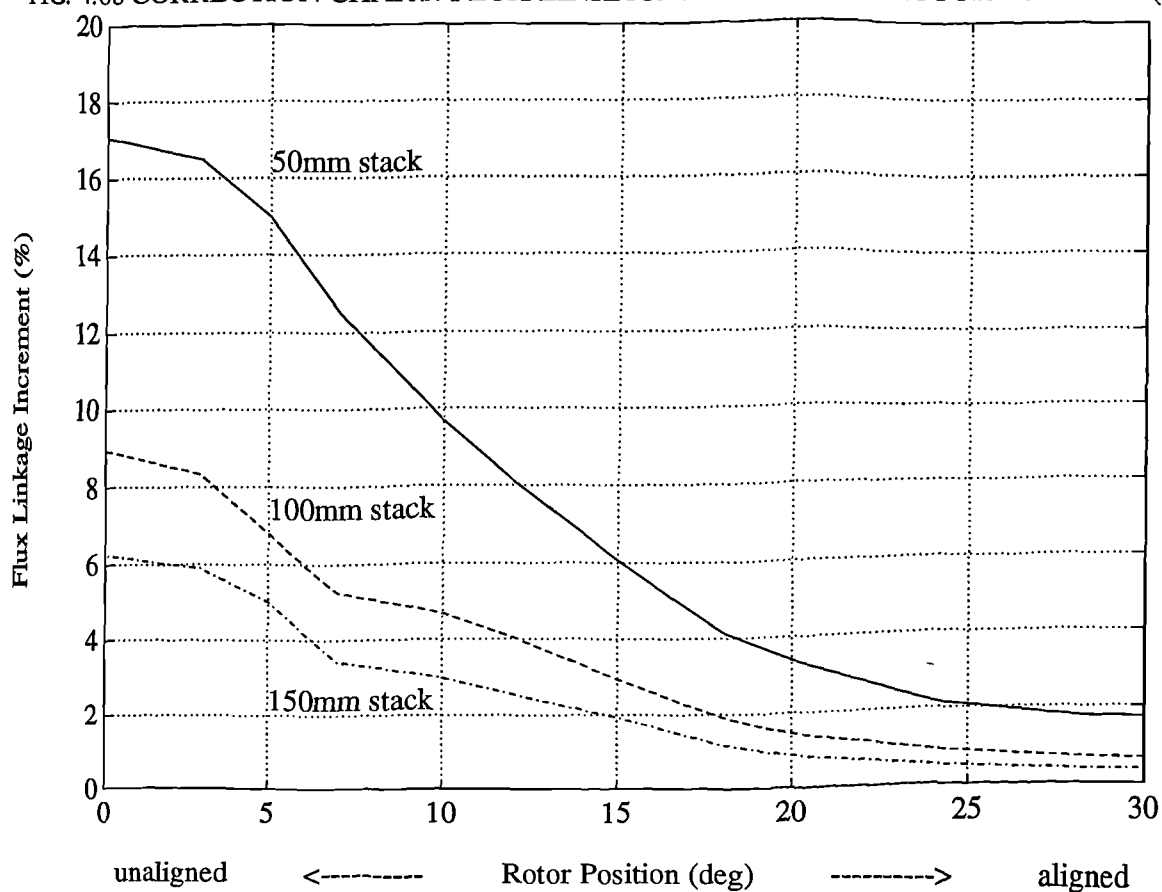


FIG. 4.6b CORRECTION CHART: FLUX LINKAGE INCREMENT / ROTOR POSITION ($I=10A$)



principle.

4.4.2 Comparison with a 140mm stack 7-phase switched reluctance motor.

The guidelines and correction charts have been verified on a 4kW 7-phase switched reluctance motor. This motor has 14 stator poles and 12 rotor poles. Although the dimensions of the 7-phase motor are completely different to the 8/6 configuration that was used to produce the correction charts, it has been found that it demonstrates the same percentage increase in flux linkage due to end-core flux, at a given mid-stack stator pole flux density. This machine has a stack length of 140mm and an airgap length of 0.4mm. The percentage increment in flux linkage due to end-core flux was plotted as a function of flux density in the excited stator pole. The profile fits the correction chart convincingly (see fig. 4.5).

Solutions of a two-dimensional and a three-dimensional model of the 7-phase machine at different rotor positions revealed a similar trend to that obtained from solutions on the 4-phase switched reluctance motor model. In the unaligned position, a small variation of the percentage increment in flux linkage due to end-core effects was noted for different excitations (6.4 to 7.11%). This result is consistent with earlier findings on the 4-phase machine (ref. fig. 4.5 and fig. 4.6 at $\theta = 0^\circ$). At constant (high) excitation, end-core flux decreased linearly in the region where the stator and rotor poles overlap to reach a minimum at alignment. Results for an excitation of 10A are given in fig. 4.7.

4.4.3. Static torque.

The percentage increment in static torque due to end-core flux as a function of rotor position, for low and high excitation levels, is illustrated in fig. 4.8a, b. The discrepancy in static torque calculations performed using a two-dimensional finite element model is not analogous to errors in flux linkage calculations. The relationship that governs static torque production in the switched reluctance motor

FIG. 4.7a FLUX LINKAGE / ROTOR POSITION DIAGRAM (7-PH MOTOR, I=10A)

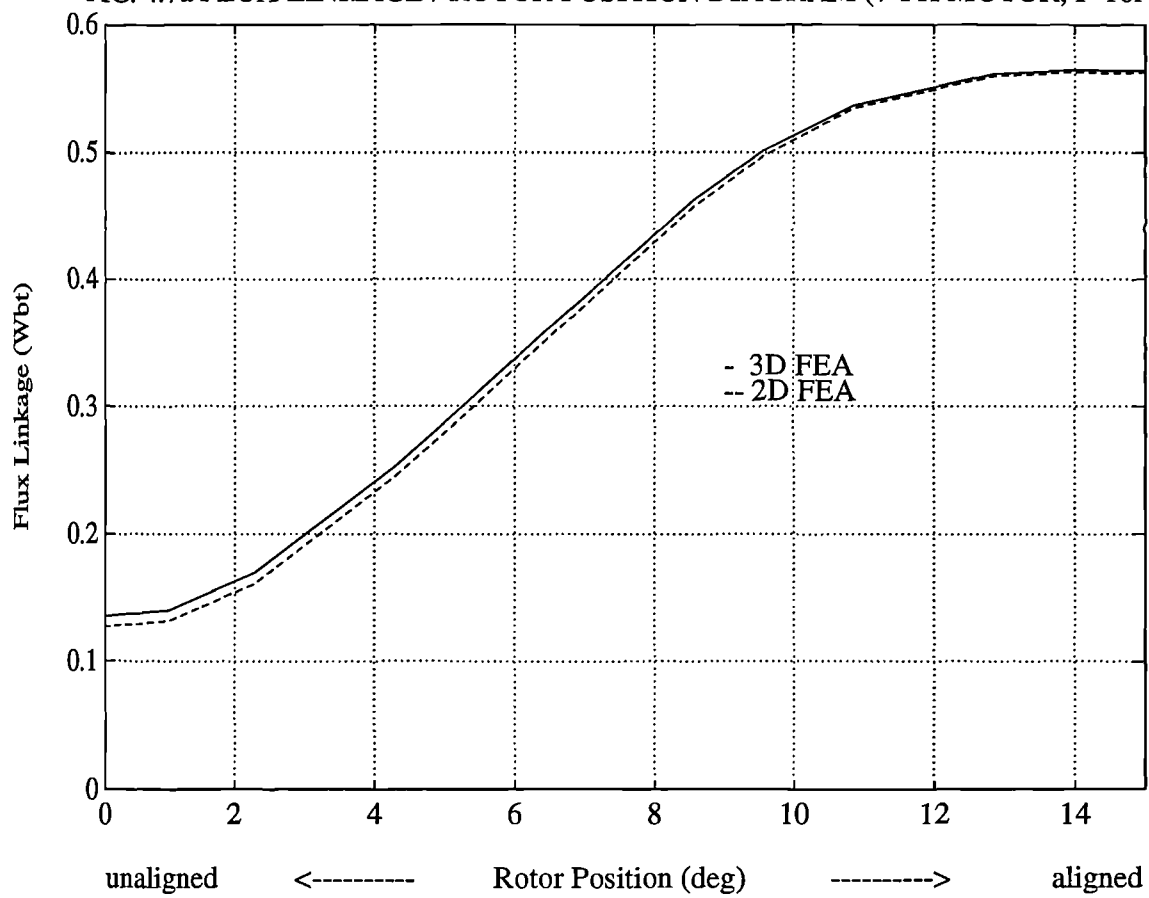


FIG. 4.7b FLUX LINKAGE INCREMENT / ROTOR POSITION (7-PH MOTOR, I=10A)

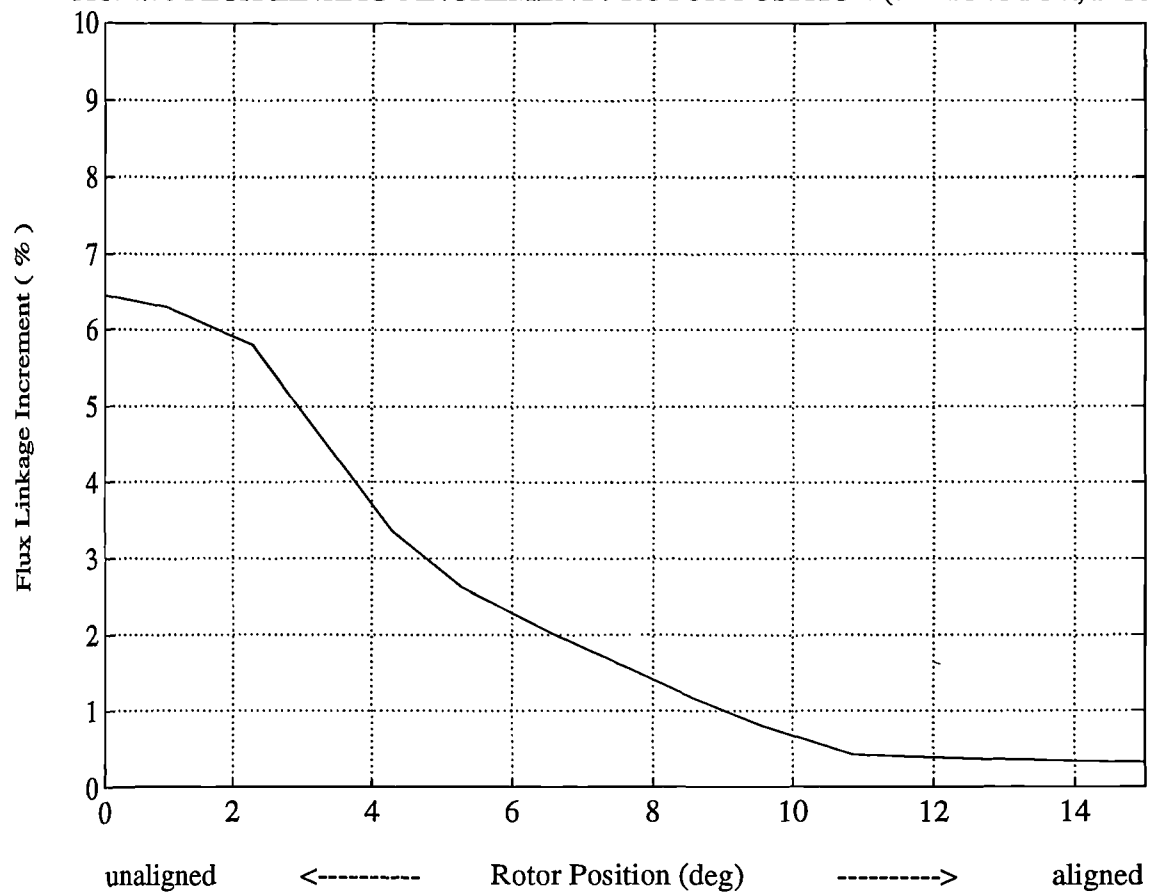


FIG. 4.8a CORRECTION CHART: STATIC TORQUE INCREMENT / ROTOR POSITION (I=5A)

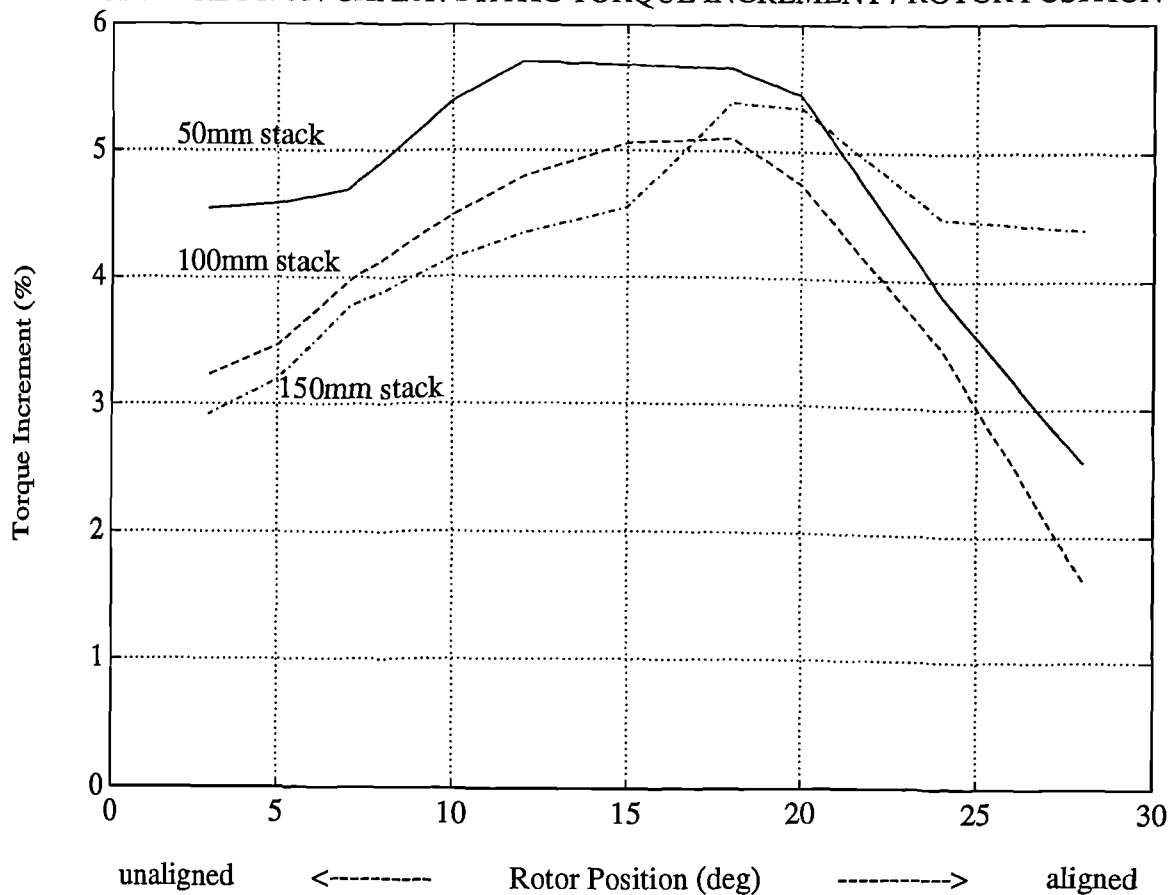
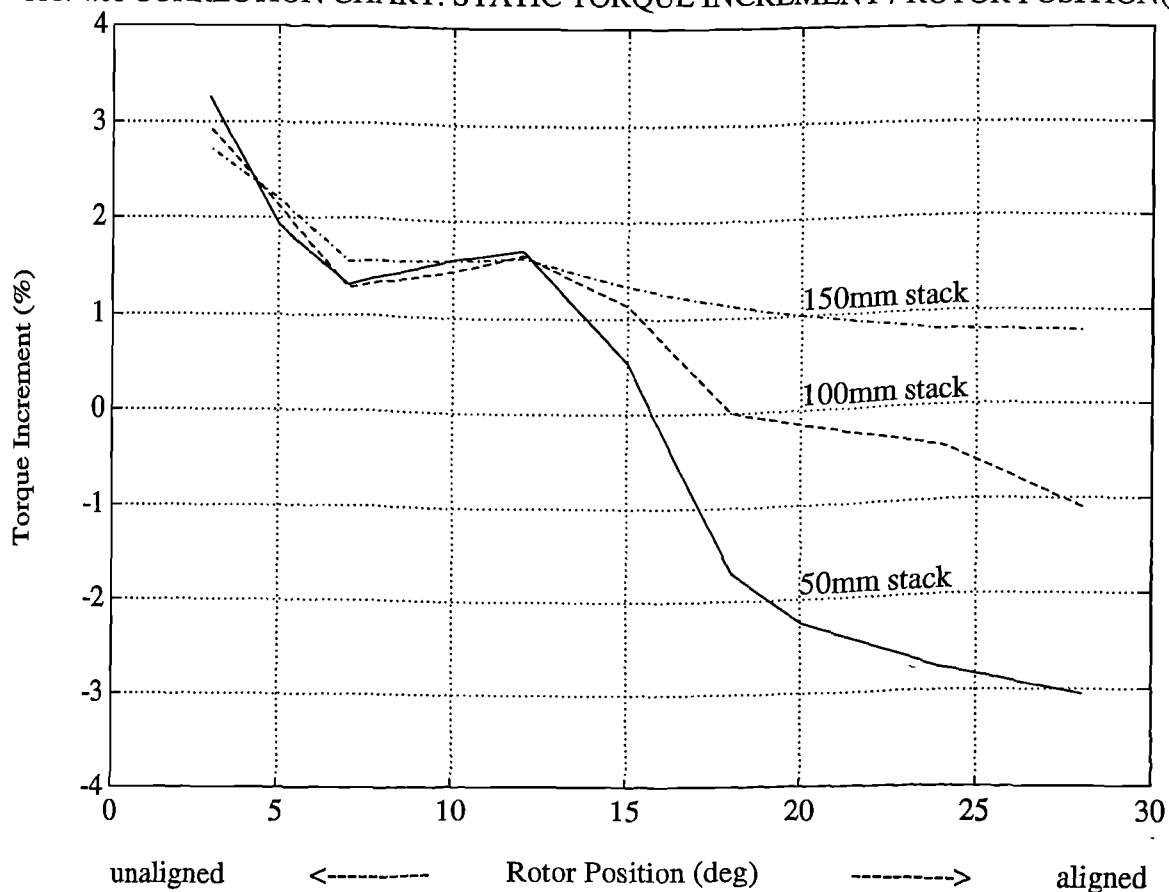


FIG. 4.8b CORRECTION CHART: STATIC TORQUE INCREMENT / ROTOR POSITION (I=10A)



dictates that the axial field B_z , a strong component of which is induced by end windings, does not contribute to positive torque. Torque is maximised by optimising the shearing force τ_{xy} acting on the rotor, a direct consequence of maximising the tangential component of flux density on the rotor, B_t . The radial component B_r , tends to keep the rotor in position, by subjecting it to tension or compression. It must be pointed out that not only the direction but also the magnitude of the flux density components is important. This is the reason why maximum torque is obtained in the region where there is significant overlap between the excited stator and rotor poles ($\theta = 10^\circ$ - 20°), and not earlier in the excitation cycle.

End windings induce all three components of flux density (B_x , B_y , and B_z). The first two components acting parallel to the XY plane contribute to torque. However, at high excitations and towards alignment a higher value of static torque was predicted by two-dimensional model solutions. This is thought to be due to the fact that in positions close to alignment the radial component of flux B_r , produced by end windings may be more dominant than component B_t .

4.5 Discussion on other effects.

4.5.1 Anisotropy.

In three-dimensional finite element models of the switched reluctance motor using anisotropic materials, the iron permeability in the axial direction is assigned a low value, making flux penetration in this direction difficult. As a result, a significant axial component of field arises solely at the ends of the excited stator poles. Flux is forced to penetrate iron parallel to the plane of laminations where the relative permeability is very high. However, at very high excitations as the iron becomes saturated, more flux penetrates the iron axially. In field solutions of the machine using isotropic materials, the axial component of flux is at its highest value at the ends of the excited stator poles and decreases more uniformly toward the middle

of the stack. The net flux linking the stator windings is higher in the isotropic materials machine due to the higher permeability, although higher flux densities appear at the pole edges of the laminated structure. Therefore, in the three-dimensional finite element code, the equations governing the behaviour of the magnetic field in an anisotropic structure appear to provide a faithful representation. However, one might argue that parallel to the plane of each lamination the permeability of iron should not be affected. This leads to the two approaches used to scale two-dimensional model solutions. Figure 4.9 illustrates the λ / i diagram of the experimental machine, computed using two-dimensional models that were either set up by scaling the **BH** curve data (method B) or prepared using the original **BH** curve data and scaling field solutions per unit length by the stack length times the packing factor (method A). When the rotor poles are aligned with the excited stator poles, the results produced by the two methods converge as the excitation increases due to the marked decrease in iron permeability, but they are never equal.

This trend may be understood more easily if the case is considered where three-dimensional models, structurally identical, were assigned packing factors of 0.96, 0.92 and 0.88 and solved for different excitations. Figure 4.10 shows that at low excitations, field values calculated in all three variants were in close agreement, somewhat higher values being obtained from the model that was assigned the highest packing factor. This is because the motor was operated in the linear, high permeability region and the iron was ‘seen’ as infinitely permeable in comparison to air. At higher excitations, as the relative permeability of iron approaches that of air, the field values obtained from the three variants diverged and the loss in performance due to a poor packing factor was evident.

Referring to fig. 4.9, the reader will notice that the λ / i diagram computed using scaling method B is in closer agreement with measurement. This, however, is misleading. It must be remembered that end-core flux has not been accounted for. The use of the original **BH** curve data to set up a two-dimensional model, and the subsequent scaling of the field values per unit length by the stack length times the

FIG. 4.9 FLUX LINKAGE / CURRENT DIAGRAM FOR VARYING SCALING METHODS

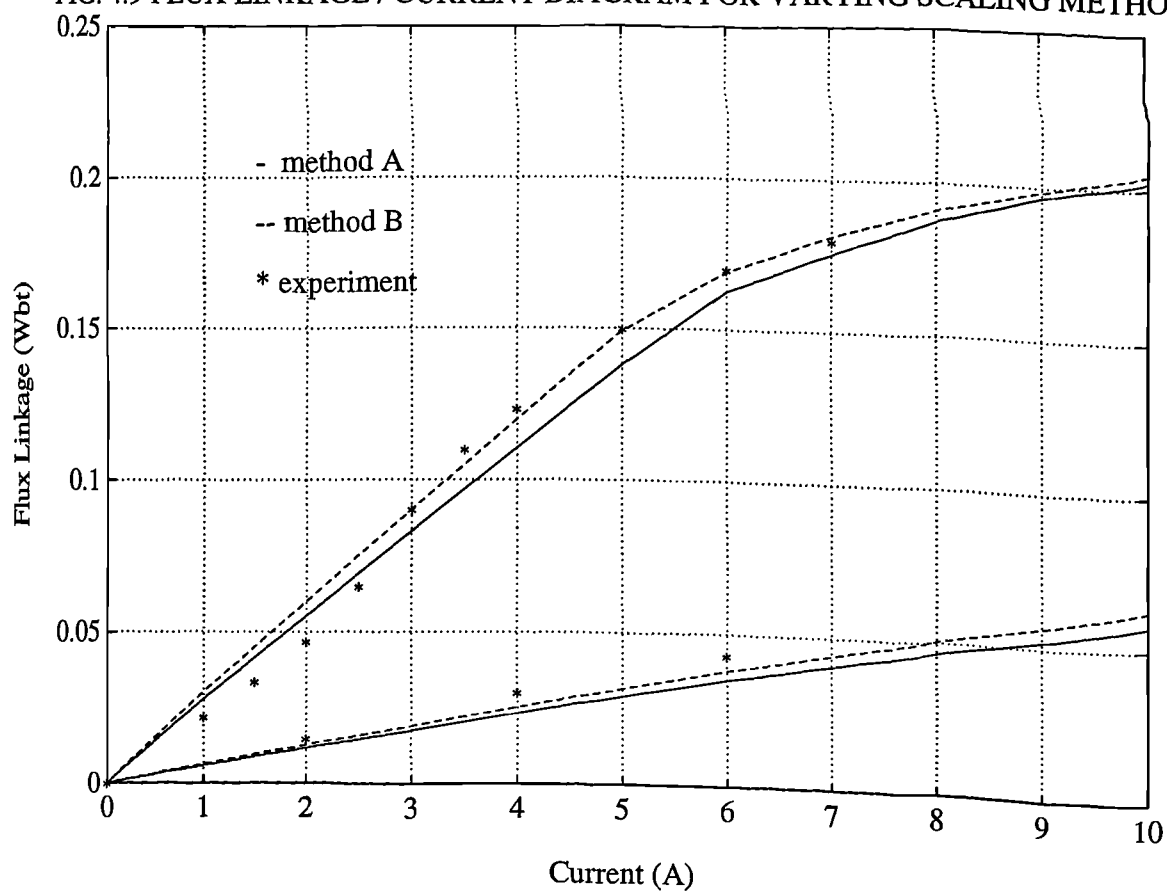
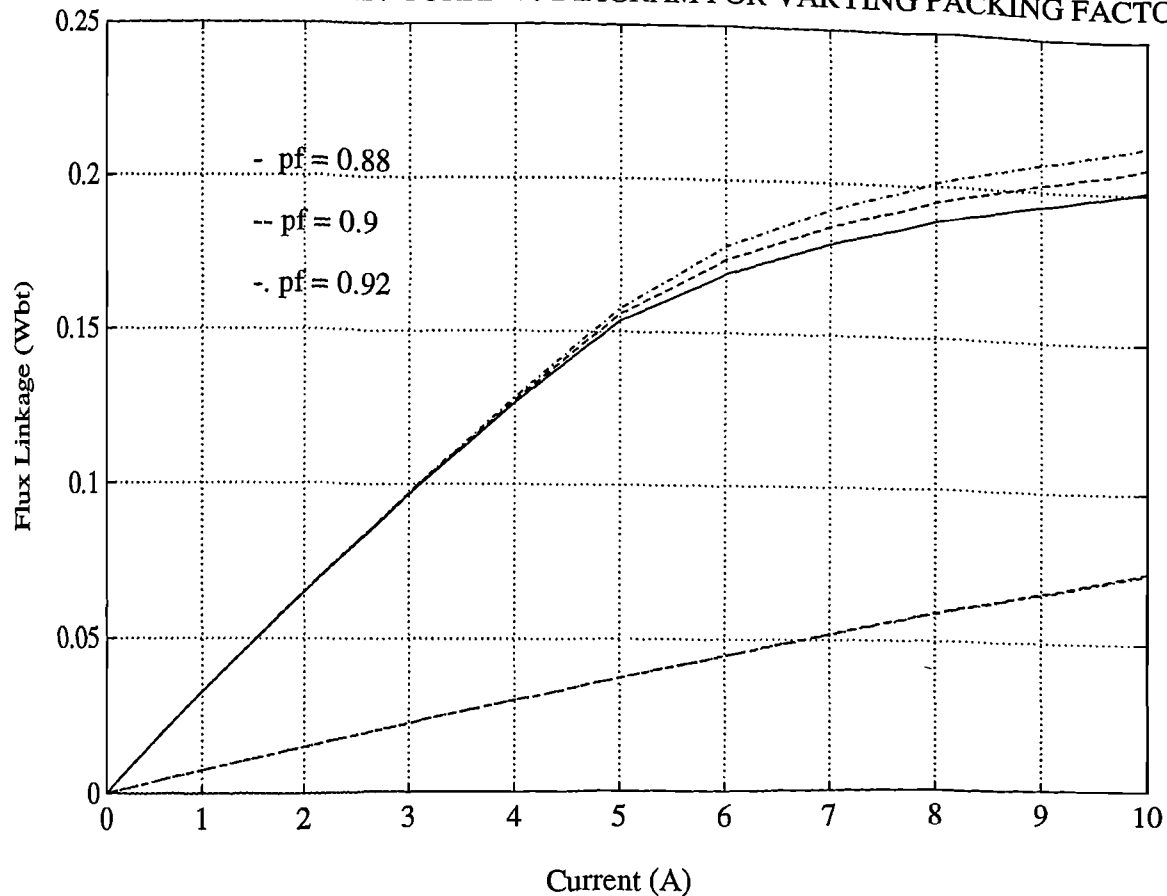


FIG. 4.10 FLUX LINKAGE / CURRENT DIAGRAM FOR VARYING PACKING FACTORS)



packing factor (method A), constitutes a more realistic scaling approach. It provides information on the true flux densities that drive the machine by assuming no change in the magnetic properties of a single lamination. Despite the fact that this approach yields higher field values in the post-processor, it still predicts lower overall (scaled) values of flux linkage and static torque when compared to solutions of finite element models prepared using scaling method B.

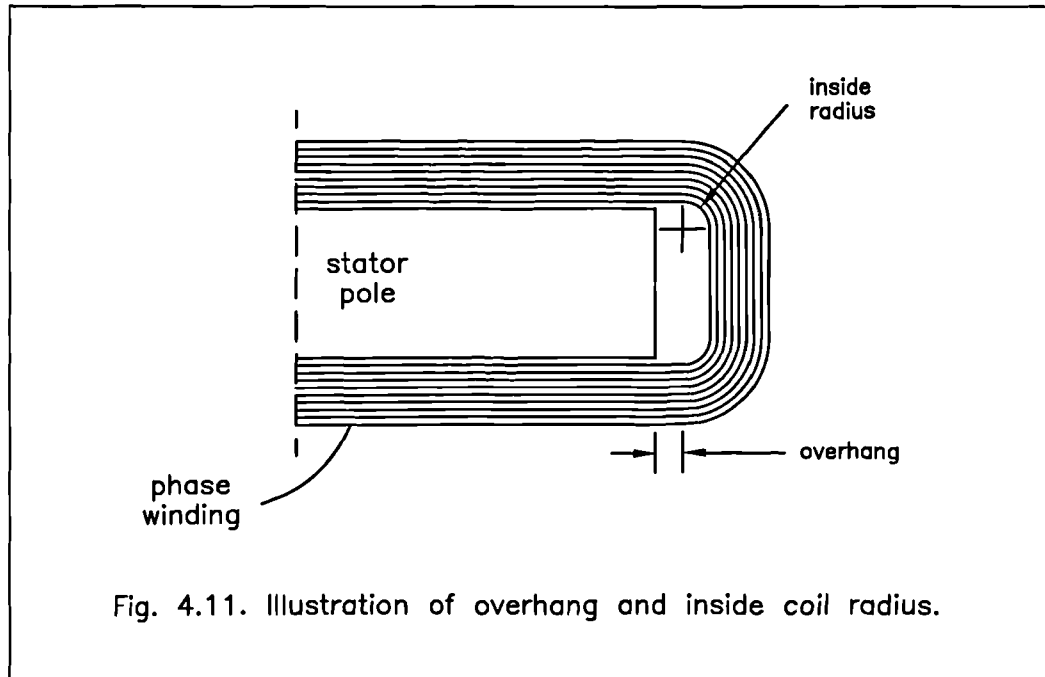
The three-dimensional model consistently yields more accurate field solutions of the motor, at any rotor position and excitation, in comparison to the two-dimensional model. However, flux linkage and static torque values are, even marginally, overestimated by three-dimensional model solutions. One reason for this discrepancy could be the properties assigned to anisotropic material structures, and in particular eqn. 4.2. The margin of error is still very acceptable though, and defining a three-dimensional model with layers of iron and air interleaved would be unnecessarily expensive, if not impossible.

4.5.2. Conductor overhang / inside coil radius.

The variation in length of the conductor overhang and inside coil radius, shown diagrammatically in fig. 4.11, has little effect on the end-core flux linking the excited stator poles of the switched reluctance motor. Three models were set up with a conductor overhang of 3mm and an inside coil radius of 3mm, 4.5mm and 6mm respectively. The value of end-core flux plotted against excitation, when the rotor poles are aligned with the excited stator poles, is shown in fig. 4.12. As the inside coil radius increases the end-core flux decreases, but only marginally, because the end conductors are positioned further away from the stator poles.

The results suggest that the overhang, present in all machines, plays the most significant role in producing the marked increase in flux at the ends of the excited stator pole. The B -field lines generated by current flowing in the overhang, follow a shorter path through air in order to ‘creep into’ the stator poles. These findings were confirmed by extending the end windings a considerable distance away from

the pole ends (the overhang was set to 10mm) and repeating the computation of flux linkage. The results are superimposed on fig. 4.12 and demonstrate clearly that the dominant cause of the end-core flux is the coil overhang and not the tangential (XY) part of the end winding.



4.5.3. Sources of error.

The most significant source of error in finite element modelling is that incurred due to the level of discretisation. In order to minimise this, the discretisation of the two-dimensional (base plane) mesh was repeatedly refined until field solutions obtained from the most finely discretised model were within 1.0% of the previous. Discretisation in the third dimension was also optimised, although a very fine mesh here would produce a model of unrealistic element size. The ends of the machine were more finely discretised in order to 'capture' the end effects. This is important when dealing with anisotropic structures, where there are abrupt changes in field values at the excited stator pole ends. A small margin of error should however be allowed to the results presented to account for discretisation errors.

FIG. 4.12 VARIATION OF END CORE FLUX WITH COIL RAD. / OVERH. (ALIGNED POSN)

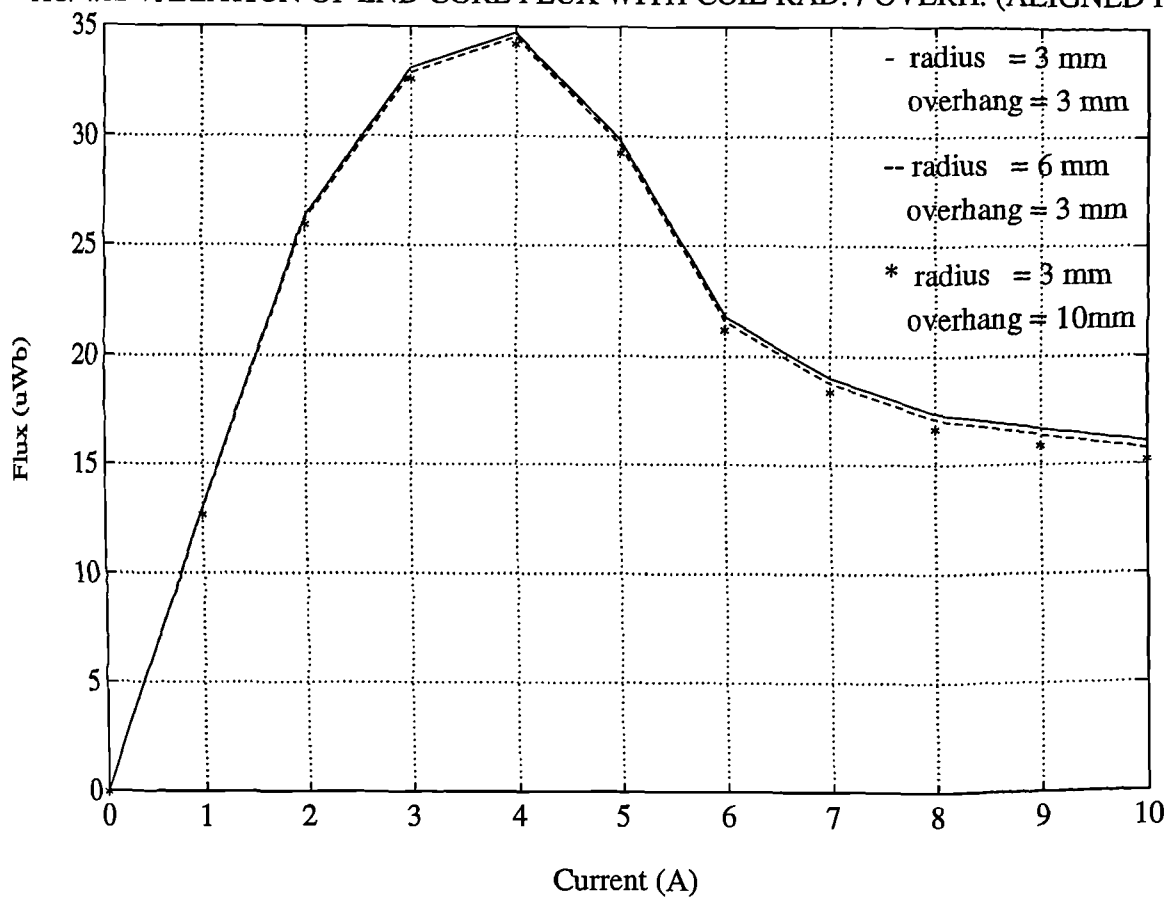
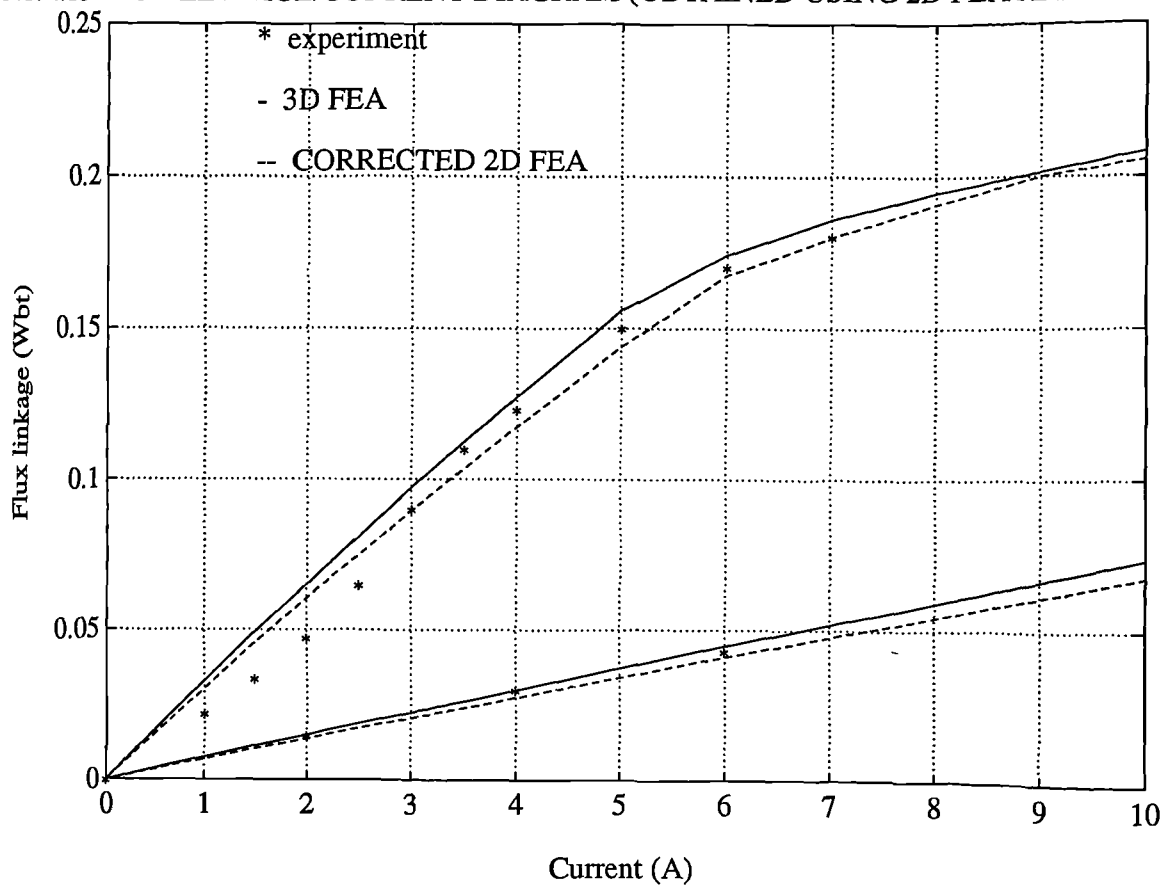


FIG. 4.13 FLUX LINKAGE/CURRENT DIAGRAM (OBTAINED USING 2D FEA AND CORRECTED)



4.6 Conclusions.

The effect of end-core flux on the performance of switched reluctance motors has been presented. Experimental results from a 4-phase motor verified the superiority of three-dimensional modelling. The percentage increment in flux linkage due to end effects was found to be maximum when the excited stator poles face the interpolar airgap depth. The percentage increment in flux linkage due to end effects decreased linearly as the overlap between stator and rotor poles increased, reaching a minimum value in the aligned position. The correction charts that were set up for different machine lengths may be used to account for end-core flux at a range of rotor positions and excitations. An application to an alternative 4kW 7-phase machine confirmed the reliability of the charts. The value of end-core flux was found to be heavily dependent on excitation, rotor position and magnetic saturation. An extensive discussion into the modelling of anisotropic material structures was put forward.

It is thought that the most realistic approach of accounting for three-dimensional effects when modelling switched reluctance machines in two dimensions, constitutes the scaling of field values per unit length by the stack length times the packing factor and, at a particular rotor position and stator pole flux density, adding the end-core flux value provided by the correction charts. This procedure was applied to the experimental four phase machine, and the resultant λ / i diagram, shown in fig. 4.13, compares favourably with measurement (except at very low current, as explained earlier). A similar procedure may be followed for static torque estimation.

Chapter 5

THE SRDESIGN PACKAGE: MODELLING AND SIMULATION

SRDESIGN is a computer simulation program, written in Turbo Pascal by C. Pollock and A. Michaelides to characterise the performance of the switched reluctance motor under running conditions. This chapter shall describe fundamental design and modelling considerations supported in SRDESIGN.

The structure of SRDESIGN, shown in fig. 5.1, is based on screen menus which control the flow of data and sequence of calculations. A design entry interface and a facility for design changes in the lamination geometry or the power converter specification is provided. Once a complete switched reluctance drive specification has been entered, the program offers the choice of either (internally) computing the magnetisation curves at 'extreme' rotor positions, or importing them from finite element analysis. Magnetisation curves at intermediate rotor positions are subsequently computed within SRDESIGN. Information on the operating speed and level of excitation is used to calculate the output torque, power input and efficiency. A collection of additional data that may be of interest to the designer is also provided. Included are the operating flux density in different parts of the magnetic circuit, the rms current and current density and information on the stator slot area, winding resistance and slot fill factor.

With the aid of mathematical formulations, this chapter will predominately describe the work that was undertaken only in this project to improve SRDESIGN.

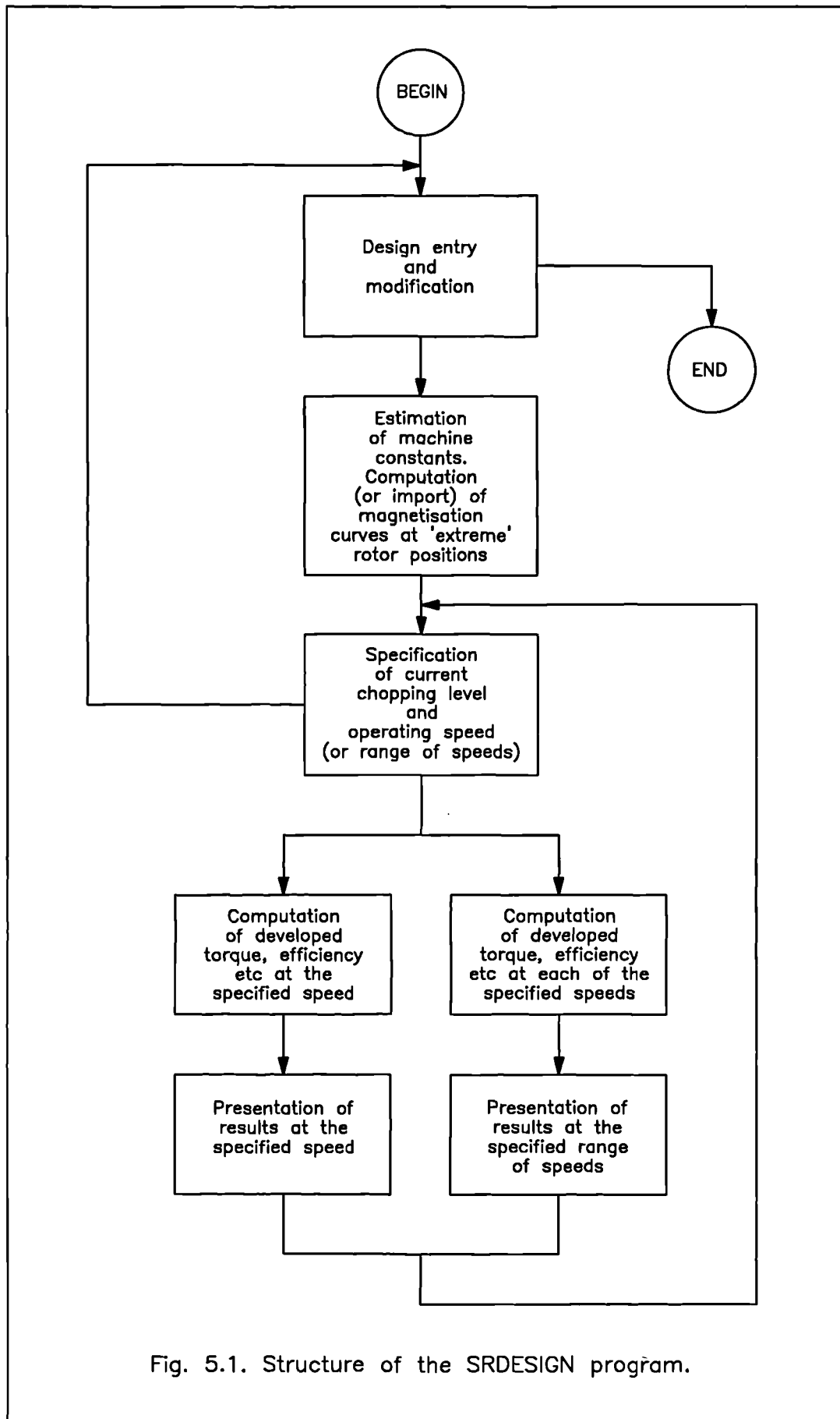


Fig. 5.1. Structure of the SRDESIGN program.

5.1 Modelling magnetisation curves for singly excited systems.

5.1.1 'Extreme' (aligned and unaligned) rotor positions.

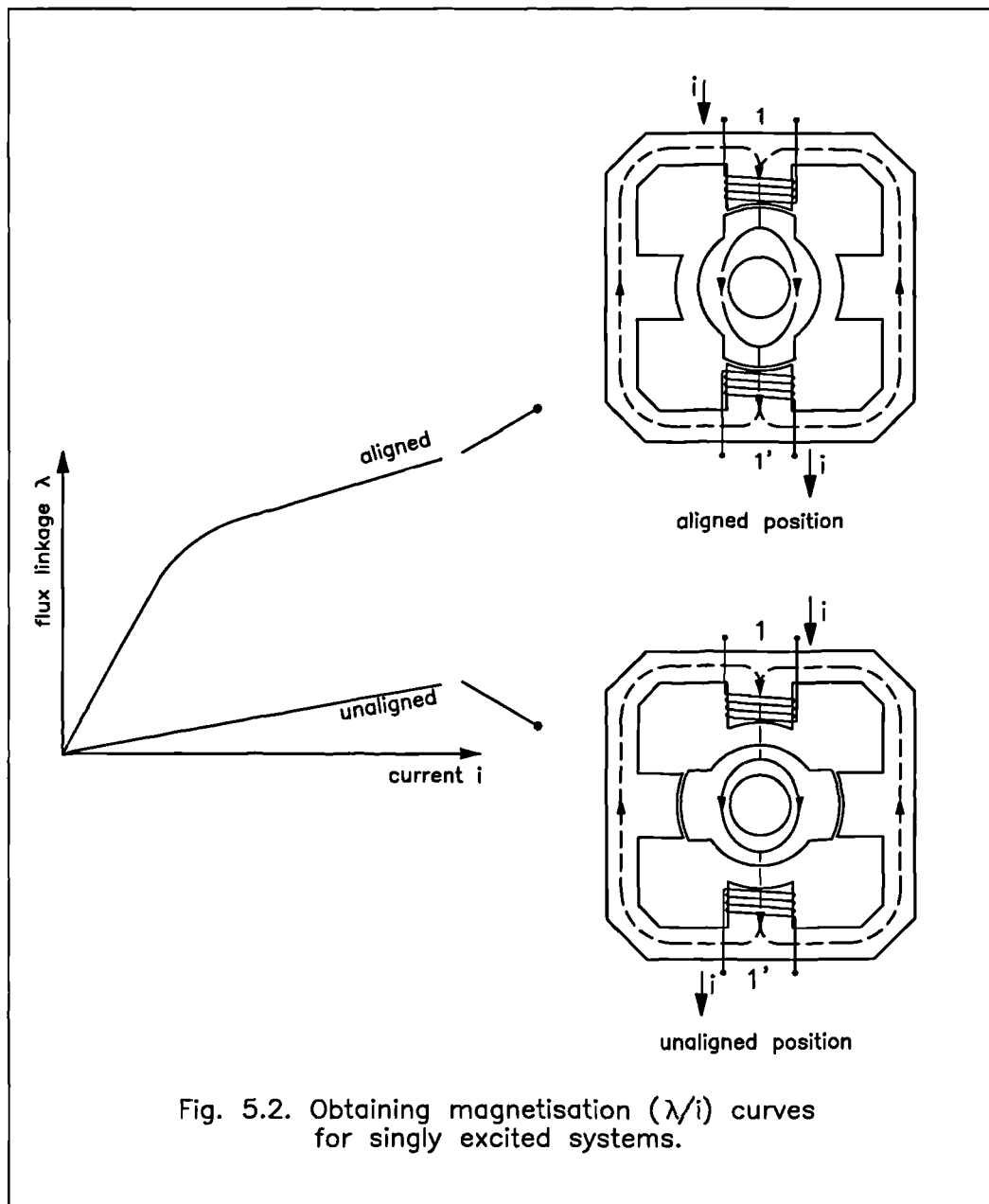
The λ / i diagrams for the aligned and unaligned rotor positions play a significant role in the modelling structure. It is therefore advantageous to obtain these curves from a finite element analysis program. A PASCAL routine has been written to import λ / i data calculated by finite element analysis into the SRDESIGN package. The PASCAL program interpolates linearly between the imported λ / i array, as needed. If finite element software is not available, the curves can be computed within the package, with routines which find their source in [51].

Figure 5.2 shows the laminations of a 2-phase switched reluctance motor. The magnetic flux pattern in the unaligned position is illustrated. The unaligned λ / i characteristic is shown to be approximated with a straight line. The magnetic path reluctance is highest at this position because of the large interpolar airgap between the rotor and the excited stator teeth. The magnetic circuit is not subject to saturation effects and therefore

$$\lambda_{un} = L_{un} i \quad (5.1)$$

where λ_{un} and L_{un} denote the flux linkage and inductance in the unaligned position.

In the aligned position the reluctance of the magnetic circuit is at its lowest; for a constant excitation level the phase winding flux linkage is therefore at its highest. At very low excitation the flux linkage varies linearly with current. The iron paths are highly permeable, with a relative permeability, μ_r , of over 6000. 'Reverse curvature effects' are neglected to aid the convergence of nonlinear finite element problem solutions. At high current levels the magnetic circuit becomes saturated, with the iron relative permeability μ_r decreasing rapidly.



5.1.2 Intermediate rotor positions.

I. Low excitation.

As a pair of rotor poles turn from the unaligned position to the point where they begin to overlap with the excited stator poles, there is a small increase in the flux linking the excited stator phase. The large rotor interpolar airgap facing the excited stator poles maintains a high magnetic circuit reluctance. B -field lines tend to

fringe from the stator pole tips to the approaching rotor teeth. Fringing effects become more pronounced near the onset of overlap. Fringing \mathbf{B} -field lines account for the small increase in flux linkage from λ_{un} to λ_{bo} in this region. The flux linkage at the beginning of overlap, λ_{bo} , is estimated using an empirical formula derived from finite element analysis studies; λ_{bo} varies linearly with excitation i.e.

$$\lambda_{bo} = L_{bo} i \quad (5.2)$$

A sharper increase in phase winding flux linkage is noted with the onset of overlap. As the excitation is low, λ varies linearly with θ , throughout the overlap region as shown in fig. 5.3a. The reluctance of the magnetic circuit decreases as the rotor teeth approach the excited stator poles, though the excitation is never high enough to saturate the magnetic circuit. The slope of this linear function is expressed as

$$k_{le} = \frac{\lambda_{al} - \lambda_{bo}}{\beta_s} \quad (5.3)$$

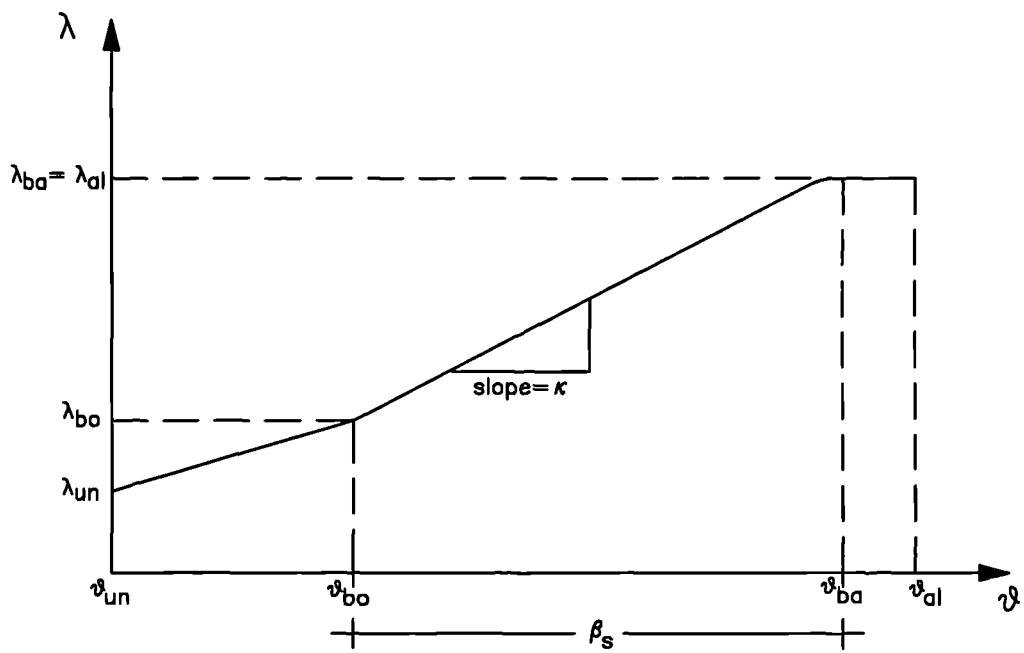
Byrne and Lacy [56] recognised the gradient of this profile to be analogous to the back-emf constant of a dc motor, and appropriately assigned the symbol k to it.

II. High excitation.

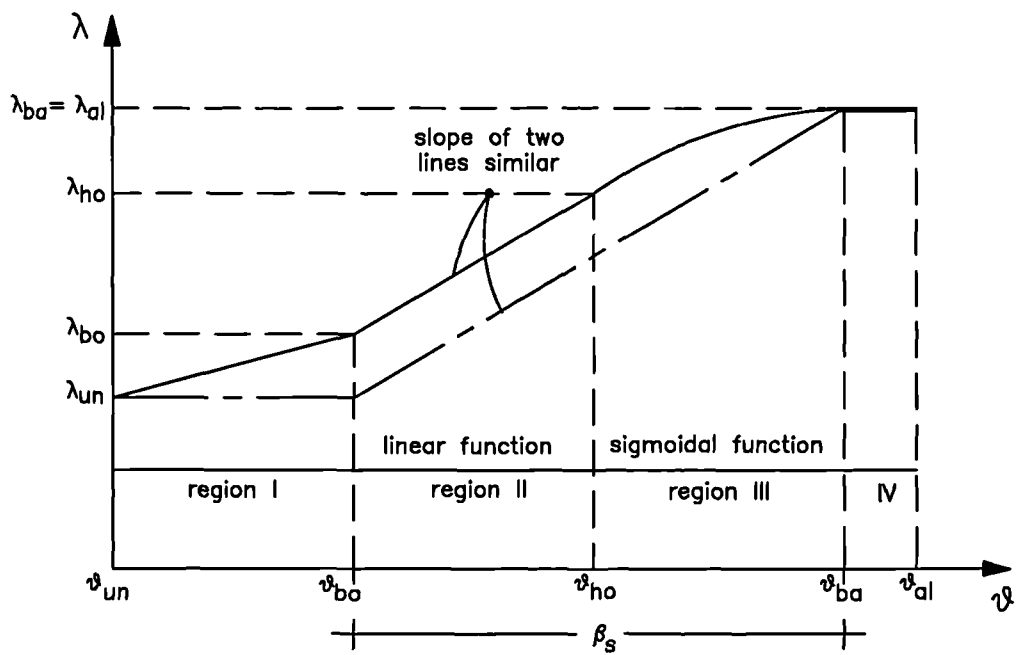
At higher current levels, the λ / θ profile in the overlap region can be approximated by a linear function followed by a sigmoid. The rotor travel angle may be separated in four regions as shown in fig. 5.3b. The slope of the linear region (II) is similar to that of the idealised (trapezoidal) inductance characteristic, i.e.

$$k_{he} = \frac{\lambda_{al} - L_{un} i}{\beta_s} \quad (5.4)$$

This observation was first made by Miller and McGilp [57]. It must, however, be pointed out that the slope k is not constant; it varies with excitation from k_{le} to k_{he} .



a. Low excitation.



b. High excitation.

Fig. 5.3. λ/ψ variation in singly excited systems.

A sigmoidal function has been chosen to describe the flux linkage variation with rotor position in region III. This is of the form [58]

$$\lambda = \frac{a_f \theta^2}{\theta^2 + \beta_f \theta + \gamma_f} \quad (5.5)$$

The starting gradient of the sigmoid at $\theta = \theta_{ho}$ was set to be the slope of the λ / θ characteristic in region II. This defines two points on the sigmoidal function. A third point is needed to define the shape of the sigmoid, and this is extracted from the aligned magnetisation curve, at the specified current level. The ‘Gauss routine’ within the SRDESIGN package uses this information to compute constants a_f , β_f and γ_f and therefore completely define the sigmoidal variation of flux linkage with rotor position in the overlap region. Although a similar approach can be used to define a sigmoidal λ / θ characteristic in region I, it was thought that a linear function description would suffice.

5.2 Modelling magnetisation curves for switched reluctance motors with two phases simultaneously excited.

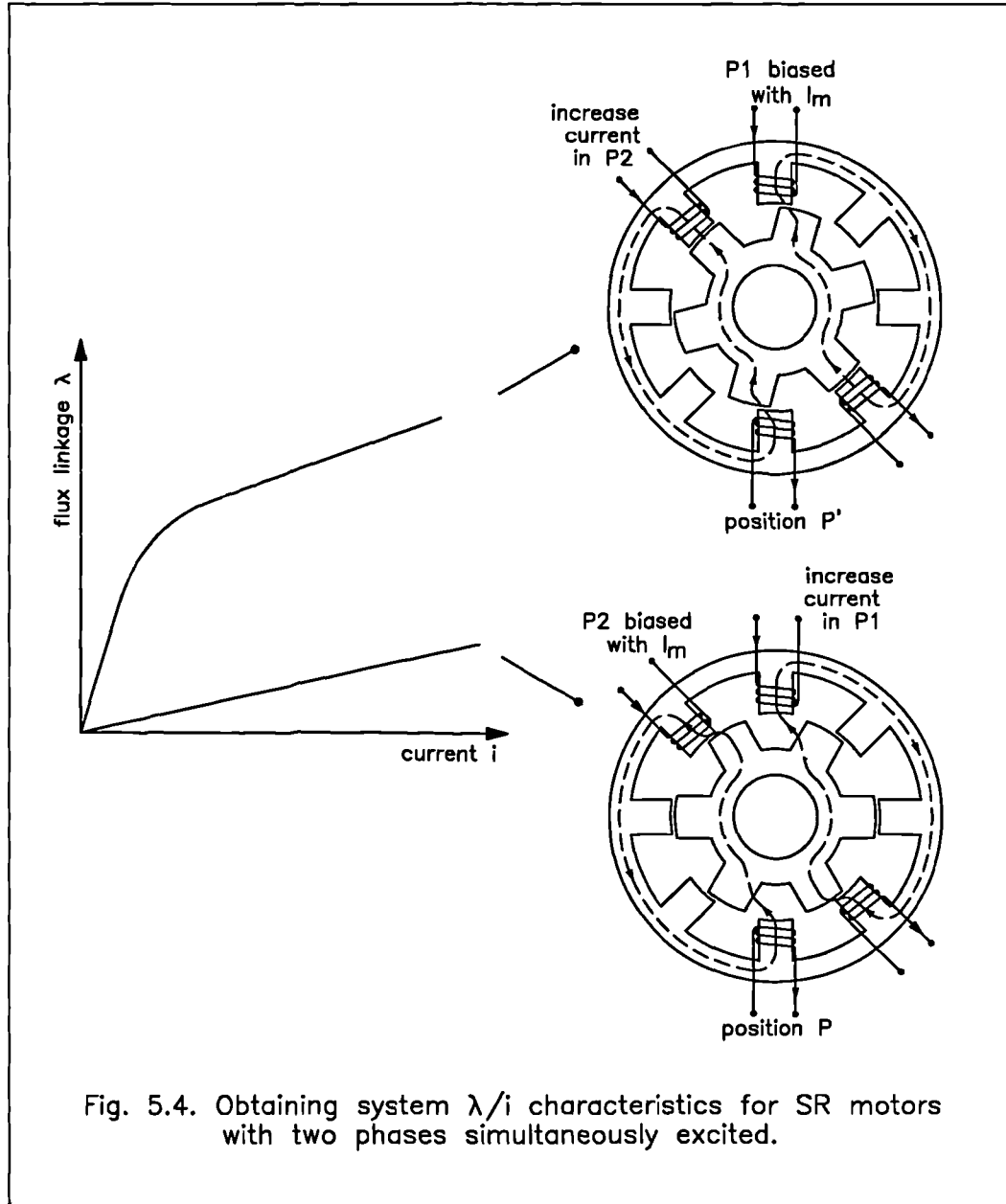
5.2.1 ‘Extreme’ rotor positions.

When modelling switched reluctance motors with two phases simultaneously excited, the advantage of importing λ / i diagrams for the ‘extreme’ rotor positions from finite element analysis is more pronounced. The analytical technique which is embodied in the SRDESIGN package does not account for magnetic interaction effects. In finite element analysis the **system** λ / i characteristic is drawn by following the new field computation procedure for motors with two phases excited at any time. The procedure, described in chapter 3, is graphically illustrated in fig. 5.4. Referring to fig. 5.4,

$$\lambda_{2(al)} = N_{ph} \int B ds \quad i_1 = I_m, \text{ varying } i_2 \quad (5.6a)$$

$$\lambda_{1(un)} = N_{ph} \int B ds \quad i_2 = I_m, \text{ varying } i_1 \quad (5.6b)$$

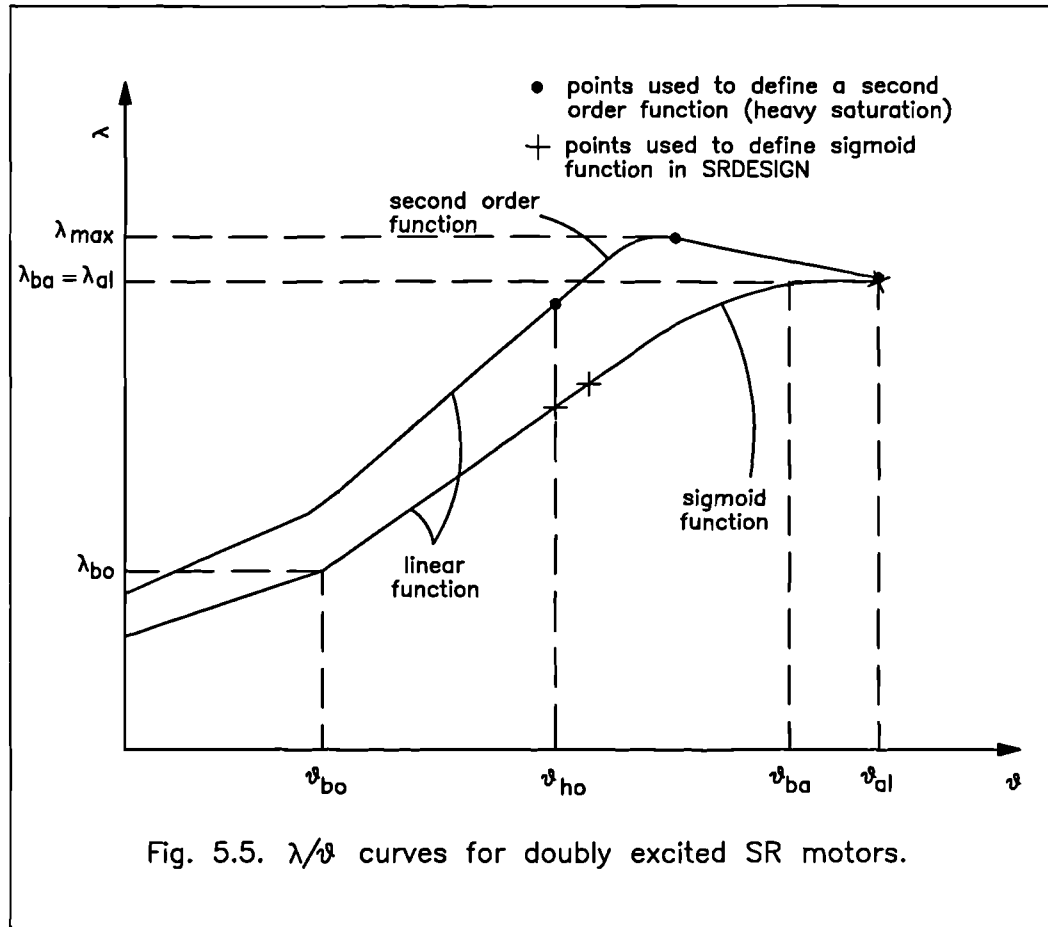
where I_m denotes the set current chopping level.



5.2.2 Intermediate rotor positions.

The modelling structure presented in section 5.1.2 is valid for motors with two

phases excited at any time, provided no part of the magnetic circuit is heavily saturated. There are cases where bulk saturation of the yoke sections may distort the usual λ / θ curve. This phenomenon was extensively discussed in chapter 3. Long flux loop machine configurations are more susceptible to yoke saturation effects because of the flux path nature. The λ / θ curve of a deeply saturated motor with two phases excited at any time is reproduced in fig. 5.5. The phase



winding flux linkage in the leading stator phase increases rapidly with rotor position in the overlap region. However, the flux linkage value reaches a maximum before the approaching rotor poles reach alignment. Beyond this peak towards alignment, and while the system energy increases, the flux linking the leading stator phase decreases.

It is possible to use a second order function to fit a heavily saturated λ / θ

characteristic within the SRDESIGN package so as to obtain an accurate model of the behaviour of the motor. However, additional data needs to be imported from finite element analysis in order to perform this task. In addition to the magnetisation curves at the extreme rotor positions, the maximum flux linkage, λ_{max} , and the rotor position at which it is obtained must be entered. This operating point moves along the θ axis with changing excitation. The data is therefore valid for a single operating current, I_m . The approximate curve fitting procedure is illustrated in fig. 5.5.

5.3 Dynamic operation considerations.

Under running conditions, it is necessary to commutate the current in the phase winding before the approaching rotor teeth align with the excited stator poles. Early commutation ensures that the current and associated flux linkage reduce to zero before the rotor teeth move beyond alignment, as shown in fig. 5.6.

When the rotor speed is low, the supply voltage exceeds the motor back-emf. It is therefore essential to limit the phase current to its rated value with the aid of a current chopping regulator. There exists a speed, known as the base speed ω_b , at which the applied voltage is equal to the back-emf. In theory, at this speed a flat topped current pulse may be maintained without chopping. In practice this cannot be achieved as the back-emf constant varies with rotor position, as illustrated in section 5.1.2.

When the motor is running above base speed, the supply voltage is not enough to overcome the back-emf. In this case the phase current rises to a set value and immediately decreases as the approaching rotor teeth begin to overlap with the excited stator poles. Figure 5.6 demonstrates how the electrical energy that is converted to mechanical work during each working stroke decreases with speed.

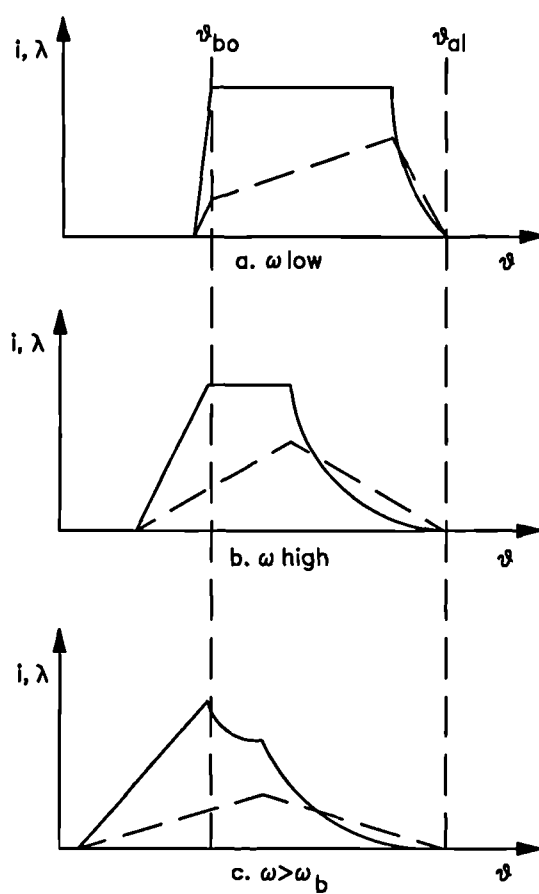
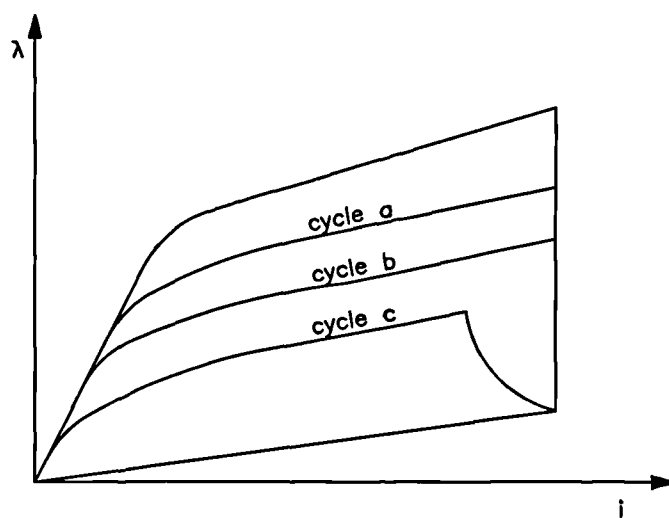


Fig. 5.6. Dynamic operation considerations.

5.3.1 Base speed estimation.

If the phase current is constant, and a linear variation of inductance with rotor position is considered in the overlap region, the back-emf is also constant. The speed at which the back-emf is equal to the supply voltage is known as the base speed.

As the rotor turns through an angle equal to the stator pole arc, β_s , the flux linkage increases from λ_{bo} to λ_{al} . The time taken to complete the move is given by β_s / ω , where ω represents the average speed of rotation. If the motor is running at base speed, ω_b , the current must have risen to (and maintained) a constant value under the influence of the supply voltage, V_s . Hence

$$\lambda_{al} - \lambda_{bo} = (V_s - I_m R) \frac{\beta_s}{\omega_b} \quad (5.7)$$

where R denotes the phase winding resistance. The base speed is therefore given by

$$\omega_b = \frac{(V_s - I_m R) \beta_s}{N_{ph} (\Phi_{al} - \Phi_{bo})} \quad (5.8)$$

Φ denotes the flux linking the excited stator phase at the rotor position specified by the subscript. In this form, eqn. 5.8 indicates to the switched reluctance motor designer that the key parameters which must be considered when tailoring the base speed are the supply voltage, V_s , and the number of turns per phase, N_{ph} .

5.3.2 Commutation.

The rotor angle, beyond the onset of overlap, at which negative (or zero) voltage is applied across the phase winding in order to decrease the current and flux linkage to zero is defined as the commutation angle. The commutation angle may be expressed as the product of the stator pole arc, β_s , and the commutation ratio, c , where $0 < c \leq 1$. Upon commutation, the angular duration available for the

current to decrease to zero is equal to θ_{fall} , where

$$\theta_{fall} = \beta_r - c\beta_s \quad (5.9)$$

Commutation must be delayed as much as possible in order to ‘capture’ the maximum possible area within the ideal (square current pulse) energy conversion loop. There is therefore an ideal commutation angle for each rotational speed and current level. If the ideal commutation angles are adhered to in practice, the drive efficiency is optimised and the power converter kVA rating is kept to a minimum. Here it must be stressed that the commutation angles proposed in SRDESIGN may not always be ideal. The program assumes that commutation must be delayed as much as possible but regeneration must be completely avoided. However, there may be cases where the motor performance stands to gain by delaying commutation even further. If the extra time the current has been maintained at I_m lies in the peak torque producing region, then substantially higher torque will be developed. This would overwhelm any negative torque produced as the current tail enters the generating region.

The commutation ratio prediction is dependent on the choice of the unipolar converter that powers the switched reluctance motor. Full negative volts ($-V_s$) can be impressed on a phase winding connected to the asymmetric half-bridge converter. In power converters with a split dc rail, only half the supply voltage ($-V_s / 2$) is available for commutation. A more complicated situation arises when the shared switch converter is employed. The switching algorithm which allows current control in two phase windings connected to the same switching leg was presented in chapter 1. One disadvantage of this technique is the increased current fall time in phase P1 due to the switching requirements of the adjacent phase, P2. During the current fall time in P1, negative volt loops are interspersed with zero volt loops, each time the adjacent phase P2 requires a positive volt loop to maintain the current at its rated value.

The computation of the commutation angles for the asymmetric half-bridge, split dc and shared switched converter will serve as an illustrative example. In this

example it is assumed that the motor is running below base speed, and therefore current chopping is required in order to maintain a predetermined current level. It is appropriate to derive an expression for the average voltage, V_c , that is impressed across the motor winding during chopping. The average voltage during chopping, V_c , is equal to the sum of the generated back-emf and the resistance drop in the phase windings. Faraday's law states that, at a rotational speed ω , below the base speed ω_b , the average chopping voltage V_c must satisfy

$$\lambda_{al} - \lambda_{bo} = (V_c - I_m R) \frac{\beta_s}{\omega} \quad (5.10)$$

It has also been shown that

$$\lambda_{al} - \lambda_{bo} = (V_s - I_m R) \frac{\beta_s}{\omega_b} \quad (5.11)$$

Equating 5.10 and 5.11, and rearranging to give an expression for V_c at a rotational speed below ω_b yields

$$V_c = V_s \frac{\omega}{\omega_b} + I_m R \left(1 - \frac{\omega}{\omega_b}\right) \quad (5.12)$$

A straight substitution for V in Faraday's equation gives the rate of change of flux linkage during chopping

$$\frac{d\lambda}{dt} = \frac{\omega}{\omega_b} (V_s - I_m R) \quad (5.13)$$

The time taken for the rotor to turn through the commutation angle, $c\beta_s$, is equal to $c\beta_s / \omega$. The flux linkage at commutation λ_{com} is therefore given by

$$\frac{\lambda_{com} - \lambda_{bo}}{\frac{c\beta_s}{\omega}} = \frac{\omega}{\omega_b} (V_s - I_m R) \quad (5.14)$$

or

$$\lambda_{com} = \lambda_{bo} + (V_s - I_m R) \frac{c\beta_s}{\omega_b} \quad (5.15)$$

De-energisation of the phase winding follows the chopping mode. The time, t_{fall} available for the current to fall to zero is given by

$$t_{fall} = \frac{\beta_r - c\beta_s}{\omega} \quad (5.16)$$

The equation governing the fall of flux linkage in a phase winding, connected to an asymmetric half-bridge converter is

$$\int_{\lambda_{com}}^0 d\lambda = \int_0^t (-V_s - iR) dt \quad (5.17)$$

The second term of the integral on the right hand side of the equation may be evaluated upon application of the trapezoidal rule. An expression for λ_{com} may be obtained as follows

$$\lambda_{com} = (V_s + \frac{I_m R}{2}) (\frac{\beta_r - c\beta_s}{\omega}) \quad (5.18)$$

Equating 5.15 and 5.18 yields an expression for the commutation angle, assuming an asymmetric half-bridge converter:

$$c\beta_s = \frac{V_s \beta_r + \frac{I_m R}{2} \beta_r - \omega L_{bo} I_m}{V_s (1 + \frac{\omega}{\omega_b}) + I_m R (\frac{1}{2} - \frac{\omega}{\omega_b})} \quad (5.19)$$

Should a split dc rail converter be used, eqn. 5.19 is modified, to

$$c\beta_s = \frac{\frac{V_s}{2} \beta_r + \frac{I_m R}{2} \beta_r - \omega L_{bo} I_m}{\frac{V_s}{2} (1 + \frac{\omega}{\omega_b}) + I_m R (\frac{1}{2} - \frac{\omega}{\omega_b})} \quad (5.20)$$

Upon commutation, the average negative voltage V_{neg} that is impressed on a phase

winding connected to a shared switch converter is given by

$$V_{neg} = V_s - V_c \quad (5.21)$$

Substituting for V_c (see eqn. 5.12),

$$V_{neg} = (V_s - I_m R)(1 - \frac{\omega}{\omega_b}) \quad (5.22)$$

V_{neg} arises because the lower switching device, to which the commutated phase is connected, is off whereas the top switching device is chopping. The top switching device is shared with the adjacent phase which carries the rated current.

The equation that governs the fall of flux linkage is given below:

$$\lambda_{com} = \{(V_s - I_m R)(1 - \frac{\omega}{\omega_b}) + \frac{I_m R}{2}\}(\frac{\beta_r - c\beta_s}{\omega}) \quad (5.23)$$

Equations 5.15 and 5.23 may be equated and rearranged to yield an expression for the commutation angle, assuming a shared switch converter

$$c\beta_s = \frac{V_s \beta_r (1 - \frac{\omega}{\omega_b}) - I_m R \beta_r (\frac{1}{2} - \frac{\omega}{\omega_b}) - L_{bo} I_m \omega}{V_s - \frac{I_m R}{2}} \quad (5.24)$$

This section has illustrated how an SRDESIGN routine can be employed to automatically compute the phase current commutation angle at any speed ω , chopping current level, I_m , and supply voltage V_s . The user does, however, reserve the option of manually specifying the commutation angles, as an attempt to further optimise the torque production capability of a motor design.

5.3.3 Maximum speed for a given current.

Once the stator and rotor poles begin to overlap, the motor back-emf increases substantially and, depending on the running speed, can limit or decrease the current. It is therefore desirable to increase the current to the desired value before

the onset of overlap. Speed limit ω_{max1} is computed on this basis, and represents the maximum speed at which current of magnitude I_m can be switched in (but not necessarily out of) the winding at the specified supply voltage. Similar considerations must be adopted for commutation. Negative motoring torque is avoided if phase current I_m is reduced to zero before the rotor poles move beyond alignment, into the generating region. If necessary, commutation may be brought forward to $c = 0$ (i.e. $\theta_{com} = \theta_{bo}$). This defines a second speed limit ω_{max2} . The maximum speed routine compares ω_{max1} and ω_{max2} and warns the user of the smaller speed limit for the chosen current level.

The algorithm chosen to compute the maximum speed limit depends on the type of converter employed in the switched reluctance drive and on the switching technique adopted, that is, whether the firing and commutation angles are fixed by the drive electronics or calculated by the SRDESIGN program.

5.3.4 Variation of current with angle.

The current profile can be predicted, having specified the current chopping level and running speed. The time, t_r , taken for the current to rise to a specified value is computed using

$$\int_0^{\lambda_r} d\lambda = \int_0^{t_r} V_s dt - R \int_0^{t_r} i dt \quad (5.25)$$

where λ_r lies between λ_{un} and λ_{bo} . The trapezoidal rule is used to compute the second integral on the right hand side. The time interval, t_r , can be expressed as a function of rotor angle and rotational speed,

$$t_r = \frac{\theta_r}{\omega} \quad (5.26)$$

When the rotational speed, ω , is lower than the base speed, ω_b , the phase current rises to the predetermined chopping level and maintains a 'flat top' until it is commutated. At commutation,

$$\lambda_{com} - \lambda_{bo} = (V_c - I_m R) \frac{c\beta_s}{\omega} \quad (5.27)$$

If the rotational speed is higher than the base speed, the switched reluctance motor back-emf exceeds the supply voltage in the overlap region and, as a result, causes the current to decay though the flux linkage increases. At the onset of overlap the program enters a time stepping algorithm which estimates the phase current and winding flux linkage during the angular period $c\beta_s$.

This time stepping algorithm, which was written in a general format, is also used to predict the current fall in the phase winding during the commutation period ($\beta_r - c\beta_s$).

5.3.5 Time stepping algorithm for current prediction.

The variation of phase current with time must always obey Faraday's law

$$V_s = iR + \left. \frac{\partial \lambda(i, \theta)}{\partial \theta} \right|_{i=const.} \frac{d\theta}{dt} + \left. \frac{\partial \lambda(i, \theta)}{\partial i} \right|_{\theta=const.} \frac{di}{dt} \quad (5.28)$$

The second term on the right represents the motor back-emf, Vb . The rate of change of flux linkage with current at a specified rotor position is otherwise known as the incremental inductance, L_{inc} . Equation 5.28 can therefore be rewritten as

$$V_s = iR + Vb + L_{inc} \frac{di}{dt} \quad (5.29)$$

The discrete time equivalent of eqn. 5.29 may be obtained by taking finite differences to give

$$V_s = i_t R + Vb_t + L_{inc} \frac{i_t - i_{t-1}}{t_{si}} \quad (5.30)$$

where t_{si} represents the discrete time (sampling) interval. Solving for the phase current i_t , at time t ,

$$i_t = \frac{(V_s - Vb_t)t_{si}}{Rt_{si} + L_{inc}} + \frac{L_{inc}i_{t-1}}{Rt_{si} + L_{inc}} \quad (5.31)$$

In the overlap region, and at a specified current level, the back-emf of a non-saturated motor is constant. The back-emf constant, k , can be found by evaluating the gradient of the λ / θ characteristic at that current level. Therefore, the back-emf is equal to

$$Vb = \frac{\lambda_{al} - L_{bo}I_m}{\beta_s} \omega \quad (5.32)$$

or, in the customary dc machine equation format

$$Vb = k\omega \quad (5.33)$$

This quantity plus the resistive drop may be regarded as the applied voltage that would be required to maintain the specified current value constant at a given speed.

The back-emf of a saturated motor varies with position in the overlap region. The variation of flux linkage with rotor position is described by a linear followed by a sigmoidal function. At a specified current level, the corresponding λ / θ diagram is drawn with the aid of the ‘Gauss routine’ and the gradient of the λ / θ curve is then computed at a given rotor position to give k .

Information on the incremental inductance, L_{inc} , is also needed to predict the phase current value, i_t . In the overlap region and at constant excitation, the incremental inductance of a non-saturated motor increases linearly with position from L_{bo} to L_{al} . A PASCAL routine has been written to interpolate between aligned λ / i data imported from FEA, in order to compute λ_{al} at any phase current value. At the operating point ($i[t-1], \lambda[t-1]$),

$$L_{inc} = L_{bo} + r(L_{al} - L_{bo}) \quad (5.34)$$

where the ratio r is expressed as

$$r = \frac{\lambda[t-1] - i[t-1]L_{bo}}{\lambda_{ai} - i[t-1]L_{bo}} \quad (5.35)$$

The incremental inductance of a saturated motor is found by computing the gradient of the λ / i diagram at the required rotor position and phase current value.

SRDESIGN generates three arrays namely *Aphase*, *Iphase* and *Fphase* which contain instantaneous values for rotor position, phase current and winding flux linkage respectively.

5.4 Computation of output power and losses.

5.4.1 Computation of the rms phase current I_{rms}

The profile of the phase current pulse is defined by two arrays, namely *Iphase[count]* and *Aphase[count]*, which contain values for the instantaneous current magnitude and the corresponding rotor angle.

The equation of the line joining two consecutive points (*Aphase[count]*, *Iphase[count]*) and (*Aphase[count+1]*, *Iphase[count+1]*) is arranged in the form

$$I_{prof}(\theta) = M\theta + C_o \quad (5.36)$$

where M denotes the profile slope

$$M = \frac{Iphase[count+1] - Iphase[count]}{Aphase[count+1] - Aphase[count]} \quad (5.37)$$

and C_o is the zero crossing.

Equation $I_{prof}(\theta)$ is squared and integrated with respect to the rotor angle. The process is repeated for all values of variable 'count', from count = 0 to count = *Tcount*. The integrals are summed and the total is divided by the phase current repetition angle, before finally taking the square root, i.e.

$$I_{rms} = \sqrt{\frac{\sum_{count=0}^{Tcount-1} (\int I_{prof} d\theta)}{\frac{2\pi}{N_r}}} \quad (5.38)$$

5.4.2 Copper losses.

The switched reluctance motor copper losses, P_{Cu} , may be computed from

$$P_{Cu} = I_{rms}^2 R q \quad (5.39)$$

where q represents the number of phases. The phase winding resistance, R , is given by

$$R = \rho \frac{l_w}{A_w} \quad (5.40)$$

where l_w denotes the copper wire length and A_w its cross-sectional area.

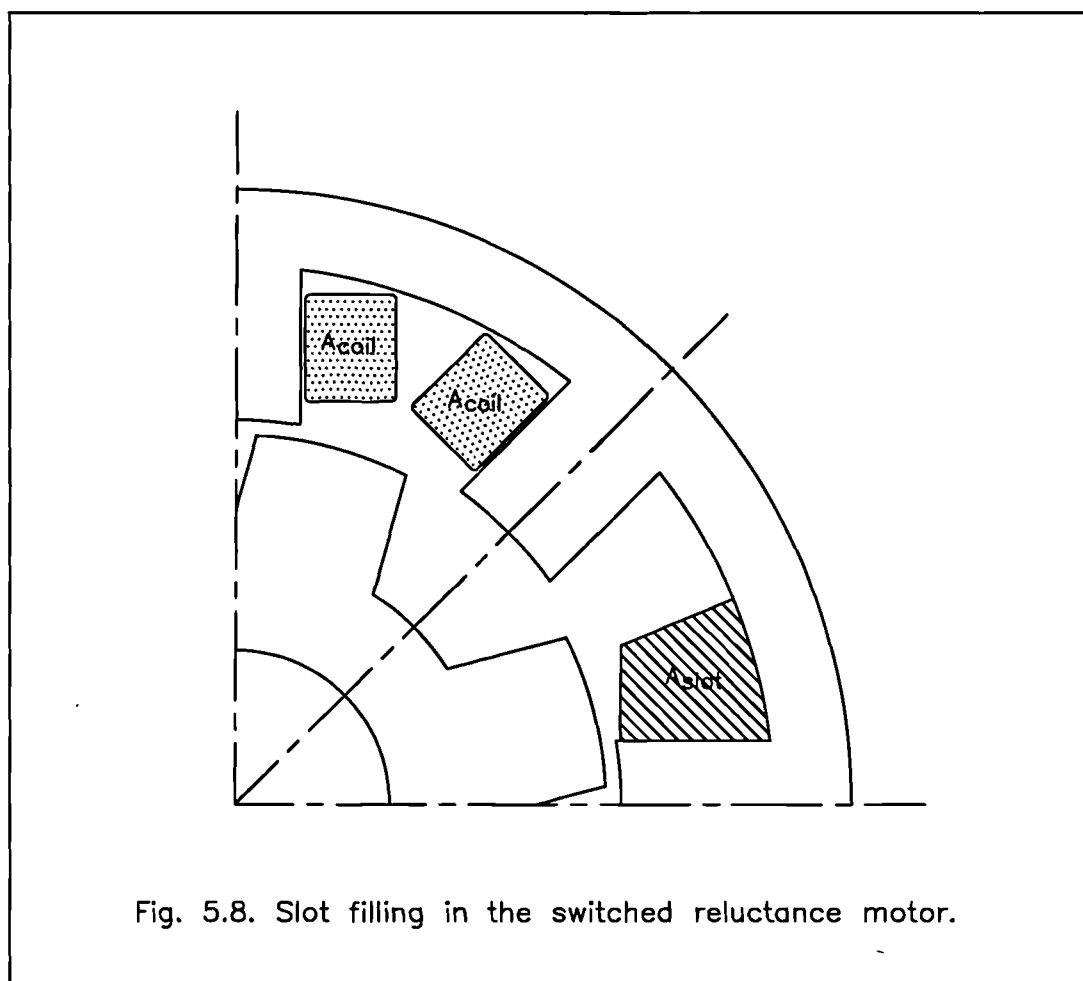
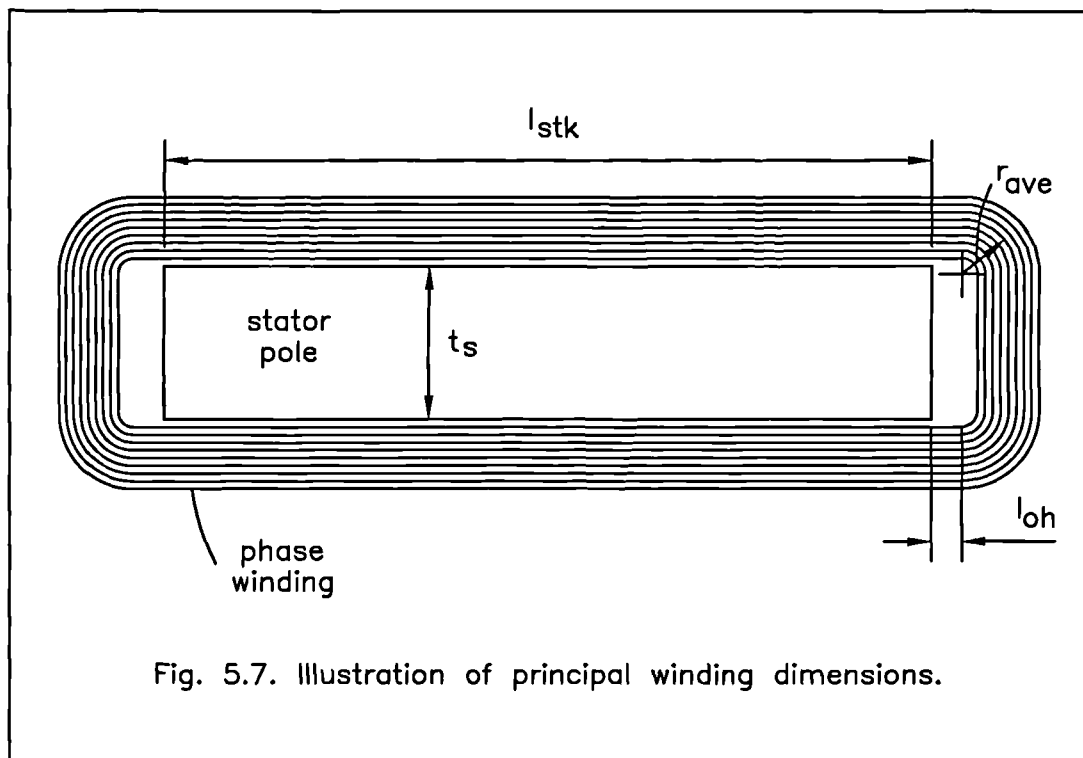
An average turn length of copper wire, l_{ave} , wound around the stator tooth is considered in order to compute the total length of the phase winding. Referring to fig. 5.7,

$$l_{ave} = 2l_{stk} + 4l_{oh} + 2t_s + 2\pi r_{ave} \quad (5.41)$$

and

$$l_w = N_{ph} l_{ave} \quad (5.42)$$

The slot area, A_{slot} of the motor is also calculated and, for a specified number of turns, the maximum (standard) copper wire diameter is estimated. An empirical approach to the slot fill factor computation is taken. In production, switched reluctance motor coils can be pre-wound and slid over the poles without interfering with each other, as shown in fig. 5.8. Hence the actual coil area A_{coil} is compromised. Each wire takes up a slot area fractionally higher than the area of



a square with a side equal to the wire diameter. This accounts for the insulating varnish coating the copper wire. The coil fill factor K_c , is therefore equal to

$$K_c = \frac{\pi r_w^2}{4(r_w + t_v)^2} = 0.7 \quad (5.43)$$

where r_w denotes the copper wire radius and t_v the thickness of the varnish. The overall slot fill factor, K_s , is equal to

$$K_s = \frac{K_c A_{coil}}{A_{slot}} \quad (5.44)$$

This parameter works out to approximately 0.4 for a 4-phase machine, but increases with increasing number of stator poles. It is also acknowledged that methods may be found by which the fill factor is increased. The SRDESIGN package therefore allows the user to input the copper wire diameter from the keyboard, should one choose to do so.

The resistivity of copper, ρ , is a function of the operating temperature θ_{op} . R increases with temperature at the rate of about 20% for every 50°C rise in the copper windings according to

$$R_{op} = R_{20^\circ C} [1 + \alpha(\theta_{op} - \theta_{20^\circ C})] \quad (5.45)$$

where α denotes the temperature coefficient of resistance of copper. The program computes $R_{20^\circ C}$ and R_{op} given a nominal operating temperature. The skin effect is neglected.

5.4.3 Iron losses.

Hysteresis losses, P_h , can be expressed as

$$P_h = \frac{K_h B_{max}^n f}{\rho} \quad (5.46)$$

where B_{max} is the maximum flux density in the iron, ρ is the mass density of iron

and K_h is the hysteresis constant [59]. This expression holds for a system excited with a sinusoidal waveform of frequency f . The exponent n may not necessarily be constant.

Eddy current losses are expressed as

$$P_e = \frac{K_e B_{\max}^2 f^2}{\rho} \quad (5.47)$$

where K_e is the eddy current constant.

Loss data in W/Kg for different lamination materials is provided by the manufacturers for frequencies ranging from 50 to 500Hz. These curves were used to obtain constants K_e and K_h . Exponent n was found to be a second order function of the flux density B , yielding values between 1.5 and 2.5 in the region of 0 to 2T. Hence, a general analytical expression was formed, predicting core losses at any excitation frequency, and assuming the iron to be excited with sinusoidal (alternating) current. In the switched reluctance motor the flux waveforms in different parts of the magnetic circuit are non-sinusoidal, and as a result, an error in the calculation of the iron losses is expected.

Hysteresis and eddy current losses are calculated from eqns. 5.46 and 5.47 in W/Kg and multiplied by the weight of the iron of the respective magnetic circuit section. This procedure requires some information on magnetic circuit parameters. The 'active' (or 'excited') volume of iron, V_{act} , is equal to

$$V_{act}[section] = l[section] A[section] l_{stk} \quad (5.48)$$

where $l[section]$ and $A[section]$ represent the length and cross-sectional area of different sections of the magnetic circuit (such as the stator pole and stator yoke). The program incorporates a routine to compute V_{act} based on the motor winding configuration (short or long flux paths).

5.4.4 Output power, input power and efficiency.

The area A_o enclosed by the operating trajectory on the flux linkage / current diagram of the switched reluctance motor system is equal to the electrical energy per 'stroke' that is converted to mechanical work. The net power delivered by the motor shaft is given by

$$P_{out} = A_o \left(\frac{qNr}{2\pi} \right) \omega - P_{fw} - P_{Fe} \quad (5.49)$$

where P_{fw} denotes friction and windage loss and P_{Fe} is the sum of hysteresis and eddy current losses. The average torque output is expressed as

$$T_{ave} = \frac{P_{out}}{\omega} \quad (5.50)$$

In each working stroke, energy is delivered to the switched reluctance motor from the power supply during the transistor conduction period. A proportion of the total energy supplied is converted to mechanical work during this period while the remainder is stored in the magnetic field. During the diode conduction period, some of the stored field energy is converted to mechanical work and the remainder, A_r , is returned to the power supply. It is not possible to convert all the electrical energy supplied during one working stroke to mechanical work. The ratio of the energy converted to mechanical work, A_o , to the electrical energy supplied in each working stroke is known as the energy ratio, E [7].

$$E = \frac{A_o}{A_o + A_r} \quad (5.51)$$

This ratio is computed in the SRDESIGN package because it reveals information on the rating of the power converter.

The total power input to the motor may be computed by summation of all power loss components of the system, P_{loss} , and the power made available to the motor shaft, P_{out} .

$$P_{in} = P_{out} + P_{loss} \quad (5.52)$$

where

$$P_{loss} = P_{Cu} + P_{Fe} + P_{fw} \quad (5.53)$$

The motor efficiency is given by

$$n = \frac{P_{out}}{P_{out} + P_{in}} \quad (5.54)$$

5.5 Structure of the SRDESIGN package.

The implementation of the modelling theory presented in previous sections has made use of the modular (or ‘unit’) structure within Turbo Pascal. This has helped to subdivide the programming task to manageable sections. The contents and purpose of each unit will now be described in brief.

5.5.1 Unit CONSTANT.

Information on the geometry of the machine and the number of turns per phase is used in this unit, in order to calculate the variation of flux linkage with current in the unaligned and aligned rotor positions. The λ / i diagram computation is based on the procedure described in [51], which applies to singly excited systems. **System** λ / i diagrams for switched reluctance motors with two phases simultaneously excited can be computed, with sufficient accuracy, using finite element analysis. Unit CONSTANT was therefore written such that the λ / i diagram can be imported from finite element analysis, should the user choose to do so. The characteristic is stored in two arrays, namely ‘Flux Linkage’ and ‘Current’.

The length of the magnetic flux pattern (short or long flux paths) is estimated and used for subsequent iron loss computations. Geometrical considerations also allow the maximum diameter of copper wire that can be used (for a given number of turns per phase) to be estimated. This information is used to compute the resistance of the phase winding at room and operating temperatures.

5.5.2 Unit CURRCALC.

The phase current and flux linkage profiles, as a function of rotor position, are computed within unit CURRCALC. Information on the maximum phase current, speed of rotation and type of converter employed in the drive is used to calculate optimum turn-on and commutation angles. Alternatively these parameters can be keyed in.

Subsequently, the variation of current and flux linkage with rotor position is predicted within a time stepping algorithm, based on the theory presented in sections 5.1-5.3. At each time step, the values of the rotor angle, phase current and winding flux linkage are stored in arrays *Aphase*, *Iphase*, *Fphase*. Unit CURRCALC could be thought of as the 'heart' of SRDESIGN.

5.5.3 Unit DRAW.

This unit makes use of pre-written graphic routines within Turbo Pascal in order to display graphics on the screen. A plot of any two arrays of the same size against each other may be created, displayed on the screen and subsequently sent to a printer if required. The plot facility features automatic scaling of the axes. The unit was written in a general format such that plots of the variation of all major parameters with speed (such as torque) and rotor angle (such as flux linkage) may be obtained.

5.5.4 Unit GLOBALS.

All variable and constant definitions are included in this unit, and it is accessed by all other units including the main (control) program.

5.5.5 Unit INPUTS.

Unit INPUTS allows the user to interactively key in the geometry of the machine which is to be analyzed. Information on the power converter configuration and rating is also essential. A machine design may be stored as a file on / or retrieved from the disk. A built-in facility checks the machine design for errors and prompts the user for corrections.

5.5.6 Unit MENUS.

Unit MENUS comprises four procedures that activate and display an 'Input Panel Menu', an 'Operating Conditions Menu' and two 'Results Menus'. The 'Input Panel Menu' lists user options regarding data input from the keyboard or disk, such as motor geometry entry and modification. The 'Operating Conditions Menu' prompts the user to specify the operating speed (or range of) and maximum phase current for the present run. Presentation of results and user options for a 'single' or 'batch' run are controlled within the appropriate 'Results Menu'.

5.5.7 Unit RESULTS.

Program results may either be displayed on the screen or sent to a printer. In 'batch mode' the motor performance is predicted, for a specified maximum phase current value, at a range of speeds. The program tabulates results, indicating the variation of rms phase current, average torque, total machine losses and efficiency with speed. A 'single run' examines the motor performance at a specified motor speed and maximum phase current. A detailed results file is provided for a single

run, listing additional information on phase winding resistance, average flux density values in the iron parts and commutation angle(s).

5.5.8 Main Program.

The main program acts as a data flow controller. Data flow control is achieved by sequentially calling key procedures within the units. The program also contains short procedures which use data supplied from units INPUT, CONSTANT and CURRCALC to compute the average torque, power output, power losses and machine efficiency.

5.6 Summary.

This chapter presented the 'back bone' theory supported in SRDESIGN. SRDESIGN is used for sizing and dynamic simulation of the switched reluctance motor. The program is capable of computing the motor magnetisation curves using internal (analytical) routines (ref. Unit CONSTANT). However, it does also offer the facility of importing the curves from finite element analysis.

The λ / θ characteristic is subsequently computed within SRDESIGN. At low excitations the λ / θ diagram is approximated by a linear function. At higher excitations, a set of linear and sigmoidal functions are calculated to accurately define the variation of flux linkage with rotor position. These observations and the resulting mathematical formulations are the product of extensive finite element modelling of the switched reluctance motor.

The phase current and flux linkage variation with rotor position is estimated with the aid of a time stepping algorithm within Unit CURRCALC, having specified the current chopping level I_m and operating speed.

The area enclosed by the operating trajectory described on the λ / i diagram yields

the average torque developed in the motor. Program MAINSR includes a procedure to calculate this. MAINSR also includes procedures to calculate motor losses and efficiency. SRDESIGN is thought to be a valuable tool to a switched reluctance motor designer. At the design stage the performance of a motor may be completely characterised within minutes. The geometry of the motor (stator / rotor pole width, rotor diameter etc) can then be altered to improve its performance. More accurate results from a 'reasonable' design may subsequently be sought by obtaining a finite element model of the motor and importing magnetisation curves into SRDESIGN. This is advisable in cases where a switched reluctance motor operating with two phases simultaneously excited is examined.

Chapter 6

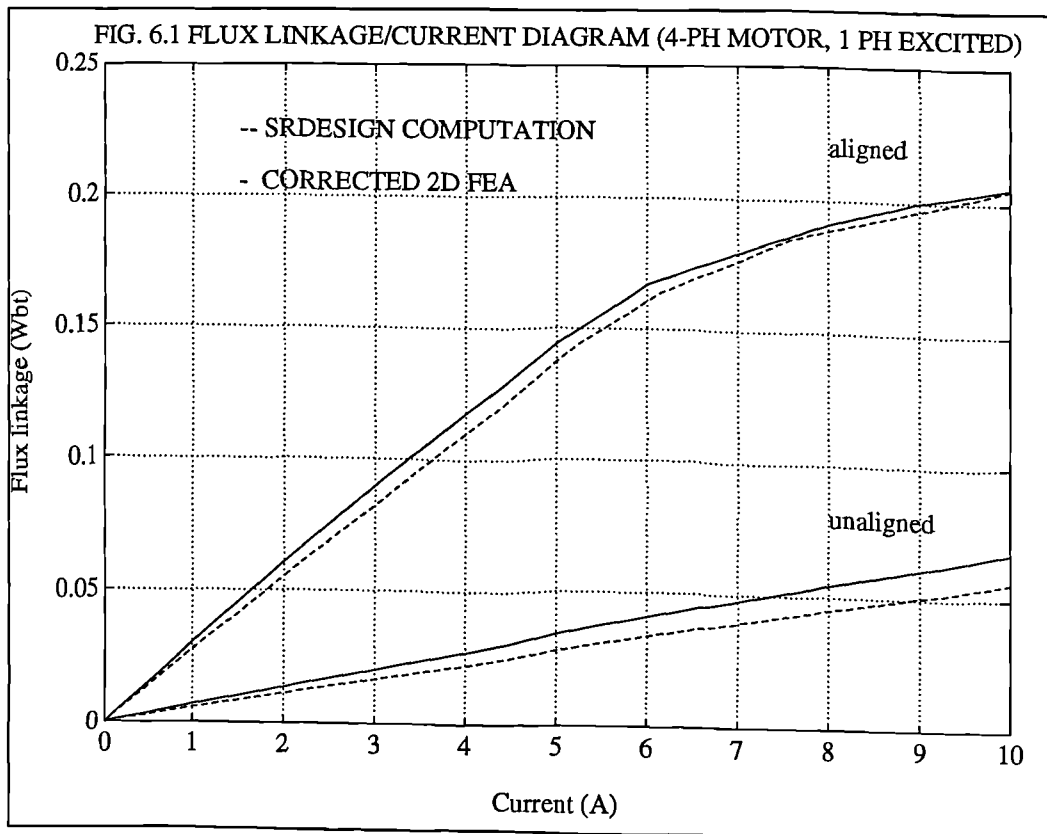
SRDESIGN VERIFICATION: DYNAMIC TESTING OF SWITCHED RELUCTANCE MOTORS

The previous chapter described in detail the ‘back bone’ structure of SRDESIGN. The accuracy of this dynamic simulation program was verified by testing the switched reluctance machines that were available in the laboratory: a 150W 4-phase motor and a 4kW 7-phase motor. This chapter will present a comparison of simulated data and experimental results obtained from these machines. The strengths and weaknesses of SRDESIGN, which was used for the design of the 5-phase prototype, are identified.

6.1 The use of λ / i diagrams in SRDESIGN.

Chapter 3 demonstrated that when modelling switched reluctance motors with two phases excited at any time, electromagnetic theory of doubly excited systems ought to be adopted. The proposed procedure of computing **system** λ / i diagrams for doubly excited switched reluctance motors was implemented using finite element analysis. The 150W 4-phase motor is operated with two phases conducting simultaneously. Therefore, λ / i diagrams at the ‘extreme’ rotor positions were imported from FEA to SRDESIGN for dynamic simulation of the experimental motor. Two-dimensional finite element modelling was used to obtain the magnetisation curves; end-core flux correction was applied, as described in chapter 4. The magnetisation (λ / i) curves at intermediate rotor positions were computed within SRDESIGN using mathematical formulations described in chapter 5. A similar procedure was adopted for the 4kW 7-phase motor configured for long or short flux loops.

In SRDESIGN, it is possible to compute λ / i diagrams at the 'extreme' (unaligned and aligned) rotor positions, for singly excited switched reluctance motors. This would be applicable to 1,2 and 3-phase motors. In order to assess the accuracy of the SRDESIGN algorithm, the λ / i diagram of the 150W 4-phase motor (assumed to operate with one phase excited at any time for comparison purposes) was computed. This was compared with the corresponding plot obtained using two-dimensional finite element analysis and corrected for end-core effects. Figure 6.1 illustrates that, at any excitation level, SRDESIGN tends to yield a lower value of flux linkage, especially in the unaligned position. However, taking into account the vast difference in computation speed (SRDESIGN yields the λ / i curve within seconds), the results are satisfactory.



6.2 Testing the 4-phase 150W motor.

6.2.1 Experimental arrangement.

The purpose of testing the 4-phase motor was to assess the accuracy of the simulation package in predicting the dynamic performance of a switched reluctance motor. The SRDESIGN algorithm that is implemented on a motor powered by an asymmetric half-bridge converter is simpler in comparison to the shared switch converter algorithm. As a first step, it was therefore thought appropriate to analyze a drive that employs an asymmetric half-bridge converter. This power converter was chosen further because it reduces the complexity of the digital controller and provides increased flexibility.

The SKM181F power MOSFETs that were made available for the research project were rated at 800V / 32A, suitable for driving a 4kW motor. The gate drive circuitry has been described in chapter 2. The on-state losses of the SKM181F modules may well have been higher than the losses that a smaller device, suitable for a 150W motor, would exhibit. This however was not considered important as the aim of the exercise was to validate a computer model and not to optimise the drive efficiency.

Rotor position sensing was present in the 4-phase drive in the form of (four) optical sensors and a shaft mounted slotted disk. This method produced a resolution of 7.5°, though this was improved with digital electronic circuits integrated into the drive controller.

The switched reluctance drive energy ratio, E , is significantly reduced when the motor is driven in saturation. It was shown by Miller [8] that in a magnetically linear motor

$$E = \frac{(\lambda_{al} / \lambda_{un}) - 1}{2(\lambda_{al} / \lambda_{un}) - 1} \quad (6.1)$$

The energy ratio improves with increasing $\lambda_{al} / \lambda_{un}$ but can never exceed 0.5. In the saturating motor an energy ratio of 0.6 - 0.7 can be achieved and this reduces the converter volt ampere requirement.

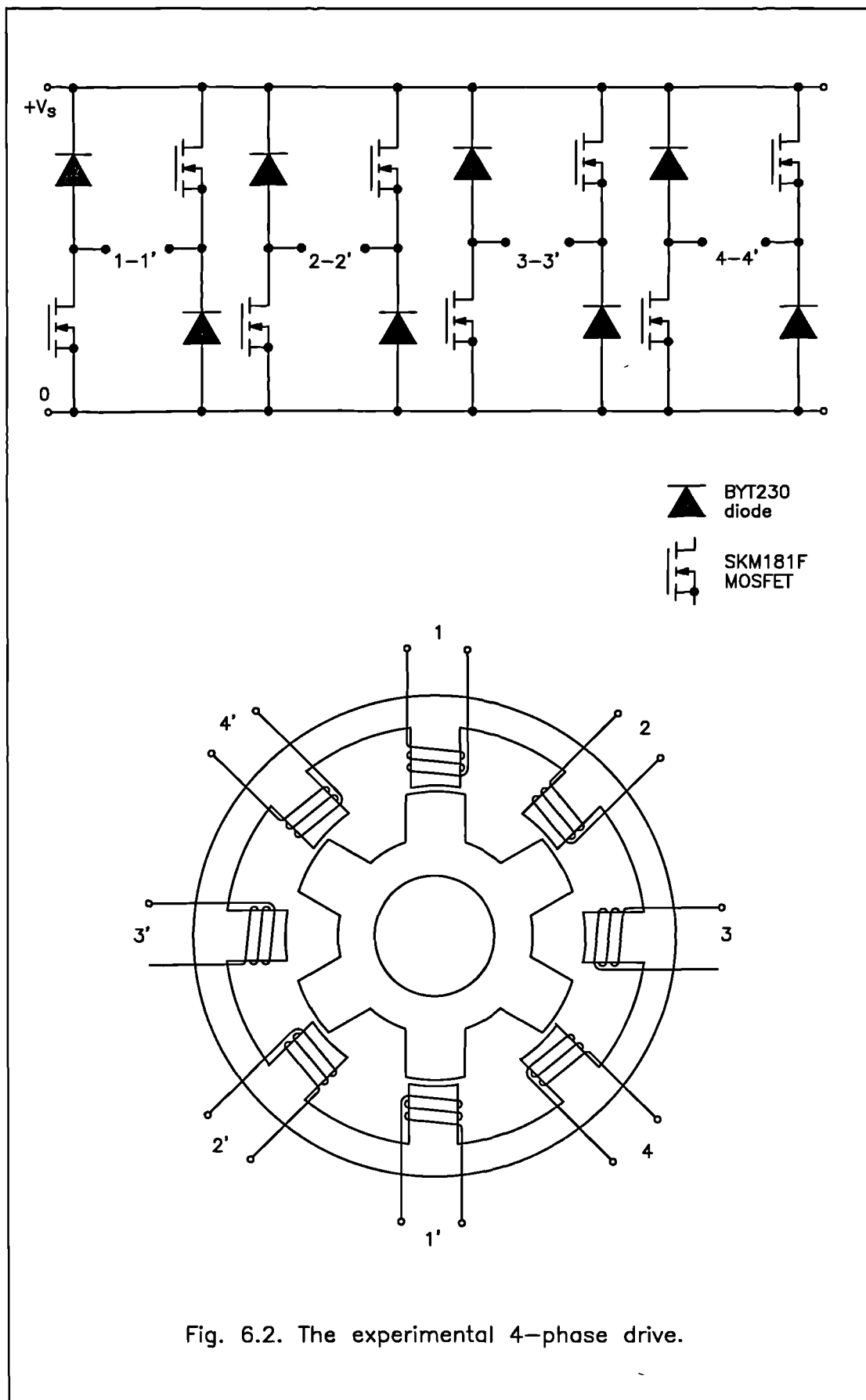
Finite element studies and flux linkage measurement indicated that the 150W 4-phase motor must be excited with a peak phase current of 10A in order to be driven into saturation. This, however, could not be achieved in practice due to thermal limitations. The frame that was constructed for the motor was not finned and no provision was made for a shaft mounted fan. As a result, heat generated by copper and iron losses was only removed by natural (and not forced) convection. The current level in the 4-phase motor winding was limited to 5A with the aid of a pwm current regulator. The pwm current regulator circuit diagram and description of operation have been presented in chapter 2. One LEM Hall effect current sensor was used for each phase winding in order to simplify current control. The experimental 4-phase drive is shown in fig. 6.2.

6.2.2 Test presentation.

A series of tests were carried out to validate the SRDESIGN program. In order to optimise the motor performance, the onset of excitation was retarded and the phase current commutation angle was varied. A selection of experimental results together with computer-aided predictions shall be presented in this section. The reader is reminded of the notation that is used throughout this section in fig. 6.3.

The predicted and experimental torque / speed curve obtained for $I_m = 5A$ $\theta_f = 1^\circ$ and $\theta_{on} = 15^\circ$ is illustrated in fig. 6.4. The power loss in the motor as a function of speed is shown in fig. 6.5. Sample SRDESIGN printouts, listing the most important operating parameters are given for a running speed of 1500rpm in Table 6.1.

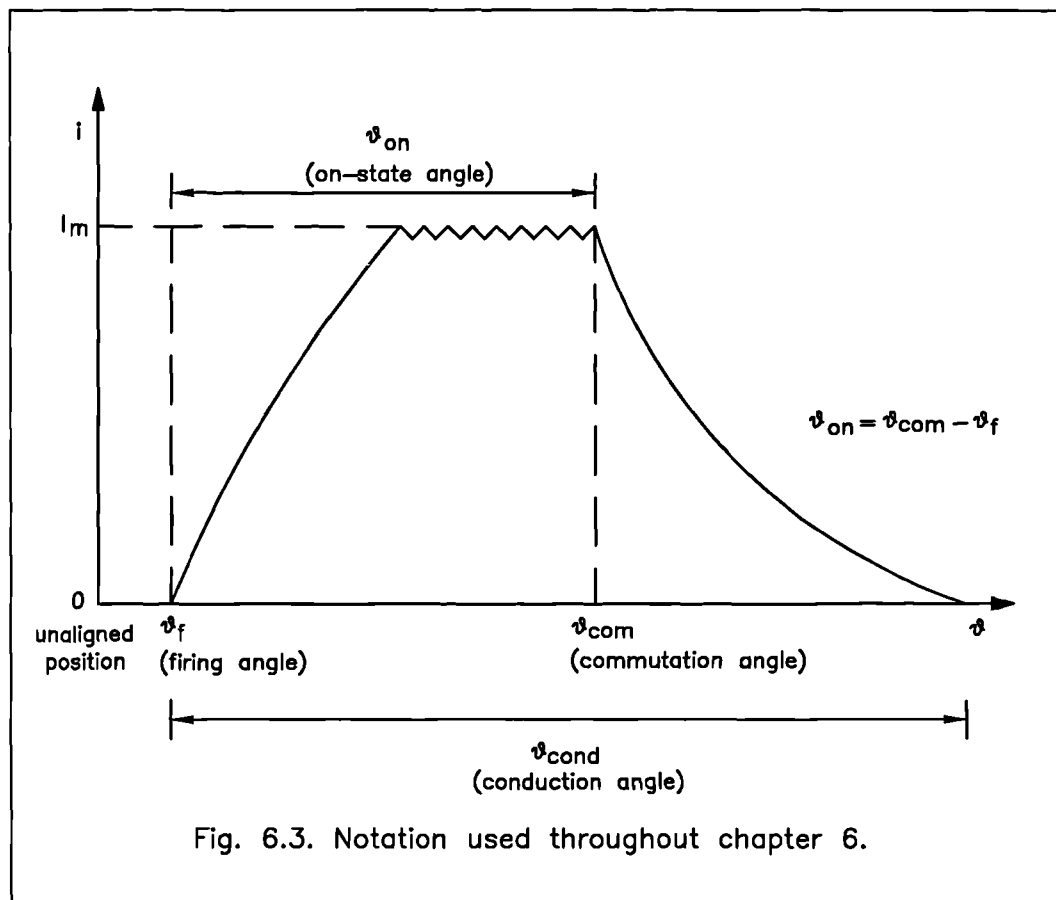
A series of tests was conducted in which the on-state angle was kept constant ($\theta_{on} = 15^\circ$, $I_m = 5A$). Measurements on the 4-phase motor were repeated for a firing



Parameter	Value	Units
Number of stator poles	8	poles
Number of rotor poles	6	poles
Air gap length at alignment	0.615	mm
Inter-polar air gap depth	9.500	mm
Rotor diameter	56.000	mm
Stator outside diameter	106.500	mm
Stator back iron width	10.000	mm
Core length	50.000	mm
Stator pole arc	0.365	rad
Rotor pole arc	0.436	rad
Shaft diameter	14.000	mm
Supply voltage	100.000	Volts
Turns per phase	220	Turns
Chosen wire diameter	Auto	
Switching strategy	Normal	
Angle control technique	Predefined	Commutation angles
Stepping mode	Single	
Winding configuration	Long flux	loops
Step angle	0.262	rad
Maximum wire diameter	0.730	mm
Actual wire diameter	0.710	mm
Resistance of each winding (at $T_{op} = 80^{\circ}\text{C}$)	2.021	Ohms
Total mass of steel	1.676	kg
Total mass of copper	0.536	kg
Minimum inductance	6.800	mH
Phase current	5.000	A
RMS phase current	2.480	A
Peak current density	12.629	A/mm/mm
RMS current density	6.264	A/mm/mm
Maximum speed at this current	2413.753	r/min
Base speed for flat topped current	3205.109	r/min
Running speed	1500.000	r/min
Commutation Ratio	0.425	
Current at commutation	5.000	A
Flux linkage at commutation	0.088	Wb Turns
Flux linkage at alignment	0.000	Wb Turns
Current at alignment	0.000	A
Average torque	0.540	Nm
Average torque per rms phasecurrent	0.218	Nm/A
Stator heat loss	49.711	W
Windage and friction losses	2.069	W
Hysteresis and eddy current losses	5.545	W
Total losses in machine	57.324	W
Bridge rating	252.423	W
Power returned to supply	110.312	W
Net power input	142.111	W
Shaft power output	84.787	W
Efficiency	59.662	%
Energy ratio	0.336	
No. of phases conducting at one time	1	phases
Flux density in stator poles	0.835	T
Flux density in air gap	0.706	T
Flux density in rotor poles	0.716	T
Flux density in rotor body	0.377	T
Flux density in stator yoke	0.434	T

Table 6.1. Sample SRDESIGN printout for the 150W 4-phase motor.

angle of $\theta_f = 0^\circ$ to $\theta_f = 5^\circ$. At low speed it was found that for approximately equal losses, higher average torque is obtained by retarding the excitation. As the speed increased, it was more beneficial to impress the supply voltage across the phase winding early so as to allow sufficient time for the current to rise to I_m . Figure 6.6 illustrates the maximum torque / speed characteristic that was derived from this exercise. A similar experiment was performed for $I_m = 5\text{A}$, $\theta_{on} = 20^\circ$; figure 6.7 shows the resulting maximum torque / speed curve.



Two simulated phase current pulses are shown in fig. 6.8 and compared with measurement at a rotor speed of 450rpm and 1500rpm. The current pulse on-state angle, θ_{on} , was set to 15° . The simulated λ / θ and λ / i curves at 450rpm are also illustrated in fig. 6.9a,b respectively.

FIG. 6.4 TORQUE / SPEED CURVE (4-PH MOTOR, FIXED COMMN ANGLES)

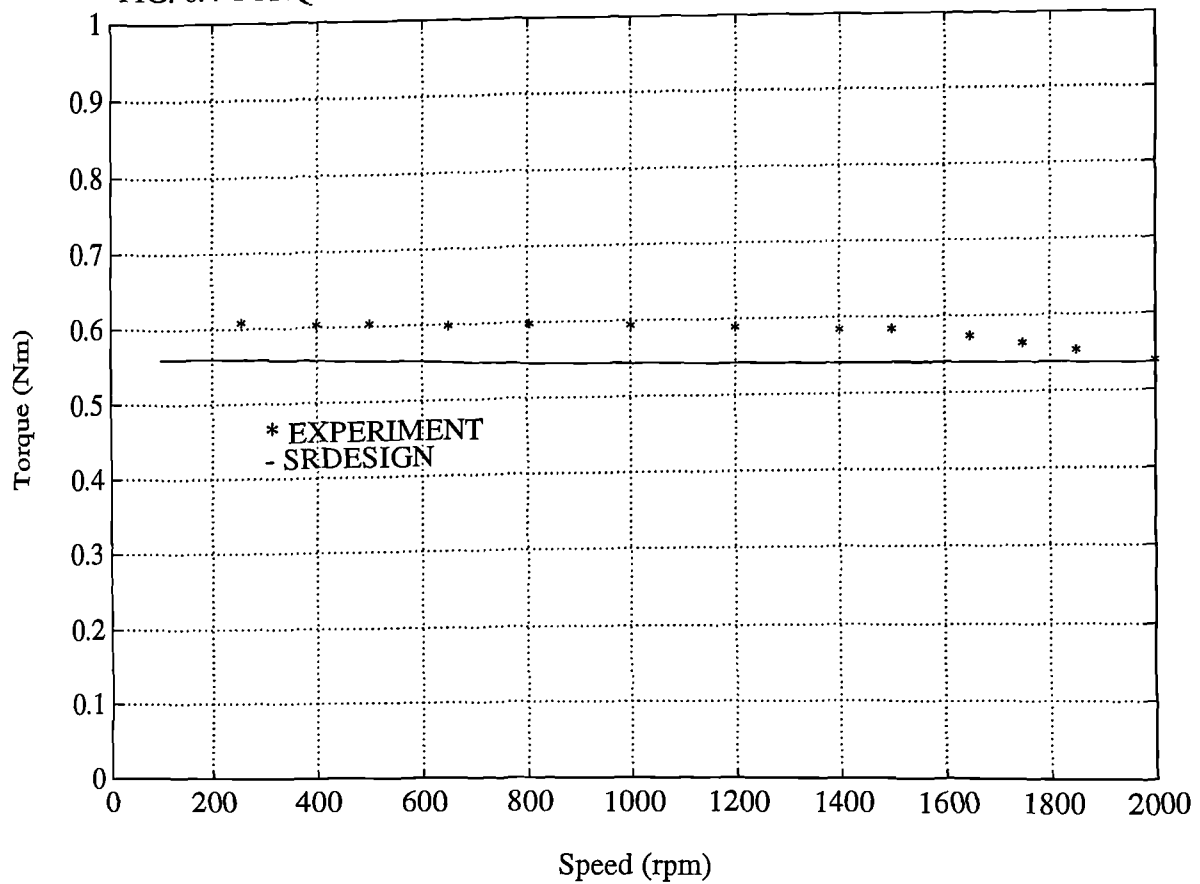


FIG. 6.5 POWER LOSS IN THE 4-PH MOTOR (FIXED COMMN ANGLES)

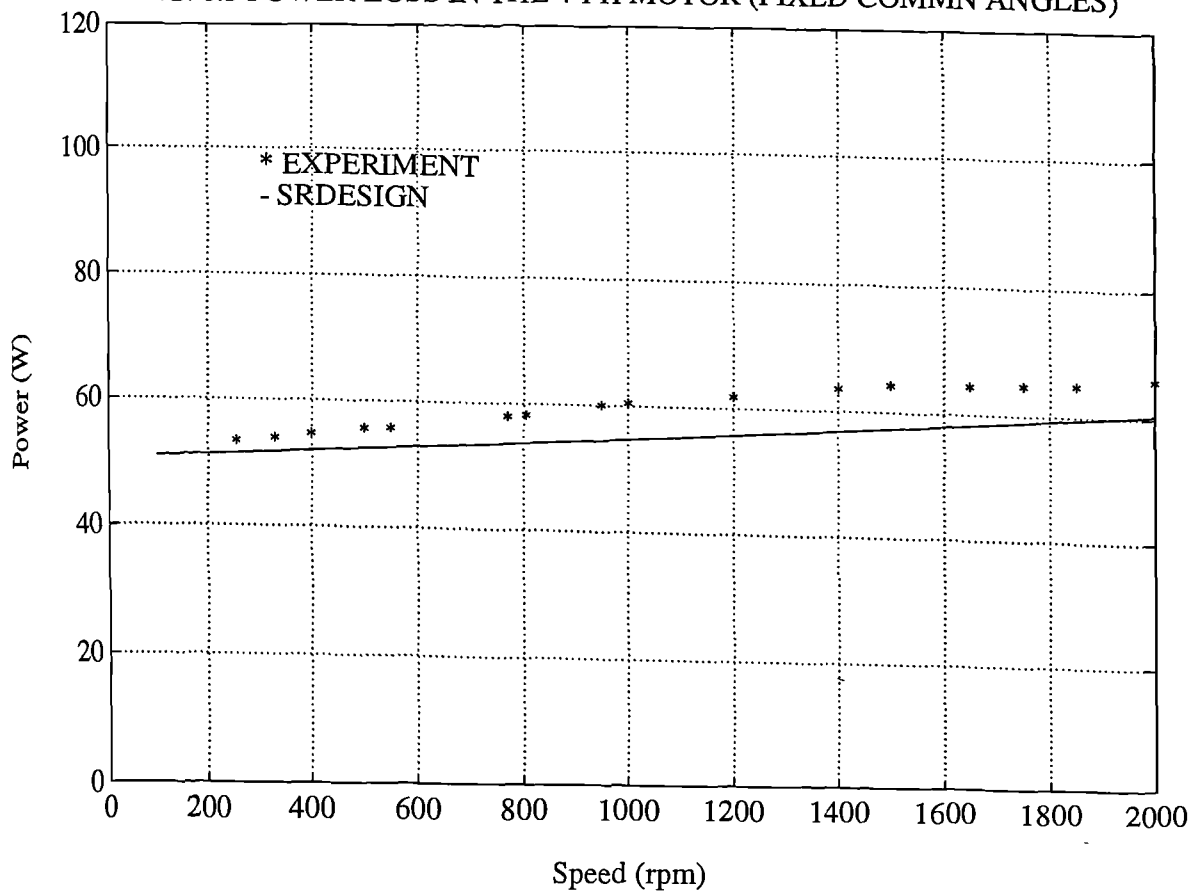


FIG. 6.6 MAX.TORQUE/SPEED CHARACTERISTIC (4-PH,CONDN PERIOD=15 DEG.)

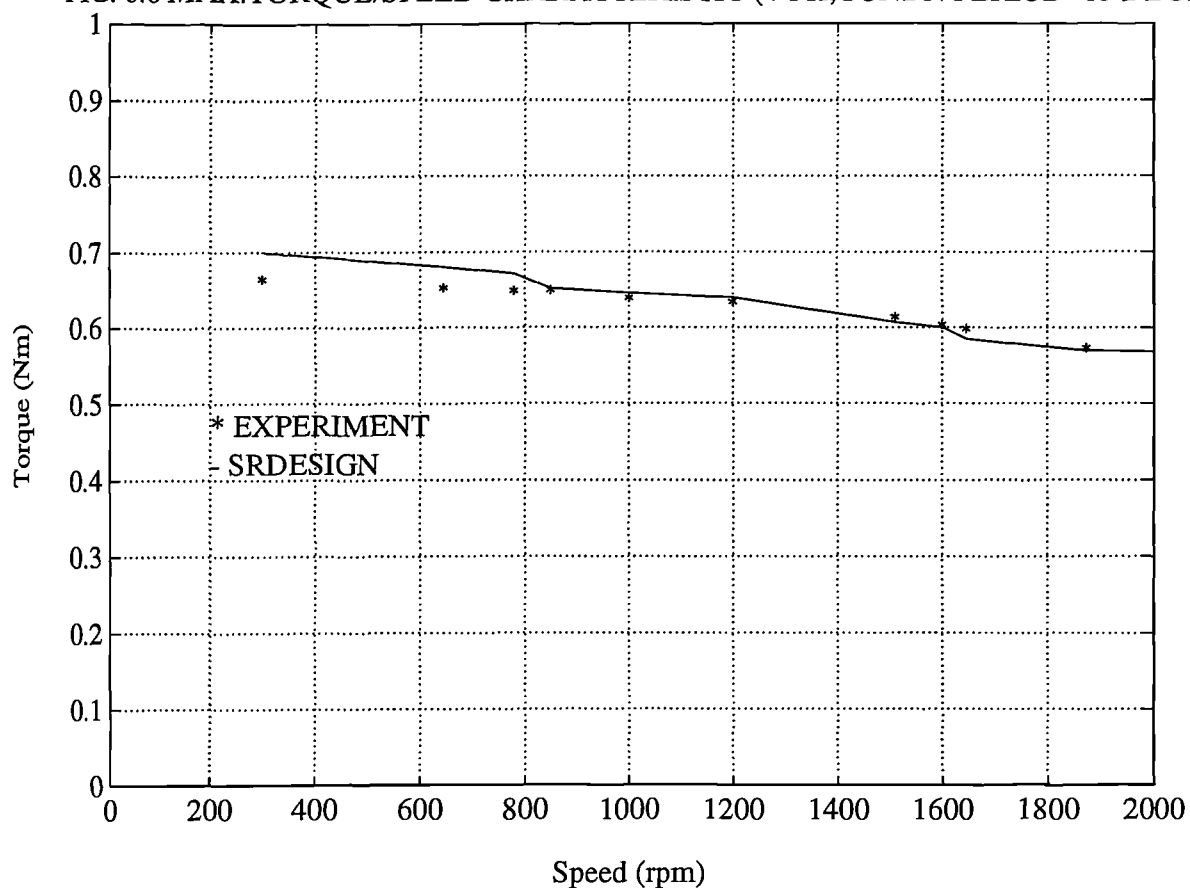
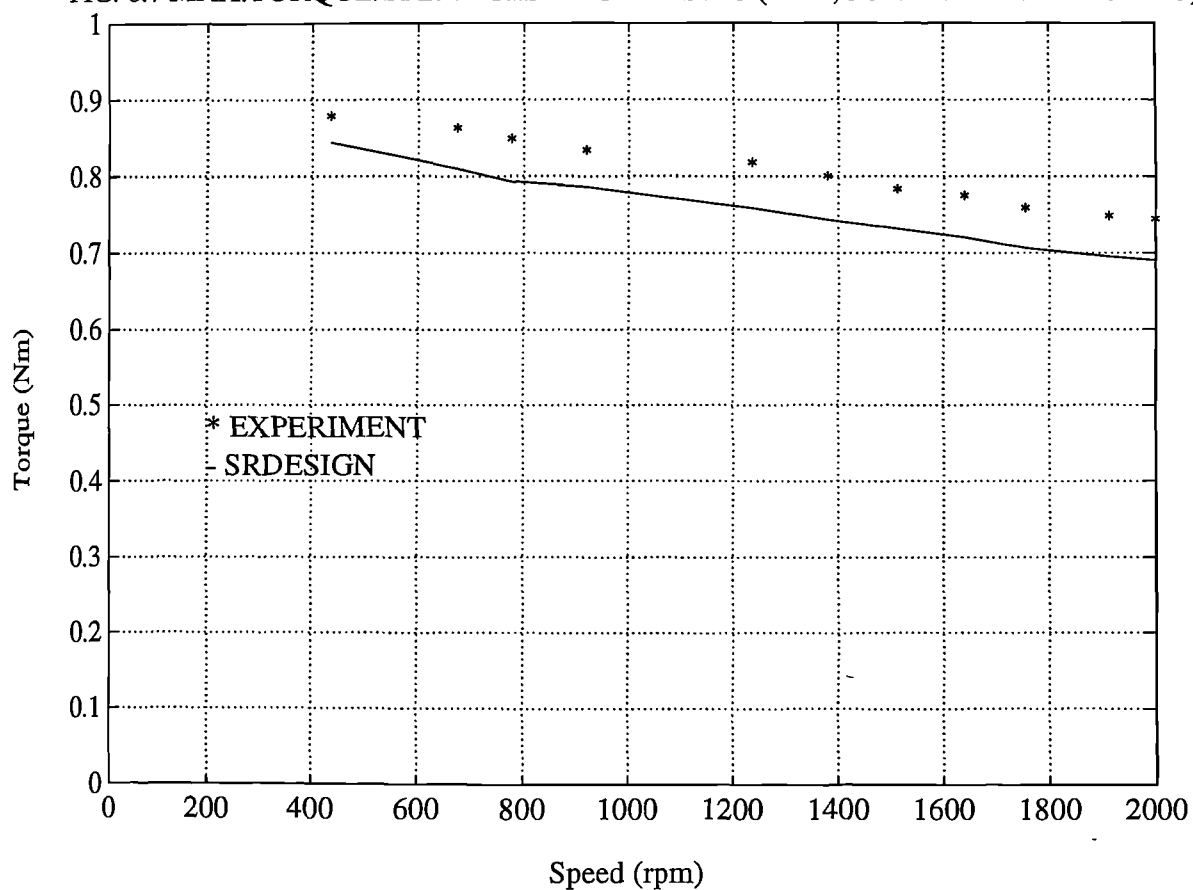


FIG. 6.7 MAX.TORQUE/SPEED CHARACTERISTIC (4-PH,CONDN PERIOD=20 DEG)



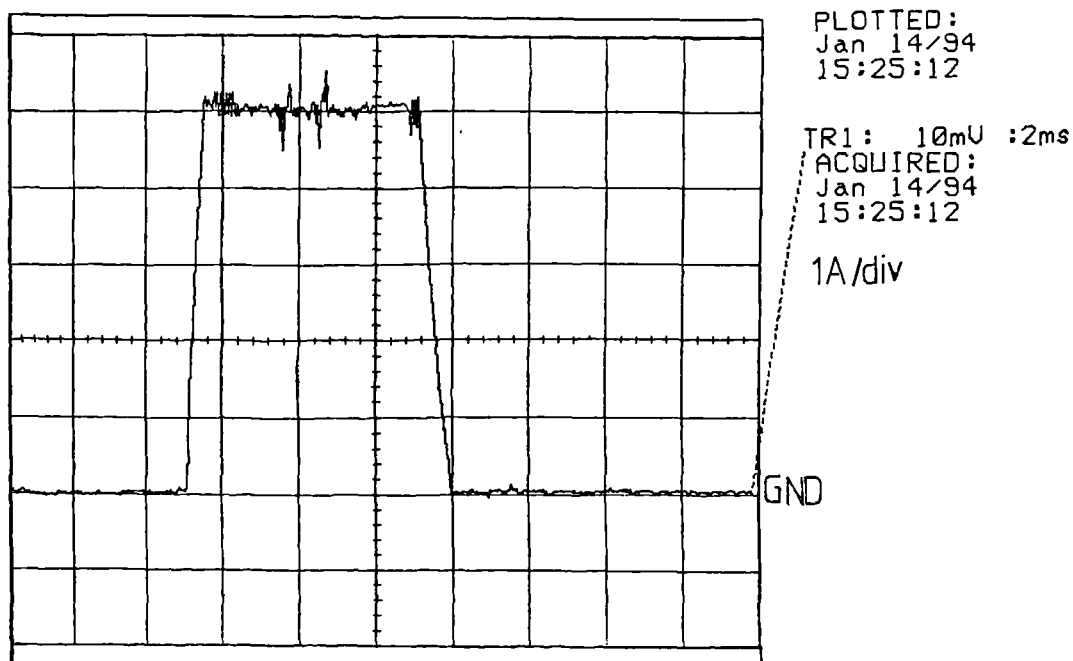


Fig. 6.8a Experimental i / θ profile @ 450rpm.

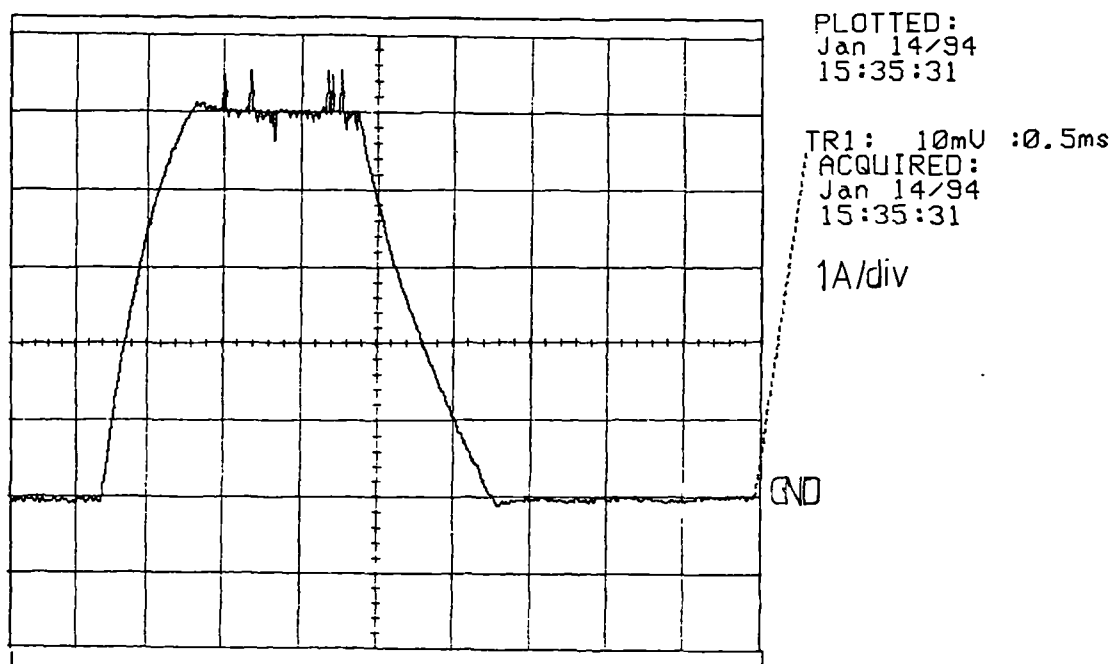


Fig. 6.8b Experimental i / θ profile @ 1500rpm.

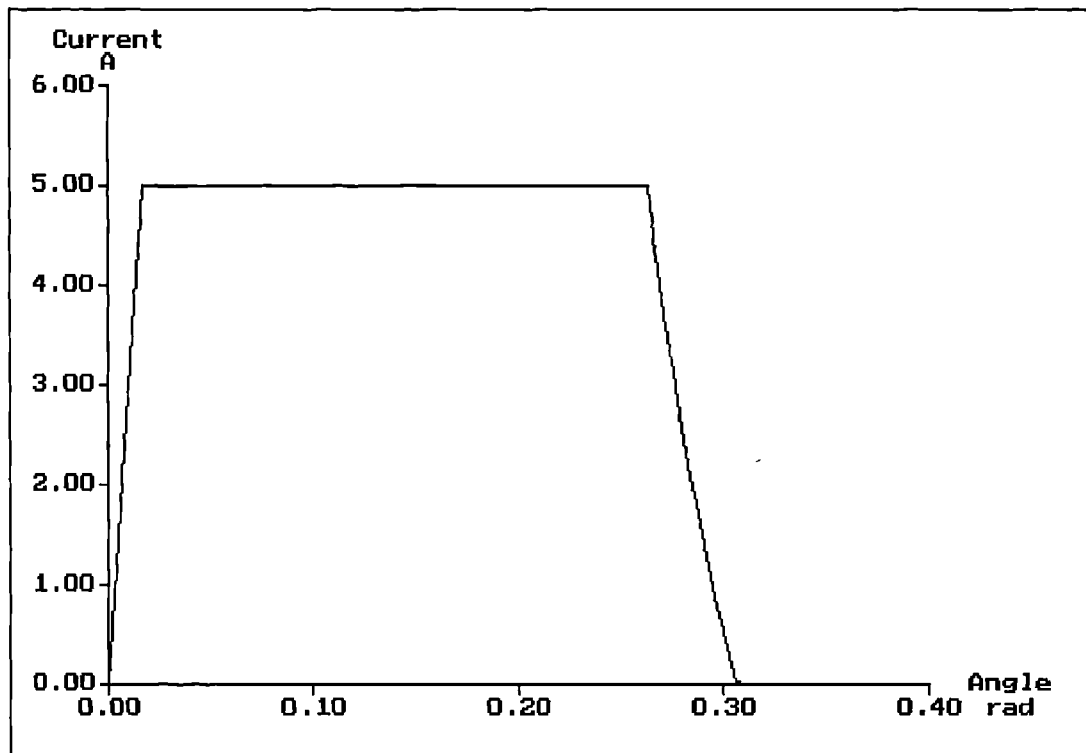


Fig. 6.8c SRDESIGN i / θ profile @ 450rpm.

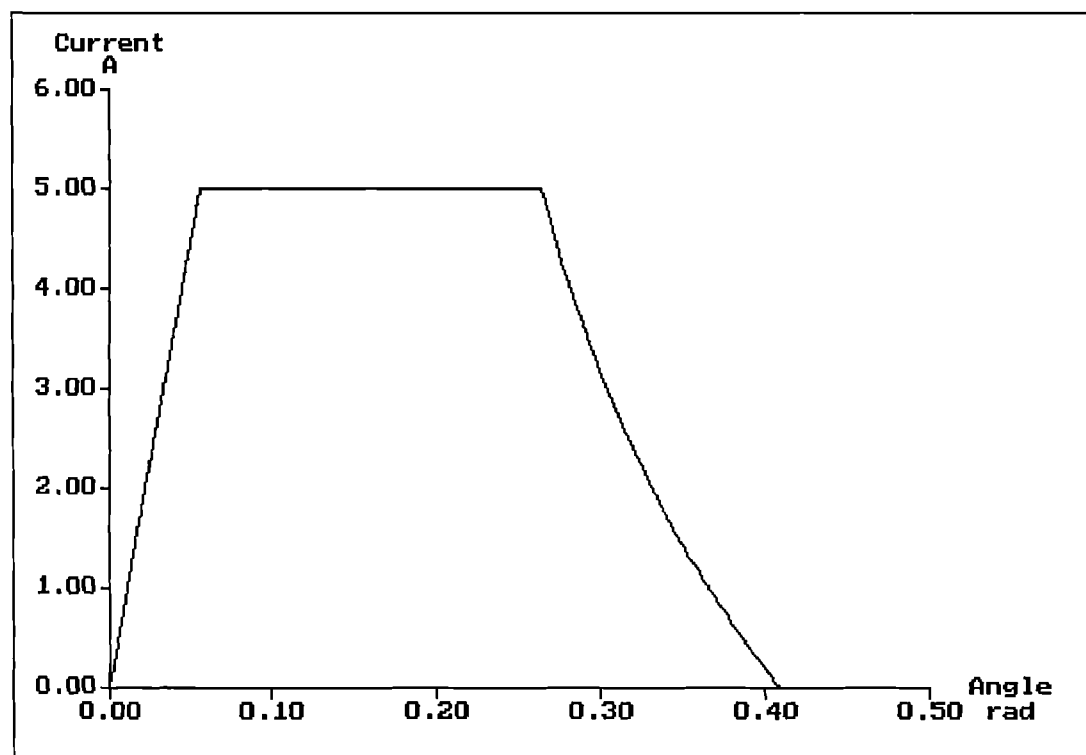


Fig. 6.8d SRDESIGN i / θ profile @ 1500rpm.

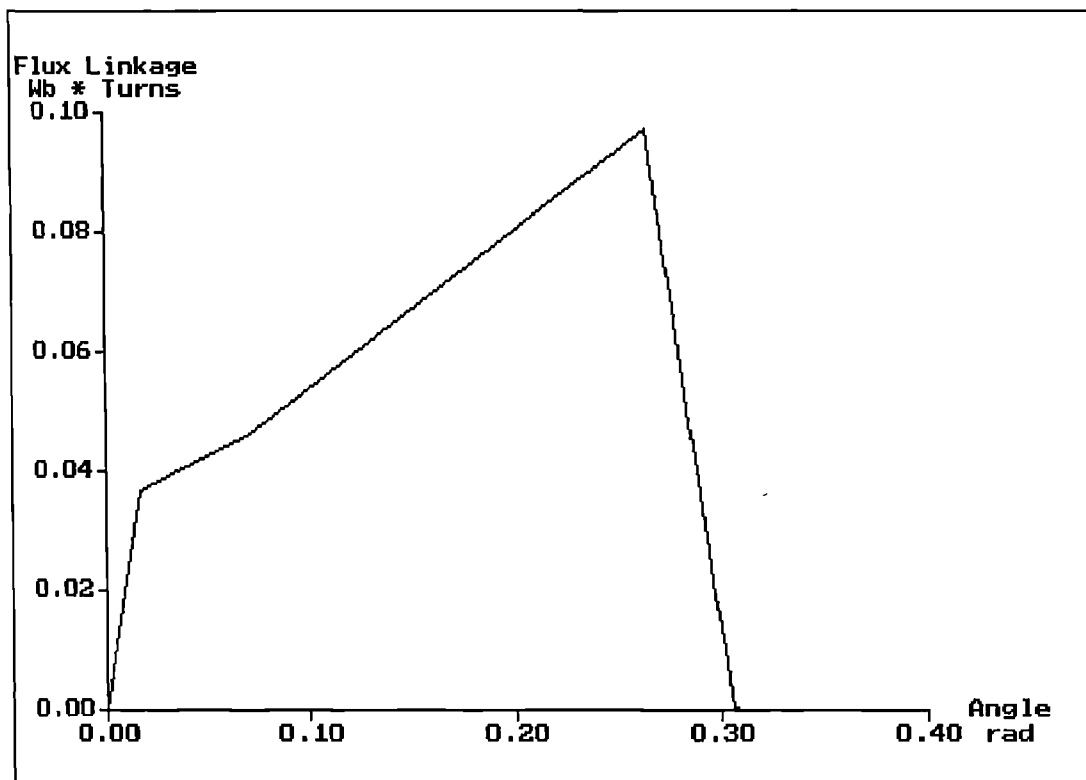


Fig. 6.9a SRDESIGN λ / θ diagram @ 450rpm.

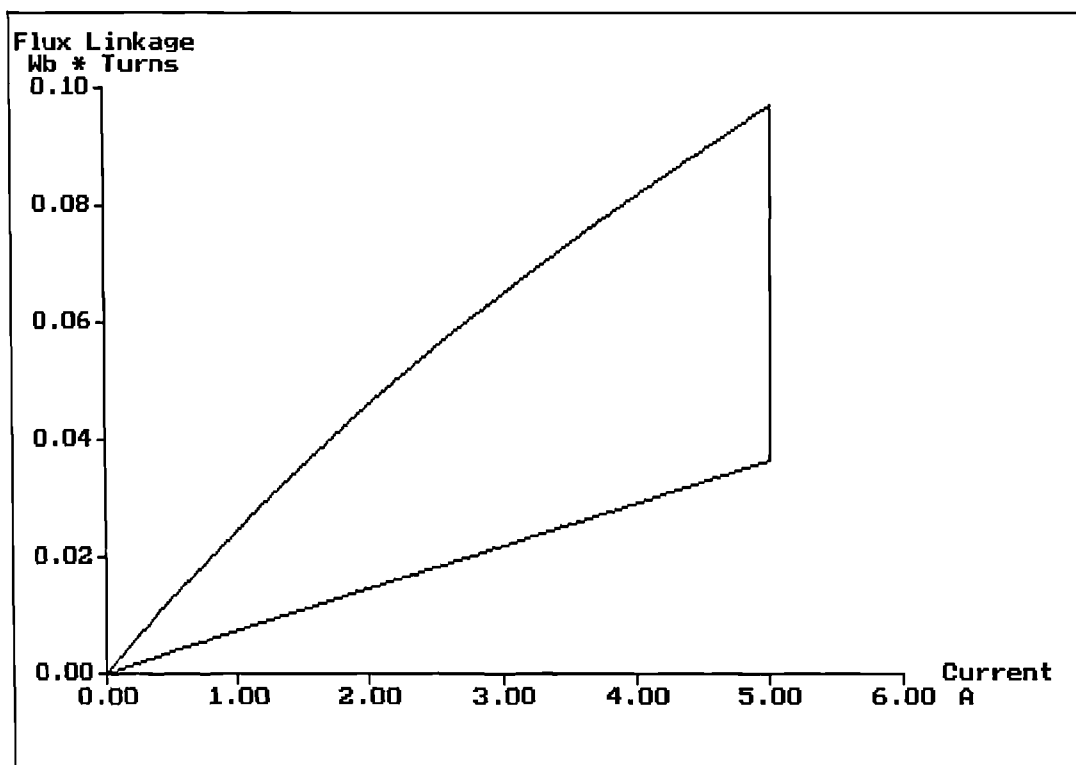


Fig. 6.9b SRDESIGN λ / i diagram @ 450rpm.

6.2.3 Sources of error.

The spring balance and torque indicating scale arrangement, mounted on the eddy current test rig, did not provide an accurate reading of the torque applied on the eddy current brake shaft. Although the equipment was repeatedly calibrated, a margin of error on the torque reading must be allowed.

In SRDESIGN, average torque is computed using the 'virtual work' method which involves the computation of the area enclosed by the operating trajectory on the λ / i diagram during each stroke. Linear and sigmoidal functions are used to interpolate between the 'unaligned' and 'aligned' magnetisation curves, and some error is expected from this.

Errors may also occur in the estimation of power losses using SRDESIGN. Power losses mainly comprise of copper and iron losses. At low speeds, the heat dissipated in the copper windings forms the major source of power loss. The estimation of rms phase current I_{rms} and phase winding resistance R has been found to be very accurate. However, the absence of a thermal model prevents the prediction of temperature rise in the copper winding and its effect on R . A transducer mounted on the coil surface measured temperature and this was used as a guideline in determining R_{op} under running conditions, since the temperature coefficient of resistance for copper was known. Finally, as the operating speed is increased the eddy current loss component becomes more pronounced. SRDESIGN uses the Steinmetz formulae to compute iron losses. However, no modifications were made to account for the non-sinusoidal flux waveforms encountered in switched reluctance motors.

6.3 Testing the 4kW 7-phase motor.

6.3.1 Experimental arrangement.

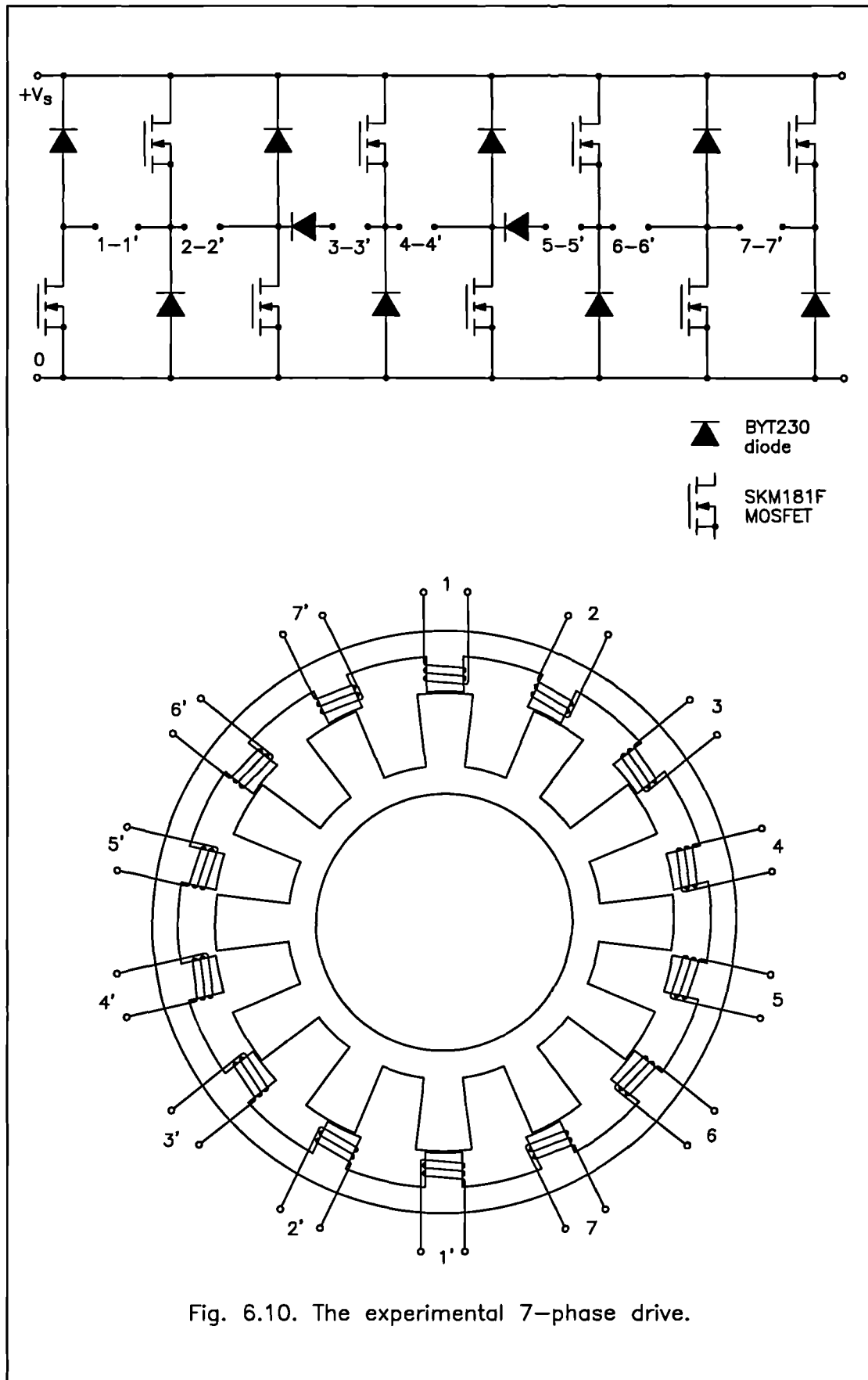
The shared switch power converter was employed in the 4kW 7-phase drive. Figure 6.10 shows seven phase windings connected to eight switching devices and associated freewheeling diodes. Two series diodes block unwanted current when more than two switches in the circuit conduct simultaneously. The series diodes are slow recovery, rectifying diodes because the voltage across them only reverses at the phase current frequency, not at the chopping frequency seen in the fast recovery freewheeling diodes.

The motor was designed to operate at a dc link voltage of 600V and a peak phase current of 10A. The top switching devices of the shared switch converter ought to be rated to withstand twice the motor rated current. These criteria were met by the SKM181F MOSFET devices.

A brushless resolver was mounted on the shaft of the 7-phase motor and was used in conjunction with the 11RS260 resolver to digital converter, to provide rotor position feedback. The digital converter offered 12 bit (0.0879°) resolution, thus allowing very fine control of the phase current firing and commutation angles.

6.3.2 7-phase motor testing.

Measurements were carried out on the 7-phase motor for a range of operating speeds up to 1500rpm. A test voltage of 200V and maximum phase current of 10A were chosen. This reduced the motor base speed below the rated speed of 1500rpm and allowed SRDESIGN 'above base speed' algorithms to be verified. The on-state angle, θ_{on} , was set to 8.57° (twice the step angle). At low speeds improved performance could be achieved by setting θ_{on} up to three step angles. However the shared switch converter algorithm allowed the current in only two



phase windings to be simultaneously controlled. The current in the third phase winding would be dependent on the voltage across one of the other two excited phases. This would be an undesirable feature.

Short and long flux loop configurations were examined. At each running speed and for a constant θ_{on} and I_m , the current firing angle θ_f was advanced (or retarded) in steps of 0.7° . The torque, input power and rms phase current were recorded and the optimum firing angle (i.e. the firing angle for which maximum torque was obtained) was established. The results of this experimental procedure shall next be analyzed.

The maximum torque / speed characteristic describing the 7-phase motor configured for short flux loops is given in fig. 6.11. Also shown is the SRDESIGN predicted curve, which was drawn having specified the firing angle, commutation angle and maximum current I_m at each operating speed. Good agreement between simulated and experimental results is achieved. In the short flux loop configuration, the 7-phase motor achieved a maximum efficiency of 78%, as shown in fig. 6.12.

The maximum torque / speed curve obtained by winding the motor for long flux loops is shown in fig. 6.13. Significantly lower torque was produced by the long flux loop configuration, although the rms phase current at each test speed was kept constant. Configuring the 7-phase motor for long flux paths also resulted in an increase in iron losses. As a result, the motor efficiency decreased significantly, as shown in fig. 6.14.

At any speed, the torque output was limited by one of two factors. Firstly, there was a limitation on the amount of losses that could be dissipated by the motor frame, if the temperature in the stator windings was to be kept within an acceptable level. This was addressed by controlling the rms phase current. At higher speeds torque production was limited by the back-emf which exceeded the supply voltage.

FIG. 6.11 MAX. TORQUE/SPEED CHARACTERISTIC (7-PH MOTOR, SHORT LOOPS)

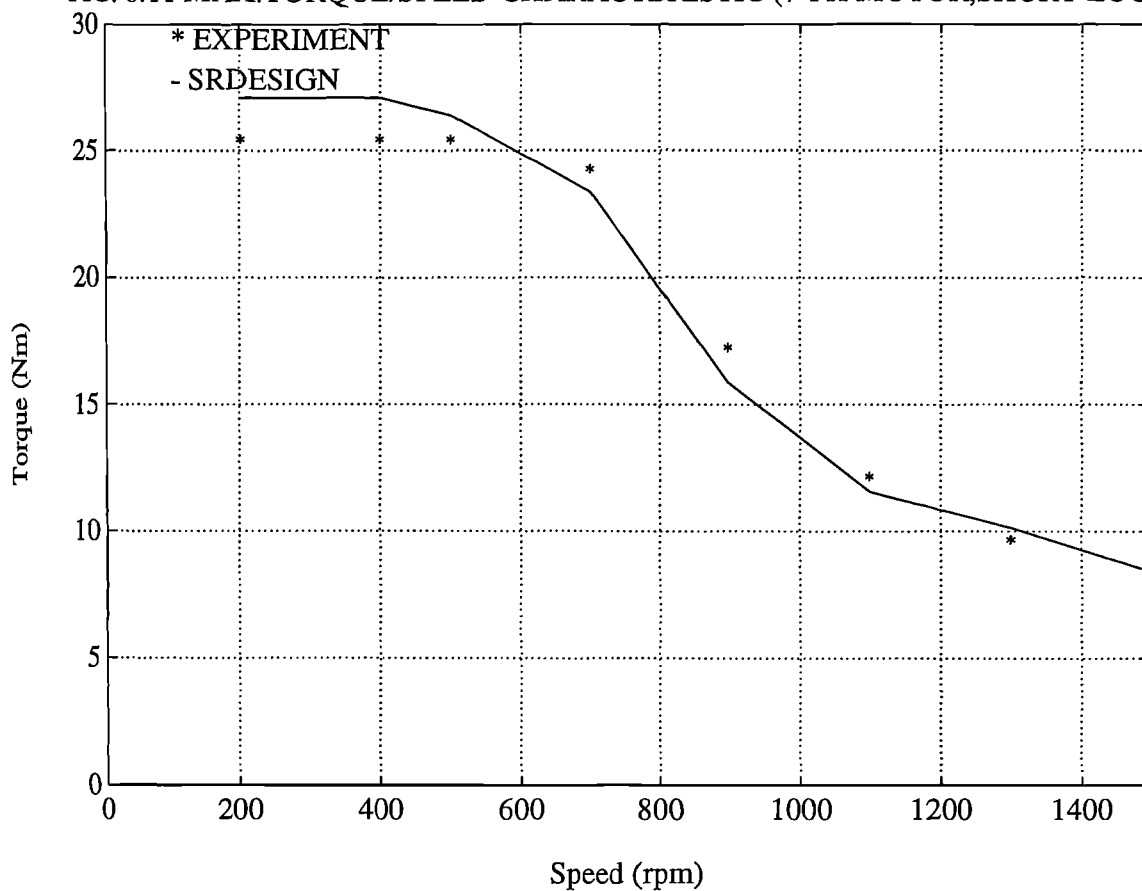


FIG. 6.12 EFFICIENCY CURVE (7-PH MOTOR, SHORT LOOPS)

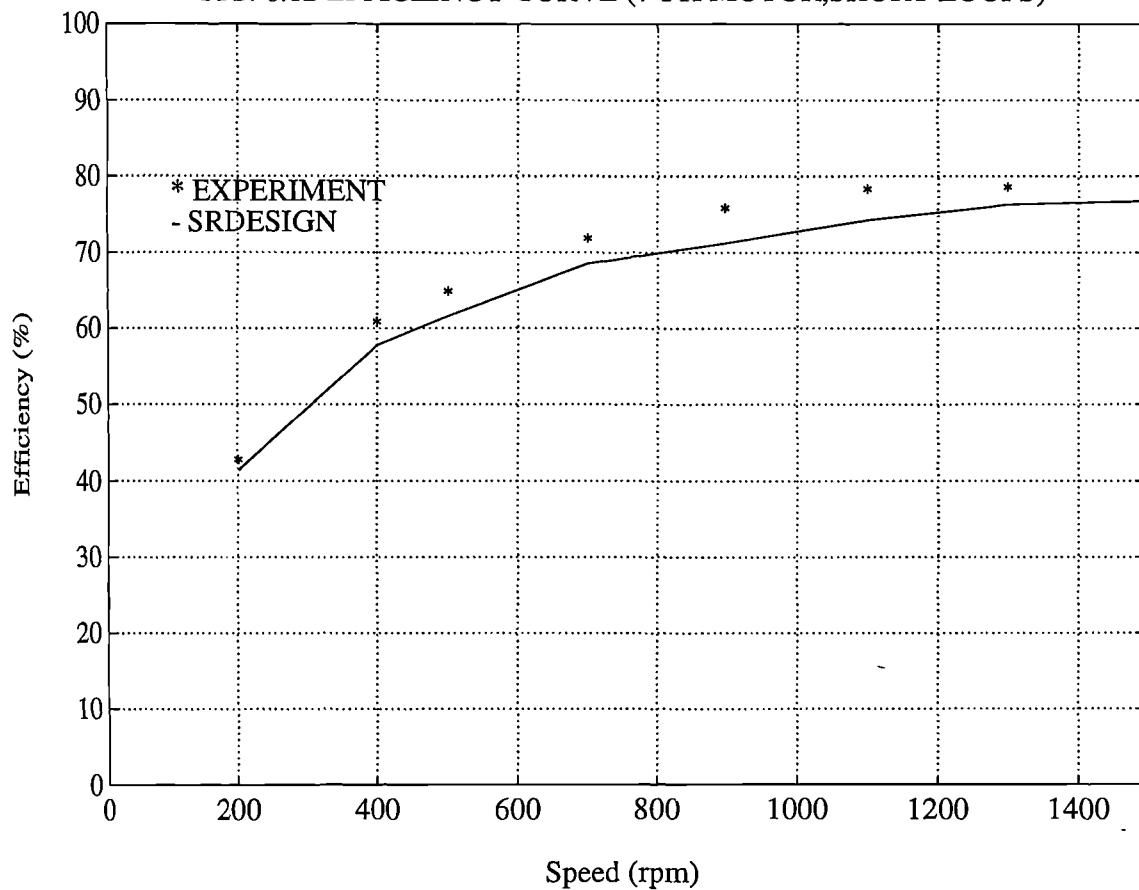


Fig. 6.13 MAX.TORQUE/SPEED CHARACTERISTIC (7-PH MOTOR, LONG LOOPS)

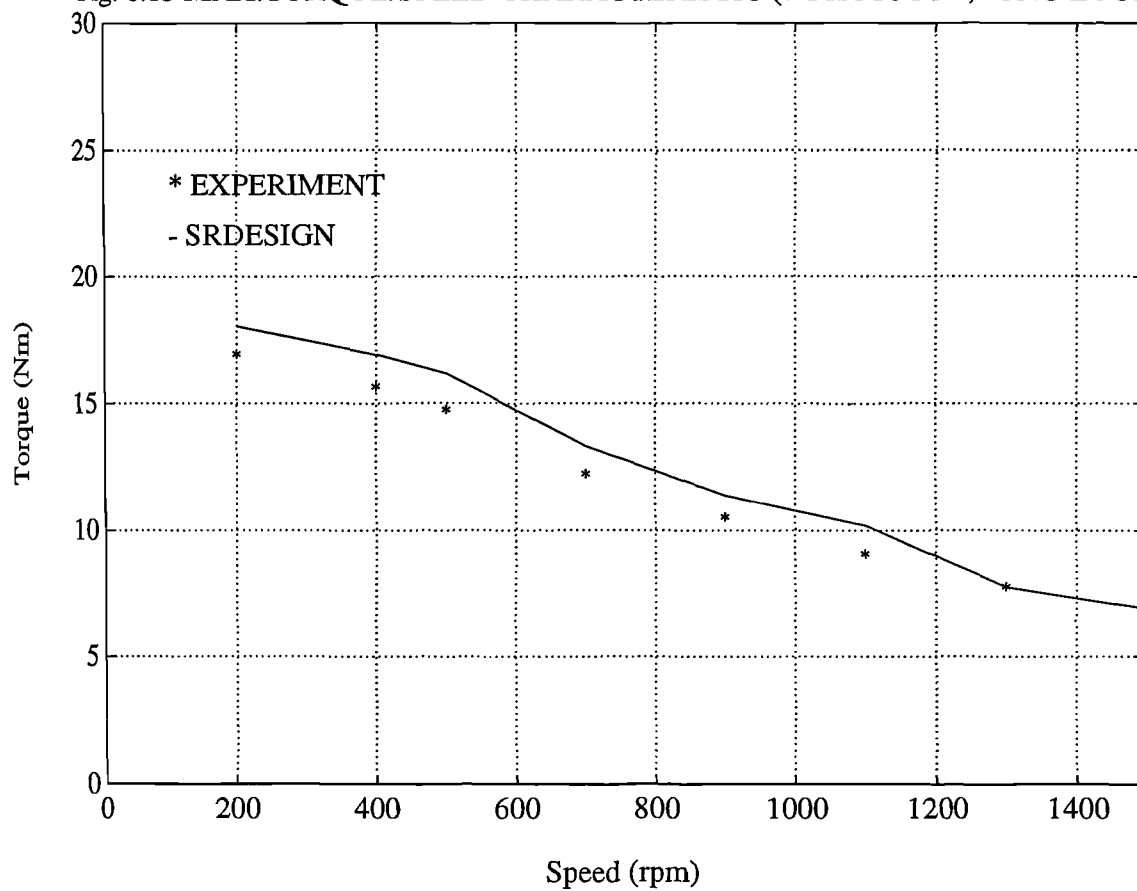
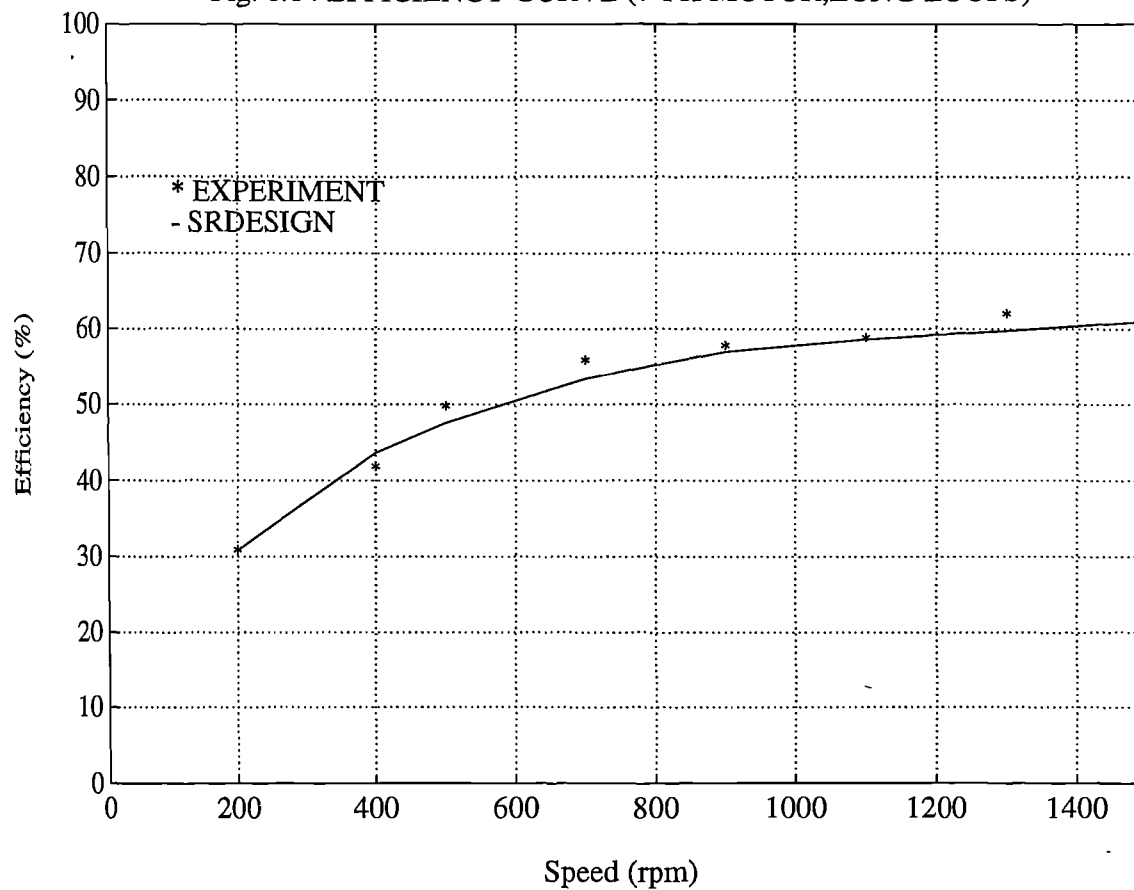


Fig. 6.14 EFFICIENCY CURVE (7-PH MOTOR, LONG LOOPS)



A collection of SRDESIGN-generated graphs that describe the 7-phase motor 'behaviour' at 1000rpm is given in fig. 6.15. It is interesting to note that at $V_s = 200\text{V}$ the motor is running above base speed when configured for short flux loops. In contrast, the same drive runs below base speed when configured for long loops. This is because the **system** λ / i characteristic predicted by finite element analysis was different for the two machine configurations. Base speed may be expressed as

$$\omega_b = \frac{(V_s - I_m R) \beta_s}{\lambda_{al} - \lambda_{bo}} \quad (6.2)$$

The difference $\lambda_{al} - \lambda_{bo}$ was greater in the short flux loop machine configuration. This example demonstrates yet again the adverse implications of neglecting magnetic interaction effects. Had the magnetisation curves at the aligned and unaligned positions been constructed using the virtual work method as applied to singly excited systems, no information on the modified λ / i curve, which results by exciting a second phase or configuring the machine for short loops, would be conveyed to the user.

Referring to the simulated phase current profiles shown in fig. 6.15, the current rises to 8.5A (chosen chopping level) and maintains this value until the rotor teeth begin to overlap with the excited stator teeth. In the overlap region, if the back-emf exceeds the supply voltage (short flux loops) the current decreases though flux linkage continues to increase. If the supply voltage exceeds the back-emf (long flux loops) then the current is maintained constant (with the aid of a current chopper in practice). Upon commutation, the phase current decreases in a zero volt loop; flux linkage also decreases, with a slower rate of fall though. Full negative volts subsequently force a faster rate of fall of flux linkage.

6.4 SRDESIGN practicality.

The purpose of SRDESIGN is to provide a design and simulation facility for switched reluctance motors. SRDESIGN is capable of completely characterising

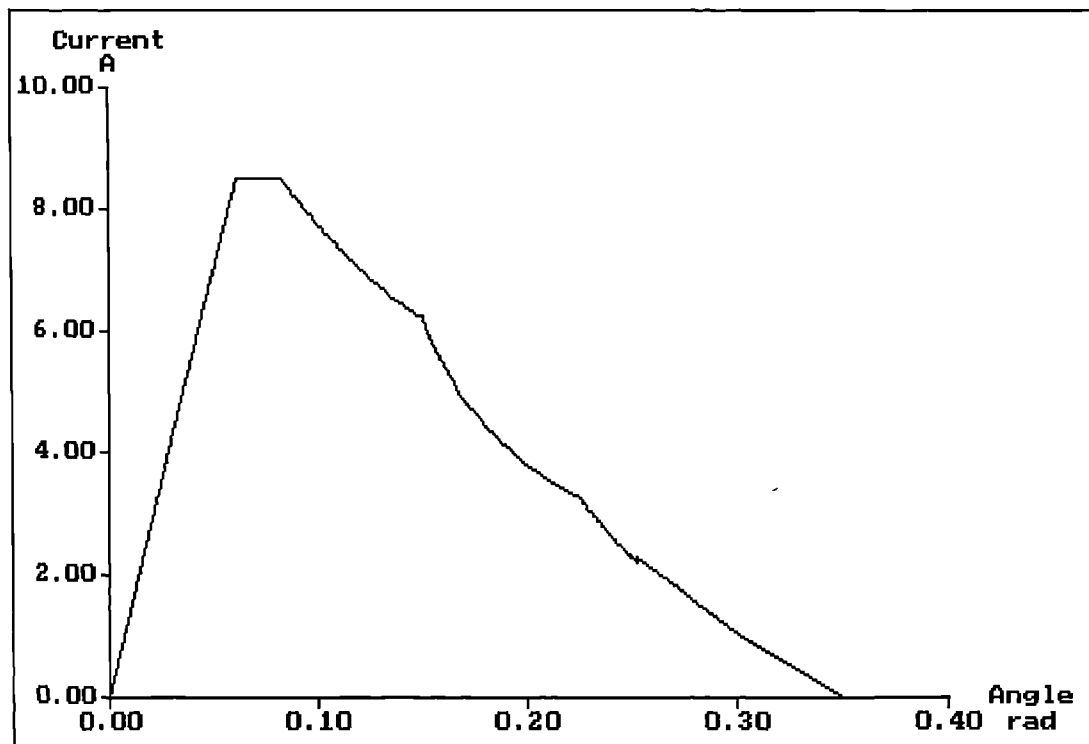


Fig. 6.15a SRDESIGN i / θ profile @ 1000rpm (short loops).

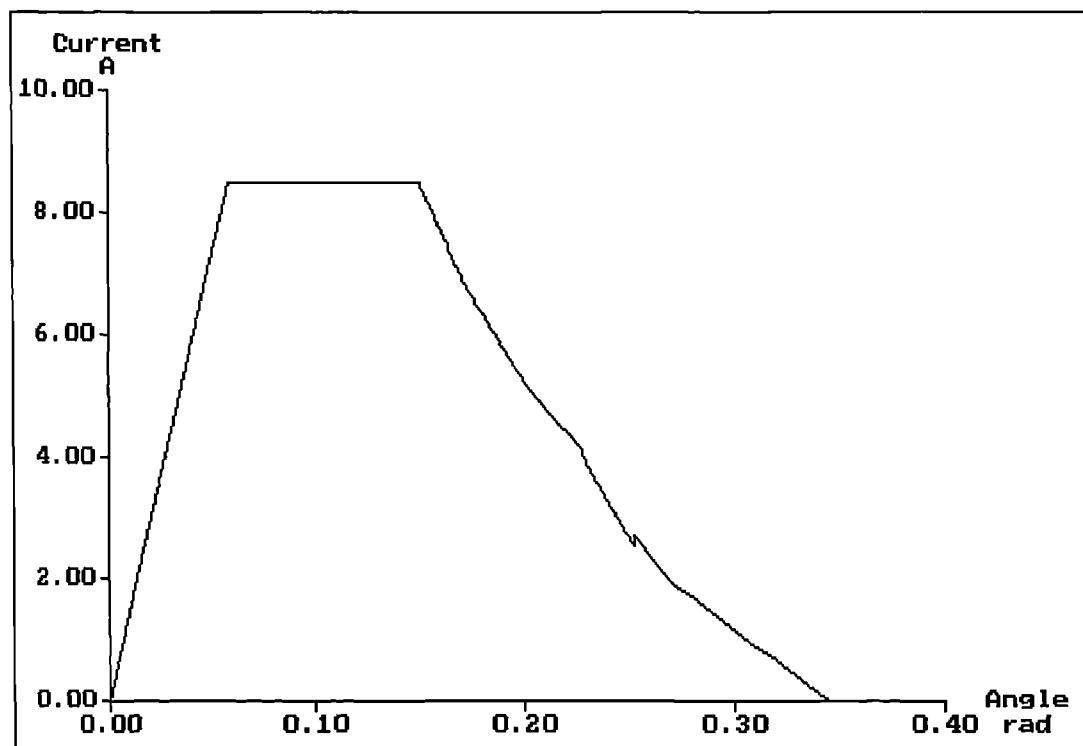


Fig. 6.15b SRDESIGN i / θ profile @ 1000rpm (long loops).

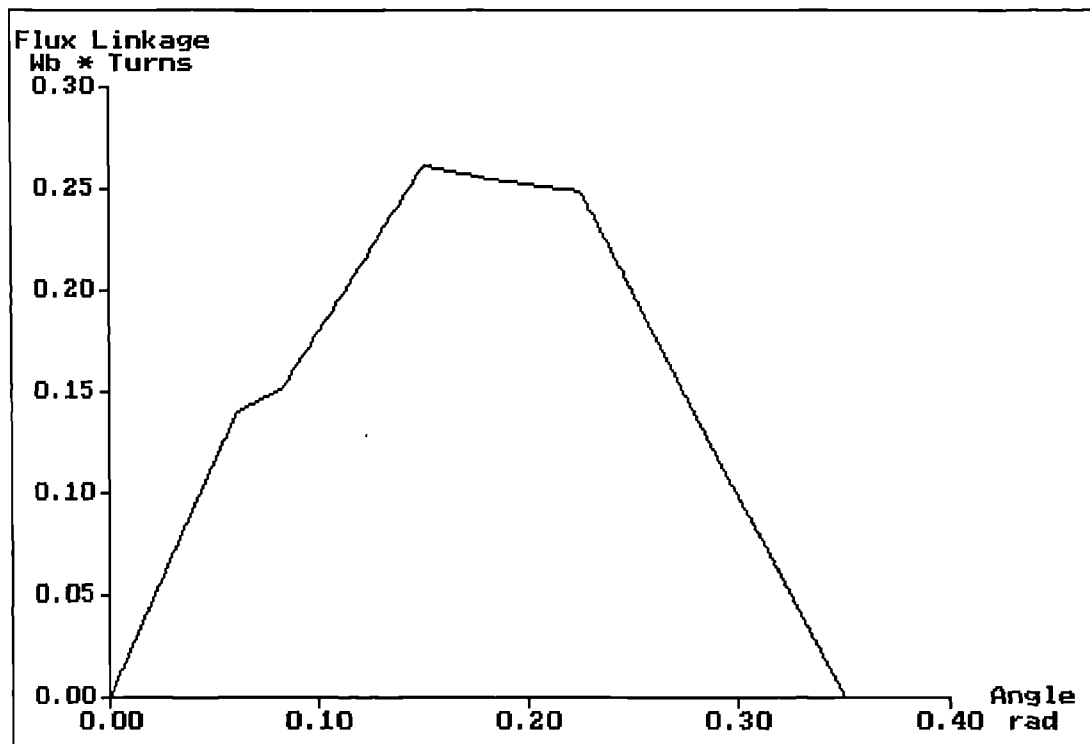


Fig. 6.15c SRDESIGN λ / θ diagram @ 1000rpm (short loops).

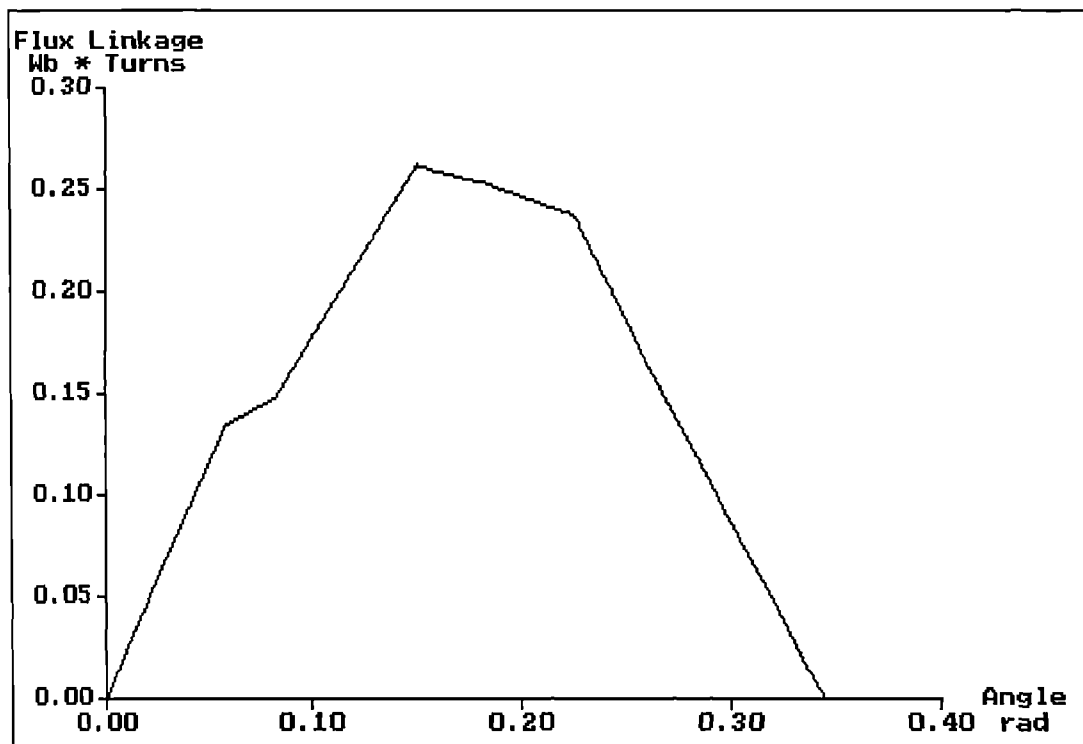


Fig. 6.15d SRDESIGN λ / θ diagram @ 1000rpm (long loops).

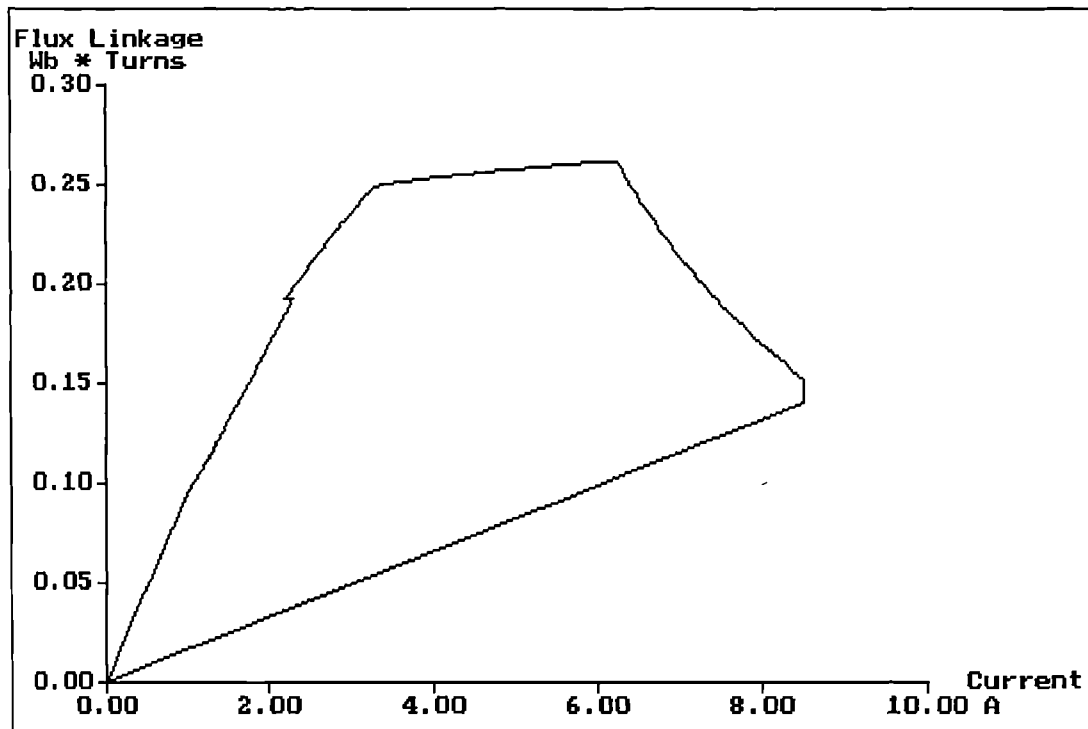


Fig. 6.15e SRDESIGN λ / i diagram @ 1000rpm (short loops).

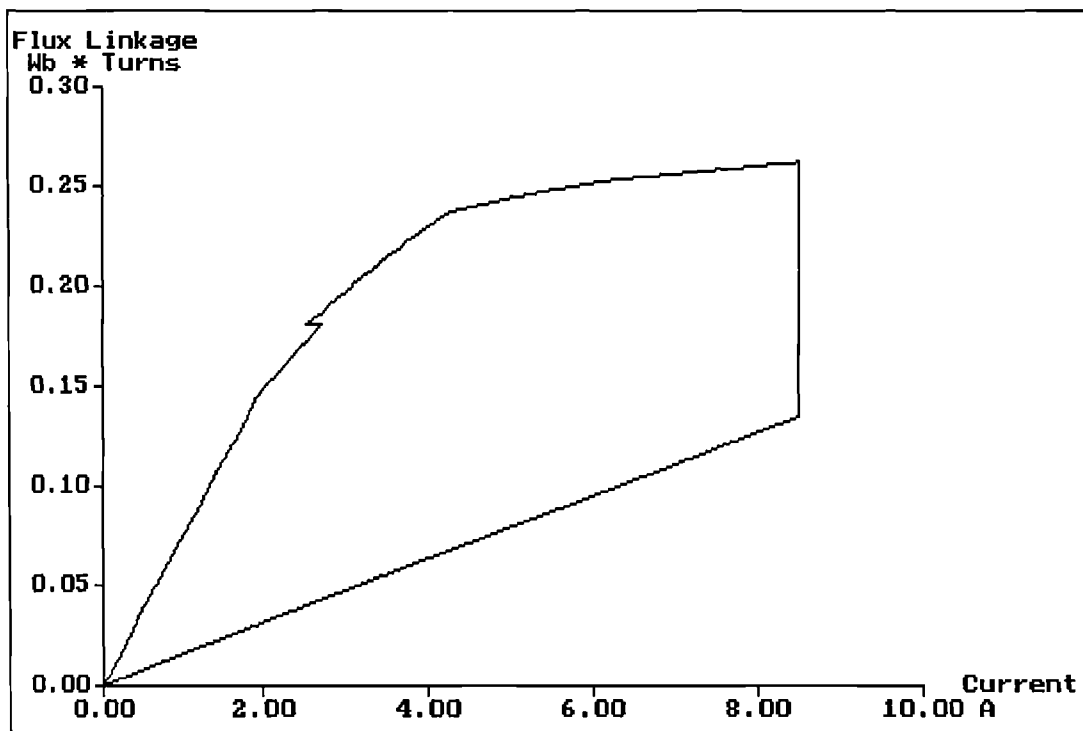


Fig. 6.15f SRDESIGN λ / i diagram @ 1000rpm (long loops).

the performance of a switched reluctance motor within minutes. However, with how much accuracy is the analysis performed?

This very much depends on the starting point: the λ / i diagram at the unaligned and aligned rotor positions. If the magnetisation curves are imported from finite element analysis, preceding sections demonstrated that the predicted motor torque at any speed or commutation angle is within 10% of the measured value. This is very acceptable considering that the λ / θ curves are computed analytically within SRDESIGN. In addition, the simulated i / θ profile at any speed compares favourably with traces obtained experimentally.

However, importing λ / i diagrams implies additional man hours to produce the finite element model. Accurate results may only be obtained by computing the λ / i diagram within SRDESIGN, if switched reluctance machines operating with only one phase excited at any time are being examined. This subject was addressed in section 6.1.

Switched reluctance motor losses are also calculated within a 10% accuracy, though this is achieved by manually entering the (measured) operating temperature in the copper windings. The absence of a thermal model suggests that an SRDESIGN user must have some basic knowledge on the permissible current density that can appear in the motor in order to avoid overheating. SRDESIGN supplies information on J_{peak} and J_{rms} . Miller [8] provides some guidelines on maximum permissible current densities for a range of motor types.

Chapter 7

THE 5-PHASE SWITCHED RELUCTANCE DRIVE: DESIGN, CONSTRUCTION AND PERFORMANCE

The design, construction and testing of the 5-phase switched reluctance drive are presented in this chapter. The electromagnetic theory of doubly excited systems is used in the motor lamination design process. Finite element analysis is employed to model the static performance of the 5-phase prototype. This is compared with the static performance of a 4-phase motor based on the Oulton³ motor design. SRDESIGN was employed for the dynamic simulation of the 5-phase drive. Experimental results from the constructed 5-phase drive are compared with simulation data. Market applications of the 5-phase switched reluctance drive are discussed.

7.1 5-phase motor design.

The task was to design a switched reluctance motor, to be constructed inside a standard D112 induction motor frame. An outer stator diameter constraint of 165mm was therefore imposed. The existing D112 frame also set a constraint on the stack length of approximately 150mm. The main aim was the electromagnetic design of an energy efficient switched reluctance motor.

7.1.1 Selection of stator pole arc and back-iron width.

A 10/8 5-phase motor, showing motor dimensions is depicted in fig. 7.1. The choice of stator pole arc and stator back-iron width must be a compromise between

³The Oulton motor is a well known motor design, manufactured by Graseby Controls.

- r rotor pole pitch (rad)
- s stator pole pitch (rad)
- d_s stator outside diameter (mm)
- t_s stator pole width (mm)
- y stator back-iron thickness (or stator yoke)
- β_s stator pole arc (rad)
- d_r rotor diameter (mm)
- β_r rotor pole arc (rad)
- g airgap (mm)
- $d_b = d_r + 2g$

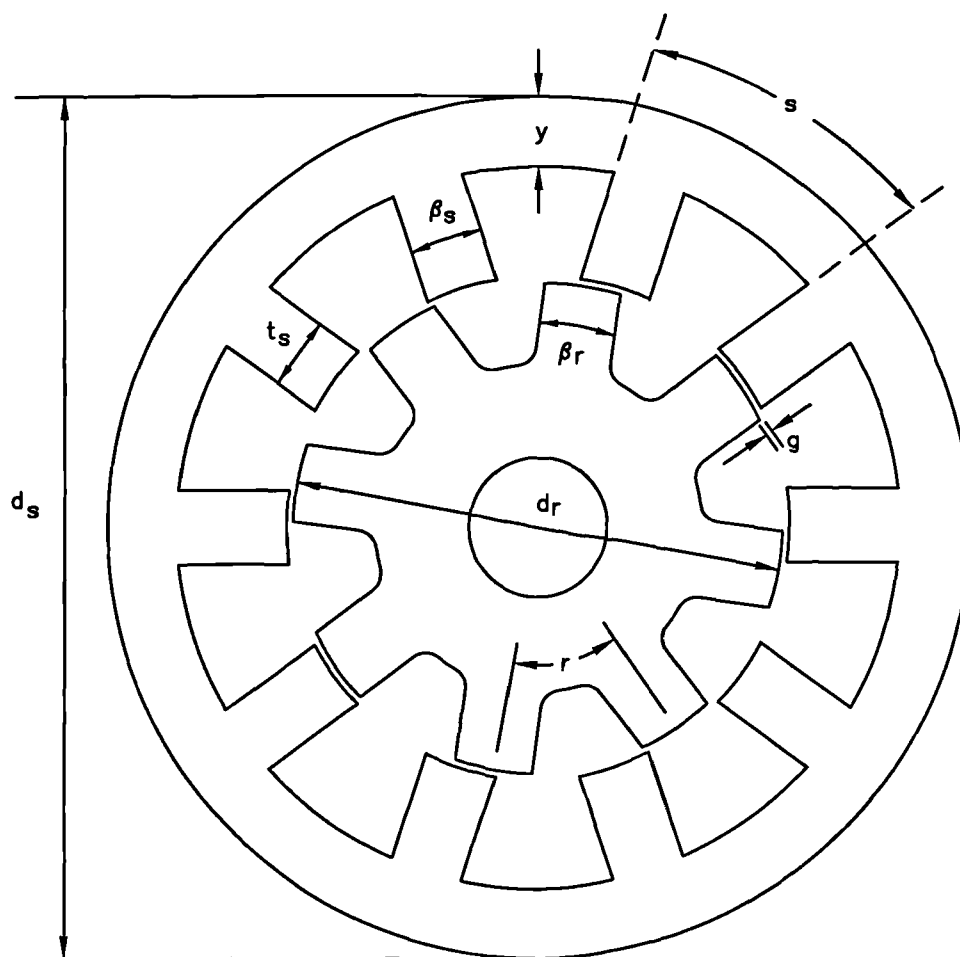


Fig. 7.1. Dimensions of a 10/8 5-phase motor.

the requirement for a low reluctance iron path and the need for sufficient space for the copper conductors. A comprehensive study on the sensitivity of stator and rotor pole arc / pole pitch ratios on 3-phase switched reluctance motors has been reported [60]. It was illustrated that average torque may be maintained at high levels if the stator pole arc / pole pitch (β_s / s) ratio is between 0.35 and 0.45. Faiz and Finch [61] reported that maintaining β_s / s within 0.42-0.47 would maximise torque production though this must be reduced, subject to Ohmic loss constraints. Miller [8] reports that the optimum β_s / s ratio increases with the number of poles. However, these observations should only be used as guidelines. The stator pole arc ought to be chosen in conjunction with the stator bore, d_b . These two dimensions set the pole width, t_s according to

$$t_s = 2\left(\frac{d_b}{2} \sin \frac{\beta_s}{2}\right) \quad (7.1)$$

which dictates the path reluctance.

In switched reluctance motors the stator bore is found to increase with increasing pole numbers. In order to establish the stator bore, suitable for the 5-phase short flux path motor, finite element models of varying bore were constructed. The stator pole arc, β_s , and stator pole width / yoke thickness ratio (t_s / y) were held constant. As a result t_s increased with increased d_b . It was found that a $d_b / d_s = 0.535$ design produced significantly less average torque, as shown in fig. 7.2. These and subsequent comparisons between different 5-phase motor designs assume equal copper loss. The $d_b / d_s = 0.535$ structure also exhibited the highest operating flux densities. The results depicted in fig. 7.2 were by no means conclusive. Thermal considerations dictate that the conductor current density must be maintained at low levels in order to limit the temperature rise in the windings. Therefore the lowest d_b / d_s ratio possible that would not limit T_{av} was chosen: d_b / d_s was set to 0.6.

In a subsequent design exercise β_s / s was varied from 0.42 to 0.45, for a constant stator bore to stator outer diameter ratio (d_b / d_s) of 0.6. It was found that

FIG. 7.2 VARIATION OF STATOR BORE WITH AVERAGE TORQUE (CONSTANT POLE ARC)

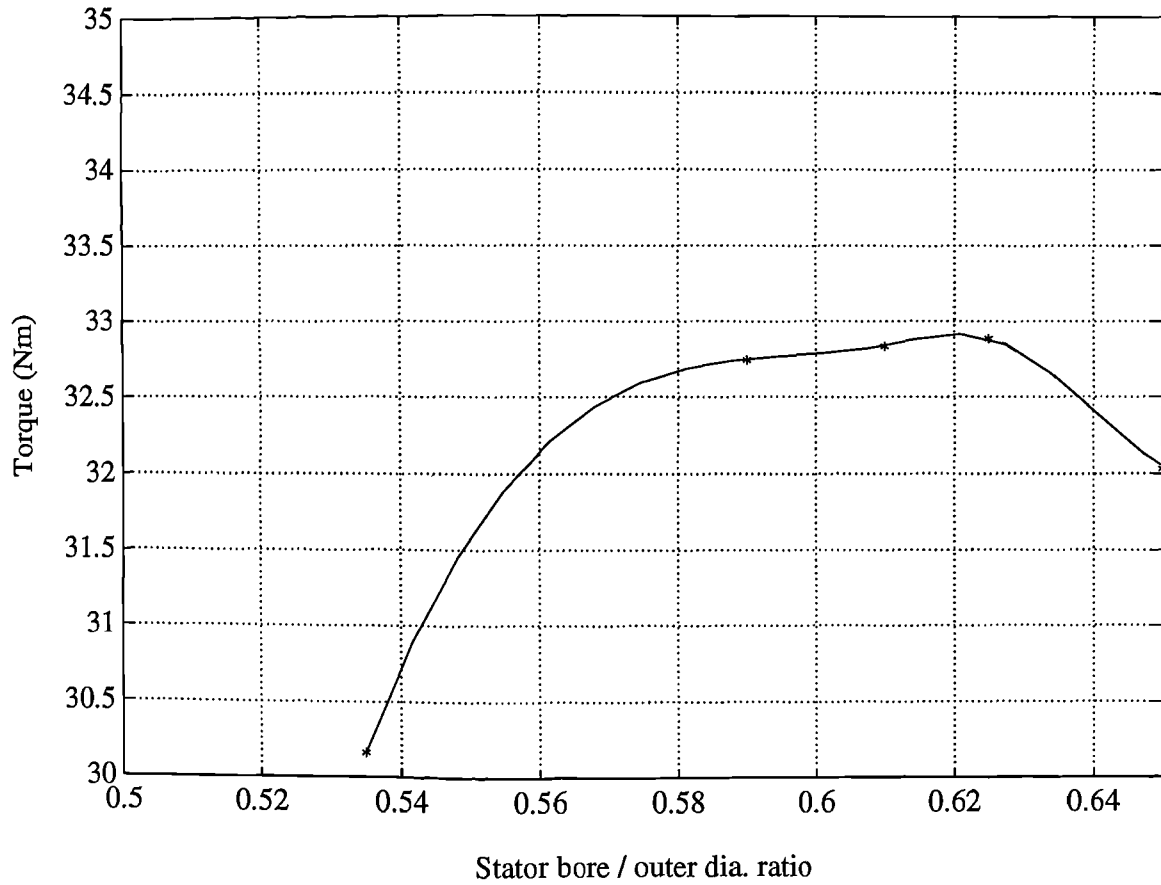
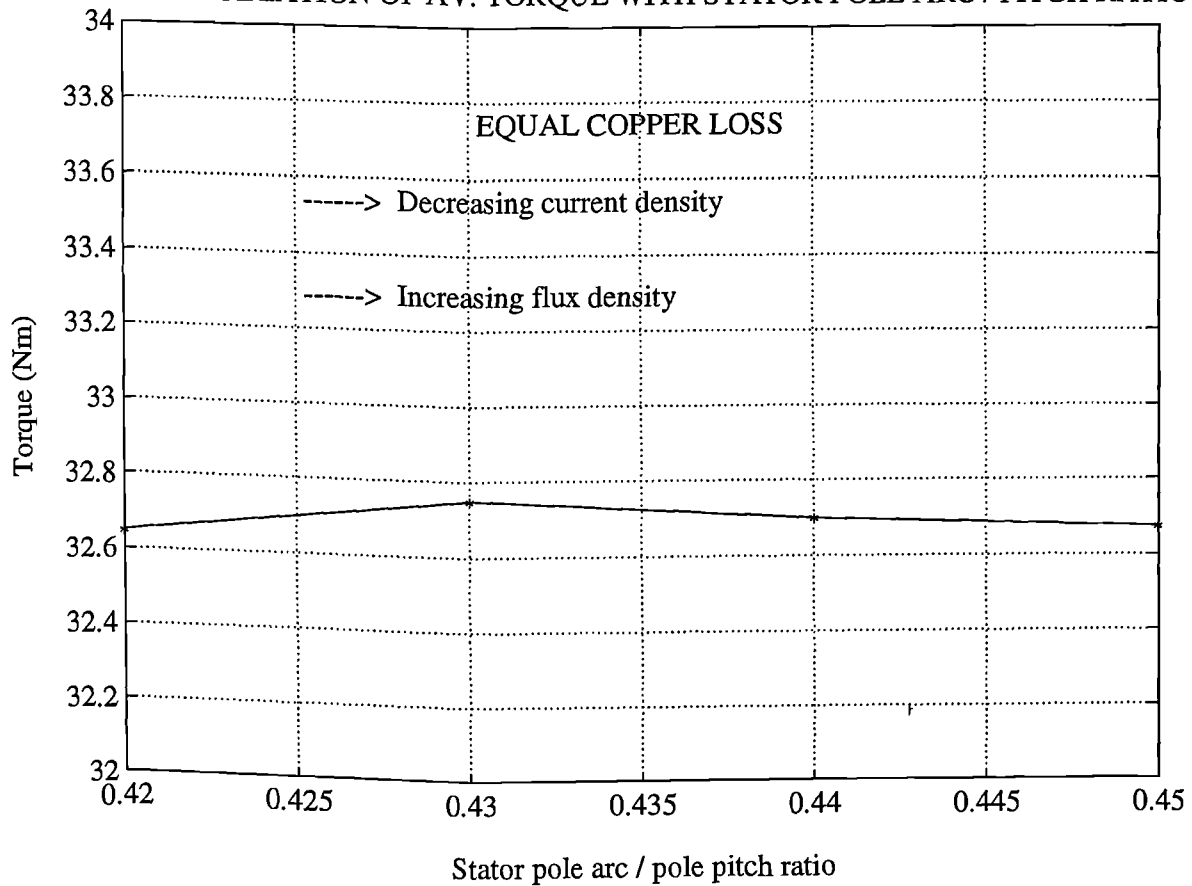


FIG. 7.3 VARIATION OF AV. TORQUE WITH STATOR POLE ARC / PITCH RATIO



marginally lower torque was produced by the $\beta_s / s = 0.42$ tooth design in comparison with higher β_s / s ratio designs, as shown in fig. 7.3. This design would also exhibit marginally higher iron loss. However, the current density in the coil would be somewhat lower. It was decided to strike a balance between high flux density and high current density by setting β_s / s to 0.435. A design validation exercise was subsequently performed. Additional finite element models were defined in which the d_b / d_s ratio was set to 0.58 and 0.62 and β_s / s was varied. No significant change in performance was noted.

The back-iron thickness must be specified having considered the magnetic flux patterns that arise in the switched reluctance motor. If the system is singly excited (e.g. a 2-phase 4/2 motor), the back-iron need only be as thick as approximately half the stator pole width. The two 180° yoke sections can then share the flux linking the diametrically opposite excited stator poles. The stator yoke thickness must be increased in 3-phase 6/4 designs to account for the partial overlap between phase current pulses. In motors with two phases excited simultaneously (such as the 4-phase 8/6), the back-iron thickness ought to be (approximately) equal to the stator pole width. If however a switched reluctance machine is designed for short flux paths, the back iron does not constitute a significant part of the magnetic circuit. The back-iron thickness can therefore be decreased for the benefit of increased copper area (and hence reduced copper loss). Alternatively, for the same slot area, the stator bore of a short flux loop machine can be increased, resulting in a linear increase in torque production.

Finite element studies have shown that, as the back-iron thickness of the 5-phase 10/8 motor is reduced from t_s to $0.65t_s$, the average torque per unit copper loss is increased when the motor is configured for short flux loops. This is because the benefit that arises from the increased copper area overwrites the penalty incurred by narrowing the stator yoke and, as a result, increasing the yoke reluctance. This result does not hold for the long flux path-configured 5-phase motor. The reluctance of the long B-field path around the stator yoke increases significantly when the yoke thickness is reduced beyond $0.8t_s$, and the average torque output is

compromised.

In contrast to the electromagnetic design, it is required mechanically that the stator yoke is thick in order to maximise the stiffness of the stator against compressive forces. This is important in reducing acoustic noise. Therefore, a compromise between the two requirements (bigger slot area or stiffer structure) was reached. The copper area was shaped for rectangular coil sections and the coil was designed to make contact with both the stator pole side and the back-iron for improved heat transfer capability. The average stator yoke thickness in the 5-phase motor was set to $0.8t_s$.

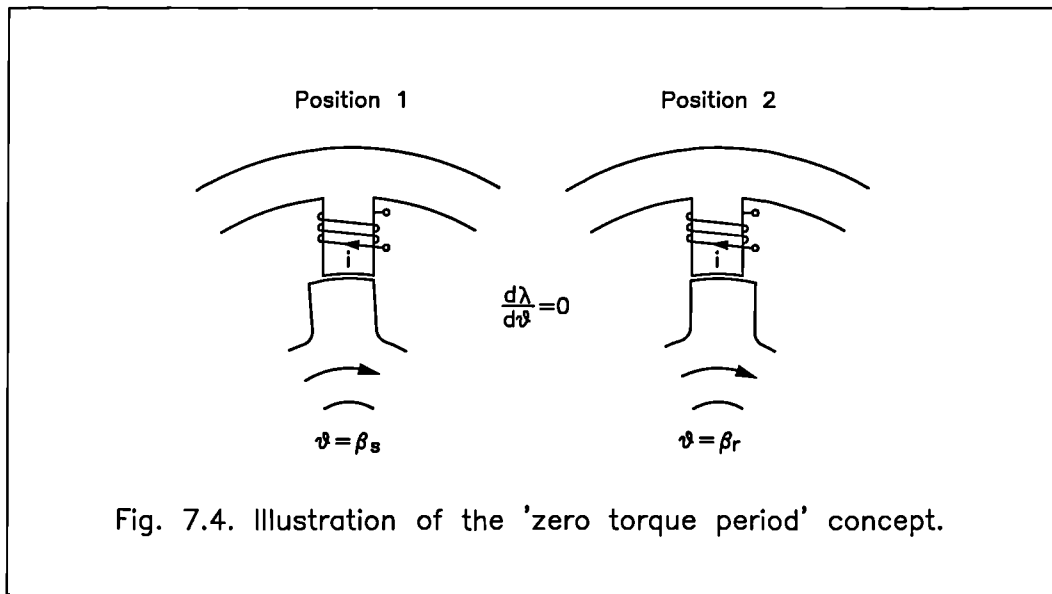
7.1.2 Stator / rotor pole arcs.

A simple ‘rule of thumb’ that is applicable to singly excited switched reluctance systems states that the rotor and stator pole arcs ought to be approximately the same. The ‘useful’ energy converted to mechanical work, is equal to the difference in the system coenergy at the ‘aligned’ and ‘unaligned’ rotor positions. If for example β_r was to be increased significantly beyond β_s , there would be no noticeable increase in the ‘aligned coenergy’. In contrast, the ‘unaligned coenergy’ would be increased, hence decreasing the torque output of the machine.

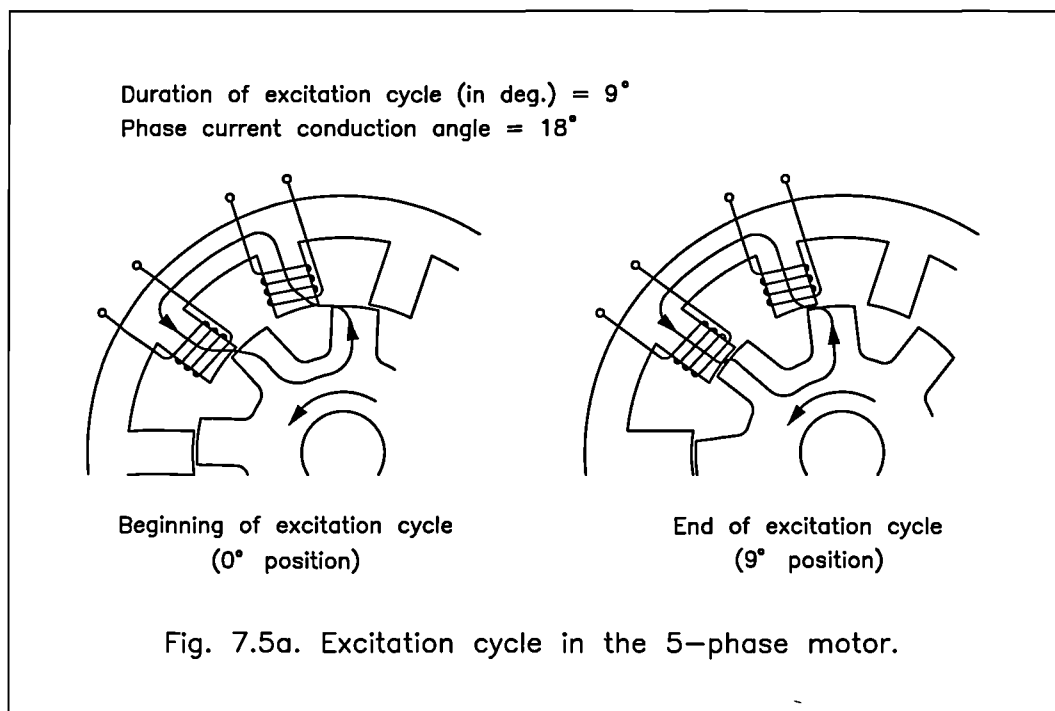
Referring to fig. 7.4, as the rotor moves from position 1 ($\theta = \beta_s$) to position 2 ($\theta = \beta_r$) the phase winding flux linkage (at constant excitation) remains constant i.e. $d\lambda / d\theta = 0$. This is the ‘zero torque period’ that compromises the average torque produced by the motor. However, the ‘zero torque period’ offers more time for the flux in the aligned pole to be forced to zero before negative torque is produced.

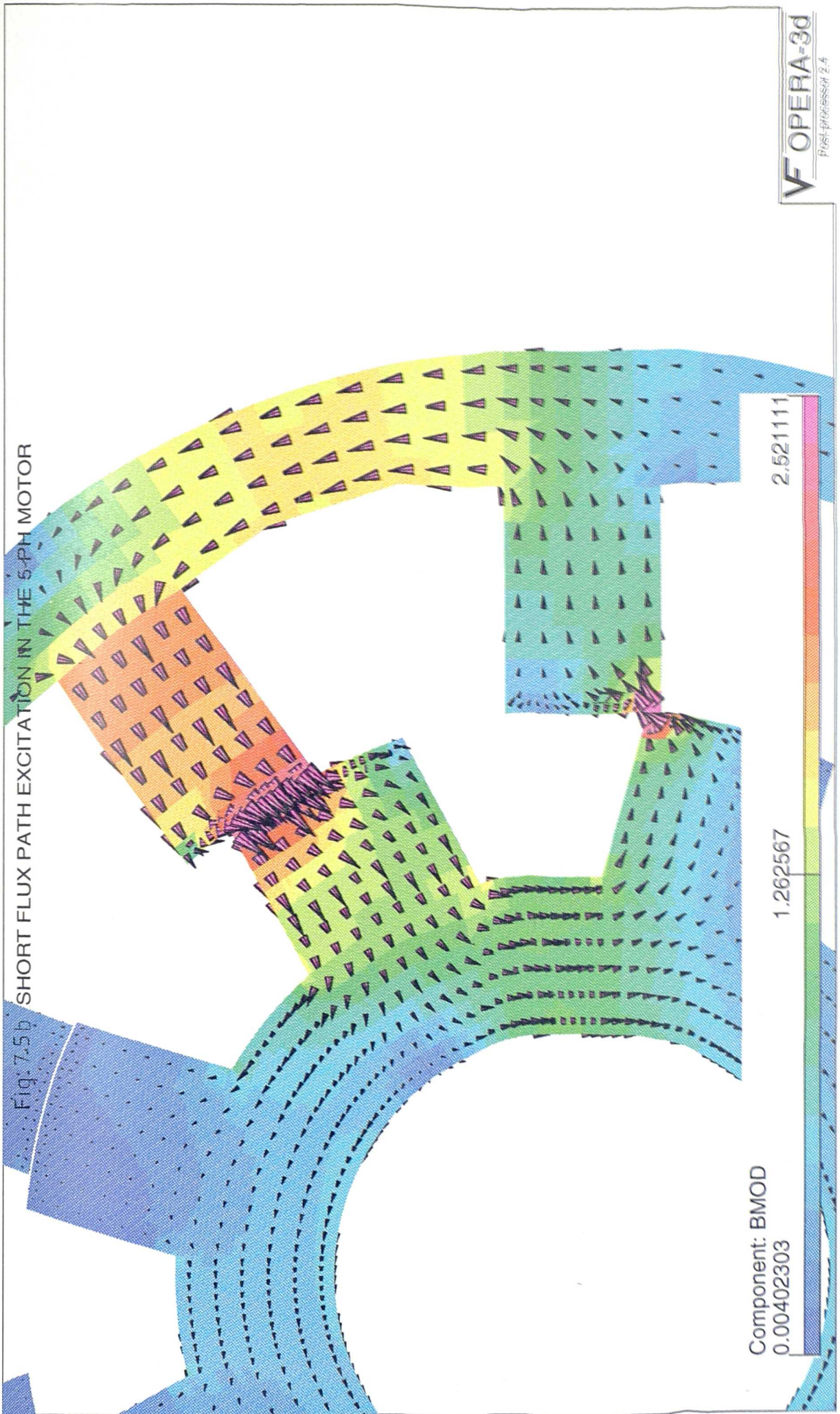
The rotor pole width of the 5-phase motor was designed marginally bigger than the stator pole width. More time was therefore made available to force the flux to zero upon commutation. This design feature would prove especially useful if the shared switch asymmetric half-bridge converter was connected to the 5-phase motor. This converter does not allow full negative volts to be impressed across the motor winding at commutation. The torque production capability of the motor is not

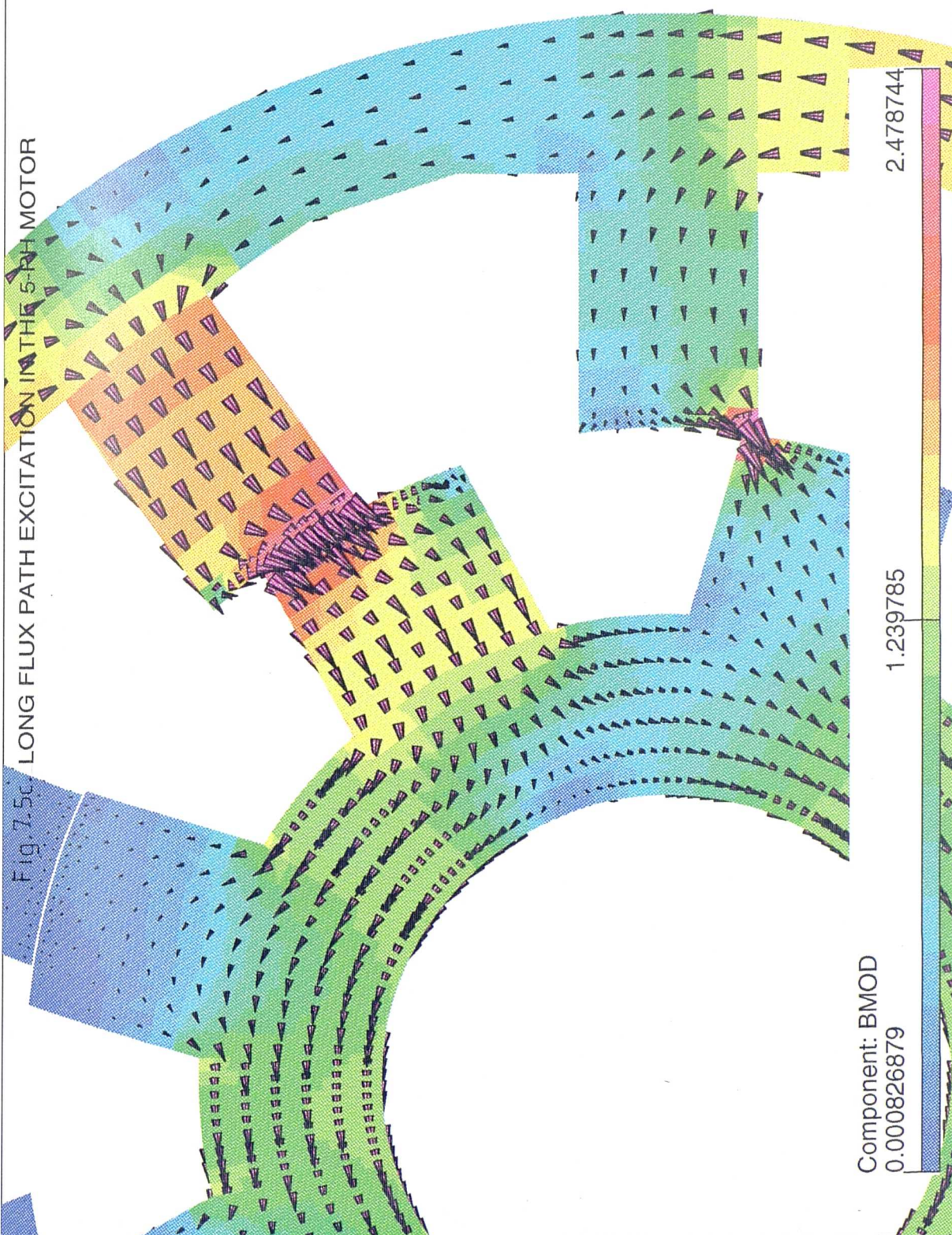
compromised by this choice; an 18° conduction period ensures that both excited phases are always in the torque producing region.

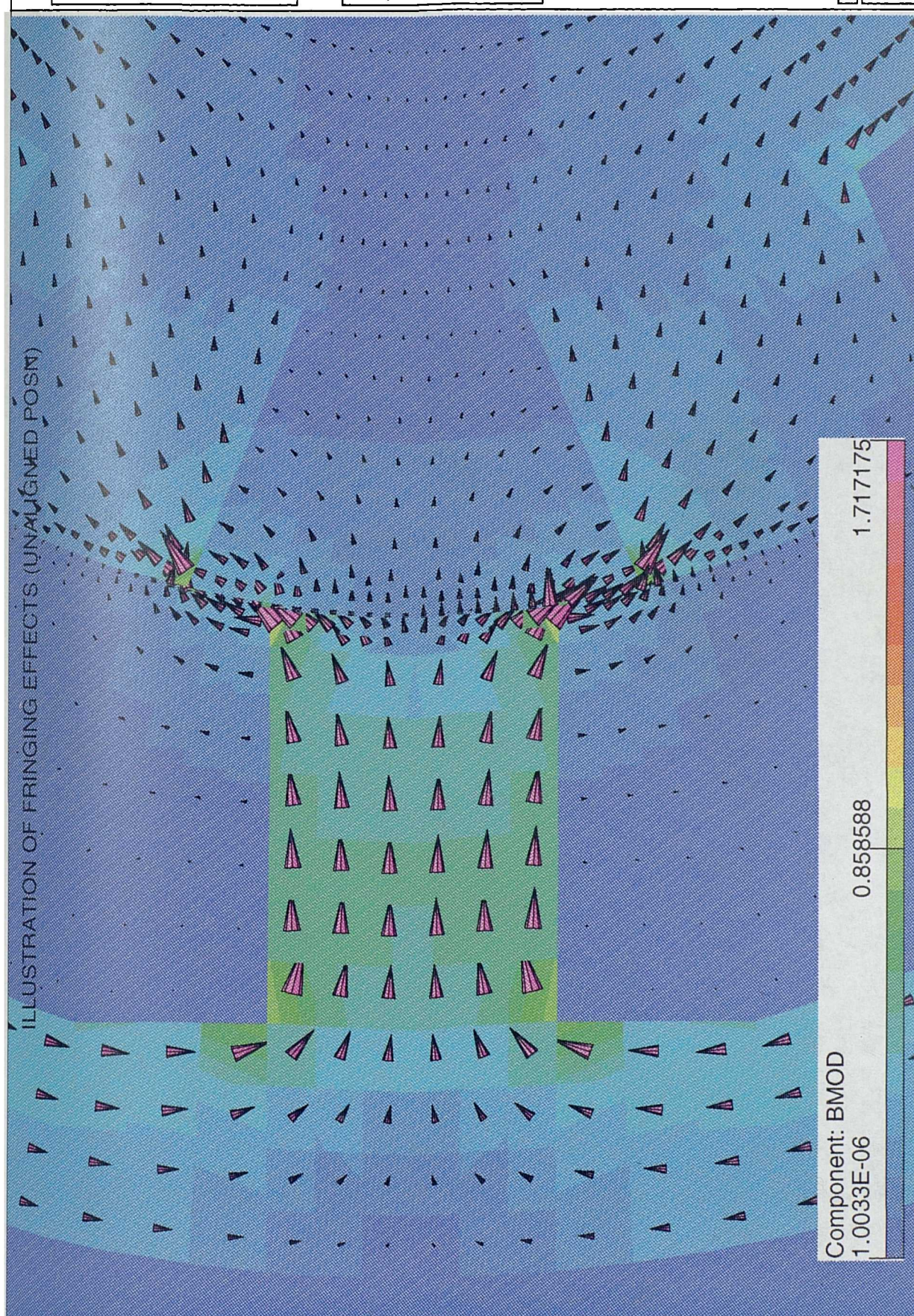


The excitation cycle of the proposed 5-phase motor is shown in fig. 7.5a. The distribution of the **B**-field in the motor configured for short or long flux paths is shown in fig. 7.5b,c respectively. The rotor is positioned at 6° with respect the unaligned position of the trailing phase.









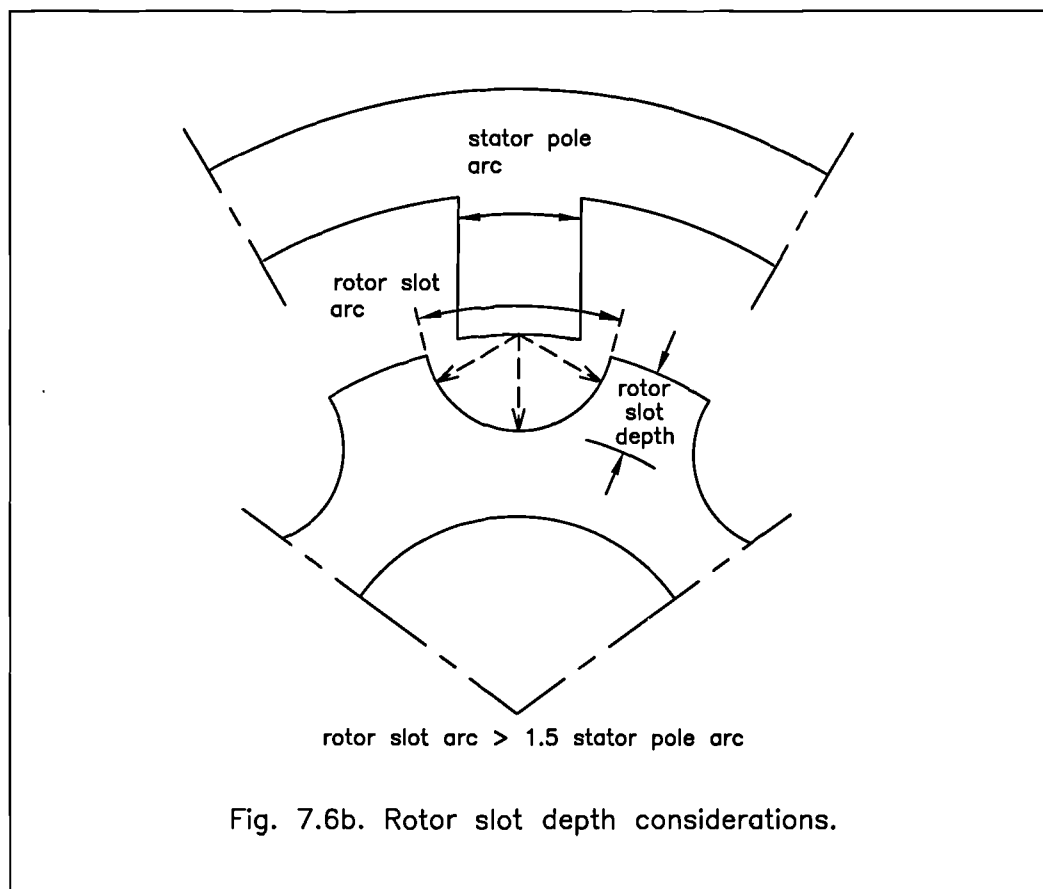
UNITS	
Length	: MM
Flux density	: TESL
Magnetic field	: OERS
Scalar potential	: OCM
Vector potential	: GCM
Conductivity	: SCM
Current density	: ACM2
Power	: WATT
Force	: NEWT
Energy	: JOUL
Electric field	: VCM

PROBLEM DATA	
manusim8.toscab	
TOSCA analysis (nl)	
3944 elements	
7924 nodes	
Shape funct. fields	
Nodal coil fields	

Fig. 7.6a.

7.1.3 Rotor slot depth.

Minimum airgap permeance data for doubly slotted structures has been presented by D. Tormey and others [62]. The authors suggested that the ratio of rotor slot depth to rotor slot arc ought to be higher than 0.4. Additionally a rotor slot to stator pole arc ratio of 1.5 or higher ensures low airgap permeance. However, there is no point in making the rotor slot too deep because, in unaligned the position, **B**-field lines from the stator pole tend to fringe into the rotor teeth edges as shown in fig. 7.6a. Finite element studies on the 5-phase motor have verified the notion that a semicircularly shaped rotor slot, shown in fig. 7.6b, is adequately deep to provide low airgap permeance, provided the rotor slot to stator pole arc ratio is higher than 1.5. In the 5-phase motor, it was further ensured that there was enough clearance in the unaligned position to build up the current to its full load value at the rated speed of 1500 rpm.



7.1.4 Choice of steel grade.

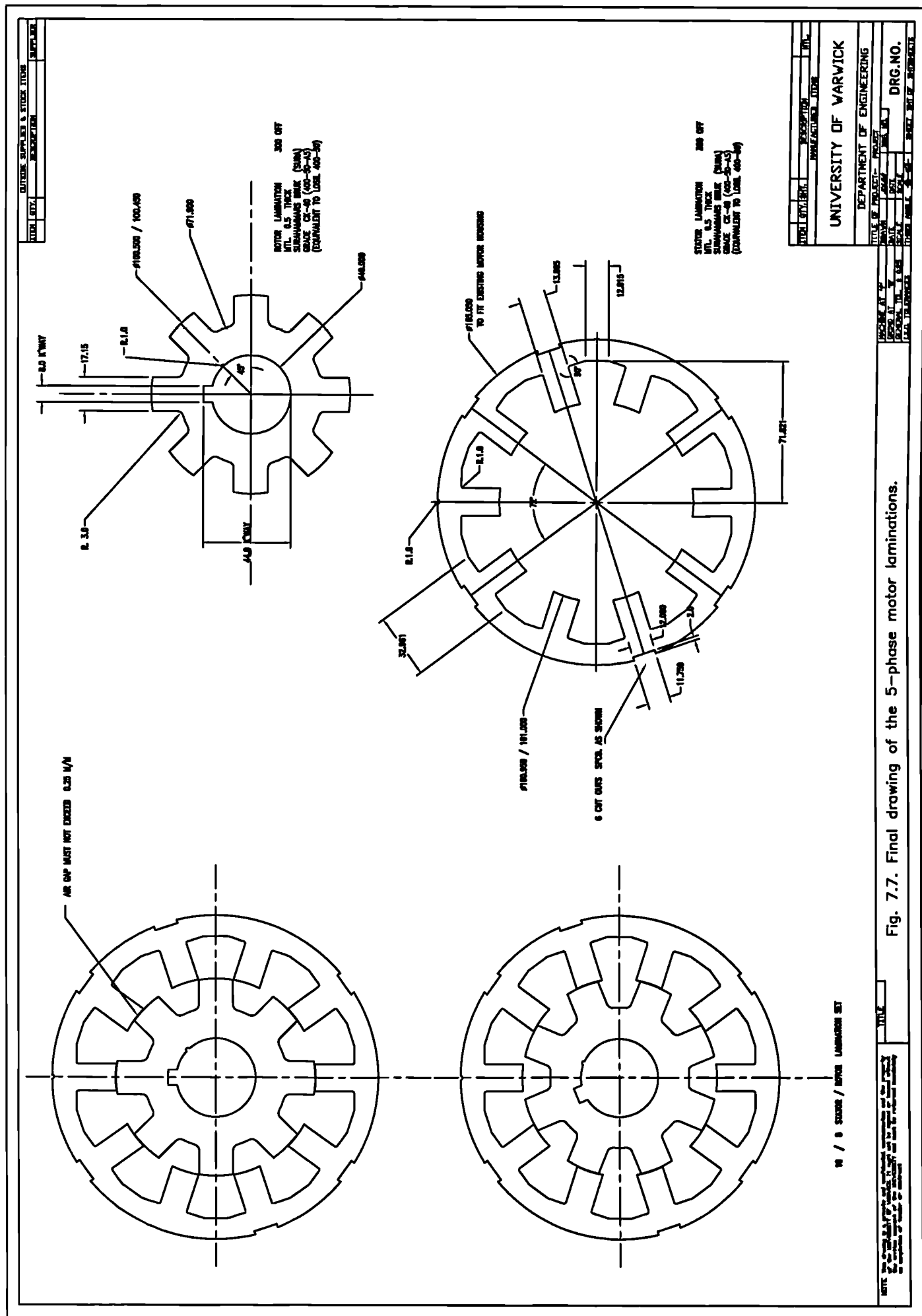
The choice of silicon steel grade to be employed in a switched reluctance motor is dependent on the number of phases (i.e. fundamental frequency of excitation) and the motor rated speed. High speed machines employ low loss TRANSIL grade steel in order to limit eddy current losses. Low speed machines employ NEWCORE grade steel which is highly permeable in order to reduce copper losses. The 5-phase switched reluctance motor can be configured for short flux loops. This excitation pattern reduces core losses substantially. The need for expensive TRANSIL grade steel was therefore removed. A LOSIL 500-50 (0.5mm in thickness) grade, which is between the NEWCORE and TRANSIL grades, was readily available from European Electrical Steels and was considered suitable for use in the construction of the 5-phase prototype.

Figure 7.7 illustrates the final drawing drafted for the 5-phase switched reluctance motor, and Table 7.1 lists the full specification. The number of turns per phase was set to 160; the maximum current level in the winding was not to exceed 15A.

7.2 5-phase motor construction.

7.2.1 Construction procedure.

The 5-phase motor laminations were laser-cut from long sheets of silicon steel. SUBCON laser cutting undertook the fabrication of the laminations. The laminations were cut to a guaranteed tolerance of 0.1mm. However, the specified guaranteed tolerance was not satisfactory for critical dimensions such as the stator bore, d_b , and rotor diameter, d_r . Dimensions d_r and d_b set the length of the airgap which was designed to be 0.25mm. Within the specified tolerance the airgap could be reduced to 0.05mm or increased to 0.45mm; this was unacceptable. SUBCON, however, agreed to cut sample laminations which were sent to Warwick for inspection. 'Batch production' commenced once all dimensional requirements were



met, and the quality of the laser cut was up to standard: free of burrs and burns.

number of stator poles	10
number of rotor poles	8
stator diameter	165 mm
stator pole arc	0.275 rad
stator pole height	20 mm
airgap length	0.25 mm
rotor diameter	100 mm
rotor pole arc	0.34 rad
stack length	150 mm
turns per phase	160
maximum phase current	15 A
maximum supply voltage	600 V

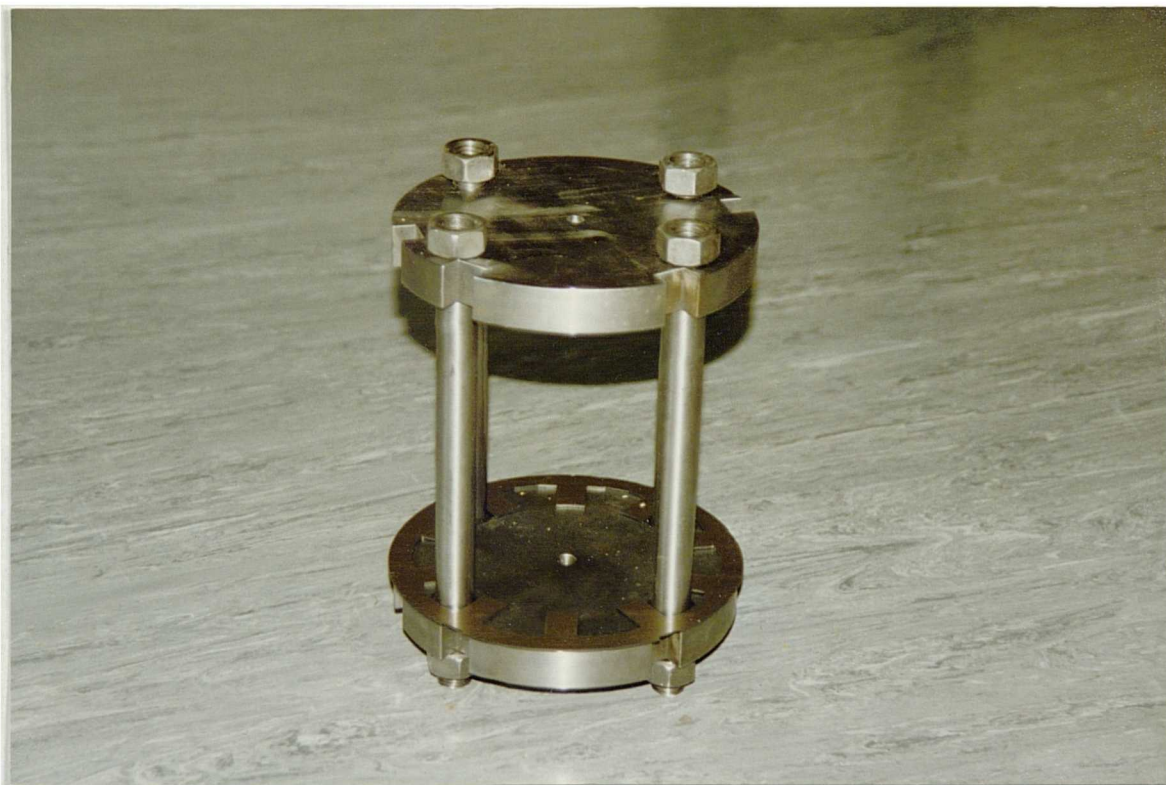
Table 7.1 Dimensions of the experimental 5-phase motor.

A stacking fixture, shown in fig. 7.8, was made in order to stack the stator laminations. The fixture consisted of two parallel plates through which four circular cross-section bars run. Each bar located at two points on the stator lamination: on the side of a stator pole and yoke section. This arrangement ensured that there was no skew on the stack. The mechanical fixture allowed access to the circumference of the stator laminations.

It was thought initially that the stack could be held together by spring-steel strips, located in the pre-fabricated grooves on the outside diameter. This was a 'clean' method that is successfully adopted in induction motors. However, the facilities

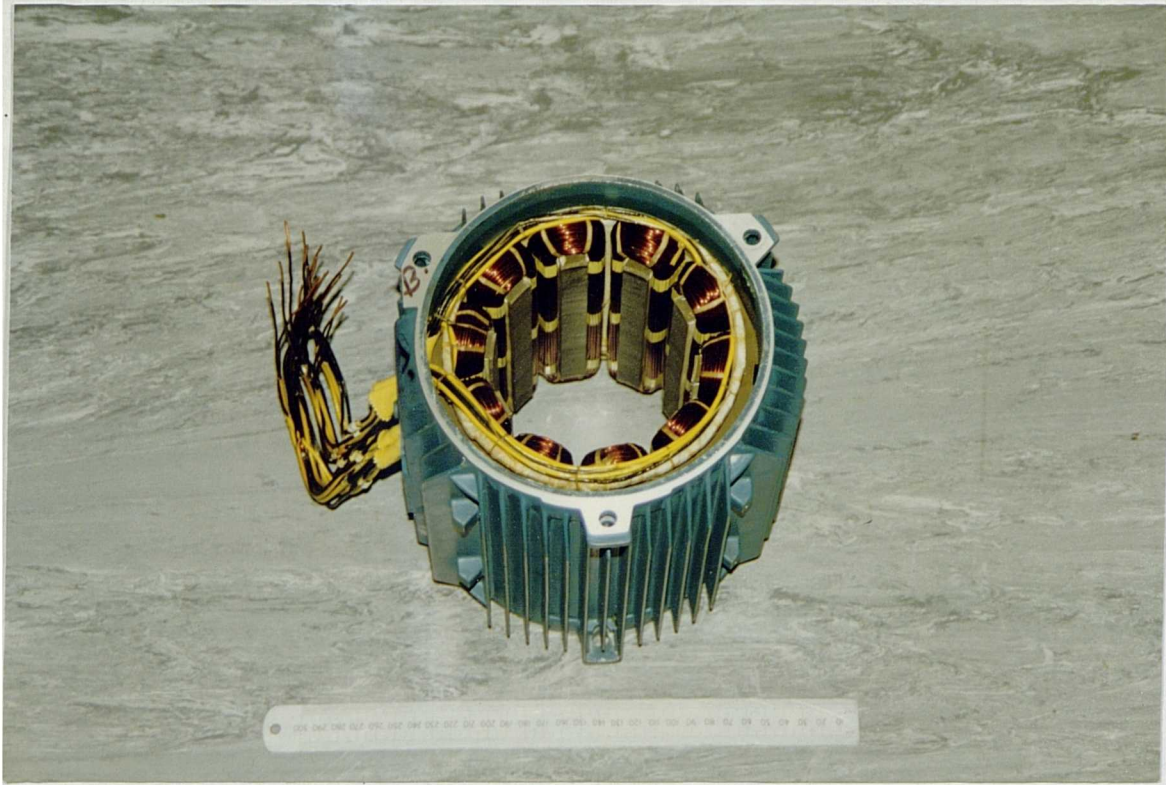


Stator and rotor laminations.

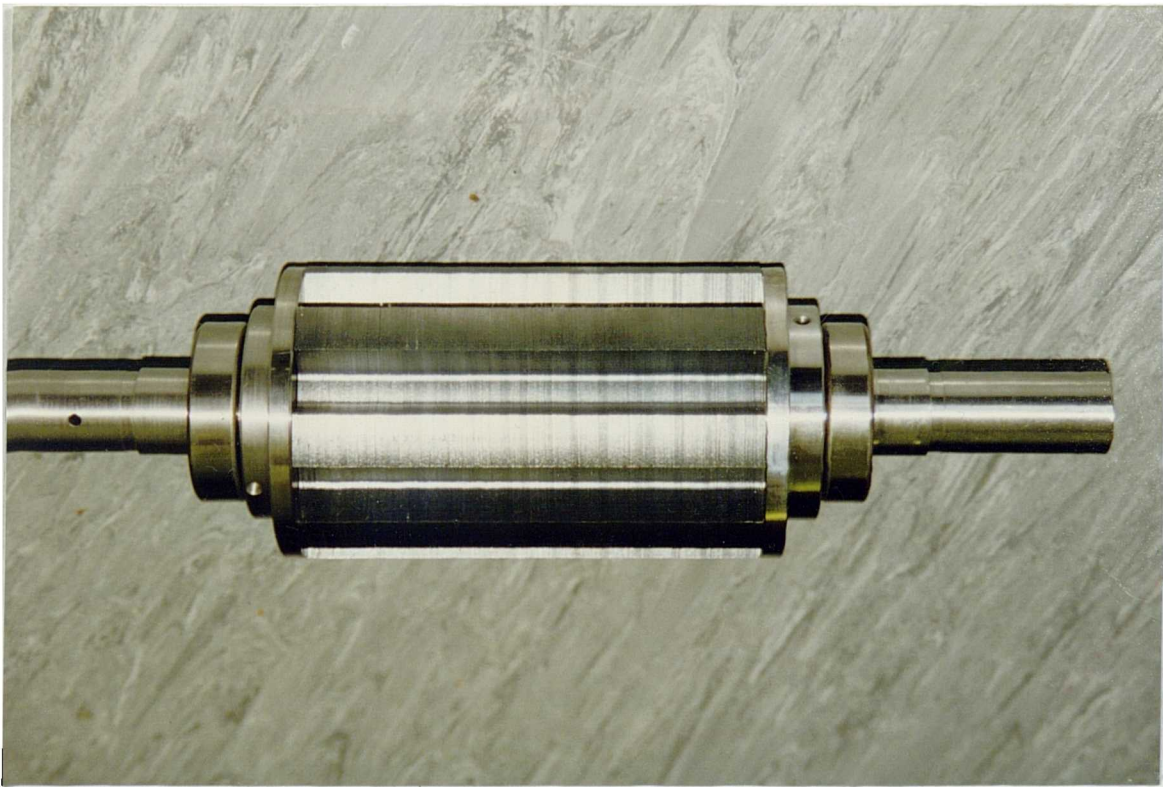


The stacking fixture for the stator laminations.

Fig. 7.8 The 5-phase motor construction process through a set of photographs.



The wound stator assembly.



The rotor assembly.

Fig. 7.8 (cont.) The 5-phase motor construction process through a set of photographs.

at Warwick workshops proved inadequate to fit the strips firmly in place. 'This job was also made difficult by the unevenness of the grooves, presumably caused by the poor laser-robot repeatability. Therefore, once the stacking fixture plates were pressed on, the laminations were welded at two points on the outside diameter. The quality of the MIG weld proved poor in comparison to resistance welds adopted on a manufacturing process in industry. A stacking factor of 0.945 was achieved for the stator stack.

The 5-phase motor outside diameter and stack length was designed to shrink-fit into a standard D112 induction motor frame. The aluminium cast frame was supplied by Electrodrives Ltd. The assembly procedure involved heating up the frame to 100°C at which temperature the aluminium expanded and the stator stack was pushed in. The arrangement was left to cool at room temperature and the aluminium frame contracted to fit onto the stack. Once the lamination assembly was rigid, the mechanical stacking fixture was dismantled. Subsequently, 80 turns of 1.32mm diameter copper wire were wound around each stator pole. The slot fill factor of 0.45 estimated by the SRDESIGN program was achieved.

The rotor laminations were stacked on the shaft and located on the shaft key. The laminations were subsequently pressed into position using two steel endplates. Endcaps placed on each end of the stack ensured that the rotor laminations were held firmly in place. A stacking factor of 0.93 was achieved for the rotor stack assembly.

7.2.2 Potential improvements of the constructed 5-phase motor.

Welding the back of the core introduces paths for eddy currents to flow and potentially degrades material properties at the weld area. Holding the stack with spring-steel strips would be preferable.

The copper slot fill factor of 0.45 that was estimated in SRDESIGN proved over-cautious. Having examined the wound stator, it was thought that 80 turns of

1.4mm diameter wire could have been wound around the stator poles, hence increasing K_c to 0.5. In addition, ample space was allowed at the ends of the stack for end windings and terminating connections. In retrospect, the motor stack length could have been increased from 150mm to 160mm.

The stacking factors achieved, though satisfactory, could be improved significantly. Stacking factors as high as 0.98 are achieved in industrial manufacturing processes, where appropriate tools are available to apply high pressure on the laminations and eliminate 'air pockets'.

All these factors would potentially improve the efficiency of the 5-phase prototype.

7.3 Measurement of flux linkage and static torque.

The static magnetisation curves at the unaligned and aligned rotor positions were measured and compared with calculated values. The measurement of magnetisation curves is based on the integration of Faraday's voltage equation, as described in chapter 2. Measurement on all phases was carried out in order to investigate the degree of potential imbalance in flux linkage (and hence torque) in the five phases. The results are depicted in fig. 7.9. It is concluded that some degree of imbalance does exist in the phase windings; the two extreme cases (phases with highest and lowest λ) are shown. Imperfections in the mechanical assembly account for this phenomenon and the results are very acceptable on the whole, considering that no subsequent stack-machining operations were performed. Figure 7.9 also illustrates the magnetisation curves calculated using two-dimensional finite element analysis. An average stacking factor of 0.94 was assumed for modelling purposes. Three-dimensional effects are not pronounced in the 5-phase prototype (such was also the case with the 7-phase prototype) because the stack length / outside diameter ratio is high. Good agreement between finite element analysis results and measurement is noted.

The predicted static torque profile is superimposed on the measured characteristic

FIG. 7.9 FLUX LINKAGE / CURRENT DIAGRAM (5-PH MOTOR, 1 PH EXCITED)

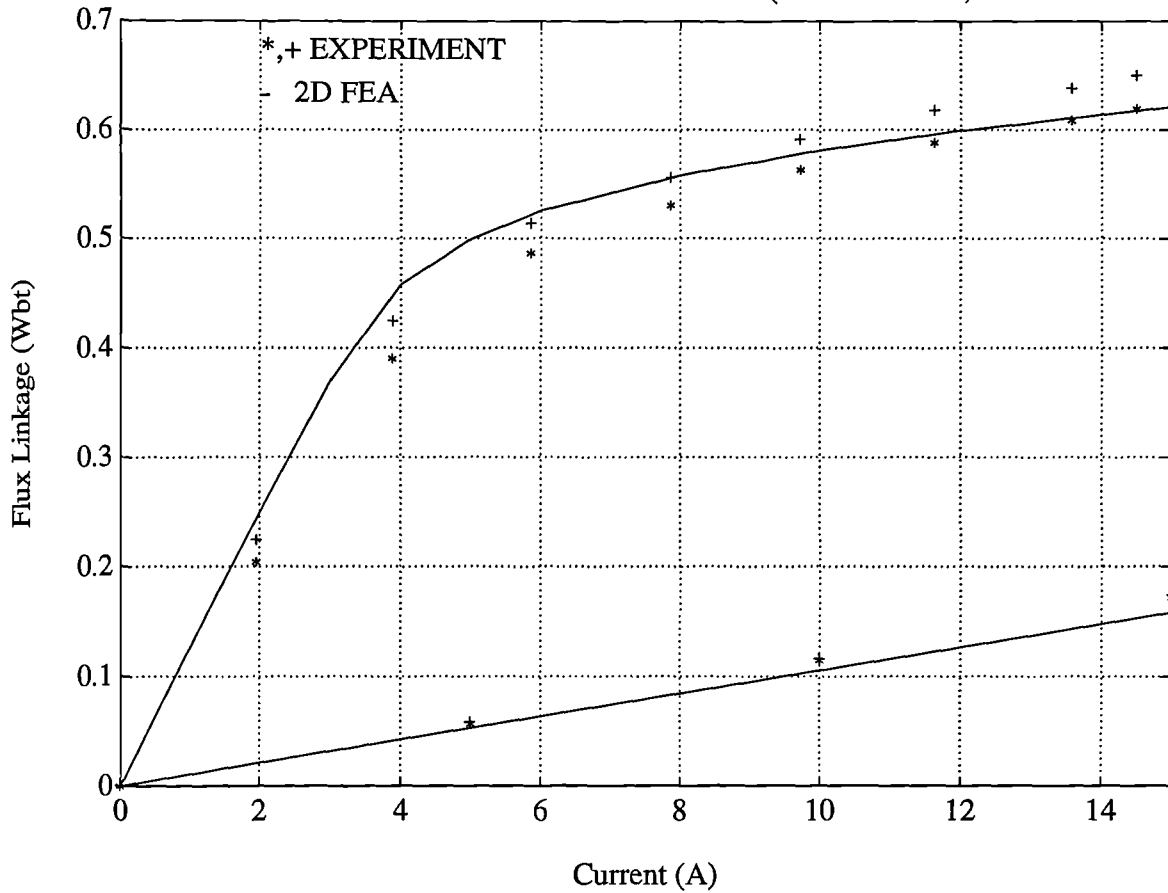
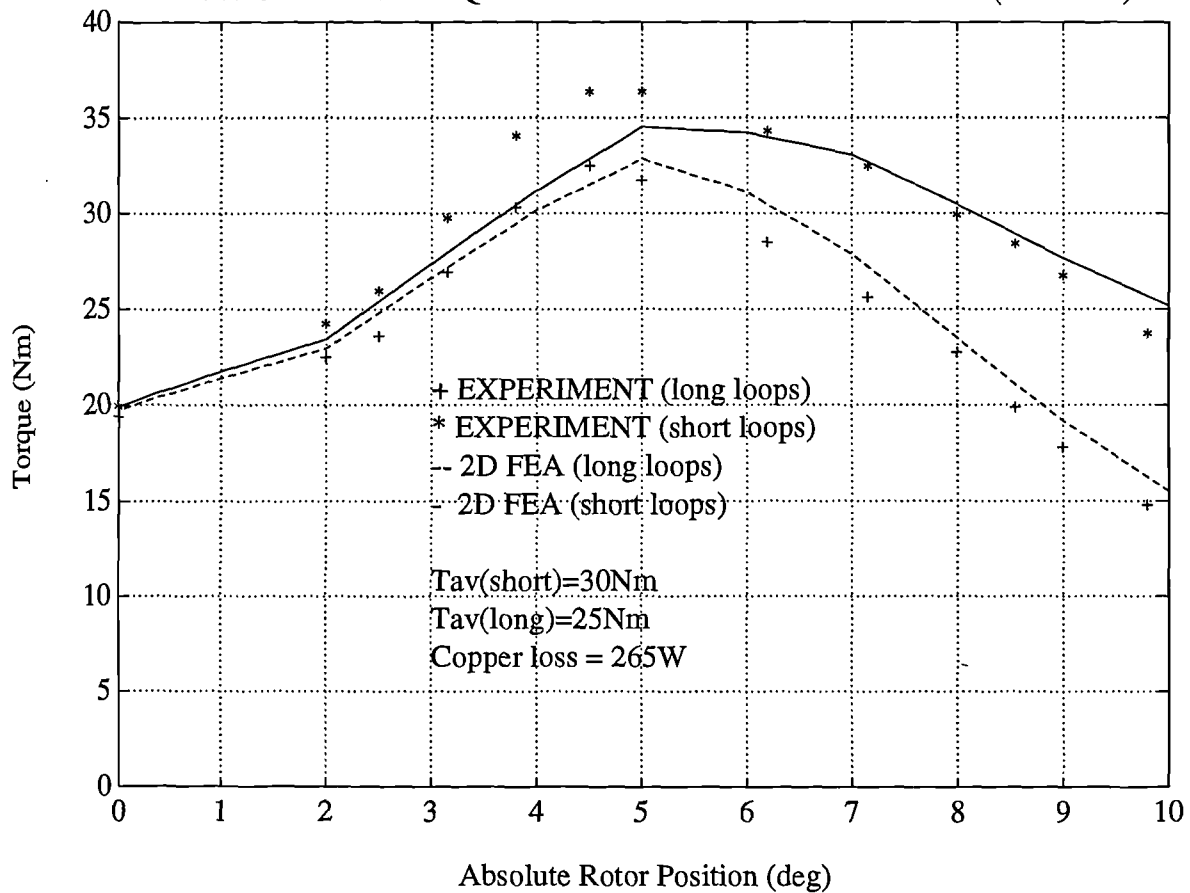


FIG. 7.10 STATIC TORQUE PROFILE FOR THE 5-PH MOTOR ($I=12.75A$)



in fig. 7.10. The T / θ characteristic was obtained by simultaneously exciting the two phase windings that were in the torque producing region with 12.75A. Short and long flux loop configurations were examined. At any rotor position, higher torque is obtained when the motor is configured for short flux paths. Figure 7.10 indicates the maximum average torque T_{av} produced at this excitation level where

$$T_{av} = \frac{1}{step} \int T d\theta \quad , \quad step = 9^\circ \quad (7.2)$$

Some error is noted between predicted and experimental results. In finite element analysis, the Maxwell stress integral was computed to yield forces acting on the rotor surface and hence torque at any rotor position. Although the mesh was refined in the airgap region, an error is expected from this computation which may be amplified when two phases are producing torque. The magnetic imbalance caused by imperfect mechanical construction may have also resulted in a discrepancy between predicted results and measurement.

7.4 Static performance comparison between the 5-phase prototype and the 4-phase Oulton motor.

For comparison purposes, the static performance of a 4-phase motor based on the ‘Oulton’ motor design was examined in finite element analysis. Unlike the 5-phase prototype, the outer diameter of the 4-phase motor was 180mm. The comparison between the 4-phase and 5-phase motors was therefore performed on a ‘torque per unit volume’ basis and for equal copper loss (ref. Appendix C). Both machines were assumed to have an airgap of 0.25mm and a stack length of 150mm.

Table 7.2 lists the results of this static performance comparison. It is interesting to note that the 4-phase motor stands to gain significantly by commutating well before alignment. This technique, first proposed in chapter 3, results in higher torque development and less copper loss. Table 7.2 confirms that, at its best, the 4-phase motor develops 17% less torque per unit volume compared with the short flux path machine. In addition, the iron losses of the 5-phase machine will be

Motor type	T_{av} per unit volume $\theta_c=18^\circ$ (Nm / m ³)	T_{av} per unit volume $\theta_c=30^\circ$ (Nm / m ³)	T_{av} per unit volume $\theta_c=26^\circ$ (Nm / m ³)
4-phase Oulton		7225	8510
5-phase short loops	10289		

Table 7.2 Static torque developed by the 4-phase Oulton and 5-phase prototype motors (equal P_{Cu} loss).

significantly lower compared with the iron losses of the 4-phase motor, because the 5-phase machine is excited with short flux paths. Manipulation of the Steinmetz core loss formulae [59] can produce an approximate comparison on the core loss per Kg exhibited by the 4-phase and 5-phase machines. The Steinmetz formulae can be written as

$$P_{Fe} = K_h f B_{\max}^n + K_e f^2 B_{\max}^2 \quad (7.3)$$

The fundamental frequency of excitation can be written as

$$f = \omega N_r \quad (7.4)$$

Constants K_h and K_e depend on material properties and active volume, and may be rewritten as

$$K_e = c_e v_o \quad (7.5)$$

$$K_h = c_h v_o \quad (7.6)$$

where v_o is the active (or 'excited') material volume, equal to the magnetic circuit length l_m times the cross-sectional area A . Geometrical considerations were used to compute the magnetic circuit length of a 4-phase long flux loop machine and a

5-phase short flux loop machine. The approximate core loss equations for the two machines were therefore found to be

$$P_{Fe-4ph} = 0.61 c_h A 6 \omega B_{\max}^n + 0.61 c_e A 36 \omega^2 B_{\max}^2 \quad (7.7)$$

$$= 3.66 c_h A \omega B_{\max}^n + 21.96 c_e A \omega^2 B_{\max}^2$$

$$P_{Fe-5ph} = 0.25 c_h A 8 \omega B_{\max}^n + 0.25 c_e A 64 \omega^2 B_{\max}^2 \quad (7.8)$$

$$= 2 c_h A \omega B_{\max}^n + 16 c_e A \omega^2 B_{\max}^2$$

These equations confirm that significantly lower iron losses are exhibited by the 5-phase motor, though this benefit decreases with speed. The cross-sectional area of the magnetic circuit, A , dictates B_{\max} and is dependent on the motor design.

The comparison did not consider temperature rise effects in the phase windings; it should be noted that the current density in the 4-phase motor was marginally lower.

7.5 Dynamic performance prediction.

SRDESIGN was used to model the performance of the 5-phase prototype under running conditions. Outlined in this section shall be the simulated results obtained for the rated voltage of 600V (rectified 3 - Ø, 415V, ac mains).

The 5-phase motor can be fed from an asymmetric half-bridge or a shared switch power converter. In either case SRDESIGN was instructed to compute optimum firing and commutation angles, using the procedure described in chapter 5. A current chopping level I_m was specified in SRDESIGN for which full load torque (25Nm) would be produced at the rated speed of 1500rpm. The current chopping level, I_m , was dependent on the type of power converter employed.

The torque / speed curve predicted by SRDESIGN, assuming an asymmetric half-

bridge converter is shown in fig. 7.11a. At each operating speed the rms current, commutation ratio, output power and losses (as predicted by SRDESIGN) are given in Table 7.3. A current chopping level of 13.425A is sufficient for the motor to produce 25.5Nm of torque at 1500rpm. The torque output is maintained fairly constant for a wide range of operating speeds. Beyond 750rpm, torque begins to fall (but not significantly) as the commutation ratio is reduced from 1.0 to 0.761 at 1500rpm. The efficiency curve for the asymmetric half-bridge powered motor is given in fig. 7.11b. It is shown that the motor efficiency climbs to above 80% at 500rpm and reaches 91% at the rated speed of 1500rpm. Every confidence was placed on the computation of copper loss at room temperature, as the phase winding resistance was computed to be equal to the measured value of 0.81Ω . However it must be pointed out that any temperature rise in the phase winding and its resultant effect on winding resistance was neglected in this exercise. An 80°C increase in winding temperature is specified as the maximum level for class B motor operation. The 5-phase motor rated rms current density never exceeds $6.5\text{A} / \text{mm}^2$. This figure is modest for a fan-cooled industrial drive [8] and winding temperature was therefore not expected to exceed the specification. It was estimated that at 1500rpm, efficiency would fall to 90.05%, if the winding temperature was to rise to 100°C .

The simulated torque / speed curve of the 5-phase prototype employing the shared switch power converter is shown in fig. 7.12a. SRDESIGN simulated performance data is given in Table 7.4. It is demonstrated that a higher current chopping level of 14.5A is required to maintain full load torque at 1500rpm. This is due to the operating requirements of this converter which result in reduced negative volts upon commutation. Therefore, in order to reduce the phase current to zero before entering the regenerative region, commutation is advanced. As a result, torque falls off faster as the speed increases, from 31.5Nm at 200rpm to 25.5Nm at rated speed. However, this requirement does not impose a penalty on the efficiency of the 5-phase motor, as fig. 7.12b suggests. The additional copper losses incurred are counterbalanced by the reduced iron loss resulting from lower operating flux densities. Efficiency is maintained above 90% at rated speed.

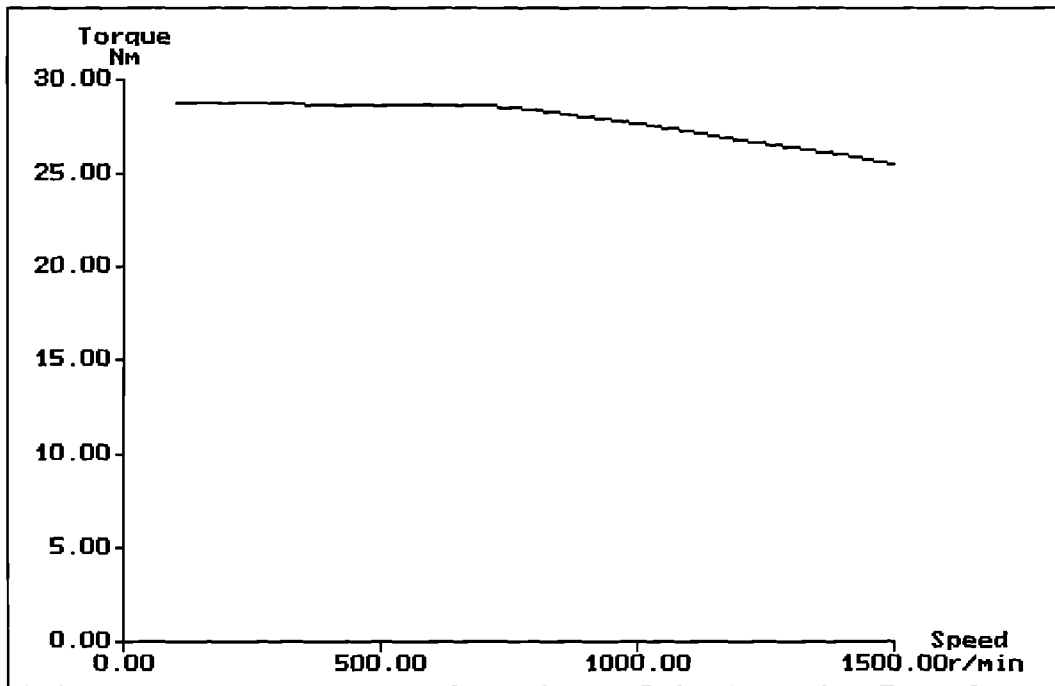


Fig. 7.11a Torque / speed curve predicted by SRDESIGN (asymmetric half-bridge converter).

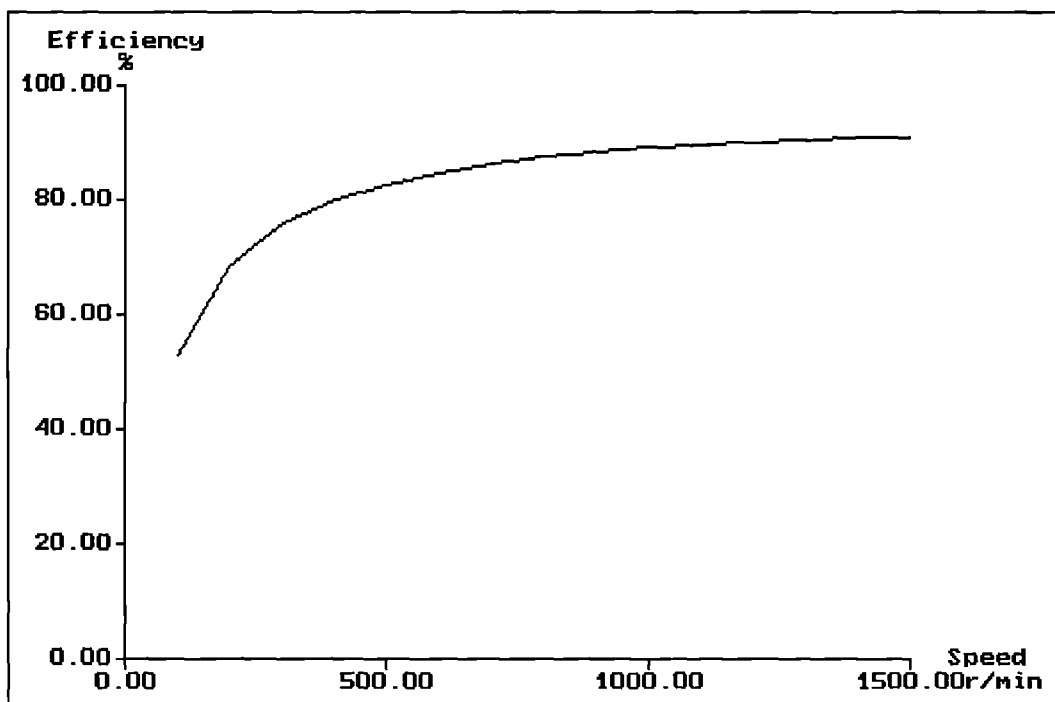


Fig. 7.11b Efficiency / speed curve predicted by SRDESIGN (asymmetric half-bridge converter).

Parameter	Value	Units
Number of stator poles	10	poles
Number of rotor poles	8	poles
Air gap length at alignment	0.250	mm
Inter-polar air gap depth	15.000	mm
Rotor diameter	100.000	mm
Stator outside diameter	165.000	mm
Stator back iron width	10.750	mm
Core length	150.000	mm
Stator pole arc	0.275	rad
Rotor pole arc	0.340	rad
Shaft diameter	40.000	mm
Supply voltage	600.000	Volts
Turns per phase	160	Turns
Chosen wire diameter	1.320	mm
Switching strategy	Normal	
Angle control technique	Automatic angle selection	
Stepping mode	Single	
Winding configuration	Short flux loops	

Speed results for phase current of 13.425A.

Speed (r/min)	Torque (Nm)	com ratio	RMS current	Pout (W)	Power Loss/W	Efficiency (%)
100.000	28.808	1.000	7.974	301.678	266.863	53.062
200.000	28.762	1.000	8.003	602.389	277.427	68.468
300.000	28.716	1.000	8.033	902.134	288.957	75.740
400.000	28.670	1.000	8.062	1200.912	301.454	79.935
500.000	28.624	1.000	8.091	1498.723	314.917	82.636
600.000	28.577	1.000	8.120	1795.568	329.347	84.501
700.000	28.620	0.977	8.050	2097.929	337.011	86.159
800.000	28.372	0.946	7.950	2376.883	342.719	87.398
900.000	27.996	0.917	7.856	2638.573	349.137	88.314
1000.000	27.635	0.888	7.764	2893.910	355.958	89.047
1100.000	27.230	0.861	7.677	3136.638	363.270	89.621
1200.000	26.801	0.834	7.593	3367.903	370.962	90.078
1300.000	26.373	0.809	7.511	3590.308	378.889	90.454
1400.000	26.017	0.784	7.429	3814.324	386.884	90.791
1500.000	25.523	0.761	7.355	4009.095	395.332	91.024

Table 7.3 SRDESIGN simulated data for the 5-phase short flux loop motor (asymmetric half-bridge converter).

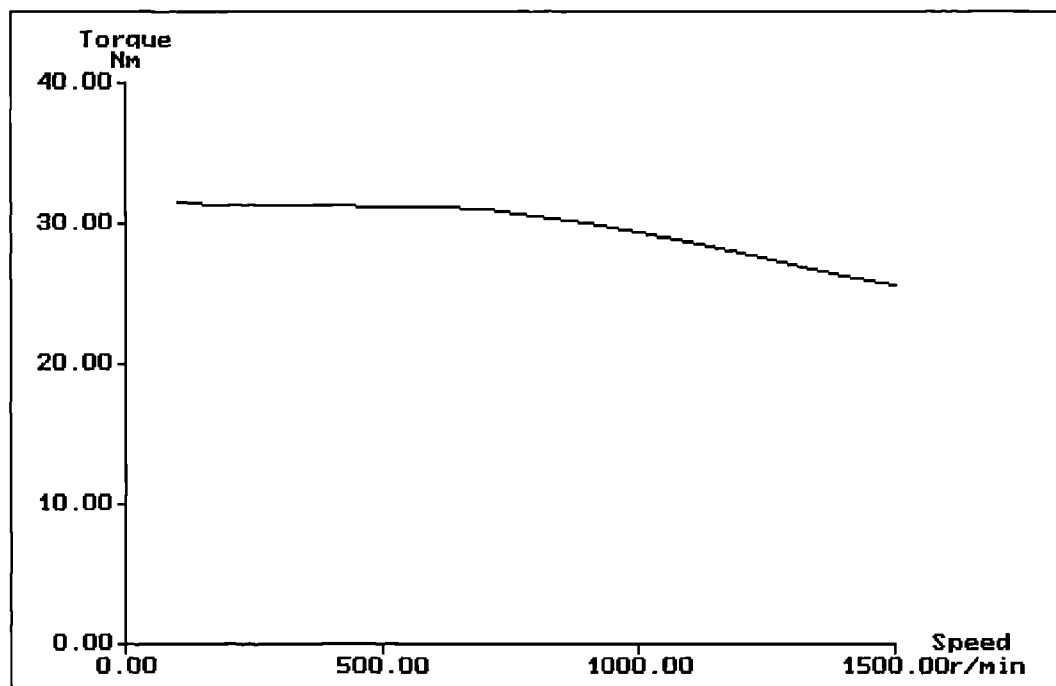


Fig. 7.12a Torque / Speed curve predicted by SRDESIGN (shared-switch converter).

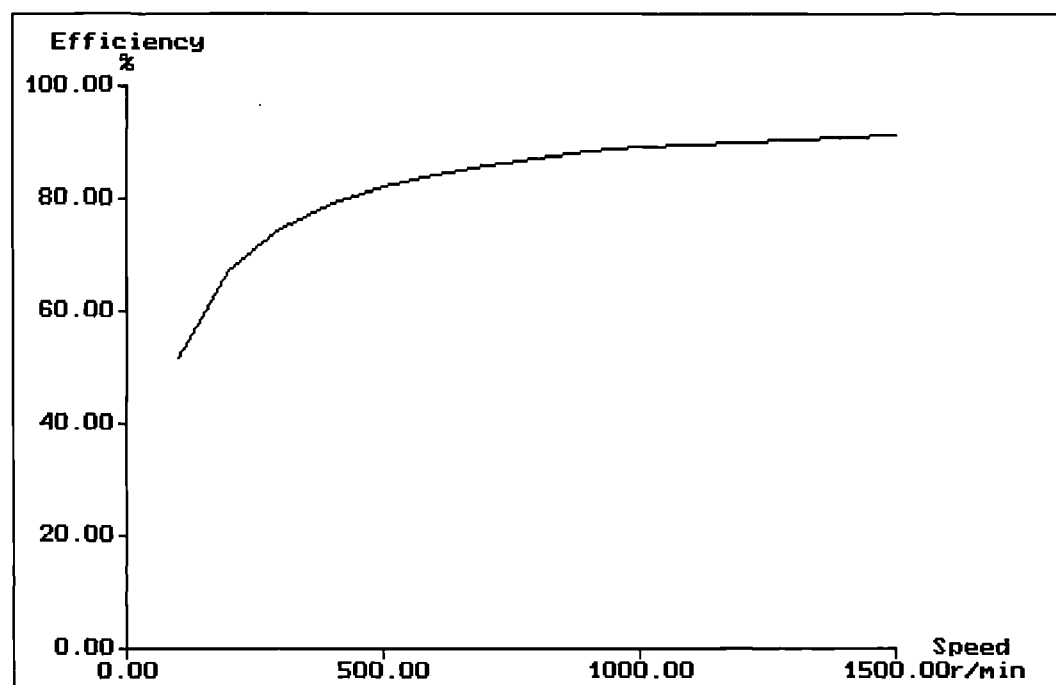


Fig. 7.12b Efficiency / Speed curve predicted by SRDESIGN (shared-switch converter).

Parameter	Value	Units
Number of stator poles	10	poles
Number of rotor poles	8	poles
Air gap length at alignment	0.250	mm
Inter-polar air gap depth	15.000	mm
Rotor diameter	100.000	mm
Stator outside diameter	165.000	mm
Stator back iron width	10.750	mm
Core length	150.000	mm
Stator pole arc	0.275	rad
Rotor pole arc	0.340	rad
Shaft diameter	40.000	mm
Supply voltage	600.000	Volts
Turns per phase	160	Turns
Chosen wire diameter	1.320	mm
Switching strategy	Novel Switching Algorithm	
Angle control technique	Automatic angle selection	
Stepping mode	Single	
Winding configuration	Short flux loops	

Speed results for phase current of 14.500A.

Speed (r/min)	Torque (Nm)	com ratio	RMS current	Pout (W)	Power Loss/W	Efficiency (%)
100.000	31.433	1.000	8.613	329.170	310.296	51.476
200.000	31.386	1.000	8.647	657.346	321.535	67.153
300.000	31.338	1.000	8.682	984.528	333.838	74.678
400.000	31.291	1.000	8.717	1310.716	347.210	79.058
500.000	31.244	1.000	8.754	1635.909	361.658	81.895
600.000	31.191	0.990	8.748	1959.814	373.656	83.987
700.000	31.012	0.949	8.600	2273.302	374.955	85.841
800.000	30.511	0.908	8.458	2556.116	376.782	87.153
900.000	29.939	0.868	8.312	2821.711	378.488	88.173
1000.000	29.332	0.827	8.164	3071.677	379.916	88.993
1100.000	28.642	0.786	8.014	3299.292	380.900	89.650
1200.000	27.804	0.745	7.864	3493.917	381.464	90.157
1300.000	26.969	0.704	7.709	3671.388	380.960	90.599
1400.000	26.116	0.663	7.553	3828.733	379.623	90.979
1500.000	25.499	0.633	7.443	4005.361	382.312	91.287

Table 7.4 SRDESIGN simulated data for the 5-phase short flux loop motor (shared switch converter).

Finally it must be pointed out that the D112 frame supplied by Electrodrives Ltd is designed to dissipate approximately 800W when cooled by a shaft mounted fan at the rated speed of 1500rpm [63]. SRDESIGN simulated data suggests that power losses are maintained below 400W, irrespective of the type of power converter employed. It therefore follows that the 5-phase prototype is capable of producing in excess of 4kW at rated speed.

7.6 Experimental arrangement.

The simulation program dictated that the 5-phase switched reluctance drive, employing either an asymmetric half-bridge or a shared switch converter, is capable of delivering 4kW at 1500rpm with a motor efficiency in excess of 90%. This prediction was based on the assumption that the power converter dc link voltage was 600V (3 - \emptyset , 415V, rectified).

A SORENSEN DCR 600V-16A power supply, capable of meeting the converter requirement, was available in the laboratory. However, it was (repeatedly!) found that this power supply could not cope with the dv / dt rates imposed by this type of load. The next option available was the Electronic Measurements TCR power supply. This supplied a maximum of 2.25kW at 300V (1 - \emptyset , 240V, rectified) and proved reliable in operation. At higher speeds two TCR power supplies were connected in parallel ('master' / 'slave' configuration) to increase the supply of current. However, the 'master' did not share current equally with the 'slave'. A peak power of approximately 3.5kW could be drawn from the power supplies. The available dc power supplies therefore imposed a limitation in testing the motor above 3.5kW input power.

The load machine (dc generator) was capable of generating 7.5kW at 1500rpm. Large resistor banks were connected across the armature terminals of the dc machine.

A schematic from the experimental 5-phase switched reluctance drive is illustrated

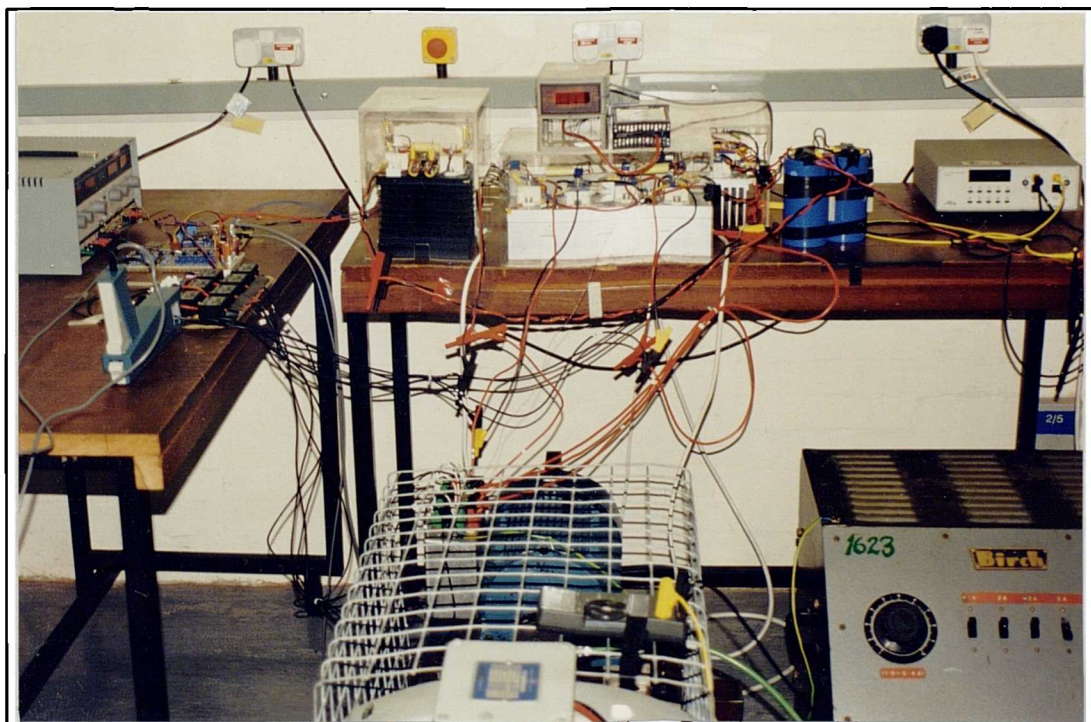
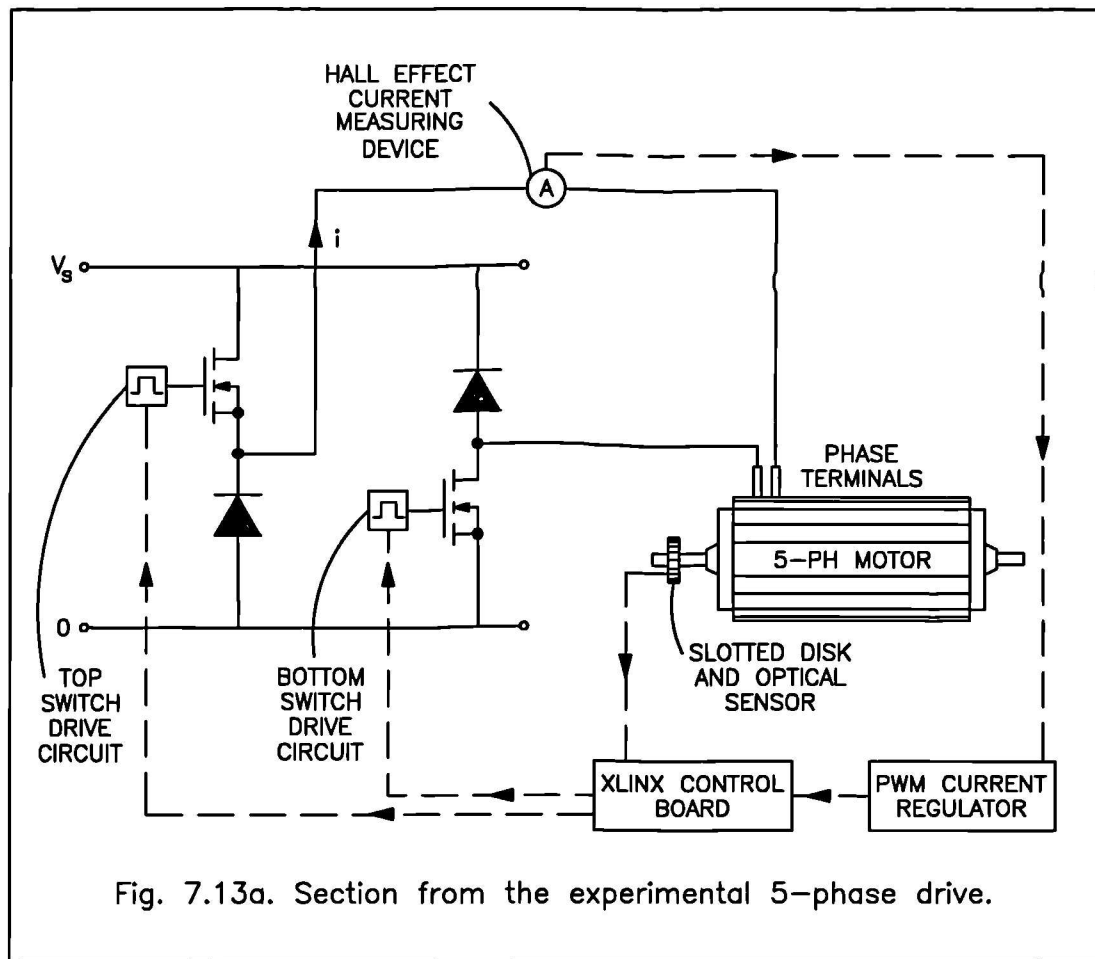
in fig. 7.13a. A photograph of the drive is also shown in fig. 7.13b. The drive employed an asymmetric half-bridge power converter with ten SKM181F MOSFET devices and associated freewheeling diodes. This arrangement provided the flexibility in operation needed to optimise the efficiency of the motor at the reduced supply voltage of 300V. Increasingly important became the ability of impressing full negative volts across the commutated phase winding, especially at higher running speeds. The shared switch converter can only supply full negative volts interspersed with zero volts upon commutation. The commutation point must therefore be advanced in order to avoid regeneration. The SRDESIGN simulation program predicted that at $V_s = 300\text{V}$ and $I_m = 15\text{A}$, the 5-phase drive would not deliver the rated torque of 25.5Nm at high speeds if a shared switch converter was employed.

All logic functions were performed in XILINX. Five optoelectronic devices in conjunction with a shaft mounted slotted disk provided rotor position feedback to the XILINX control board. The resolution of this system was 4.5° . Phase current was measured by an LEM Hall effect transducer. The current demand was compared with the measured value and the error signal was converted to a digital PWM signal and passed to the XILINX control board. The correct switching signals were subsequently fed from the control board to the gate drivers.

7.7 Test presentation.

Measurements were taken on the 5-phase motor for a range of torque loadings and operating speeds up to 1500rpm. At each running speed and torque loading, the total input power to the drive was measured in order to compute the drive efficiency. The phase current waveform and rms phase current value were also recorded. A thermocouple, fitted on the surface of a motor coil, provided an approximate value of winding temperature.

Short and long flux loop winding configurations were examined for comparison purposes. At each running speed and torque loading, the efficiency of the short



and long flux loop motor configurations was recorded for two on-state angles (ref. fig. 6.3), $\theta_{on} = 13.5^\circ$ and 18° . This choice of on-state angles was dictated by the resolution of the position sensing system. However, it was possible to alter the firing angle, θ_f (and hence the commutation point) by changing the position of the shaft mounted slotted disk with respect to the optoelectronic devices.

7.7.1 On-state angle analysis.

In order to assess the implications in drive performance of changing the on-state angle from 13.5° to 18° , measurements at a constant torque of 5Nm, 10Nm and 12.5Nm (half-load torque) were taken for the short and long flux loop configurations. Operating points of equal efficiency were joined on a torque / speed diagram. Figures 7.14a,b illustrate the performance of the 5-phase drive (configured for long or short flux loops respectively) for the on-state angle of 18° . Drive efficiency contour plots for $\theta_{on} = 13.5^\circ$ are shown in fig. 7.15a,b for long and short flux paths respectively. It is demonstrated that the long flux path configuration operates inefficiently when an 18° on-state angle is adopted. The long flux loop drive efficiency increases when θ_{on} is set to 13.5° . The short flux path configuration maintains high efficiency at $\theta_{on} = 18^\circ$, though performance is still improved by reverting to $\theta_{on} = 13.5^\circ$. This trend can be understood by examining the static torque profile of the 5-phase motor, shown in fig. 7.10. It is shown that, although short flux paths result in higher static torque output at any rotor position, the benefit is more significant as the rotor poles move toward alignment with the excited stator poles (i.e. at rotor positions toward the end of the excitation cycle). The static torque profile and the (dynamic) experimental results presented suggest that, in the short flux path configuration, performance may be improved even further (depending on speed) by choosing an on-state angle in between 13.5° and 18° . However, such resolution was not offered by the present slotted disk and optical sensor arrangement.

FIG. 7.14a EFFICIENCY CONTOURS AT HALF LOAD (LONG LOOPS, COND.=18 DEG)

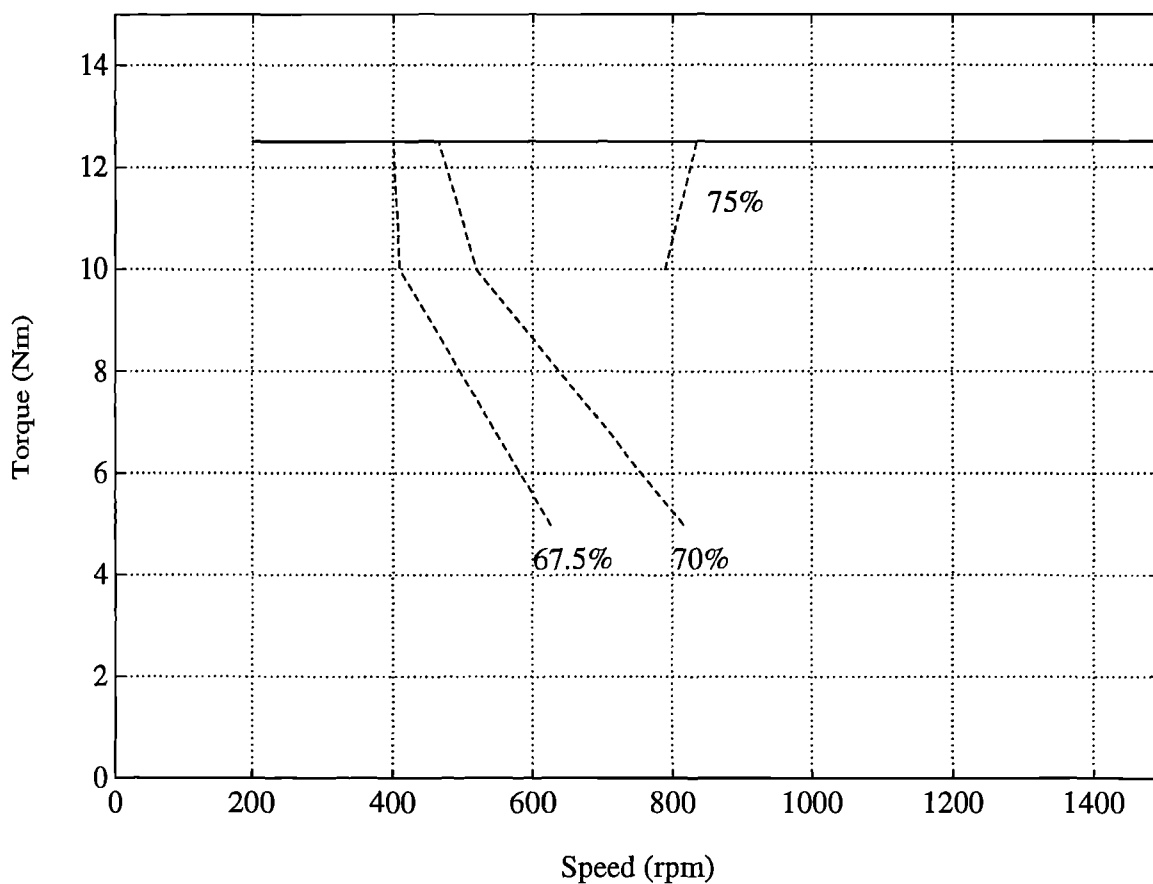


FIG. 7.14b EFFICIENCY CONTOURS AT HALF LOAD (SHORT LOOPS, COND.=18 DEG)

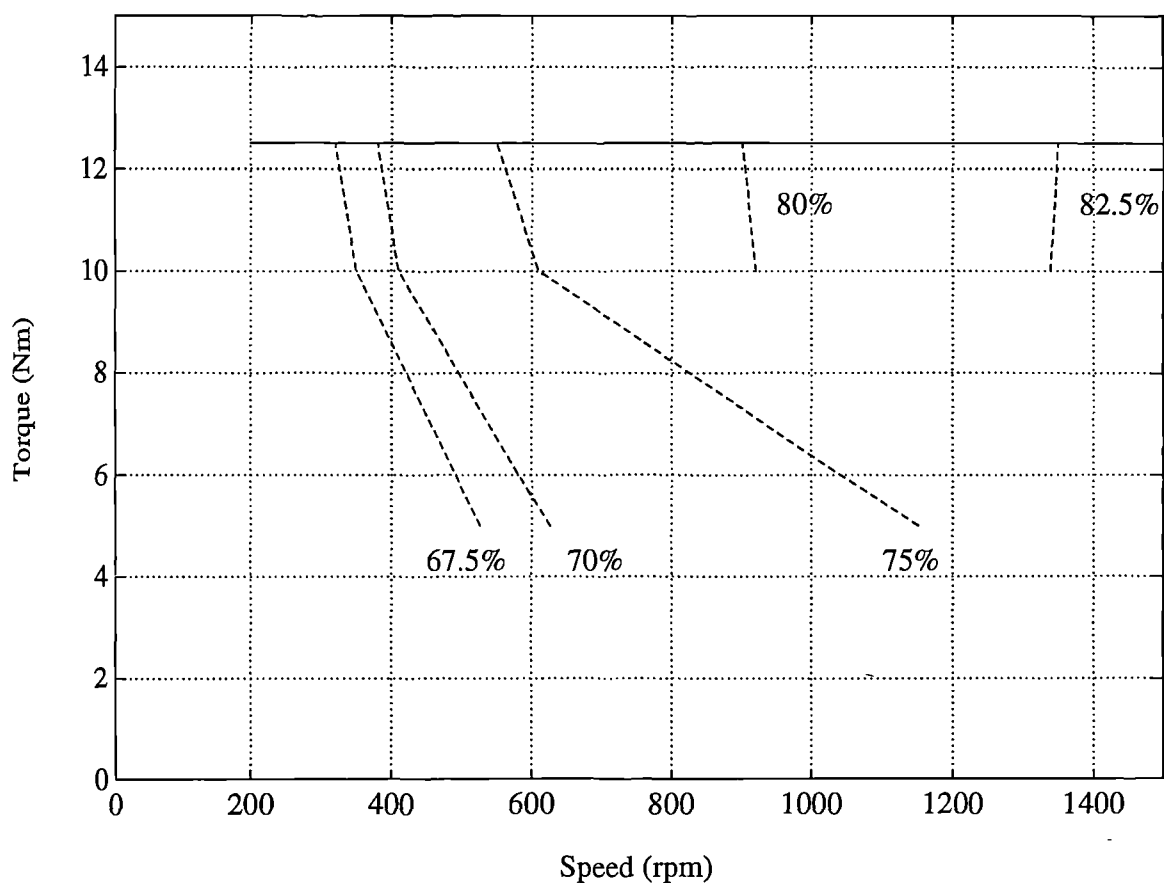


FIG. 7.15a EFFICIENCY CONTOURS AT HALF LOAD (LONG LOOPS, COND.=13.5 DEG)

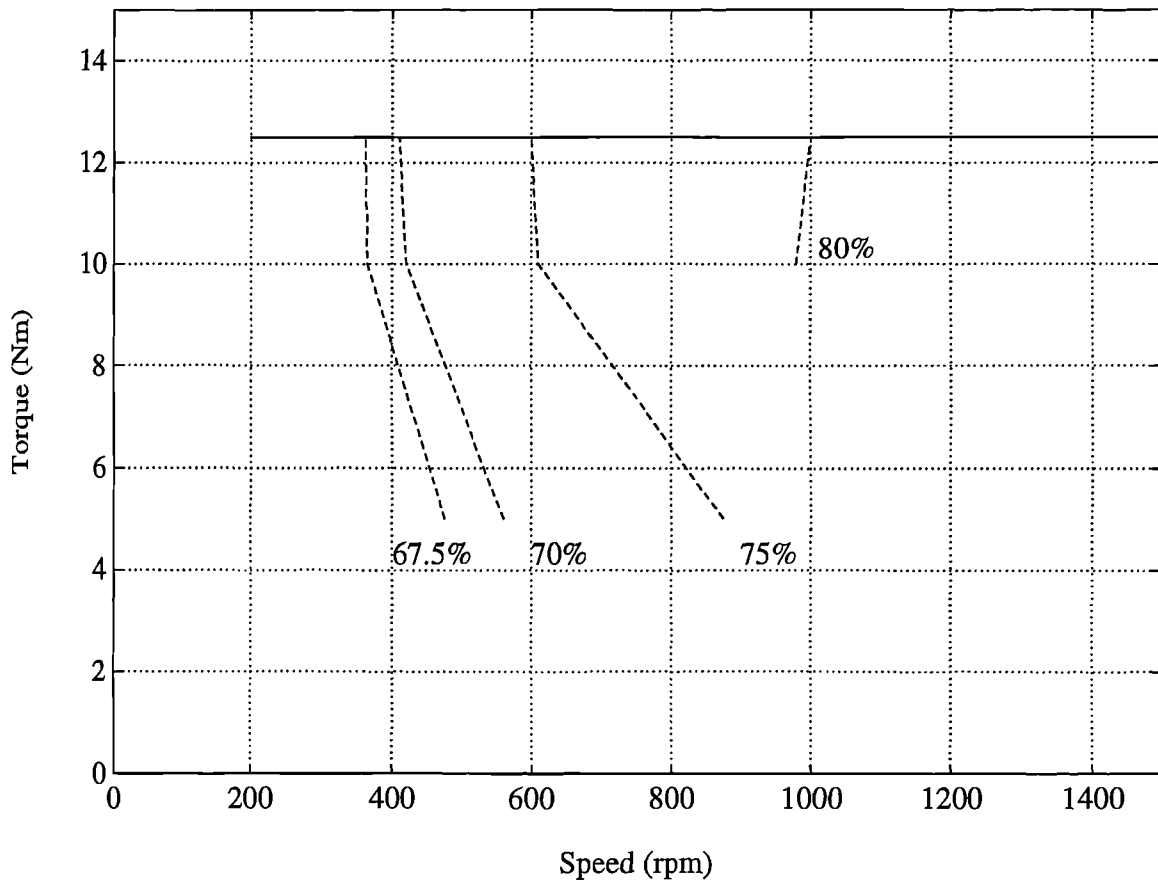
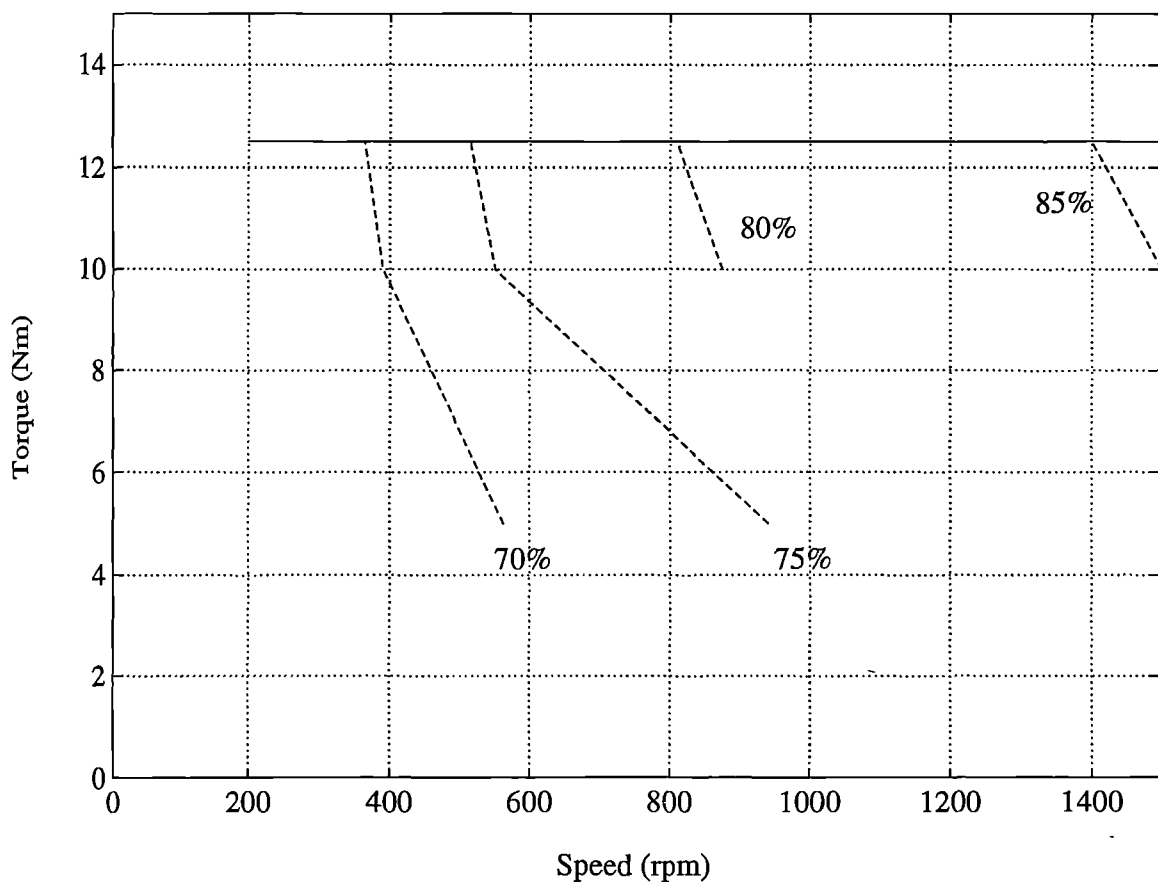


FIG. 7.15b EFFICIENCY CONTOURS AT HALF LOAD (SHORT LOOPS, COND.=13.5 DEG)



7.7.2 Maximum drive efficiency analysis.

Following on from the on-state angle analysis, measurements at higher torque loadings (15, 20 and 25Nm) were taken to examine the variation of the 5-phase drive efficiency with torque and speed. The maximum torque / speed profiles (within the constraints of the power supplies) obtained by configuring the 5-phase motor for long or short flux paths are shown in fig. 7.16a,b respectively. The profiles were obtained for a firing angle, θ_f , of 1.5° and an on-state angle, θ_{on} , of 13.5° . This firing angle was chosen because it was found that for $\theta_{on} = 13.5^\circ$, higher efficiency was obtained by retarding the excitation (making $\theta_f > 0$).

At operating speeds ranging from 200rpm to approximately 1000rpm, the current chopping level, I_m , was set to the value necessary to maintain full load torque (25Nm). Beyond 1000rpm there was not enough time for the current to rise to I_m before the onset of overlap because the drive operated from a reduced dc link voltage of 300V. In the overlap region, the back-emf severely limited the rate of rise of current and hence the torque developed. Therefore, beyond 1000rpm the average torque developed by the motor fell rapidly from 25Nm to less than 15Nm. In the 1000 to 1500rpm region, where the current followed its 'natural' profile higher torque was developed when the motor was configured for short flux paths. At lower speeds, a lower current chopping level was required to produce 25Nm when the motor was configured for short flux paths. This is confirmed by experimental current profiles shown in fig. 7.17; these were obtained at an operating speed of 900rpm. The lower current chopping level implies reduced copper loss. In addition, at any speed iron losses are decreased when the motor is configured for short flux paths hence resulting in a significant increase in motor efficiency.

In addition to the maximum torque profiles, the graphs of fig. 7.16 show contours joining the operating points of equal drive⁴ efficiency and thus indicate the

⁴Drive efficiency includes the losses in the power converter.

FIG. 7.16a VARIATION OF TORQUE AND EFFICIENCY WITH SPEED (300V, LONG LOOPS)

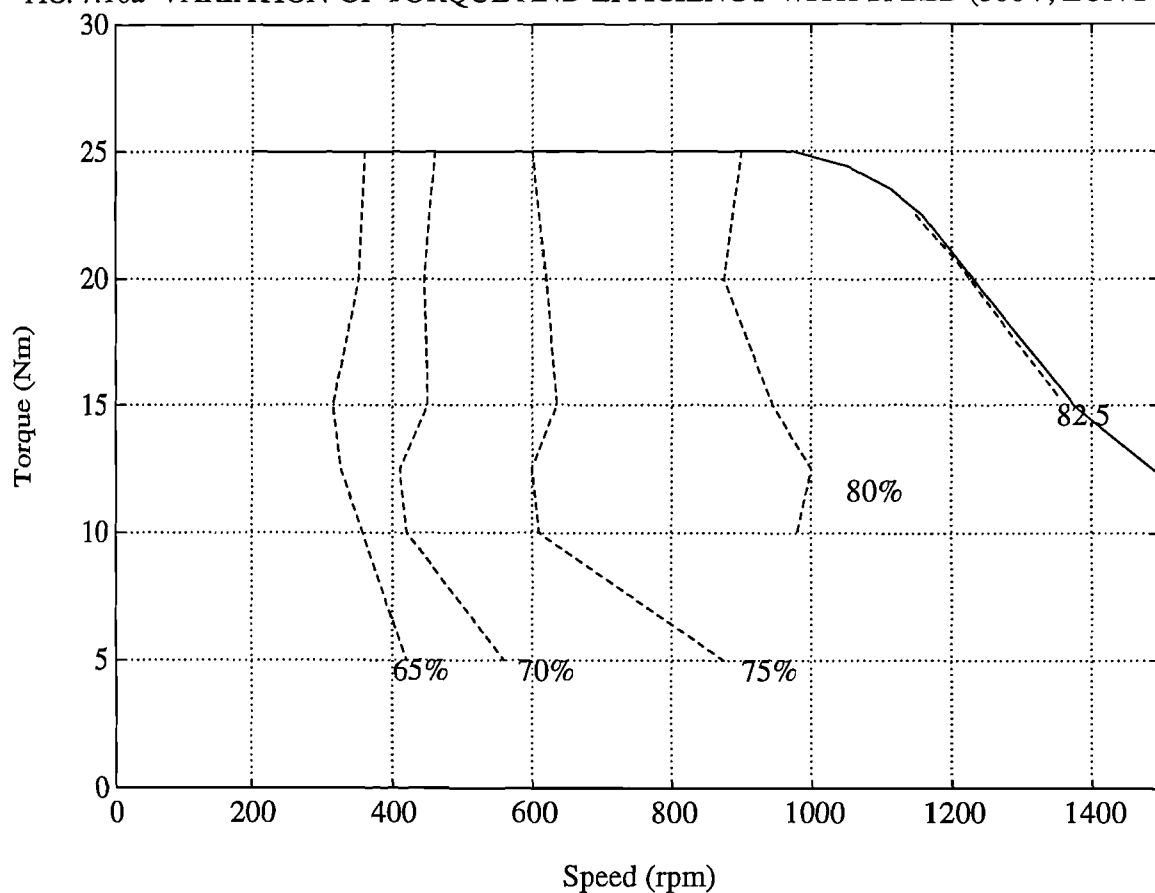
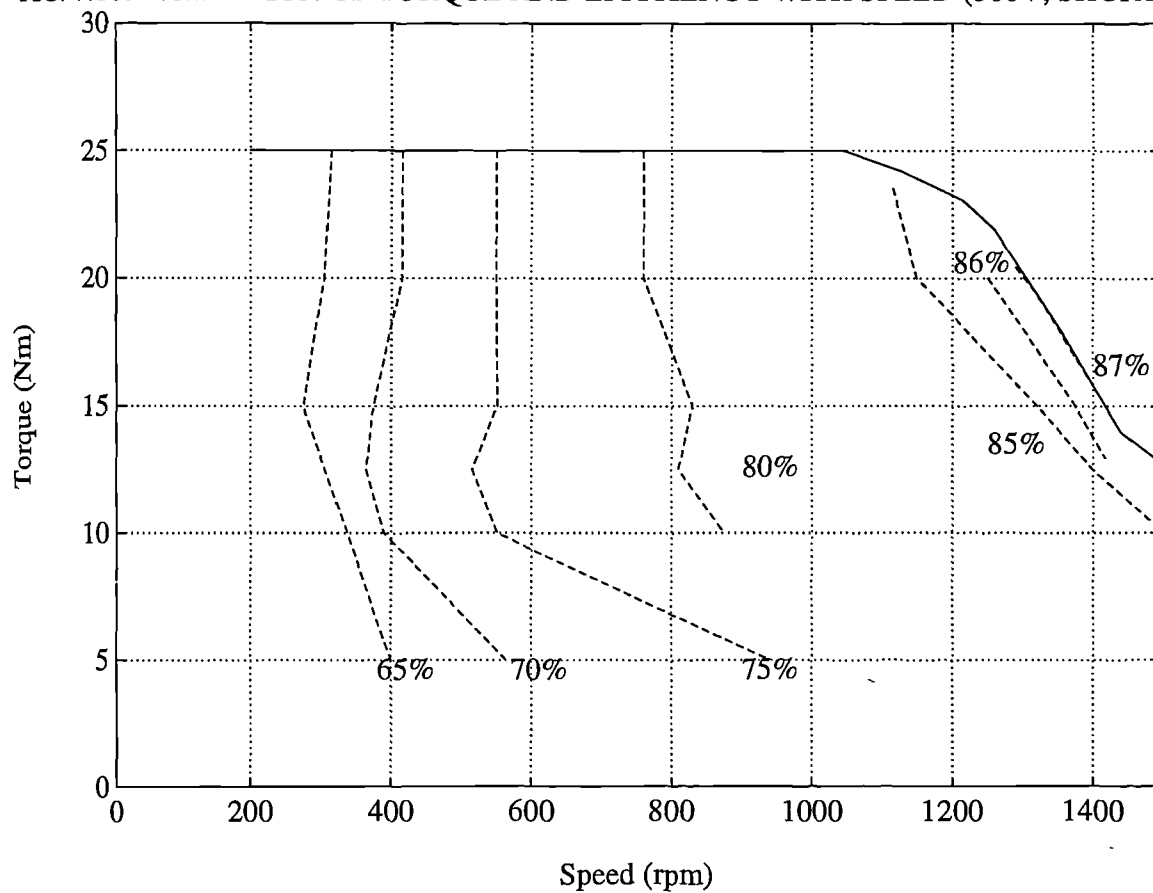


FIG. 7.16b VARIATION OF TORQUE AND EFFICIENCY WITH SPEED (300V, SHORT LOOPS)



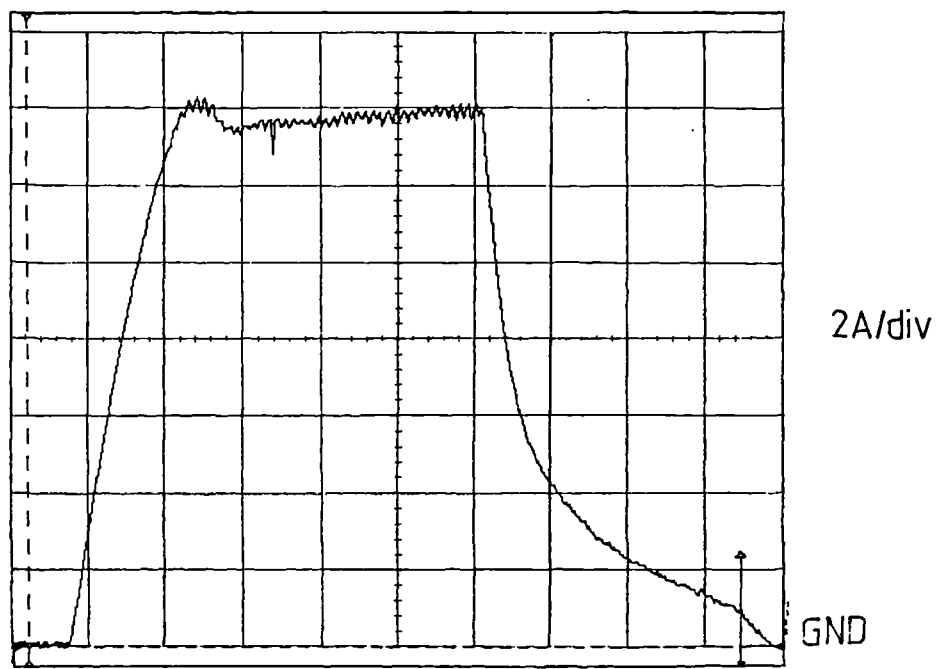


Fig. 7.17a Experimental current profile at 900rpm, 25Nm (long loops).

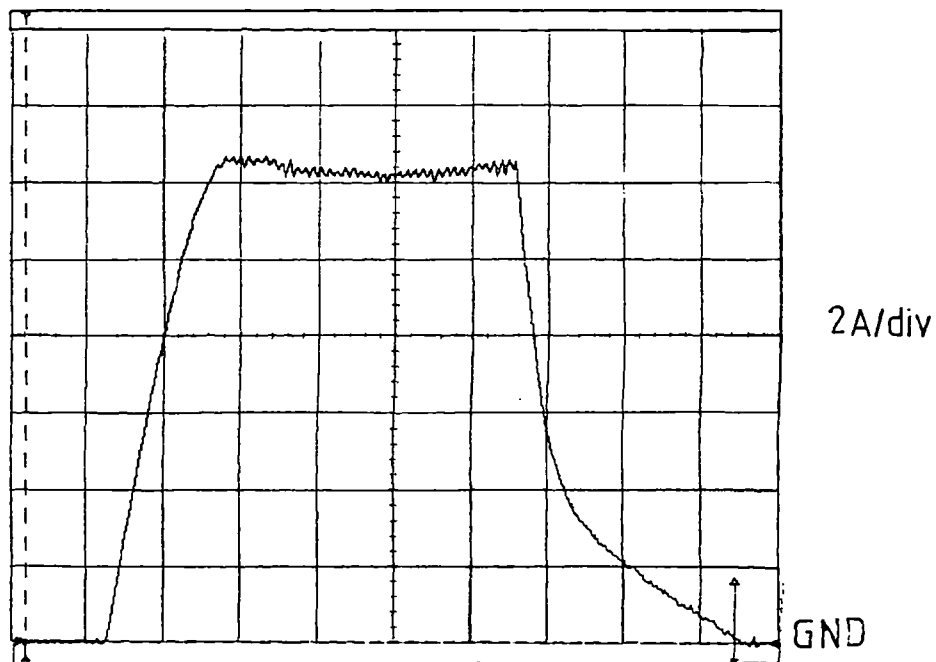
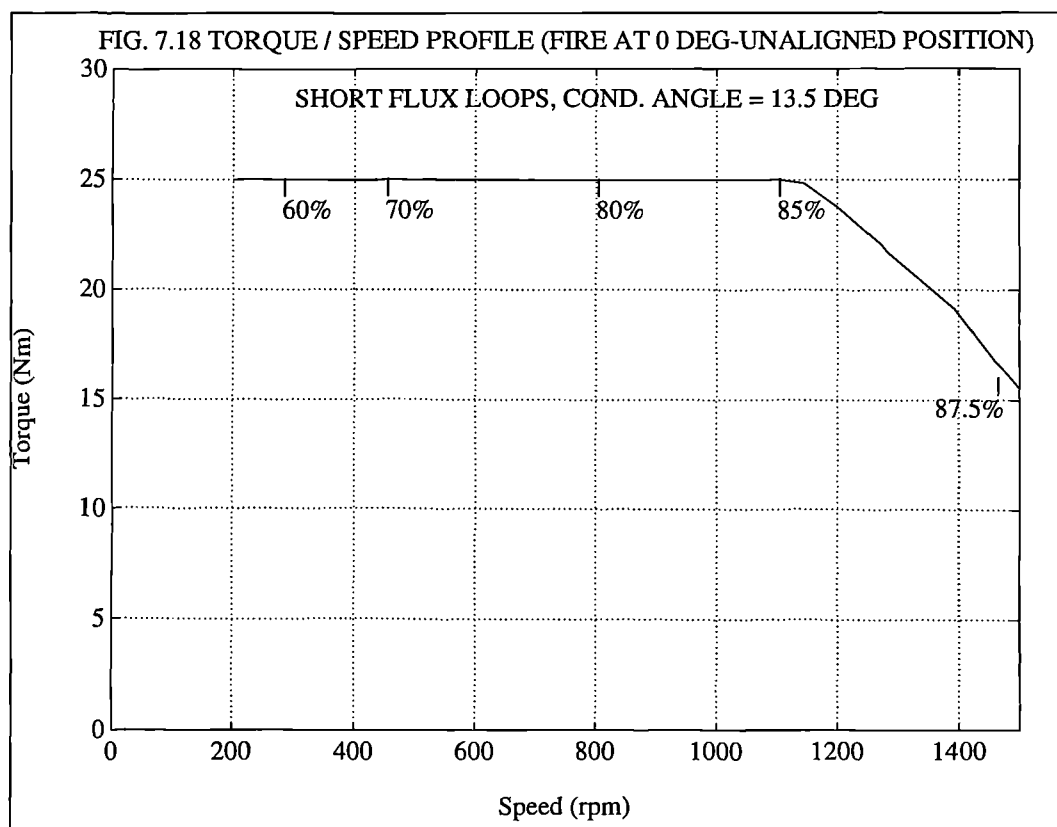


Fig. 7.17b Experimental current profile at 900rpm, 25Nm (short loops).

variation of efficiency with torque and speed. At any operating point, higher efficiency is obtained from the short flux loop configuration. At the [1300rpm, 20Nm] operating point the 5-phase drive configured for short flux loops achieves an efficiency of 87%. There is also a general tendency (subject to experimental error) for the efficiency to increase slightly with torque, but more significantly with speed. Hence, the 5-phase drive efficiency is likely to increase further as the full load [1500rpm, 25Nm] operating point is approached.

In order to develop higher torque beyond 1000rpm the firing angle, θ_f , was set to 0° (firing at the unaligned position). This allowed more time to increase the current to I_m before the onset of overlap. The result of this exercise is shown in fig. 7.18. Comparison of the maximum torque profiles of figures 7.16b and 7.18



reveals that the experiment was successful. However it was still not possible to reach the 4kW [1500rpm, 25Nm] operating point. Beyond 1100rpm output power was limited by the maximum input power of 3.5kW that the two TCR supplies

could deliver when connected in parallel. Beyond approximately 1300rpm the reduced voltage of 300V was not enough to force maximum phase current before the onset of overlap. A maximum drive efficiency of 87.5% was recorded in this experiment at the [1450rpm, 16.8Nm] operating point.

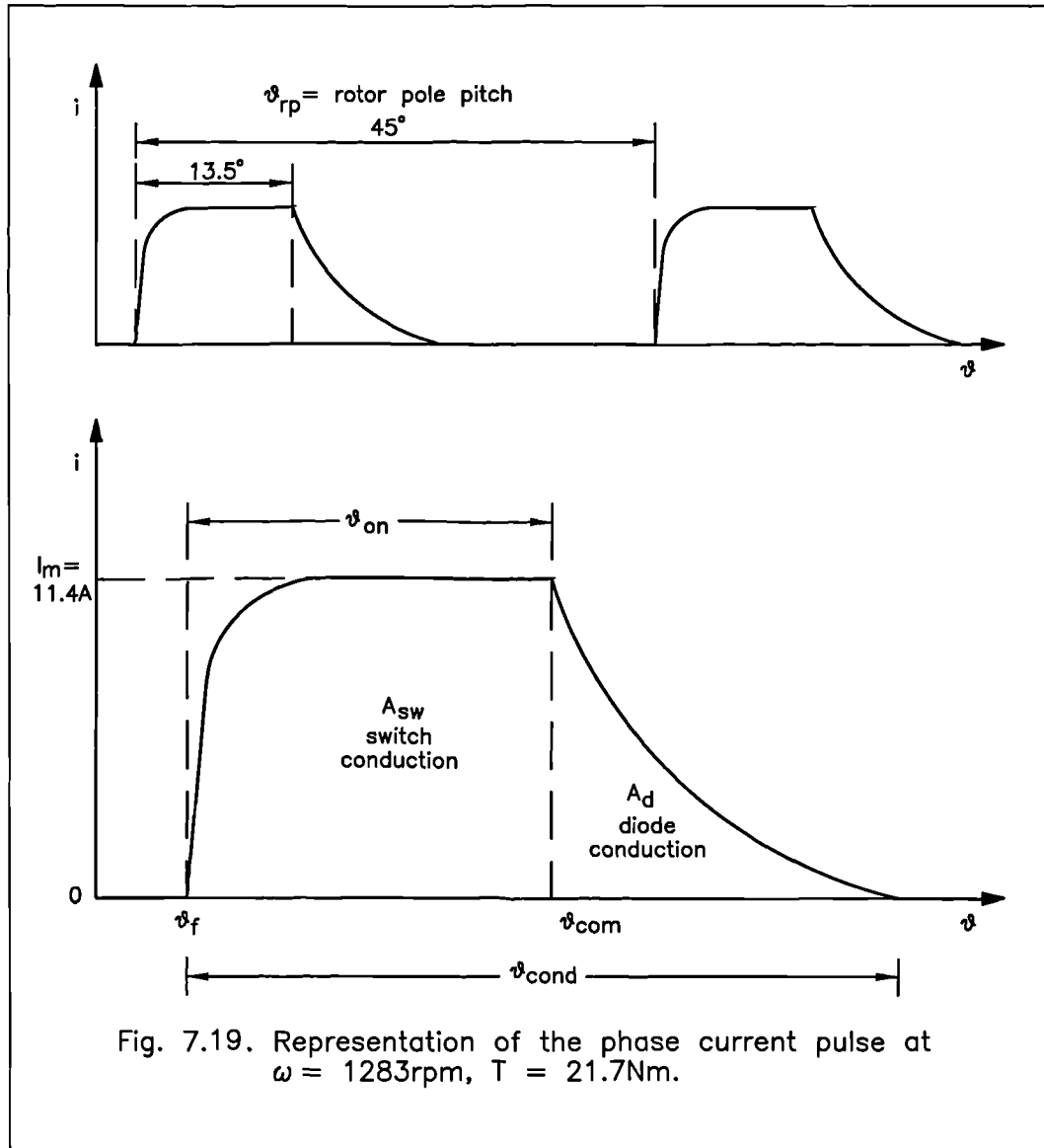
The motor frame was cooled with a shaft mounted fan. At low speeds though, fan-forced cooling is minimal. Losses are therefore dissipated through 'natural convection'. At low speeds and rated (25Nm) torque output, the temperature in the motor winding attained a steady state at approximately 80°C. This is well within the Class B operating specifications, which dictate that the winding temperature should not exceed 105°C. The temperature rise in the coil would be even further decreased, had the winding been impregnated. Winding impregnation significantly increases the rate of heat transfer from the copper to the iron. The steady state temperature of the frame at low speeds and rated torque was found to be approximately 50°C. At 1500rpm, 15Nm a steady-state coil temperature of approximately 58°C was recorded. Temperature measurements were cross-checked by measuring the resistance of the phase winding at the operating temperature, and comparing this with the room temperature resistance. This all implies that the motor is capable of producing more than 25Nm without exceeding Class B temperatures.

7.7.3 Drive and motor efficiency considerations.

Although the maximum drive efficiency contour was not reached, it was shown that the 5-phase prototype drive configured for short flux paths did achieve an efficiency of 87% at approximately 1300rpm, 20Nm. This figure is higher than the efficiency of all known prior art switched reluctance drives of the same rating. It is known that a 3-phase 12/8 switched reluctance design, currently manufactured in industry, achieves a drive efficiency of 85% at full load (1500rpm, 25Nm).

In order to obtain an approximate figure for the 5-phase motor efficiency, an estimation of the power converter loss component has been made. As an example,

the analysis for the operating point [$\omega = 1283\text{rpm}$, $T = 21.7\text{Nm}$, $\theta_f = 0^\circ$, $\theta_{on} = 13.5^\circ$] will be presented. At this operating point the phase current followed its 'natural' profile, as it was limited by the motor back-emf. Both switching devices connected across each phase winding were therefore continually conducting during the angular period θ_{on} . The current chopping regulator was inactive and hence switching losses were small and can be neglected.



The current profile can be divided into two periods: the switch conduction period and diode conduction period, as shown in fig. 7.19. The area A_{sw} , enclosed by the current profile, the horizontal datum and the vertical limits of $\theta = \theta_f$ and $\theta = \theta_{com}$

can be used to compute the rms current, I_{rms} , 'seen' by the switching devices as follows:

$$I_{rms} = I_{ave} \sqrt{\frac{\theta_{on}}{\theta_{rp}}} \quad (7.9)$$

where

$$I_{ave} = \frac{A_{sw}}{\theta_{com} - \theta_f} \quad (7.10)$$

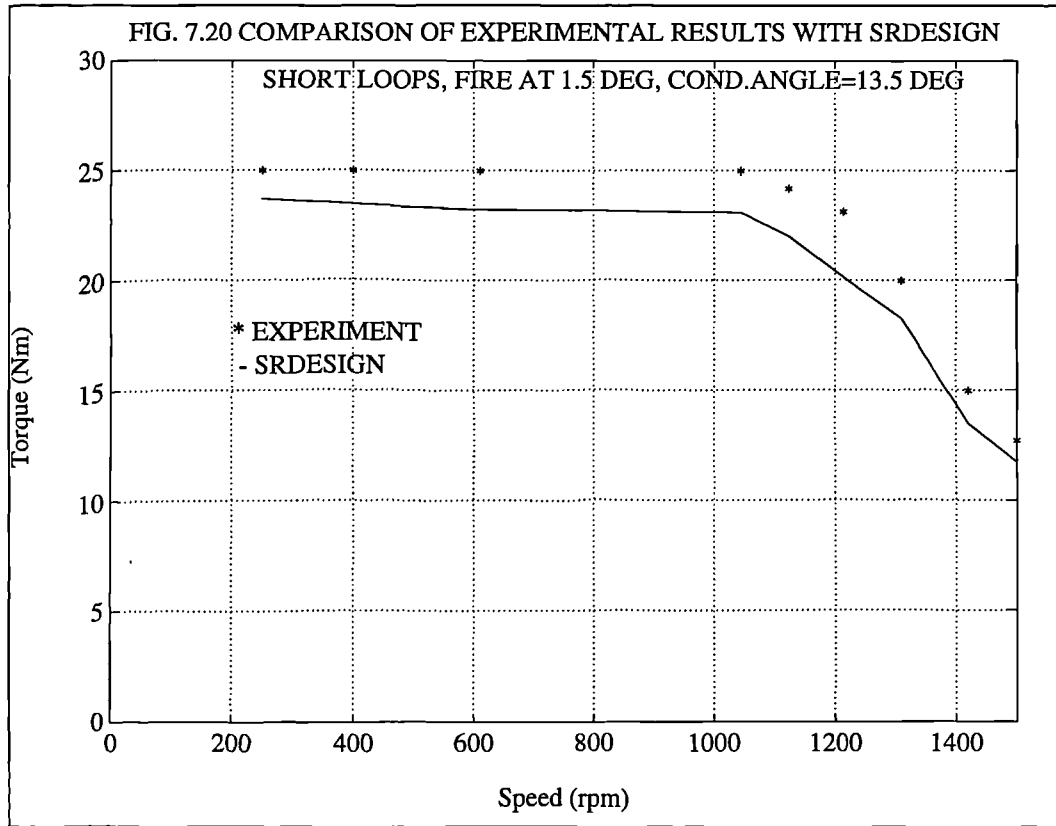
The rms current can then be squared and multiplied by the on-state resistance of the MOSFET to yield the on-state power loss in each MOSFET. The power loss in each freewheeling diode was computed by the BYT230 power loss formula (ref. Appendix B). Switching losses in the power devices and the snubbers were neglected to make this a conservative estimation. In this example, the losses in the power converter total approximately 108W. The drive efficiency at this operating point approaches 87%; the corresponding motor efficiency is therefore approximately 89.7%. Motor efficiency is known to increase with speed and therefore at 1500rpm it is expected to comfortably exceed 90%.

7.8 Comparison of experimental results with simulated data.

SRDESIGN was used for the dynamic simulation of the prototype 5-phase short flux path motor. This section aims at drawing a brief, sample comparison between experimental results and simulation data obtained from SRDESIGN, in order to reassess the accuracy of the computer program. For precise simulation, the λ / i diagram at the 'extreme' rotor positions was imported from finite element analysis to SRDESIGN.

Figure 7.20 shows the maximum torque produced by the short flux path motor, for a range of speeds up to 1500rpm. The profile was obtained at the reduced supply

voltage of 300V, and for $\theta_f = 1.5^\circ$, $\theta_{on} = 13.5^\circ$. Also shown in fig. 7.20 is the torque profile predicted by SRDESIGN. At each running speed, the current chopping level (recorded during the experiment), firing and commutation angles



were keyed in SRDESIGN. The simulation program yielded average torque within a 10% accuracy, though there was a general tendency to underestimate experimental torque values. The experimental and predicted torque profiles converged at higher running speeds. An experimental current pulse, recorded at 800rpm is compared with the SRDESIGN simulated pulse in fig. 7.21. SRDESIGN simulates the experimental phase current profile with sufficient accuracy. The rms current estimation at any speed also compares favourably with the digital oscilloscope recording. Therefore, copper loss computation within SRDESIGN is expected to be accurate. However, only motor (and not drive) efficiency can be estimated in SRDESIGN, because an algorithm has not been written to compute losses in the power converter. No comparison can therefore be drawn with experimental drive efficiency figures. SRDESIGN simulated λ / θ and

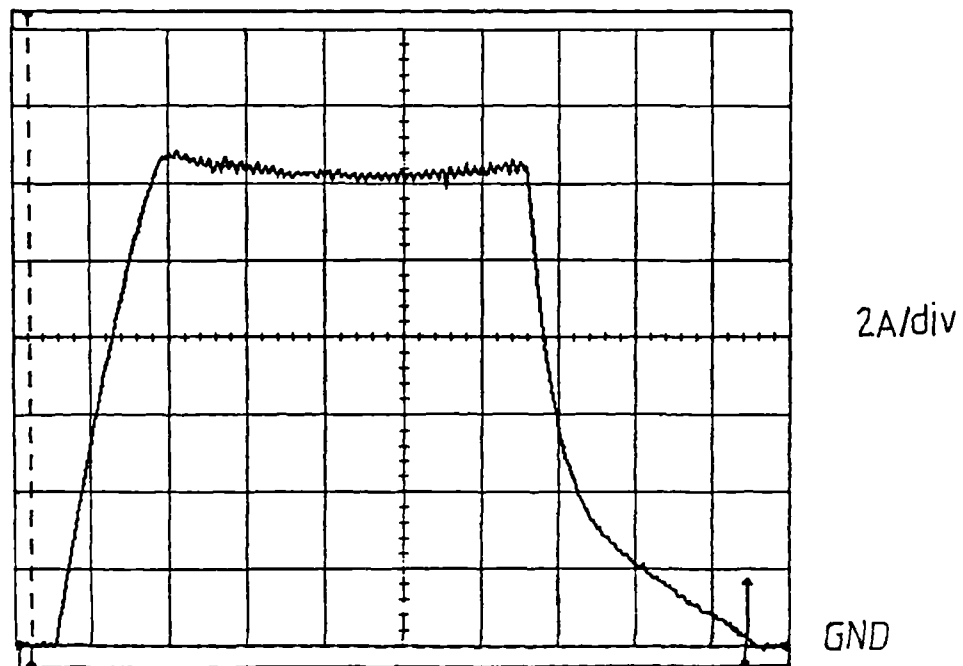


Fig. 7.21a Experimental current profile at 800rpm (short loops).

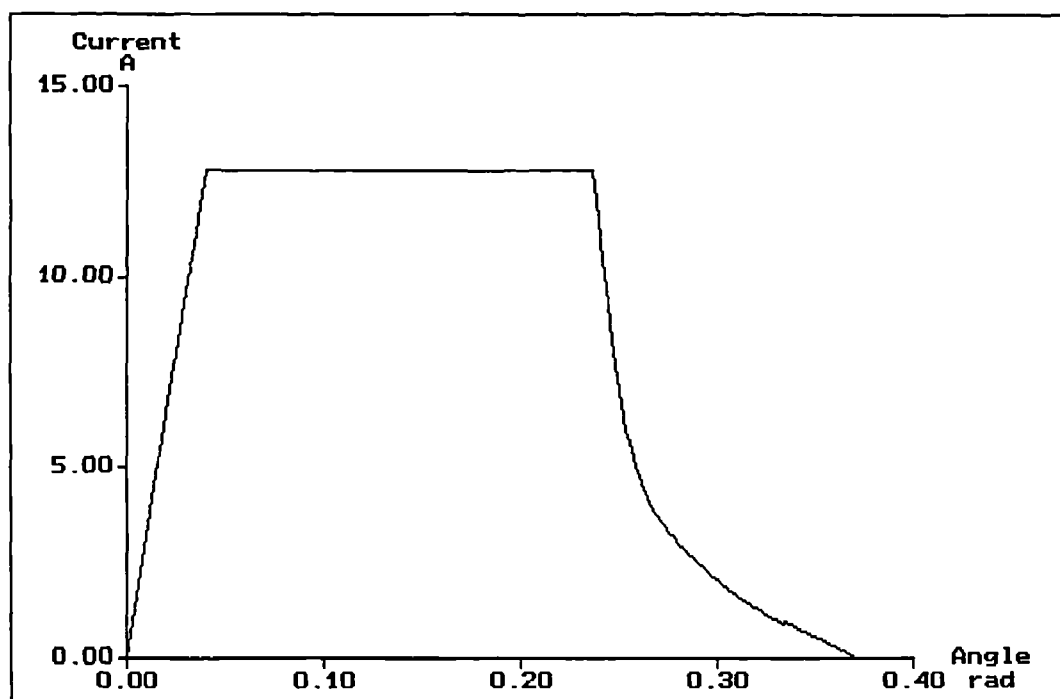


Fig. 7.21b SRDESIGN simulated phase current profile at 800rpm (short loops).

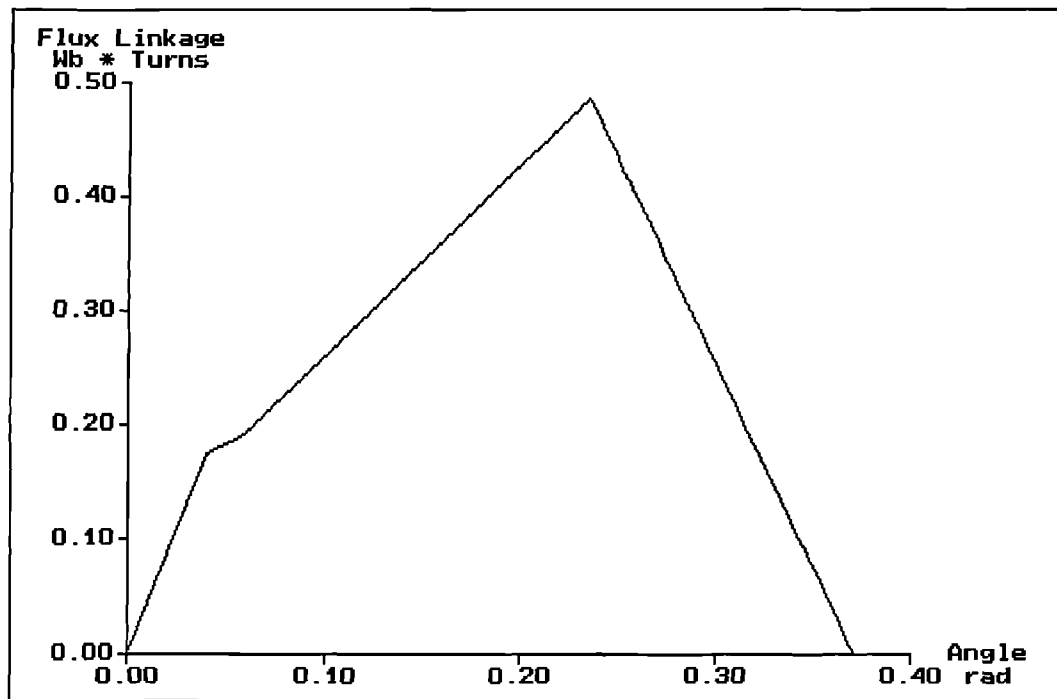


Fig. 7.22a SRDESIGN simulated λ / θ diagram at 800rpm (short loops).

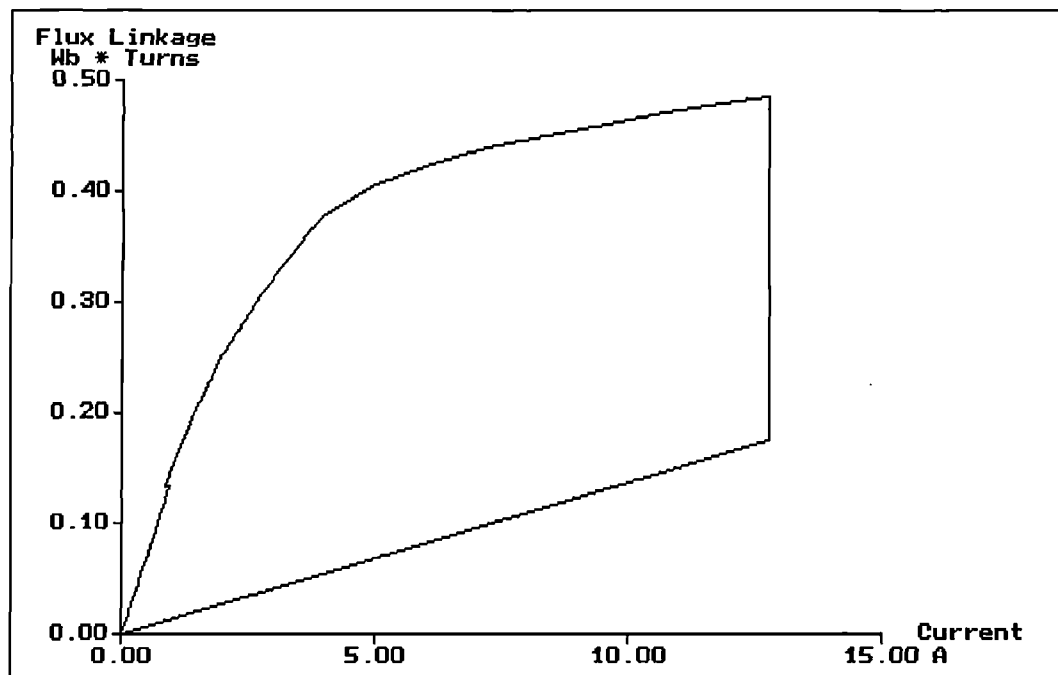


Fig. 7.22b SRDESIGN simulated λ / i diagram at 800rpm (short loops).

λ / i characteristics at 800rpm are given in fig. 7.22 for reference.

7.9 Market applications of the 5-phase switched reluctance drive.

The switched reluctance motor is identical in construction to a single stack variable reluctance stepping motor (VRM). As the name suggests, in a stepping motor the rotor moves in discrete steps. The angular rotation is determined by the number of current pulses fed to the stator winding during each revolution. There are two further stepping motor arrangements: the permanent magnet (PM) stepping motor and the hybrid stepper. The basic operating principles and characteristics of these motors are described in Appendix E.

The physical construction and / or operating characteristics of the VR, PM and hybrid stepping motors make them differ from the switched reluctance in the applications they are suited for (ref. Appendix E). In fact, the constructed 5-phase switched reluctance prototype is targeting the industrial variable speed drive market which is currently dominated by the 3-phase induction motor.

The 3-phase inverter-fed induction motor, described in Appendix F, is now well established as an industrial variable speed drive. The rugged rotor structure and simple power electronic converter have contributed significantly to its success. In terms of performance, polyphase excitation of appropriately designed stator windings produces a symmetrical rotating field which leads to smooth torque development and low noise levels. However, the stator end winding in the induction motor is long and contributes significantly to copper losses. In addition, copper losses are incurred in the rotor and are more difficult to dissipate. 'Standard efficiency' 4kW 3-phase induction machines develop 26.5Nm at 1420rpm, with a motor efficiency of 83%. The 'energy efficient' design, which uses low-loss steel laminations, achieves an efficiency of 85.3% at full load [63].

The switched reluctance motor structure is rugged and potentially cheaper to build in comparison to the induction motor. The salient pole stator has concentrated excitation windings with short end turns. The phase winding resistance is therefore reduced and the active core length occupies a higher proportion of the overall frame length than in the induction motor. There are no windings on the rotor and therefore rotor losses are lower than in induction motors. The bulk of the losses occur in the stator and can be dissipated easily through the motor frame.

	5-phase 10/8 prototype (measured) 1300rpm 20Nm	5-phase 10/8 prototype (projected) 1500rpm 25Nm	Most efficient 3-phase 12/8 motor design known 1500rpm 25Nm	Energy efficient 3 - Ø induction motor
Motor efficiency	89.75% (appr.)	above 90%		85.3%
Drive efficiency	87%	above 88%	85%	81% (appr.)

Table 7.5 Comparison of the 5-phase drive efficiency with competing induction motors and switched reluctance drives. (All constructed in D112 frames).

In addition to the switched reluctance motor advantages mentioned above, the proposed 5-phase drive offers the significant advantages associated with short flux paths. Short flux paths reduce the MMF required to establish the flux in the airgap and hence decrease copper losses. Hysteresis and eddy current losses are also decreased as the 'active' iron volume is reduced. The 5-phase switched reluctance motor was constructed inside a standard D112 induction motor frame. SRDESIGN simulation data suggested that, at the rated supply voltage of 600V and a peak phase current of approximately 13.5A, the 5-phase prototype would develop

25.5Nm at 1500rpm with a motor efficiency in excess of 90%. Experimental results demonstrated that, at the reduced supply voltage of 300V, the 5-phase motor developed 20Nm at 1300rpm with a drive efficiency of 87% and a corresponding motor efficiency of approximately 89.75%. The 5-phase prototype therefore achieved far superior performance in comparison with the 'energy efficient' induction motor before reaching the maximum drive efficiency operating point(s). Table 7.5 summarises efficiency figures for the 5-phase prototype and competing induction motors and switched reluctance drives of the same frame size.

With eight poles on the rotor low ripple torque can be achieved with the 5-phase motor. The high starting torque available shall be most useful in traction applications (crane and lift drives). The high efficiency also makes the 5-phase drive suitable for battery operated vehicles or other applications where the power / weight ratio is important and permanent magnet motors are not appropriate. However, the fundamental excitation frequency of the drive increases significantly at higher speeds and exaggerates the eddy current loss component. It is for this reason that it is thought the 5-phase drive can be established more comfortably as a variable speed drive running up to 3000rpm. In general, specialised applications are more likely to employ switched reluctance drives. This is because a dedicated power converter and control system must be designed for a switched reluctance motor. In contrast, any induction motor can operate from a standard 3 - ϕ inverter. This makes the induction motor particularly attractive, as a general purpose variable speed drive.

Chapter 8

CONCLUSION

8.1 Main conclusions and author's contribution to knowledge.

A new configuration of switched reluctance motor has been described, in which the windings are arranged to encourage short flux paths within the motor. Short flux paths reduce the MMF required to establish the **B**-field pattern in the motor, leading to a significant reduction in copper losses. In addition, iron losses are decreased because the volume of iron in which hysteresis and eddy current losses are generated is reduced.

It has been demonstrated that short flux paths can be encouraged if the phase windings of a switched reluctance motor with an odd number of phases are arranged so that adjacent stator poles have opposite magnetic polarity. In the proposed configuration, the **B**-field associated with two adjacent phase windings simultaneously excited forms a short magnetic circuit, linking adjacent stator poles via the rotor teeth.

A thorough electromagnetic analysis of doubly excited systems, which relates to switched reluctance motors operating with two phase windings conducting at any time, has been proposed. The analysis includes the effects of mutual coupling and the increased flux density, present in some parts of the steel when two phases are excited simultaneously. This electromagnetic theory of doubly excited systems was used to accurately model switched reluctance machines configured for short flux loops, as well as the more common 4-phase 8/6 machine. It has been demonstrated that the virtual work principle, applied to doubly excited systems as proposed in this thesis, yields average torque values which consistently compare favourably

with torque computed using the Maxwell stress tensor. It has also been shown that significant errors can arise if mutual interaction effects, frequently neglected by previous researchers, are not accounted for. A performance optimisation study on the 4-phase motor was undertaken. The design of 4-phase motors for low torque ripple has been proposed. A smooth torque characteristic was achieved by correct specification of critical motor dimensions (stator yoke thickness and rotor pole arc) coupled with an appropriate phase current conduction period.

Switched reluctance motor structures have been modelled using two and three-dimensional finite element analysis. Three-dimensional effects, i.e. anisotropy, end winding flux and axial fringing have been investigated. An extensive discussion into modelling of anisotropic material structures has been put forward. A series of correction charts account for end-core flux at a range of rotor positions and excitations. The value of end-core flux has been found to be heavily dependent on rotor position, excitation and magnetic saturation. The percentage increment in flux linkage due to 'end effects' was found to be maximum when the excited stator poles face the interpolar airgap depth. The percentage increment in flux linkage due to 'end effects' decreased linearly in the overlap region to reach a minimum at alignment.

The 'back bone' structure of SRDESIGN, a computer simulation program written in Turbo Pascal to characterise the dynamic performance of switched reluctance drives, has been presented. Fundamental mathematical formulations supported in SRDESIGN have been described. The accuracy of dynamic simulation data obtained from SRDESIGN was verified by testing switched reluctance drives that were available in the laboratory. In order to obtain accurate simulation data for doubly excited switched reluctance motors, λ / i diagrams at 'extreme' rotor positions (computed by implementing the proposed electromagnetic theory for doubly excited systems) were imported from finite element analysis. SRDESIGN estimated the magnetisation curves at intermediate rotor positions and yielded values for average torque and motor losses, always within 10% of the measured value. It was also asserted that the performance of singly excited switched

reluctance motors could accurately be simulated in SRDESIGN, with the λ / i diagrams at unaligned and aligned rotor positions computed within the program.

The design and development of a 5-phase 10/8 switched reluctance drive, which exploited the advantages of short flux paths, has been described. The 5-phase motor design procedure, which included new proposals for motors with two phases simultaneously excited, has been thoroughly presented. The static performance of the 5-phase motor, with the windings configured for short or long flux paths, was modelled using finite element analysis. It was shown that, for equal copper loss and reduced iron loss, the short flux loop motor configuration developed 16% higher average torque. In addition, the 5-phase motor configured for short flux paths was found to develop 20% higher torque per unit volume, when compared to a 4-phase machine based on the design of the Oulton motor.

Although the maximum drive efficiency contour was not reached, it has been demonstrated that the 5-phase prototype drive, with the motor configured for short loops, achieved an efficiency of 87% at the [1300rpm, 20Nm] operating point. This figure, which corresponds to a motor efficiency in excess of 89.7%, is significantly higher than the efficiency of all known prior art switched reluctance drives and induction drives of the same frame size.

8.2 Areas of further work.

The principal aim of this project was the electromagnetic design of a high efficiency switched reluctance motor. This aim has been achieved. However, further work is needed to realise the full potential of the 5-phase drive.

A more advanced control system ought to be designed for the 5-phase motor. The angular resolution of the position sensor ought to be improved in order to optimise the drive efficiency. In addition, speed feedback could be provided. These functions can be performed within a microprocessor-based controller.

The available dc power supplies imposed a limitation in testing the motor above 3.5kW input power. Measurements ought to be taken to establish the maximum power output of the 5-phase drive. A power supply capable of delivering 600V - 16A would be required to perform these tests. In addition, the 5-phase drive employing six power switches in the shared switch converter configuration ought to be experimentally evaluated. However, the dc link voltage impressed across the shared switch converter would need to be increased beyond 300V⁵ for the drive to develop 25Nm at a phase current chopping level of 15A.

Further work is needed to improve the computer simulation program SRDESIGN. Thermal modelling could be added to help predict the maximum continuous rating of a motor. Some form of model should be developed to predict the losses in the power converter. Information on the drive efficiency (rather than just motor efficiency) can then be conveyed to the user. An analytical procedure of predicting λ / i diagrams for doubly excited switched reluctance motors should also be developed.

⁵The EM TCR power supply that was available in the laboratory could supply a maximum of 300V.

REFERENCES

1. H. M. Noad, 'A Manual of Electricity', *Lockwood*, 1859.
2. W. H. Taylor, 'Obtaining Motive Power', Patent No. 8255, England, 2nd May 1840.
3. *Mechanics Magazine*, Vol. XXXII, pp. 693-696, 1840.
4. *Mechanics Magazine*, Vol. XXXIII, pp. 53, 1840.
5. A. F. Anderson, 'Robert Davidson - Father of the Electric Locomotive', *IEE History of Electrical Engineering Conference*, pp. 8/1-8/18, 1975.
6. D. Mackie, 'The Prospects of Electromagnetism as a Prime Mover', *The Practical Mechanic and Engineering Magazine*, Nov. 1842.
7. P. J. Lawrenson, J. M. Stephenson, P. T. Blenkinson, J. Corda and N. N. Fulton, 'Variable speed switched reluctance motors', *IEE Proc. B*, Vol. 127, No. 4, pp. 253-265, Jul. 1980.
8. T. J. E. Miller, 'Switched reluctance motors and their control', *Oxford Science Publications*, 1992.
9. S. Chan and H. R. Bolton, 'Development of sub-kW single-phase switched reluctance motor drives', *IEE Proc. Int. Conf. Electrical Machines*, Vol. 2, pp. 527-531, Manchester, U.K., Sep. 1992.
10. A. Michaelides and C. Pollock, 'A new magnetic flux pattern to improve the efficiency of the switched reluctance motor', *Conf. Proc. IEEE Ind. Appl. Soc. Annual Meeting*, pp. 226-234, Houston, USA, Oct. 1992.

11. W. F. Ray, R. M. Davis and R. J. Blake, 'Inverter drive for switched reluctance motor circuits and component ratings', *IEE Proc. B*, Vol. 128, No. 2, pp. 126-136, Mar. 1981.
12. T. J. E. Miller, 'Converter volt-ampere requirements of the switched reluctance motor drive', *Conf. Proc. IEEE Ind. Appl. Soc. Annual Meeting*, pp. 813-819, Chicago, USA, Oct. 1984.
13. W. F. Ray, P. J. Lawrenson, R. M. Davis, J. M. Stephenson, N. N. Fulton and R. J. Blake, 'High performance switched reluctance brushless drives', *Conf. Proc. IEEE Ind. Appl. Soc. Annual Meeting*, Toronto, Canada, pp. 1769-1776, Oct. 1985.
14. R. J. Blake, P. D. Webster and D. M. Sugden, 'The application of GTOs to switched reluctance drives', *Conf. Proc. IEE Power Electronics and Variable Speed Drives*, Birmingham, U.K, pp. 24-28, Nov. 1986.
15. J. T. Bass, M. Ehsani, T. J. E. Miller, R. L. Steigerwald, 'Development of a unipolar converter for variable reluctance motor drives', *Conf. Proc. IEEE Ind. Appl. Soc. Annual Meeting*, Toronto, Canada, pp. 1062-1068, Oct. 1985.
16. J. V. Byrne and M. F. McMullin, 'Design of a reluctance motor as a 10kW spindle drive', *Conf. Proc. Motorcon 1982*, Geneva, Switzerland, pp. 10-24, Sep. 1982.
17. D. M. Sugden, R. J. Blake, S. P. Randall and J. M. Stephenson, 'Switched reluctance drives using MOSFETs', *Conf. Proc. 2nd European Power Electronics*, Grenoble, pp. 935-940, Sep. 1987.
18. C. Pollock and B. W. Williams, 'Power converter circuits for switched reluctance motors with minimum number of switches', *IEE Proc. B*, Vol. 137, No. 6, pp. 372-384, Nov. 1990.

19. G. R. Horner, R. J. Lacey, 'Review of Currently Available Rotary Velocity and Position Transducers', *Drives, Motors and Controls journal*, pp. 121-133, Oct. 1984.
20. J. J. Tomasek, 'Integrated resolver-based position and velocity feedback modules', *Proc. 14th Annual Symp. on Incremental Motion Control Systems and Devices*, Champaign, IL, pp. 121-126, Jun. 1985.
21. P. P. Acarnley, R. J. Hill and C. W. Hooper, 'Detection of rotor position in stepping and switched motors by monitoring of current waveforms', *IEEE Trans. Ind. Elec.*, Vol. IE-32, No. 3, pp. 215-222, Aug. 1985.
22. S. R. MacMinn, P. M. Szczesny, W. J. Rzesos, T. M. Jahns, 'Application of sensor integration techniques to switched reluctance motor drives', *Conf. Rec. IEEE Ind. Appl. Soc. Annual Meeting*, Part 1, pp. 584-588, Oct. 1988.
23. W. D. Harris and J. H. Lang, 'A simple motion estimator for VR motors', *Conf. Proc. IEEE Ind. Appl. Soc. Annual Meeting*, pp. 281-286, Pittsburgh, USA, Oct. 1988.
24. J. R. Hill and P. P. Acarnley, United States Patent No. 4, 520, 302.
25. G. Buja and M. Valla, 'Control characteristics of SRM drives', *IEEE Trans. Ind. Elec.*, Vol. 38, No. 5, pp. 313-321, Oct. 1991.
26. N. Matsui, N. Akao and T. Wakino, 'High-precision control of reluctance motors', *IEEE Trans. Ind. Appl.*, Vol. 27, No. 5, pp. 902-907, Sep. 1991.
27. P. H. Chappell, W. F. Ray and R. J. Blake, 'Microprocessor control of a variable reluctance motor', *IEE Proc. B*, Vol. 131, No. 2, pp. 51-60, Sep. 1984.
28. B. K. Bose, T. J. E. Miller, P. M. Szczesny and W. H. Bicknell,

'Microcomputer control of switched reluctance motor', *Conf. Proc. IEEE Ind. Appl. Soc. Annual Meeting*, pp. 542-547, Toronto, Canada, Oct. 1985.

29. B. W. Williams, D. S. Reay and T. C. Green, 'Neural networks used for torque ripple minimisation from a SR motor', *Conf. Proc. European Power Electronics*, Vol. 6, pp. 1-8, Aachen, Germany, 1993.

30. Wallace R. S. and Taylor D. G., 'Low torque ripple switched reluctance motors for direct-drives robotics', *IEEE Trans. Robotics and Automation*, Vol. 7, No. 6, pp. 733-742, 1991.

31. C. Y. Wu and C. Pollock, 'Analysis and reduction of vibration and acoustic noise in the switched reluctance motor', *Conf. Proc. IEEE Ind. Appl. Soc. Annual Meeting*, Toronto, Canada, pp. 106-113, Oct. 1993.

32. P. St.-J. R. French, 'Switched reluctance motor drives for rail traction: relative assessment', *IEE Proc. B*, Vol. 131, No. 5, pp. 209-219, Sep. 1984.

33. W. F. Ray, P. J. Lawrenson, R. M. Davis, J. M. Stephenson, N. N. Fulton and R. J. Blake, 'Switched reluctance motor drives for rail traction: a second view', *IEE Proc. B*, Vol. 131, No. 5, pp. 220-264, Sep. 1984.

34. W. F. Ray, P. J. Lawrenson, R. M. Davis, J. M. Stephenson, N. N. Fulton and R. J. Blake, 'The control of switched reluctance motors for battery electric road vehicles', *Proc. IEE Conf. on Power Electronics and Variable Speed Drives*, pp. 361-364, London, May 1984.

35. J. V. Byrne and J. B. O'Dwyer, 'A high performance variable reluctance drive: a new brushless servo', *Power Conversion and Intelligent Motion*, Vol. 12, pt. 2, pp. 60-66, Feb. 1986.

36. P. P. Acarnley, 'Stepping motors: a guide to modern theory and practice', 2nd

edition, *P. Peregrinus Ltd on behalf of the IEE*, 1984.

37. M. A. El-Khazendar and J. M. Stephenson, 'Analysis and optimisation of a 2-phase self starting switched reluctance motor', *Int. Conf. Electrical Machines*, pp. 1031-1034, Munich, Germany, 1986.

38. J. W. Finch, M. R. Harris, A. Musoke and H. M. B. Metwally, 'Variable speed drives using multi-tooth per pole switched reluctance motors', *13th Incr. Motion Control Sys. Soc. Symposium*, pp. 293-302, Champaign, IL, 1984.

39. R. Arumugam, J. F. Lindsay and R. Krishnan, 'A comparison of the performance of two different types of switched reluctance motor', *Electric Machines and Power Systems*, Vol. 12, pp. 281-286, 1987.

40. J. R. Hendershot, 'Short flux paths cool SR motors', *Machine Design*, pp. 106-110, Sep 1989.

41. C. Pollock, 'Power converter circuits for switched reluctance motors with minimum number of switches', *Ph.D thesis - University of Heriot Watt*, 1989.

42. J. C. Maxwell, 'Treatise in electricity and magnetism', 1881.

43. 'The OPERA-2D reference manual', Vector Fields Ltd, 1993.

44. 'The TOSCA reference manual', Vector Fields Ltd, 1992.

45. J. Kraus, 'Electromagnetics', 3rd edition, *McGraw-Hill*, 1984.

46. Mohan, Undeland, Robbins, 'Power Electronics: Converters, applications and design', *Wiley*, 1989.

47. A. Malvino, 'Electronic principles', 4th edition, *McGraw-Hill*, 1989.

48. XILINX - The programmable gate array data book, USA, 1988.
49. The Jay-Jay eddy current brake manual, Lloyd Instruments, 1989.
50. A. M. Michaelides and C. Pollock, 'Modelling of a new winding arrangement to improve the efficiency of the switched reluctance motor', *IEE Proc. Int. Conf. Elec. Machines*, pp. 213-219, Oxford 1993.
51. J. Corda and J. M. Stephenson, 'An analytical estimation of the minimum and maximum inductances of a doubly salient motor', *Proc. Int. Conf. on Stepping Motors and Systems*, pp. 50-59, Leeds, 1979.
52. J. Simkin and C. W. Trowbridge, 'Three-dimensional nonlinear electromagnetic field computations using scalar potentials', *IEE Proc. B*, Vol. 127, No. 6, pp. 368-374, Nov. 1980.
53. S. Williamson and A. A. Shaikh, 'Three dimensional effects in λ / i diagrams for switched reluctance motors', *IEE Proc. Int. Conf. Electrical Machines*, pp. 489-493, Manchester, UK, Sep. 1992.
54. C. S. Biddlecombe, 'Calculating heat and bending in electromagnetic devices', *Digest No:1993 / 117, IEE Colloquium on Coupling Electromagnetics to other fields*, May 1993.
55. D. Roger, 'Coupling electromagnetic to thermal and stress fields', *Presentation at IEE Colloquium on Coupling Electromagnetics to Other Fields*, May 1993.
56. J. Byrne and J. Lacy, 'Characteristics of saturable stepper and reluctance motors', *Proc. IEE Conf. Small Electrical Machines*, pp. 93-96, London, 1976.
57. T. J. E. Miller and McGilp, 'Nonlinear theory of the switched reluctance motor for rapid computer-aided design', *IEE Proc. B*, Vol. 137, No. 6, pp. 337-347, 1990.

58. J. D. Murray, 'Mathematical biology', *Springer-Verlag*, New York, 1989.
59. A. Fitzgerald, C. Kingsley and S. Umans, 'Electric machinery', 5th edition, *McGraw Hill*, 1993.
60. R. Arumugan, J. Lindsay and R. Krishnan, 'Sensitivity of pole arc / pitch ratio on switched reluctance motor performance', *IEEE Conf. Proc. Ind. Appl. Soc. Annual Meeting*, Pittsburgh, USA, Oct. 1988.
61. J. Faiz and J. Finch, 'Aspects of design optimisation for switched reluctance motors', *IEEE Trans. Energy Conversion*, Vol. 8, No. 4, pp.704-713, Dec. 1993.
62. D. Tormey, D. Torrey and P. Levin, 'Minimum airgap-permeance data for the doubly slotted pole structures, common in variable reluctance motors', *Conf. Proc. Ind. Appl. Soc. Annual Meeting*, Seattle, USA, Oct. 1990.
63. Brook Crompton Parkinson Catalogue 3: Cast Iron TENV Motors.
64. T. Kenjo, 'Stepping Motors and their Microprocessor Controls', *Oxford Science Publications*, 1984.

APPENDIX A

Electromagnetic equations governing the finite element analysis software.

A.1 The two-dimensional finite element code (OPERA-2D).

A magnetic vector potential, A , may be defined such that

$$\mathbf{B} = \nabla \times \mathbf{A} \quad (\text{A.1})$$

Maxwell's first law (eqn. 2.4) may be rewritten in terms of the magnetic vector potential as

$$\nabla \times \left[\mathbf{E} + \frac{\partial \mathbf{A}}{\partial t} \right] = 0 \quad (\text{A.2})$$

Introducing the electrostatic potential, V , the electric field strength is expressed as

$$\mathbf{E} + \frac{\partial \mathbf{A}}{\partial t} = -\nabla V \quad (\text{A.3})$$

Current density, \mathbf{J} , may be separated into two components, namely the source current density, \mathbf{J}_s , and induced current density, \mathbf{J}_e , where

$$\mathbf{J}_s = -\sigma \nabla V \quad (\text{A.4})$$

$$\mathbf{J}_e = -\sigma \frac{\partial \mathbf{A}}{\partial t} \quad (\text{A.5})$$

The term σ denotes conductivity. Expanding the source and induced current density components in eqn. 2.8 and expressing the magnetic field strength in terms of the flux density gives

$$\nabla \times \frac{1}{\mu} \mathbf{B} + \sigma \frac{\partial \mathbf{A}}{\partial t} = -\mathbf{J}_s \quad (\text{A.6})$$

This equation describes eddy current phenomena in terms of a specified source

current density and relevant material properties. The magnetostatic model of the switched reluctance motor has coils with known current density. The current density is therefore prescribed and the conductivity is set to zero. In OPERA-2D, the equation to be solved for the static magnetic field using the magnetic vector potential, is derived by substituting for the flux density, \mathbf{B} , in eqn. A.6 [43]. In two dimensions, this simplifies to

$$\nabla \times \left(\frac{1}{\mu} \nabla \times \mathbf{A}_z \right) = -J_s \quad (\text{A.7})$$

A.2 The three-dimensional algorithm (OPERA-3D / TOSCA).

Stationary magnetic fields consist of both solenoidal and rotational components. The field produced by electric currents has a rotational component inside the volumes where currents flow. In the exterior space the field is solenoidal but the scalar potential is multi-valued. The field produced by magnetised volumes is solenoidal. It is convenient to separate the total field into two parts in order to obtain a description of the field in terms of the scalar potential. The total field intensity \mathbf{H} may be expressed as the sum of the source field intensity \mathbf{H}_s and the reduced field intensity \mathbf{H}_M

$$\mathbf{H} = \mathbf{H}_s + \mathbf{H}_M \quad (\text{A.8})$$

The source field can be obtained directly from the Biot-Savart law by integration over the region Ω_J containing current

$$\mathbf{H}_s = \int_{\Omega_J} \frac{\mathbf{J} \times \mathbf{R}}{|\mathbf{R}|^3} d\Omega_J \quad (\text{A.9})$$

The field satisfies

$$\nabla \times \mathbf{H}_s = \mathbf{J} \quad (\text{A.10})$$

so that

$$\nabla \times \mathbf{H}_M = 0 \quad (\text{A.11})$$

The reduced field intensity can now be represented using the reduced scalar potential, ϕ ,

$$\mathbf{H}_M = -\nabla\phi \quad (\text{A.12})$$

The divergence of the flux density \mathbf{B} is always zero. Introducing the permeability tensor, μ , and combining the expressions for the source and reduced field intensity, gives the partial differential equation for the reduced scalar potential

$$\nabla \cdot \mu \nabla \phi - \nabla \cdot \mu \left(\int_{\Omega_r} \frac{\mathbf{J} \times \mathbf{R}}{|\mathbf{R}|^3} d\Omega_r \right) = 0 \quad (\text{A.13})$$

This equation can easily be solved using the finite element method. However, in magnetic materials the two parts of the field \mathbf{H}_M and \mathbf{H}_S tend to be of similar magnitude but opposite direction. Therefore, cancellation occurs in computing the field intensity \mathbf{H} , that results in a loss in accuracy [44]. The errors can be completely avoided by combining the total and reduced scalar potential representations. Hence, exterior to the volumes where currents flow the total field can be represented using the total magnetic scalar potential Ψ

$$\mathbf{H} = -\nabla\Psi \quad (\text{A.14})$$

where the total magnetic scalar potential satisfies

$$\nabla \cdot \mu \nabla \Psi = 0 \quad (\text{A.15})$$

The minimal combination consists of using the reduced scalar potential only inside volumes where current flows and the total potential everywhere else.

APPENDIX B

Data sheets for power semiconductor devices used in this project

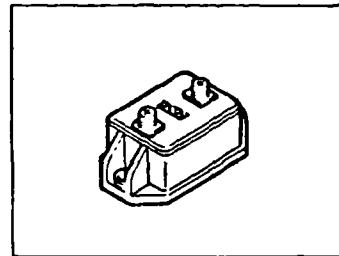
SIEMENS

SIMOPAC® MOSFET Modules

BSM 181 F (C)
BSM 181 FR

$V_{DS} = 800 \text{ V}$
 $I_D = 34 \text{ A}$
 $R_{DS(on)} = 0.32 \Omega$

- Power module
- Single switch
- FREDFET
- N channel
- Enhancement mode
- Package with insulated metal base plate
- Circuit diagram: Fig. 1a ¹⁾



Type	Ordering code
BSM 181 F (C)	C67076-A1052-A2
BSM 181 FR	C67076-A1057-A2

Maximum Ratings

Parameter	Symbol	Values	Unit
Drain-source voltage	V_{DS}	800	V
Drain-gate voltage, $R_{GS} = 20 \text{ k}\Omega$	V_{DGR}	800	
Gate-source voltage	V_{GS}	± 20	
Continuous drain current, $T_C = 25 \text{ }^\circ\text{C}$	I_D	34	A
Pulsed drain current, $T_C = 25 \text{ }^\circ\text{C}$	I_{Dpul}	136	
Operating and storage temperature range	T_j T_{stg}	$-55 \dots +150$	$^\circ\text{C}$
Total power dissipation, $T_C = 25 \text{ }^\circ\text{C}$	P_{tot}	700	W
Thermal resistance	$R_{th JC}$	≤ 0.18	K/W
Chip - case	$R_{th CH}$	≤ 0.05	
Case - heat sink			
Isolation test voltage ²⁾ , $t = 1 \text{ min.}$	V_{is}	2500	V_{ac}
Creepage distance, drain-source	-	16	mm
Clearance, drain-source	-	11	
DIN humidity category, DIN 40 040	-	F	-
IEC climatic category, DIN IEC 68-1	-	55/150/56	

¹⁾ See chapter Package Outlines.

²⁾ Isolation test voltage between drain and base plate referred to standard climate 23/50 in acc. with DIN 50 014, IEC 146, para 492.1.

Electrical Characteristics

at $T_j = 25\text{ }^{\circ}\text{C}$, unless otherwise specified.

Parameter	Symbol	Values			Unit
		min.	typ.	max.	
Static characteristics					
Drain-source breakdown voltage $V_{GS} = 0, I_D = 0.25 \text{ mA}$	$V_{(BR)DSS}$	800	-	-	V
Gate threshold voltage $V_{GS} = V_{DS}, I_D = 1 \text{ mA}$	$V_{GS(th)}$	2.1	3.0	4.0	
Zero gate voltage drain current $V_{DS} = 800 \text{ V}, V_{GS} = 0$ $T_J = 25 \text{ }^{\circ}\text{C}$ $T_J = 125 \text{ }^{\circ}\text{C}$	I_{DSS}	-	20 300	250 1000	μA
Gate-source leakage current $V_{GS} = 20 \text{ V}, V_{DS} = 0$	I_{GSS}	-	10	100	nA
Drain-source on-state resistance $V_{GS} = 10 \text{ V}, I_D = 21 \text{ A}$	$R_{DS(on)}$	-	0.25	0.32	Ω

Dynamic characteristics

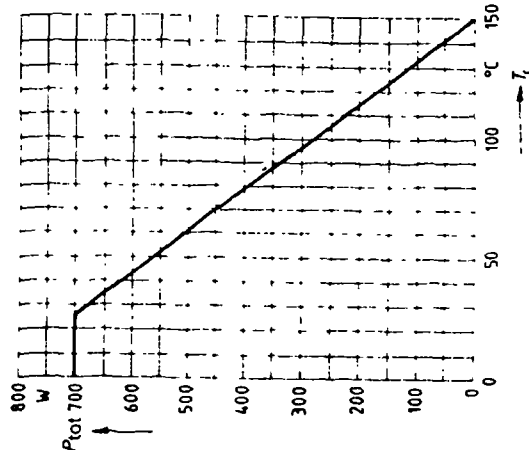
Forward transconductance $V_{DS} \geq 2 \times I_D \times R_{DS(on)max}, I_D = 21\text{ A}$	g_{fs}	15	35	-	S
Input capacitance $V_{GS} = 0, V_{DS} = 25\text{ V}, f = 1\text{ MHz}$	C_{iss}	-	22	30	nF
Output capacitance $V_{GS} = 0, V_{DS} = 25\text{ V}, f = 1\text{ MHz}$	C_{oss}	-	1	1.5	
Reverse transfer capacitance $V_{GS} = 0, V_{DS} = 25\text{ V}, f = 1\text{ MHz}$	C_{rss}	-	0.48	0.8	
Turn-on time t_{on} ($t_{on} = t_{d(on)} + t_r$) $V_{CC} = 400\text{ V}, V_{GS} = 10\text{ V}, I_D = 21\text{ A}, R_{GS} = 3.3\text{ }\Omega$	$t_{d(on)}$	-	60	-	ns
	t_r	-	90	-	
Turn-off time t_{off} ($t_{off} = t_{d(off)} + t_f$) $V_{CC} = 400\text{ V}, V_{GS} = 10\text{ V}, I_D = 21\text{ A}, R_{GS} = 3.3\text{ }\Omega$	$t_{d(off)}$	-	350	-	
	t_f	-	70	-	

Electrical Characteristics (continued)
at $T_j = 25\text{ }^{\circ}\text{C}$, unless otherwise specified.

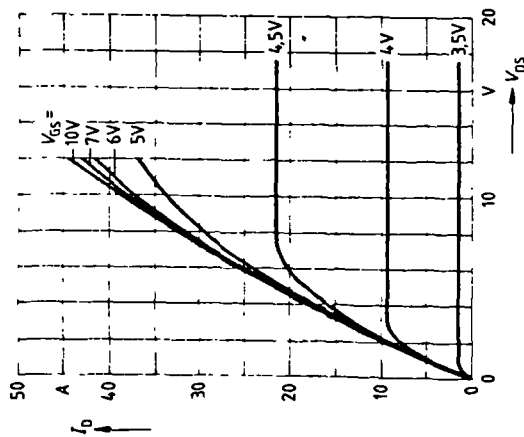
Parameter	Symbol	Values			Unit
		min.	typ.	max.	
Fast-recovery reverse diode					
Continuous reverse drain current $T_C = 25\text{ }^{\circ}\text{C}$	I_s	-	-	34	A
Pulsed reverse drain current $T_C = 25\text{ }^{\circ}\text{C}$	I_{SM}	-	-	136	
Diode forward on-voltage $I_F = 68\text{ A}$, $V_{GS} = 0$	V_{SD}	-	1.6	2	V
Reverse recovery time $I_F = I_s$, $di_F/dt = 100\text{ A}/\mu\text{s}$, $V_R = 100\text{ V}$	t_{rr}	/	300	-	ns
Reverse recovery charge $I_F = I_s$, $di_F/dt = 100\text{ A}/\mu\text{s}$, $V_R = 100\text{ V}$ $T_J = 25\text{ }^{\circ}\text{C}$ $T_J = 125\text{ }^{\circ}\text{C}$	Q_{rr}	-	-	2 16	μC

Characteristics at $T_j = 25^\circ\text{C}$, unless otherwise specified.

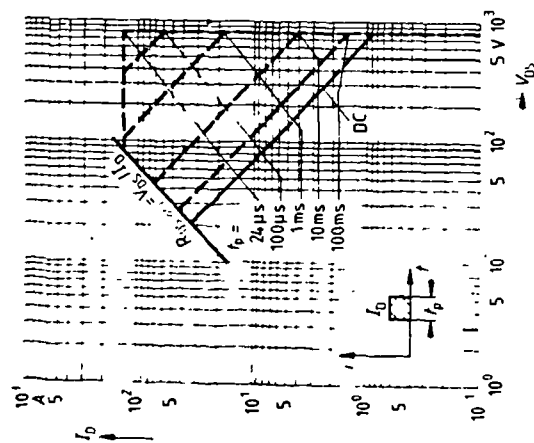
Total power dissipation $P_{\text{tot}} = f(T_c)$
parameter: $T_j = 150^\circ\text{C}$



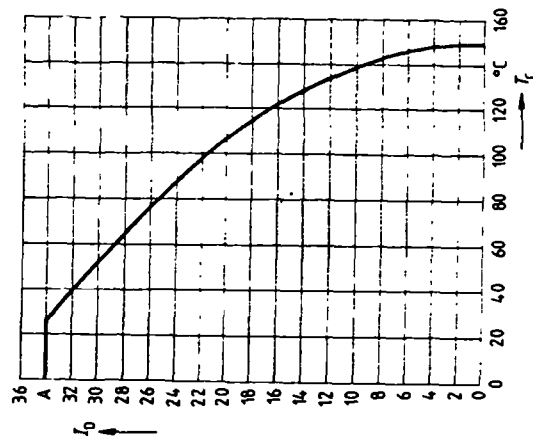
Typ. output characteristics $I_D = f(V_{DS})$
parameter: $t_p = 80 \mu\text{s}$



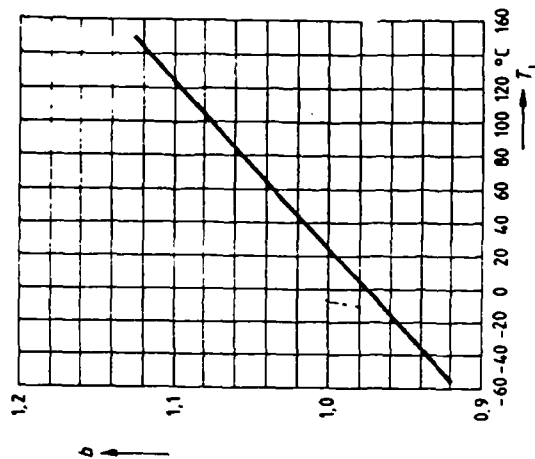
Safe operating area $I_D = f(V_{DS})$
parameter: single pulse, $T_c = 25^\circ\text{C}$, $T_j \leq 150^\circ\text{C}$



Continuous drain current $I_D = f(T_c)$
parameter: $V_{GS} \geq 10 \text{ V}$, $T_j = 150^\circ\text{C}$

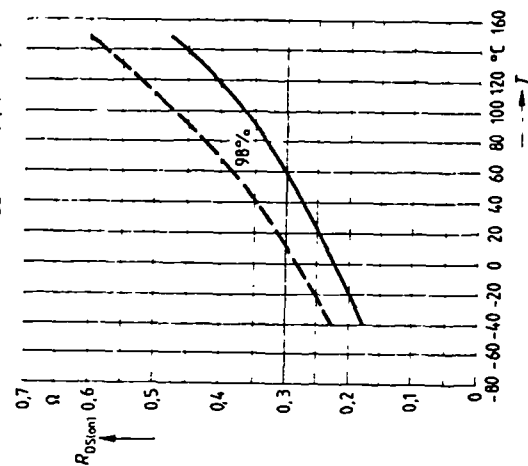


$V_{\text{arioss}}(T_j) = b \times V_{\text{arioss}}(25^\circ\text{C})$

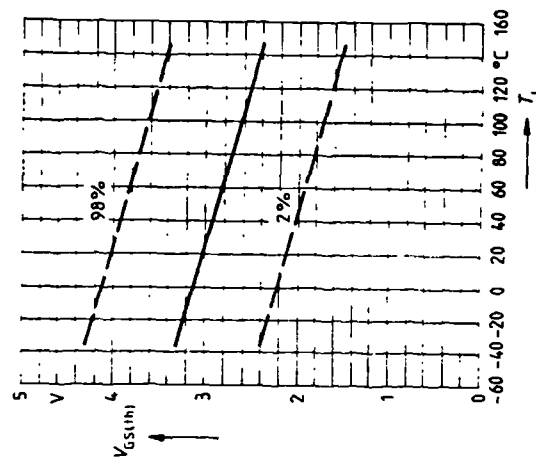


Drain-source on-state resistance
 $R_{\text{DS(on)}} = f(T_j)$

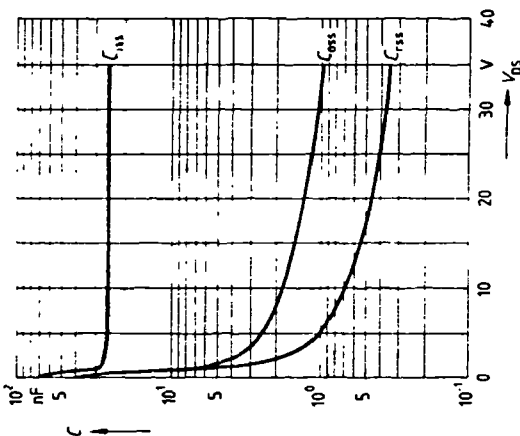
parameter: $I_D = 34 \text{ A}$, $V_{GS} = 10 \text{ V}$, (spread)



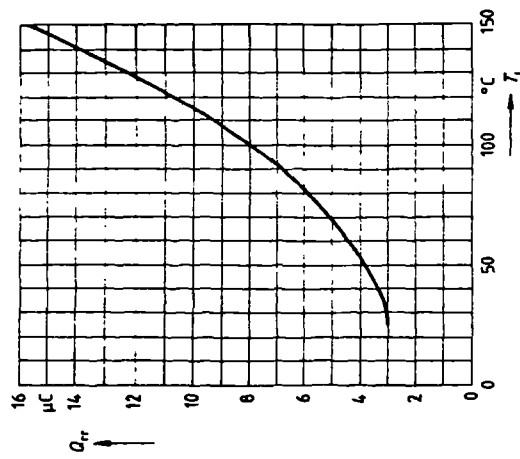
Gate threshold voltage $V_{GS(th)} = f(T_j)$
parameter: $V_{DS} = V_{GS}$, $I_D = 1 \text{ mA}$



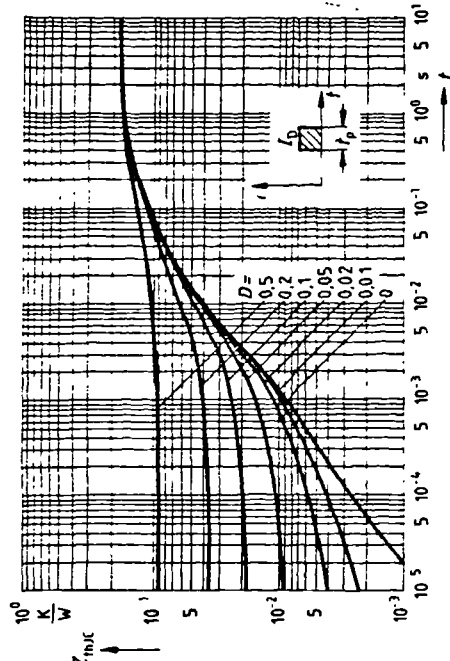
Typical capacitances $C = f(V_{GS})$
parameter: $V_{GS} = 0$, $f = 1$ MHz
(spread)



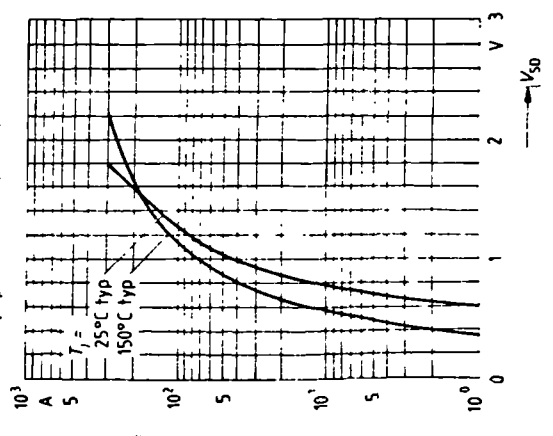
Typ. reverse recovery charge $Q_{rr} = f(T_J)$
parameter: $di/dt = 100$ A/ μ s, $I_F = 34$ A
 $V_R = 100$ V



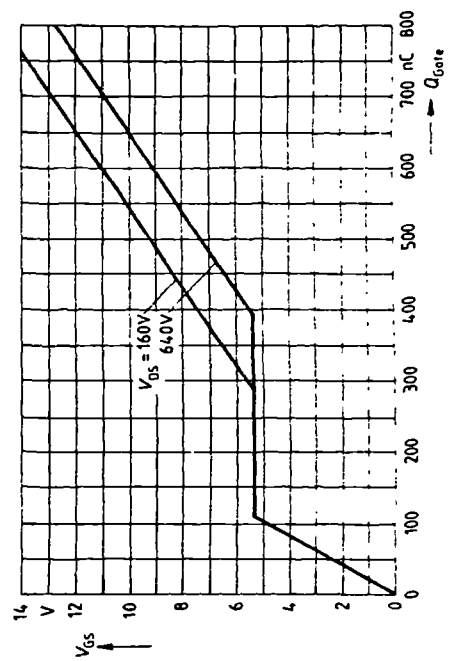
Transient thermal impedance $Z_{thJC} = f(t)$
parameter: $D = I_p/T$



**Forward characteristics of fast-recovery
reverse diode $I_F = f(V_{SD})$**
parameter: $T_J, t_p = 80$ μ s, (spread)

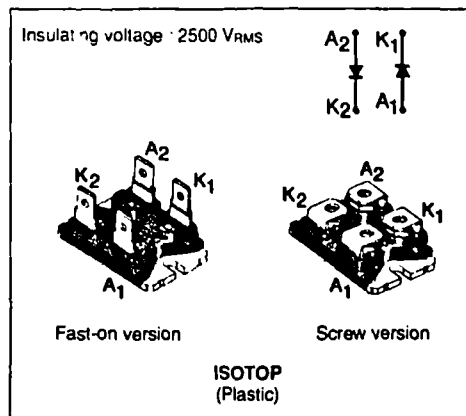


Typ. gate charge $V_{GS} = f(Q_{Gate})$
parameter: $I_{Dpul} \approx 51$ A



FAST RECOVERY RECTIFIER DIODE

- VERY HIGH REVERSE VOLTAGE CAPABILITY
- VERY LOW REVERSE RECOVERY TIME
- VERY LOW SWITCHING LOSSES
- LOW NOISE TURN-OFF SWITCHING
- INSULATED : Capacitance 45pF



DESCRIPTION

Double rectifiers suited for switching mode power supply.

ABSOLUTE RATINGS

Symbol	Parameter		Value	Unit
V_{RRM}	Repetitive Peak Reverse Voltage		1000	V
V_{RSM}	Non Repetitive Peak Reverse Voltage		1000	V
I_{FRM}	Repetitive Peak Forward Current	$t_p \leq 10\mu s$	375	A
I_{FRMS}	RMS Forward Current	per leg	70	A
$I_{F(AV)}$	Average Forward Current	$T_{case} = 50^\circ C$ $\delta = 0.5$ per leg	30	A
I_{FSM}	Surge Non Repetitive Forward Current	$t_p = 10ms$ Sinusoidal	200	A
P	Power Dissipation	$T_{case} = 50^\circ C$ per leg	60	W
T_{stg} T_J	Storage and Junction Temperature Range		- 40 to + 150	$^\circ C$

THERMAL RESISTANCES

Symbol	Parameter		Value	Unit
$R_{th(j-c)}$	Junction-case	per leg total	1.5 0.8	$^\circ C/W$
$R_{th(c)}$	Coupling		0.1	$^\circ C/W$

ELECTRICAL CHARACTERISTICS STATIC CHARACTERISTICS

Symbol	Test Conditions	Min.	Typ.	Max.	Unit
I_R	$T_J = 25^\circ\text{C}$ $V_R = V_{RRM}$			100	μA
	$T_J = 100^\circ\text{C}$			5	mA
V_F	$T_J = 25^\circ\text{C}$ $I_F = 30\text{A}$			1.9	V
	$T_J = 100^\circ\text{C}$			1.8	

RECOVERY CHARACTERISTICS

Symbol	Test Conditions	Min.	Typ.	Max.	Unit
t_{rr}	$T_J = 25^\circ\text{C}$ $I_F = 1\text{A}$ $di_F/dt = -15\text{A}/\mu\text{s}$ $V_R = 30\text{V}$ $I_F = 0.5\text{A}$ $I_R = 1\text{A}$ $I_{rr} = 0.25\text{A}$			165	ns
				70	

TURN-OFF SWITCHING CHARACTERISTICS (Without Series Inductance)

Symbol	Test Conditions	Min.	Typ.	Max.	Unit
t_{inM}	$di_F/dt = -120\text{A}/\mu\text{s}$ $V_{CC} = 200\text{V}$ $I_F = 30\text{A}$ $di_F/dt = -240\text{A}/\mu\text{s}$ $L_p \leq 0.05\mu\text{H}$ $T_J = 100^\circ\text{C}$ See figure 11			200	ns
t_{inM}	$di_F/dt = -120\text{A}/\mu\text{s}$ $di_F/dt = -240\text{A}/\mu\text{s}$		120	19.5	A
			22		

TURN-OFF OVERVOLTAGE COEFFICIENT (With Series Inductance)

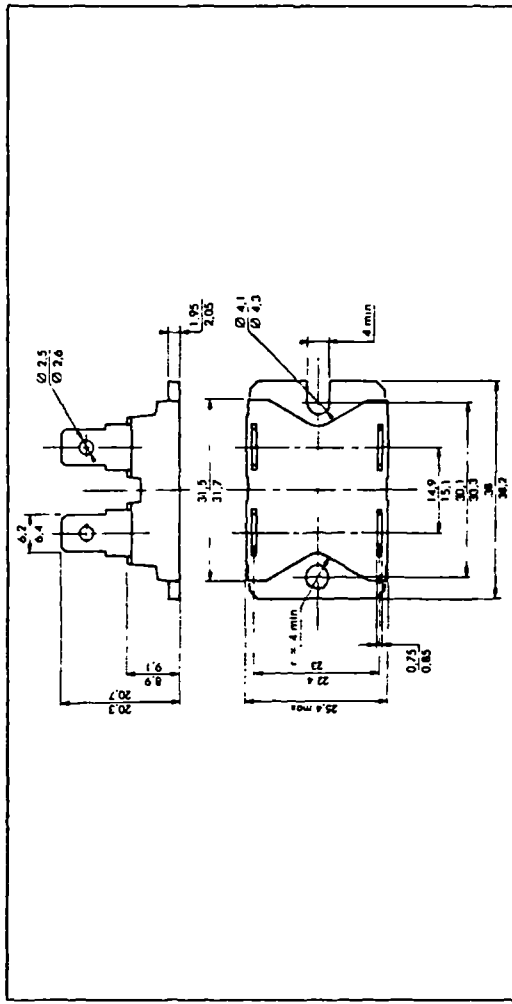
Symbol	Test Conditions	Min.	Typ.	Max.	Unit
$\frac{V_{RP}}{V_{CC}}$	$T_J = 100^\circ\text{C}$ $V_{CC} = 200\text{V}$ $I_F = I_F(AV)$ $di_F/dt = -30\text{A}/\mu\text{s}$ $L_p = 5\mu\text{H}$ See figure 12			4.6	

To evaluate the conduction losses use the following equation :

$$V_F = 1.47 + 0.010 I_F$$

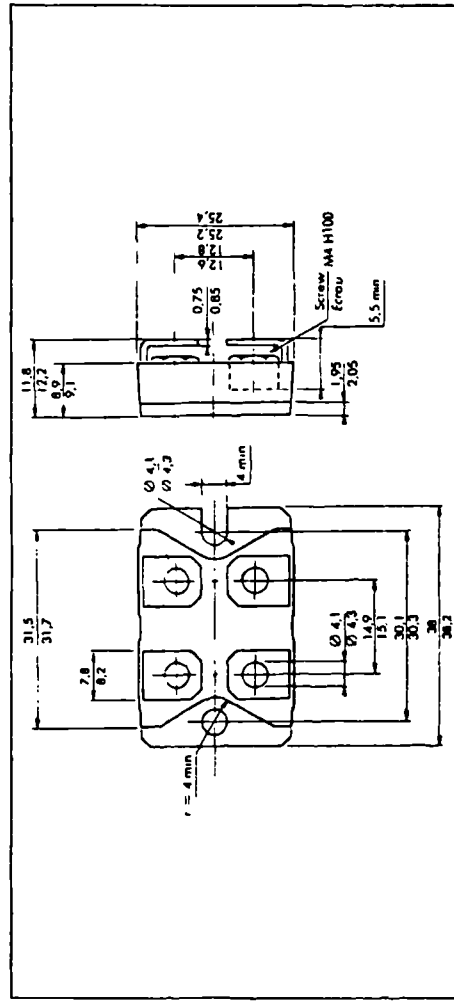
$$P = 1.47 \times I_F(AV) + 0.010 I_F^2(RMS)$$

PACKAGE MECHANICAL DATA ISOTOP Plastic : FAST-ON VERSION



Marking : type number

ISOTOP Plastic : SCREW VERSION



Marking : type number + suffix V

Recommended screw torque value : $13 \pm 2\text{kg cm}$.
Maximum screw torque value : 15kg cm .

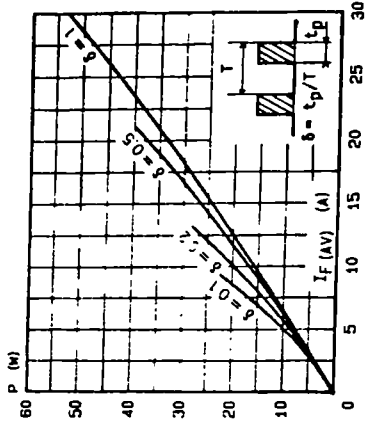


FIGURE 1 : Low frequency power losses versus average current.

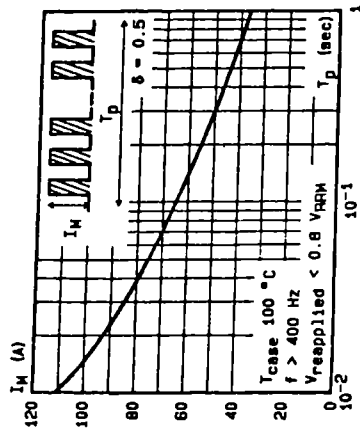


FIGURE 3 : Non repetitive peak surge current versus overload duration.

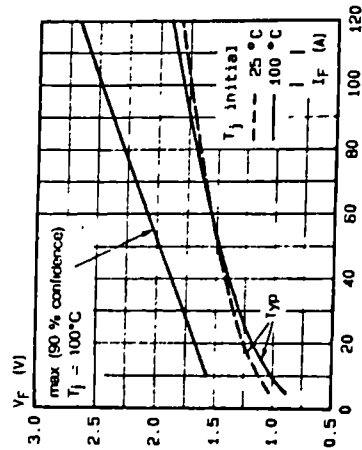


FIGURE 5 : Voltage drop versus forward current.

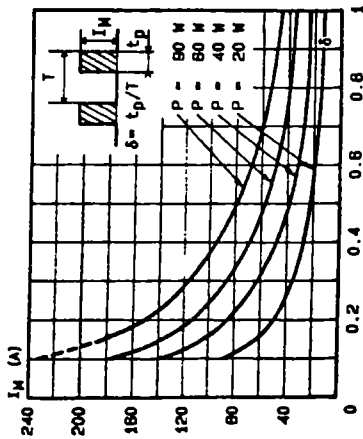


FIGURE 2 : Peak current versus form factor.

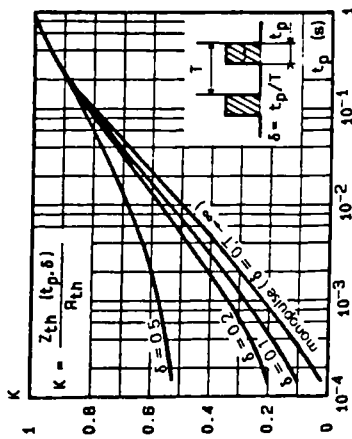


FIGURE 4 : Thermal impedance versus pulse width.

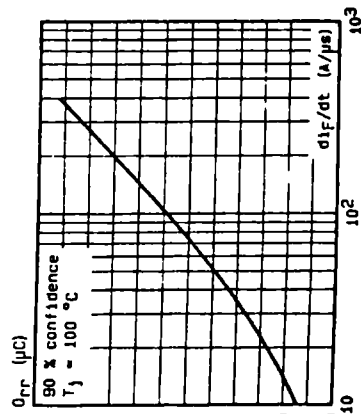


FIGURE 6 : Recovery charge versus di/dt .

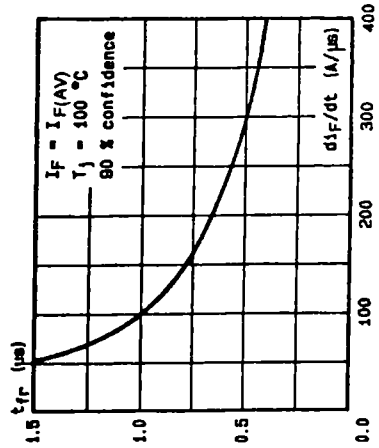


FIGURE 7 : Recovery time versus di/dt .

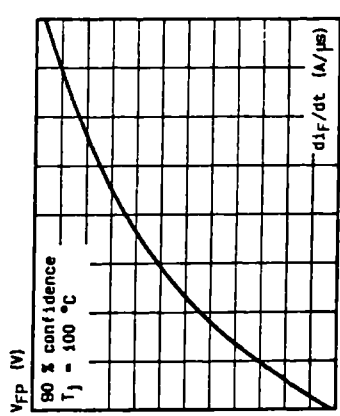


FIGURE 8 : Peak forward voltage versus di/dt .

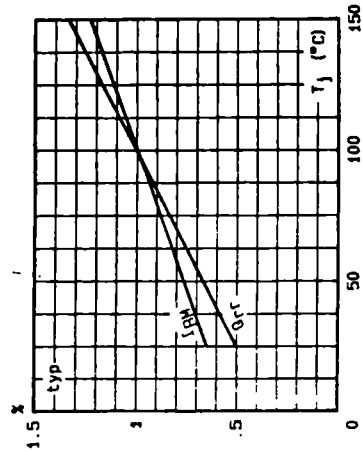


FIGURE 9 : Dynamic parameters versus junction temperature.

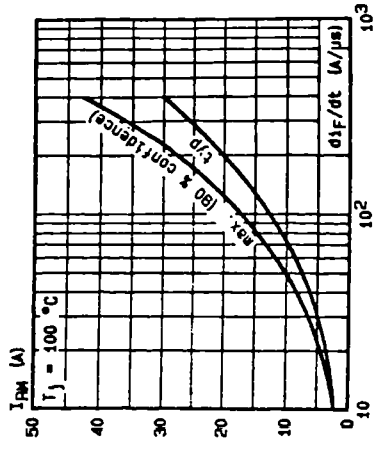


FIGURE 10 : Peak reverse current versus di/dt .

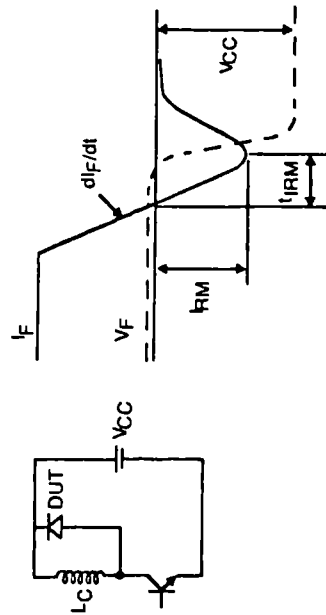


Figure 11 : Turn-off switching characteristics (without series inductance).

APPENDIX C

Comparison on the basis of equal copper losses.

The switched reluctance motor copper losses P_{Cu} may be computed from

$$P_{Cu} = I_{rms}^2 R q \quad (C.1)$$

where I_{rms} denotes the rms value of the phase current and R the resistance of the phase winding. Assuming square pulses, the rms phase current can be expressed in terms of the peak phase current, I_m , as

$$I_{rms} = I_m \sqrt{\frac{T_{on}}{T}} \quad (C.2)$$

where T denotes the period ($1/f$) of the current pulse train and T_{on} represents the on-state time. The following relations also hold

$$I_m = J_m A \quad (C.3)$$

and

$$R = \rho \frac{l_w}{A_w} \quad (C.4)$$

where A_w denotes the cross-sectional area of copper and l_w the length of copper wire. Equation C.1 can therefore be rewritten as

$$\begin{aligned} P_{Cu} &= J_m^2 A^2 \sqrt{\frac{T_{on}}{T}} \rho \frac{l_w}{A_w} q \quad (C.5) \\ &= (J_m^2 A_w) (q \sqrt{\frac{T_{on}}{T}}) (\rho l_w) \end{aligned}$$

The conductor length can be assumed constant in motors of equal stack length, though the length of the end winding is dependent on the stator tooth width. As

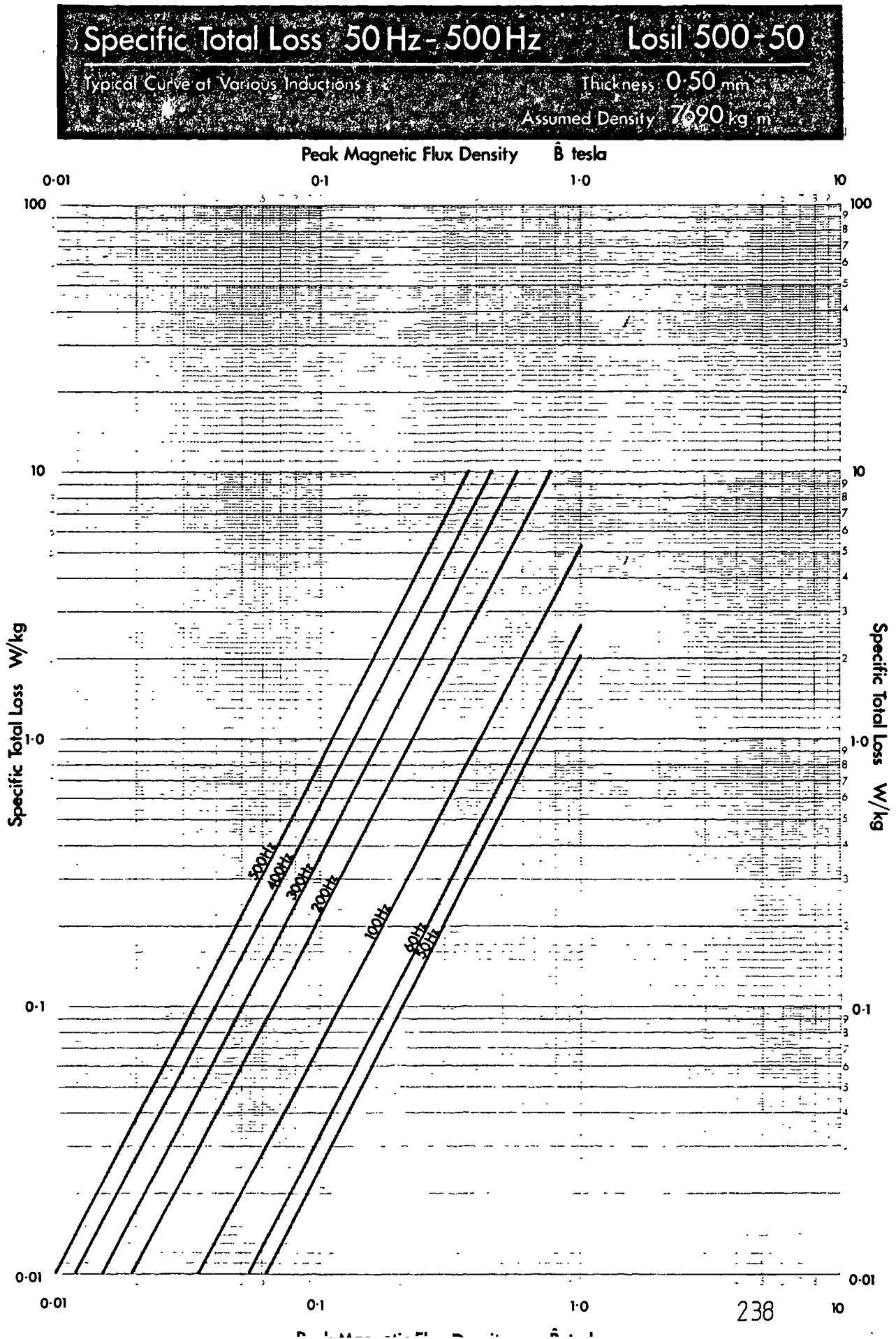
an approximation, the resistivity ρ is taken as constant. It is known however that ρ is temperature dependent, and the rate of temperature rise in the phase windings, which plays a significant role in the copper loss, increases with current density. In addition, the heat transfer coefficient from the conductor to the iron is higher in machines that exhibit lower iron losses. It is evident that an accurate loss model can only be obtained by conducting a thorough thermal analysis of the switched reluctance motor. This is beyond the scope of this argument, therefore

$$P_{Cu} \propto (J_m^2 A_w) \left(q \sqrt{\frac{T_{on}}{T}} \right) \quad (C.6)$$

In finite element modelling, area A_w is taken to be that of the largest rectangular (single turn) coil that can be slipped over the pole without interfering with its neighbouring coils.

APPENDIX D

Loss data and BH curves for LOSIL 500-50.



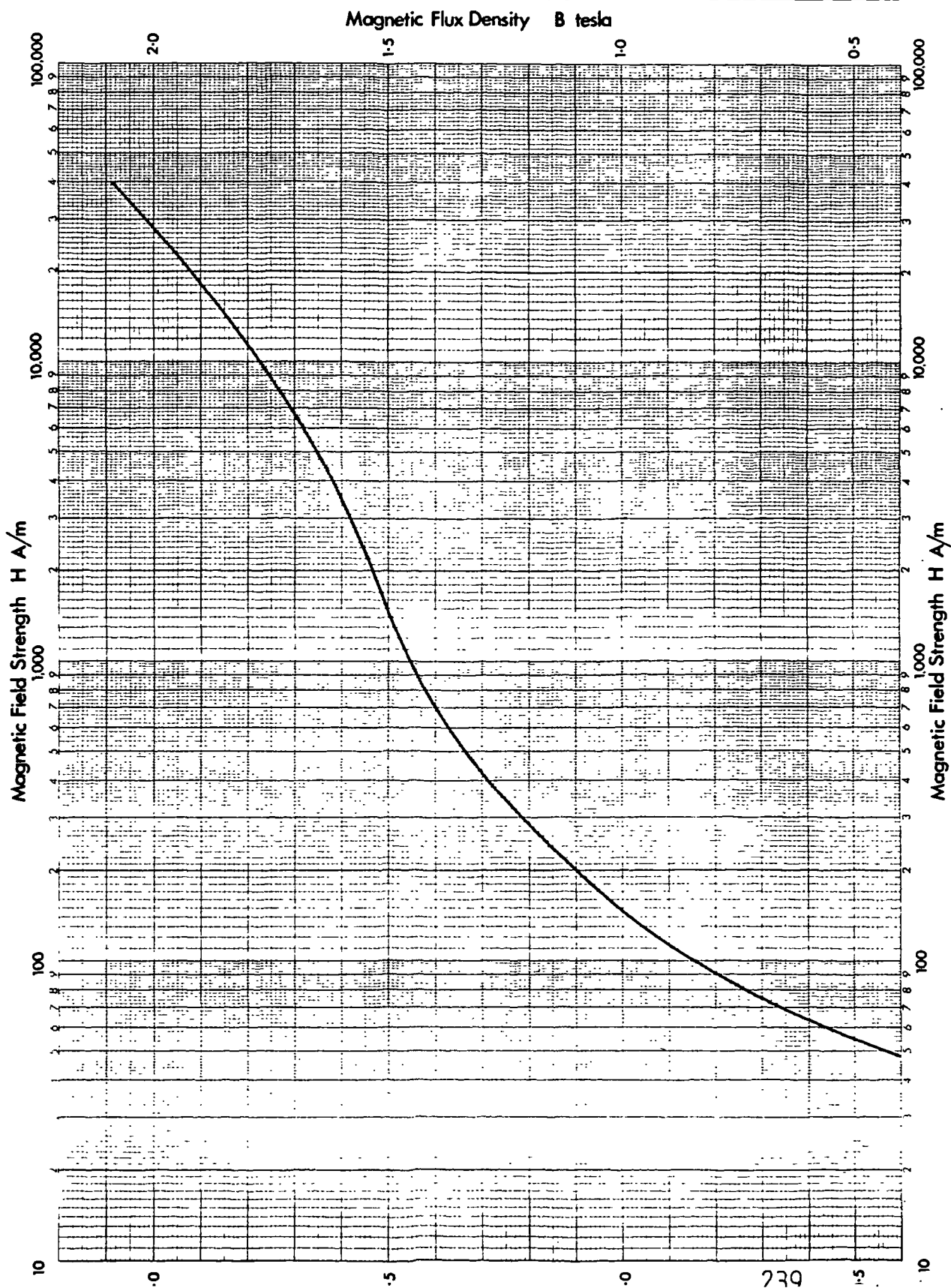
Normal Magnetization

Typical Curve

Losil 500

D.C. Permeameter Method

Assumed Density: 7690 kg m³



APPENDIX E

Operating principles of stepping motors.

E.1 The variable reluctance stepping motor.

The construction of a single-stack variable reluctance stepping motor is identical to that of the switched reluctance motor. However, the VRM is designed to operate 'open loop' (i.e. without position sensing) and maintain accurate position-control. In contrast, switched reluctance machines operate with position feedback. This is needed to produce a variable speed drive of high efficiency.

A multi-stack type of variable reluctance stepping motor is also manufactured. Each stack corresponds to a phase and is misaligned with respect to its neighbouring stacks. The stator and rotor have the same tooth pitch.

E.2 The permanent magnet (PM) stepping motor.

A stepping motor that uses a permanent magnet in a cylindrically shaped rotor is called a permanent magnet stepping motor. The operating principle of this type of motor can be illustrated by means of a cross-section of a 2-phase structure, shown in fig. E.1. The rotor consists of four radially magnetised permanent magnet sections, namely N-S-N-S. The stator has eight poles around which coils are wound to make up two phase windings. The phase windings need to be excited with positive and negative current polarities, and hence the requirement for a bipolar power converter circuit arises. This type of converter utilises more power devices than unipolar configurations and suffers from the danger of shoot-through faults.

Rotation in one direction can be achieved if the excitation sequence

$$i_{A+}, i_{B+}, i_{A-}, i_{B-}, i_{A+}$$

is adopted. Electromagnetic torque is produced by the interaction of the magnetic fields produced by the stator windings and the permanent magnet sections comprising the rotor. This gives rise to 'excitation' forces acting on the structure. The phase windings are excited in turn to produce the correct magnetic polarities in the stator poles which pull the rotor in place. The stepping action is illustrated in fig. E.1. The step angle of this motor is 45° .

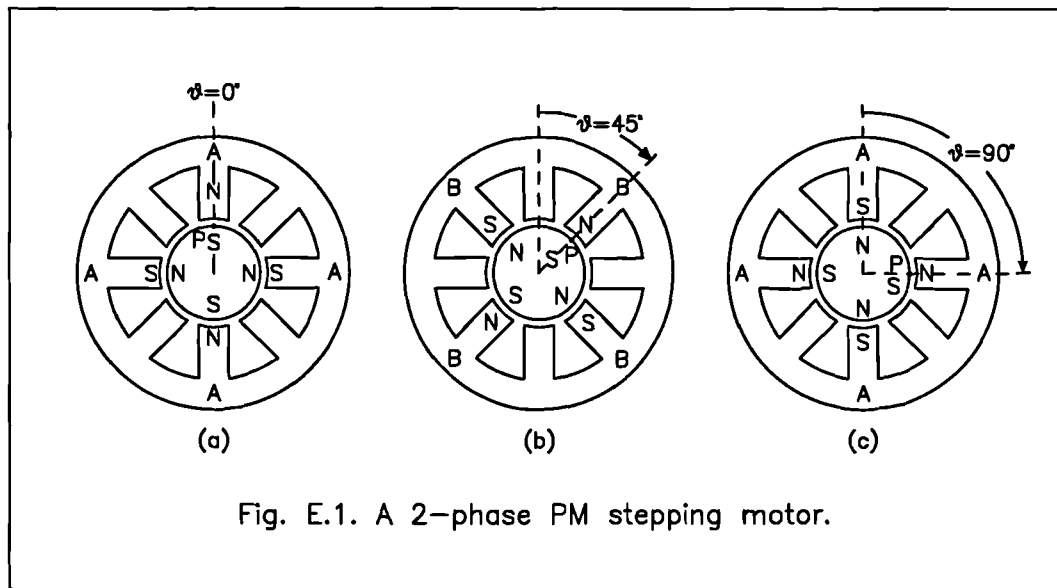


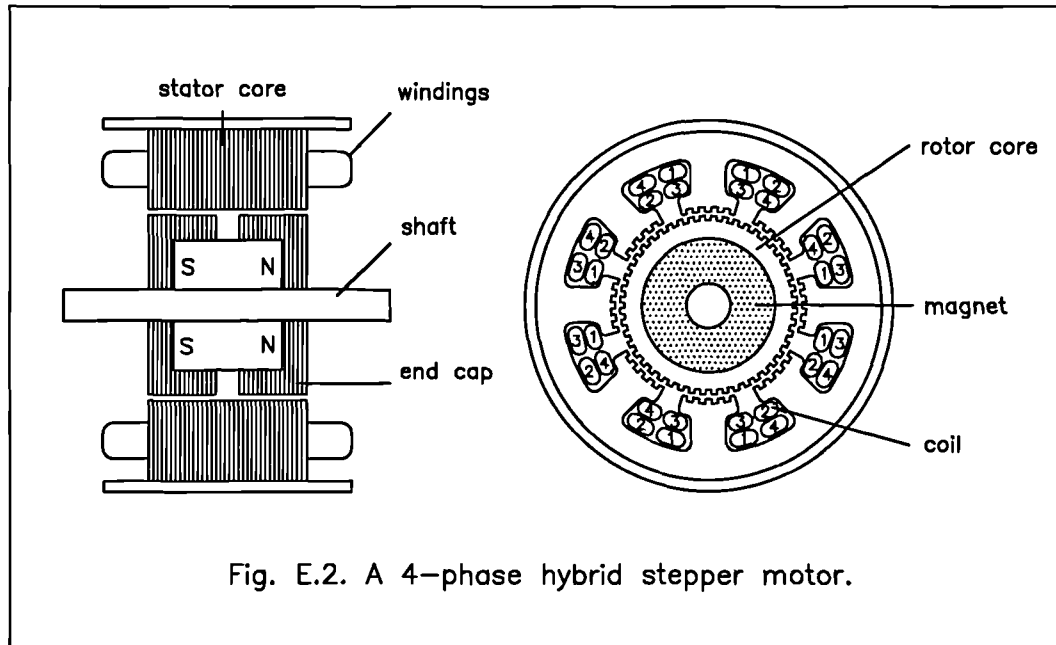
Fig. E.1. A 2-phase PM stepping motor.

The PM stepping motor exhibits good torque per unit volume and high efficiency. The main disadvantage associated with the use of a permanent magnet is the additional cost and weight penalty that is incurred. The torque / inertia ratio of the PM stepping motor is low.

E.3 The hybrid stepping motor.

Hybrid stepping motors are operated under the combined principles of the variable reluctance and the permanent magnet type of stepping motors. The construction of a 4-phase hybrid stepper is illustrated in fig. E.2. A cylindrically shaped permanent magnet lies in the core of the rotor and is magnetised along the length of the machine (axially). Two end sections, consisting of equal numbers of poles, are fitted on each end of the magnet. The teeth of the two sections are misaligned

with respect to each other by half a tooth pitch. The stator structure is similar to that of the switched reluctance type, though the winding connections are different. In the hybrid stepper, coils of two different phases may be wound on one pole.



T. Kenjo [64] demonstrates most effectively the operating principles of the hybrid stepper with the aid of a 'split-and-unrolled' model of a 4-phase motor, reproduced in fig. E.3. Dotted curves represent flux due to the magnet. Field distributions produced by excitation of phase windings are represented by solid curves. When pole II is excited as a north pole N, and pole IV as a south pole S, a driving force toward the left appears in the south pole cross-section because in the toothed structure under pole II the fields produced by the excitation windings and the permanent magnet sections act in the same direction. Field components oppose one another in the toothed structure under pole IV hence weakening the right-oriented force. A left-oriented force is also produced in the north pole cross-section. An equilibrium position is reached after the rotor has moved by one quarter tooth pitch. The stator excitation can now be transferred to poles I and III so as to maintain rotation.

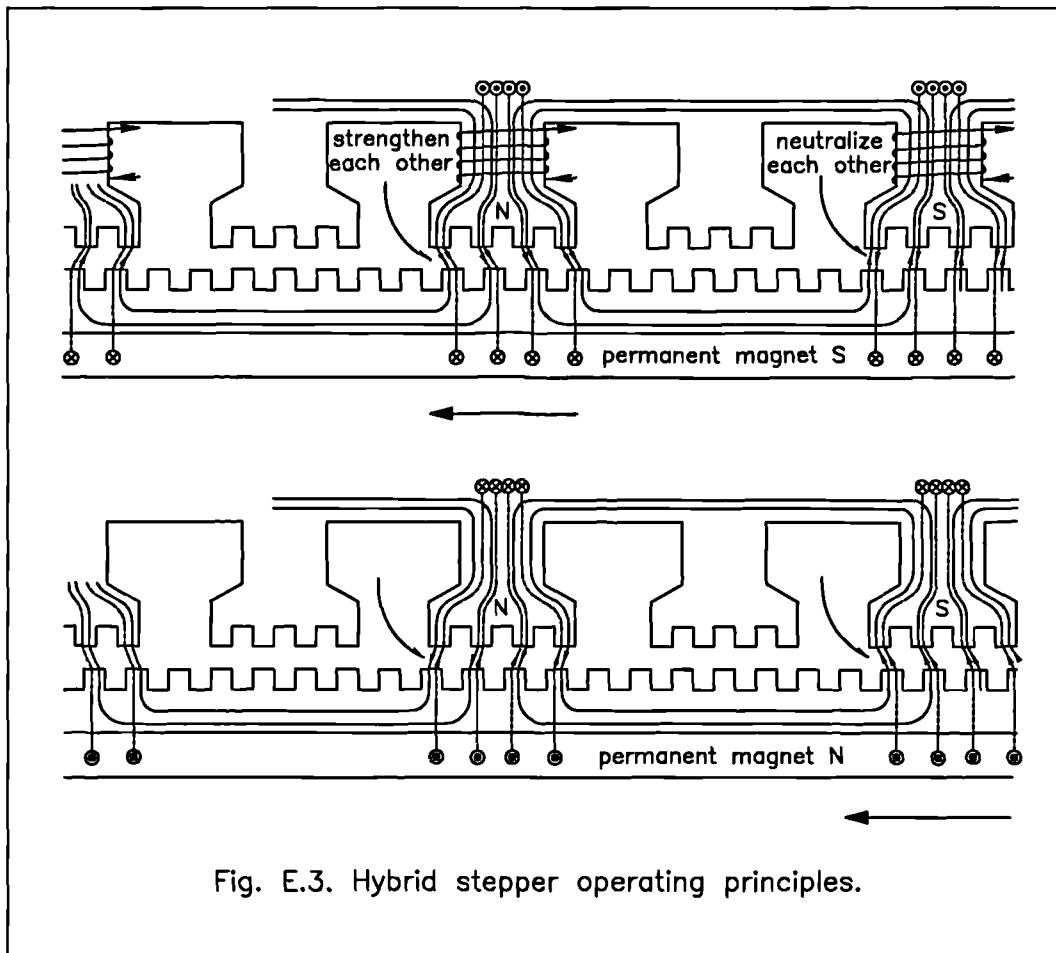


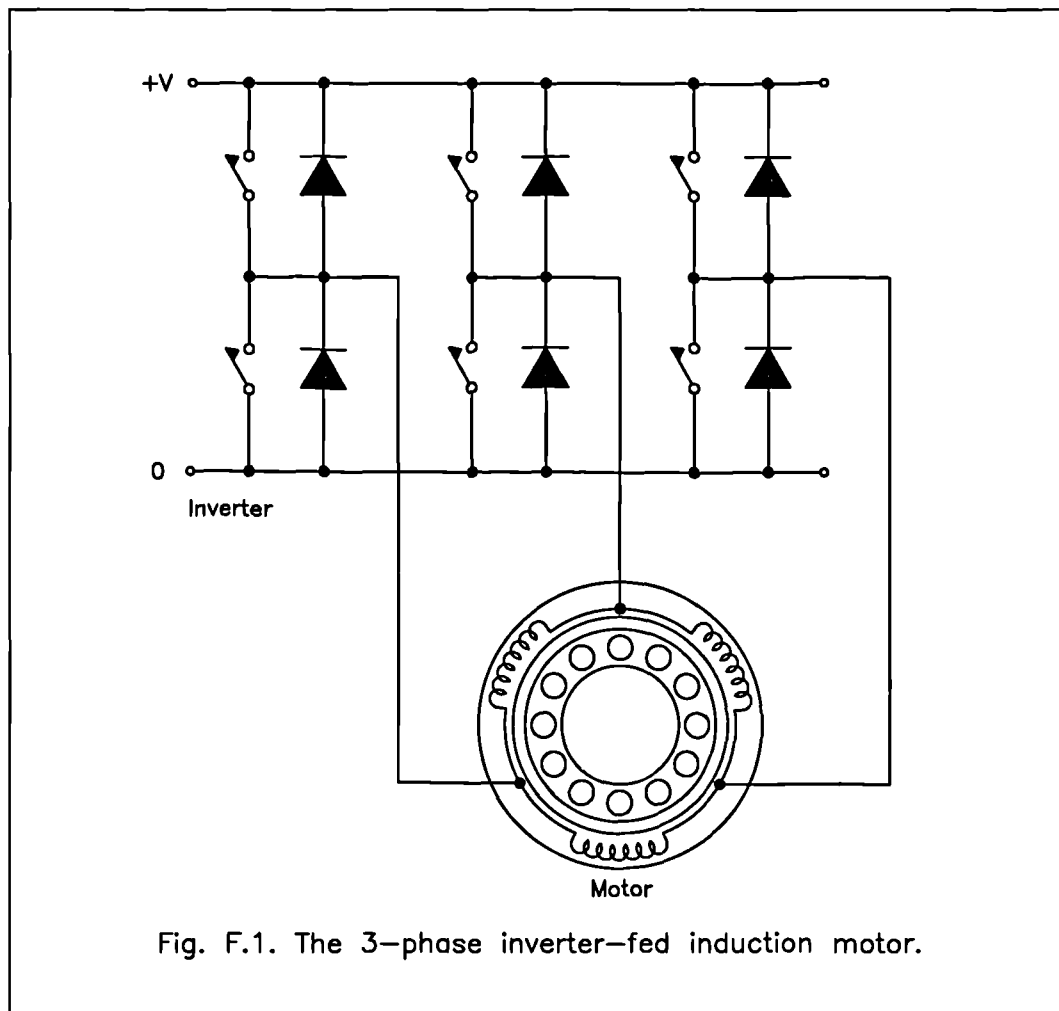
Fig. E.3. Hybrid stepper operating principles.

The tooth structures on the rotor and stator of the hybrid stepper are designed to realise small step angles which alleviates the need for position feedback. This type of stepping motor has been used extensively in positioning applications i.e. robot arms and XY tables. A high level torque output is achieved from a small volume, though the cost and weight of the permanent magnet has limited production to machines rated at only a few kW (maximum).

APPENDIX F

A brief description of the induction motor.

In the induction motor, the coils forming the stator winding are arranged so that conductors are distributed in slots around the stator periphery. The rotor can be of the 'wound' or (more commonly) 'squirrel cage' type. In the 'squirrel cage' type, solid aluminium bars are cast into the rotor slots and short circuited. This type of rotor construction is more rugged and reliable than the 'wound' type. Power electronic circuits are used to control rotor speed.



In the induction motor, alternating current is supplied directly to the stator windings and by induction (or transformer action) to the rotor windings. The stator

produced magnetic field interacts with the currents induced in the rotor windings and gives rise to excitation forces according to Lorenz's law

$$\mathbf{F} = \mathbf{J} \times \mathbf{B} \quad (\text{F.1})$$

Simple single phase motors are used extensively in industry, where rugged fixed speed drives are required. The 3-phase inverter-fed induction motor, shown in fig. F.1, holds a significant share of the variable speed drive market. Torque and speed control can be achieved in an inverter-fed induction motor by varying the voltage and frequency respectively.